Nano-sized Transition Metal Fluorides as Positive Electrode Materials for Alkali-Ion Batteries

Dissertation
zur Erlangung des akademischen Grades

doctor rerum naturalium
(Dr. rer. nat.)

im Fach Chemie
Anorganische und Allgemeine Chemie

eingereicht an der
Mathematisch-Naturwissenschaftlichen Fakultät
der Humboldt-Universität zu Berlin

von
M.Sc. Andréa Joris Quentin Martin

Präsidentin der Humboldt-Universität zu Berlin
Prof. Dr.-Ing. Dr. Sabine Kunst

Dekan der Mathematisch-Naturwissenschaftlichen Fakultät
Prof. Dr. Elmar Kulke

Gutachter/innen:
1. Prof. Dr. Erhard Kemnitz
2. Prof. Dr. Nicola Pinna
3. Dr. Damien Dambournet

Tag der mündlichen Prüfung: 27.02.2020

Abstract

Metal fluoride compounds appear as very appealing candidates for the next generation of alkali-ion battery cathodes. However, many drawbacks prevent this family of compounds to be applicable to storage systems. Metal fluorides demonstrate a high insulating character, due to the polarization of the metal-fluorine bond, which prevents the good transport of the electrons within the electrode material. Additionally, the mechanisms involved during the discharge/charge processes when more than one lithium atom is stored per metal atom engender large volume changes and a drastic reorganization of the material, which induces poor reversibility. In order to answer these problematics, the present thesis reports the elaboration of innovative synthesis routes for transition metal fluoride compounds and the application of these fluoride materials in alkali-ion battery systems. Among the compounds reported in this work, two different classes can be established: structures free of alkali ions, and structures containing alkali ions. In the first part, the syntheses and electrochemical properties of the free-alkali materials are studied, specifically, cobalt(II) fluoride and anhydrous iron(III) fluoride supported onto graphene oxide. Those materials exhibit high initial capacity but very poor cyclability and low C-rate capability. *Ex-situ* X-ray diffraction and transmission electron microscopy demonstrate that the low reversibility of the processes is mainly due to the conversion reaction occurring during their discharge/charge. In the second part, the syntheses of transition metal fluoride perovskites are reported, as well as their electrochemical properties. $NaFeF_3$ demonstrates excellent performances and reversibility. The study of the mechanisms occurring during its charge/discharge processes towards different alkali systems by *ex-situ* and *operando* X-ray diffraction reveals that its crystalline framework is maintained along the cycles, resulting in high reversibility and excellent C-rate performance. This retention of the crystal framework is possible by an electrochemical stabilization of a cubic conformation of FeF_3, which is usually only observable at high temperature (400 °C), and can be explained by lower reorganizations within the crystal framework. Similar electrochemical properties could be observed for $KFeF_3$ and NH_4FeF_3, where ammonium ions are reported for the first time as a charge carrier in alkali-ion systems.

Kurzfassung

Übergangsmetallfluoridverbindungen sind sehr vielversprechende Kandidaten für die nächste Generation von Kathoden für Alkaliionenbatterien. Dennoch verhindern einige Nachteile dieser Materialklasse ihre Anwendung in Energiespeichermedien. Metallfluoride haben aufgrund der Polarisierung der Metal-Fluor-Bindung eine stark isolierende Wirkung, was den Elektronenfluss innerhalb des Elektrodenmaterials beeinträchtigt. Außerdem bewirken die Mechanismen beim Lade-/Entladevorgang, in welchen mehr als ein Lithiumatom pro Metallatom gespeichert wird, große Volumenänderungen und somit eine drastische Reorganisation des Materials, welche nur geringfügig umkehrbar ist. Um diese Nachteile zu reduzieren, werden in dieser Arbeit innovative Syntheserouten für die Umwandlung von Metallfluoridverbindungen sowie deren Anwendung in Alkaliionenbatterien vorgestellt. Die hier gezeigten Verbindungen werden in zwei Klassen eingeteilt: alkaliionenfreie und alkaliionenenthaltende Strukturen. Im ersten Teil werden die Synthesen und die elektrochemischen Eigenschaften der alkalifreien Materialien, genauer Kobalt(II)fluorid und wasserfreies Eisen(III)fluorid auf einem Graphenoxidträgermaterial, untersucht. Diese Materialien zeigen eine hohe Ausgangskapazität aber nur bei sehr geringen C-Raten und zudem sehr geringe Zyklisierbarkeiten. *Ex-situ*-Röntgendiffraktometrie- und Transmissionenelektronenmikroskopiestudien zeigen, dass die geringe Umkehrbarkeit der Prozesse hauptsächlich aus der Umwandlungsreaktion während des Be-/Entladens resultieren. Im zweiten Teil werden sowohl die Synthesen als auch die elektrochemischen Eigenschaften von Perowskiten aus Übergangsmetallfluoriden vorgestellt. $NaFeF_3$ zeigt hierbei exzellente Leistungen und Reversibilitäten. Die Untersuchung der Mechansimen durch *ex-situ* und *operando* Röntgendiffraktometrie während der Be- und Entladeprozesse hinsichtlich verschiedener Alkalisysteme zeigt, dass das kristalline Netzwerk über den Zyklus erhalten bleibt. Dies führt zur hohen Reversibilität und hohen Leistung selbst bei hohen C-Raten. Der Erhalt der Kristallstruktur wird durch elektrochemische Stabilisierung der kubischen Konformation von FeF_3 ermöglicht, welche normalerweise erst bei hohen Temperaturen (400 °C) beobachtet wird und durch geringere Reorganisationen innerhalb des Kristallgerüsts erklärt werden kann. Ähnliche elektrochemische Eigenschaften können für $KFeF_3$ und NH_4FeF_3 beobachtet werden, wobei erstmalig von Ammoniumionen als Ladungsträger in Alkaliionensystemen berichtet wird.

Acknowledgement

First of all, I would like to express my gratitude to both of my supervisors, Prof. Dr. Erhard Kemnitz, and Prof. Dr. Nicola Pinna, who believed in my potential and gave me the opportunity to carry out my Ph.D. at the Humboldt-Universtät zu Berlin. Moreover, their guidance and support allowed me to conduct my work in the best conditions.

I would like to thank all my co-workers, from the AK-Pinna and AK-Kemnitz, with whom I spent a great time during these four years. Specials thanks to Dr. Donato E. Conte and Dr. Yafei Fan who taught me most of what I know about the battery sciences, to Dr. Guylhaine Clavel and Christoph Erdmann who always guided me along my TEM measurements and helped me with many practical issues in the laboratory, to Dr. Matthias Karg for sharing his skills about X-ray diffraction and so many other things, to Stefan Mahn and Florian Shütz who always helped me in my synthesis experiments, to Dr. Nicolas Goubard with whom I have shared my studies during the second part of my Ph.D. study, and to Wenlei Xu, Alexander Birnbaum, Kai Skrodczky and Sebastian Wahl who always supported me and with whom I spent great times apart from working in the laboratory. I would like also to thank Enrique S. Santiago and Zishu Xu who endured my supervision along their Bachelor and Master studies, respectively. Many thanks to Dr. Marie-Liesse Doublet who helped me with my researches and from whom I learned a lot. A special Thank to Clara F. Marshall, without whom this thesis would not have been possible. I would like also to thank Dr. Patricìa Russo, Dr. Gudrun Scholz, Dr. Michael Feist, Dr. Thoralf Krahl, Dr. Yu Wang, Dr. Lidia Di Carlo, Dr. Yanlin Wu, Dr. Romain Poupart, Dr. Rui Zhang, Dr. Valentina Scalise, Dr. Abdal-Azim Al-Terkawi, Dr. Lucas Ahrem, Karl Kronfled, Sayed M. El-Refaei, Xianying Han, Sofia Santi, Hamid Raza, Chengxu Shen, Jiao Wang, Yvan Ecochard, Shirin Usmani, Pooja Tomar, and the services of the Humboldt Universität zu Berlin including Analytical services, Workshops and Supplies. Thanks to the Deutsche Forschungsgemeinschaft and the Humboldt-Universität to have financed the four years of Ph.D. .

I would like of course to thank my friends and family, especially my parents who always supported me in the pathway I followed until the achievement of my studies. Finally, I would like to express a very special thanks to my partner, Maëva-Charlotte Kervarec, who encouraged me, understood me and supported me with unconditional love all along this period of my life.

Table of contents

ABSTRACT **3**

KURZFASSUNG **4**

ACKNOWLEDGEMENT **5**

TABLE OF CONTENTS **6**

CHAPTER 1

INTRODUCTION **8**

1. MOTIVATION OF THIS THESIS 8
2. OBJECTIVES AND STRUCTURATION OF THIS THESIS 12
REFERENCES 15

CHAPTER 2

BACKGROUND **17**

1. INTRODUCTION 17
1.1. A little bit of history *17*
1.2. Storage and conversion devices *17*
2. LITHIUM-ION BATTERIES 20
2.1. Generalities *20*
2.2. Working principles of a Li-ion battery *21*
2.3. Anodic active material in LIBs *24*
2.4. Active materials at the positive side *28*
3. SODIUM-ION BATTERIES 31
3.1. Generalities *31*
3.2. Active materials at the negative side *32*
3.3. Active materials at the positive side *33*
4. METAL FLUORIDES USED AS CATHODES FOR LI-ION BATTERIES 35
4.1. Generalities *35*
4.2. Metal difluorides as positive electrode for Na- & Li-ion batteries *37*
4.3. Iron(III) fluoride as positive electrode for Na- & Li-ion batteries *38*
4.4. Perovskite iron fluoride phases for alkali-ion batteries *41*
REFERENCES 43

CHAPTER 3

EXPERIMENTAL SETUP **50**

1. PREPARATION METHODS 50
1.1. Synthesis *50*
1.2. Different sol-gel routes *50*
1.3. Reactants *52*
2. CHARACTERIZATION METHODS 52
2.1. X-ray powder diffraction *52*
2.2. Transmission electronic microscopy and Energy-dispersive X-ray spectroscopy *53*
2.3. Fourier-transform infrared spectroscopy *54*
3. ELECTROCHEMICAL CHARACTERIZATION METHODS 54
3.1. Electrode preparation and cell assembly *54*
3.2. Cyclic voltammetry *55*
3.3. Galvanostatic cycling *55*
REFERENCES 56

CHAPTER 4

SYNTHESIS AND ELECTROCHEMICAL BEHAVIOR OF METAL DI- AND TRIFLUORIDES **57**

1. INTRODUCTION 57
2. COBALT(II) FLUORIDE 57
2.1. Synthesis of cobalt(II) fluoride compounds & composites and their structural and morphological characterization *57*
2.2. Electrochemical behavior of cobalt(II) fluoride compounds & composite materials *62*
3. IRON DI- & TRIFLUORIDE 66
3.1. Synthesis and characterization of iron(II) fluoride *66*
3.2. Synthesis and characterization of anhydrous iron(III) fluoride compounds and composites *69*
3.3. Electrochemical behavior of the anhydrous iron(III) fluoride composites *78*
4. CONCLUSION 85
5. EXPERIMENTAL SECTION 87
ANNEXE 90
REFERENCES 93

CHAPTER 5

SYNTHESIS, ELECTROCHEMICAL BEHAVIOR AND STRUCTURAL CHANGES OF ORTHORHOMBIC $NAMF_3$ 95

1. INTRODUCTION 95
2. SYNTHESIS OF ORTHORHOMBIC PEROVSKITE FLUORIDES 95
3. ELECTROCHEMICAL BEHAVIOR OF THE ORTHORHOMBIC PEROVSKITE FLUORIDE COMPOUNDS 100
4. MECHANISTIC STUDY OF $NaFeF_3$ CYCLING TOWARDS SODIUM AND LITHIUM 105
5. CONCLUSION 110
6. EXPERIMENTAL SECTION 112
ANNEXE 113
REFERENCES 118

CHAPTER 6

SYNTHESIS, ELECTROCHEMICAL BEHAVIOR AND STRUCTURAL CHANGES OF CUBIC FLUORIDE PEROVSKITES 119

1. INTRODUCTION 119
2. SYNTHESIS OF THE CUBIC PEROVSKITE FLUORIDES ($KFeF_3$ AND NH_4FeF_3) 120
3. ELECTROCHEMICAL BEHAVIOR OF THE CUBIC PEROVSKITE FLUORIDES ($KFeF_3$ AND NH_4FeF_3) 124
4. STRUCTURAL CHANGES DURING THE DIS/INSERTION PROCESSES OF ALKALI IONS IN CUBIC PEROVSKITE FLUORIDES 131
5. CONCLUSION 135
6. EXPERIMENTAL SECTION 137
ANNEXE 138
REFERENCES 140

CONCLUSION 142

LIST OF ABBREVIATIONS 147

LIST OF FIGURES 148

LIST OF TABLES 152

Chapter 1

Introduction

1. Motivation of this thesis

Since the beginning of the industrial revolution, the energy supply of our society has been mainly powered by fossil fuels (comprising oil, coal, and gas). Within this period, those non-renewable sources have been one of the major driving forces of the technological advancements, resulting in an economic and social boom [1,2,3]. Those combustibles are still playing a dominant role in the worldwide energy, even if they are known to have big repercussions on human health and on the environment. They are not only used in our cars but also largely in the production of our electricity [4,5]. Their abundance and accessibility determine their price, which also depends upon the geopolitical issues involved in their geographic allocations. For example, coal is the most used fossil fuel for electrical production due to its low price and high accessibility, but it is also the most polluting among fossil fuels [6,7]. Our society is currently facing big changes in the global economic balance, having great influences on energy demands across the world. The rise of Asian countries led by India and China drives to an immense increase in the world global energy consumption [8,9]. Moreover, many countries in Africa are recently experiencing a period of rapid economic growth, which will generate a huge energy demand as well [10,11]. All in all, projections assume that the demand for electricity should have doubled by 2050 [12,13]. But most of the oil fields are located in unstable countries (85% of the reserves are in the Middle East), making the oil supply sensitive to shortage and crisis as it has already been the case more than once in the past [14]. Additionally, to the dependence of oil suppliers and the harmful characters that the use of these combustibles generates regarding human health and the environment, they have above all the biggest contribution concerning the production of gases responsible in the "greenhouse effect", which has a huge impact on climate change [15,16,17]. Indeed, the main actual concern is how global warming currently occurring influences our climate. The IPCC (Intergovernmental Panel on Climate Change) predicted different scenarios directly related to greenhouse gases emissions, in which a global increase of 4.5 °C is depicted if our energy supply is still based on fossil fuels [18]. This huge increase would have catastrophic consequences on our environment, resulting in the rise of the ocean levels, draining of wetlands, climate disruptions, etc. On the contrary, if governments follow policies based mainly on sustainable development as it has been stated during the COP21, greenhouse gases emissions should be lower than it was in 1990, placing

the temperature rise under 2 °C and greatly moderating our impact on the climate. Nonetheless, regarding the actual worldwide reaction, only a small production of our energy would be generated by renewable methods by 2035 (**Figure 1.1**) and augmentation of 3 °C seems to be more credible.

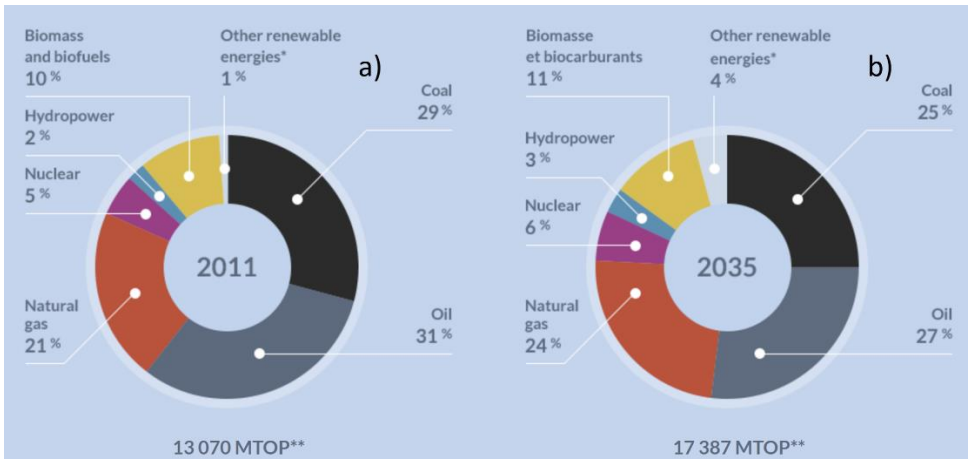

Figure 1.1. *Global energy mix* **(a)** *in 2011 and* **(b)** *previsions in 2035 according to the baseline new policies scenario* [19].

** Solar, wind, geothermal, ocean and other ** Million tons of oil equivalent.*

Therefore, greener and renewable alternatives of energy sources have to be urgently developed, as well as a "realistic" regulation of the energy supply, in order to avoid the irremediable impact that our society could have on the environment and regulate our energy supply. The energetic transition from fossil fuels to sustainable sources of energy cannot be done all of a sudden, but rather through an energy mix. Since the last decades, great advancements on wind turbines and solar panels have effectively been reached, making wind and sun viable green energy sources [20,21,22]. The proportion of these renewable energies will increase within the panel of energy sources which are already available. However, to implement these sources of energy production, efficient and cheap devices have to be developed to store large and intermittent amounts of generated electricity. Indeed, electrical energy must be stored during peak production to be able to release it during peak demand (**Figure 1.2**). For this purpose, giant battery facilities seem to be a good option. A positive example is the "big battery" implemented in Australia by Tesla in 2017, which has already proven to be useful during several electricity shortages created by serious summer conditions [23]. The technology, on which the company Tesla bet, is the Li-ion battery one, capable of storing electrical energy with high efficiency. By now, the chemistry used within this technology is too expensive to be applied worldwide in

large facilities, therefore cheaper and more powerful materials have to be found to lower the cost of these devices to make them economically viable compared to the commonly used energy storage technologies. Other similar technologies also based on electrochemical storage could be considered too, if their technologic advancements would be competitive enough compared to the already well-studied Li-ion technology. Na-ion batteries (NIBs), which have chemical working mechanisms very close to the ones of the Li-ion batteries (LIBs), appear to be a good candidate for grid energy storage. The active materials, usually made of metal oxides or polyanion structures, could become cheaper than the ones used in the Li-ion batteries, in combination to the use of aluminum at both sides of the full-cell as current collector. Their performances would probably not match the ones of the Li-ion technology, but they would be perfectly fitted for stationary [24].

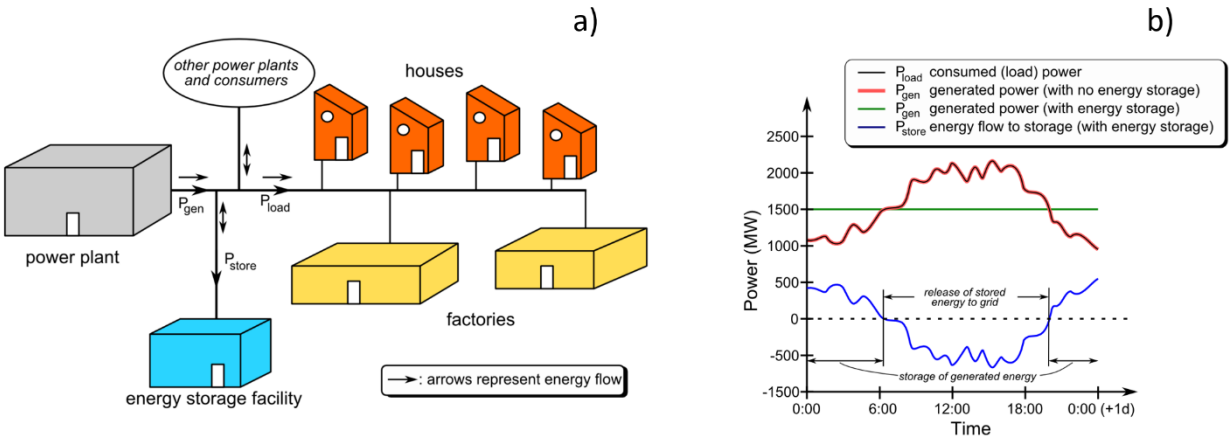

Figure 1.2. **(a)** *Scheme of the distribution and storage within the electrical grid and* **(b)** *comparison of the electrical grid with and without energy storage* [25].

On the other hand, the emergence of the electrical cars went from fantasy to reality to public opinion during the last decade, even though they were a proven concept since the end of the XIX century [26]. Towards environmental and sanitary concerns engendered by the internal combustion engine (ICE) cars, governments encouraged the development of electric cars. In China, for example, air pollution accounts for one million deaths per year without taking into account the influence on the food productions and other repercussions. That is why the Chinese government invested around $60 billion within the last decade into electric vehicles, representing by now 40% of the electrical cars on the market [27]. This rush to electric cars would allow the country to improve its air quality and to be less dependent upon the oil producer countries and to become one of the world leaders in automotive production. In Europe, the

British government stated that by 2040, the sales of ICE vehicles will be forbidden to be replaced slowly by electrical cars, as shown in **Figure 1.3**.

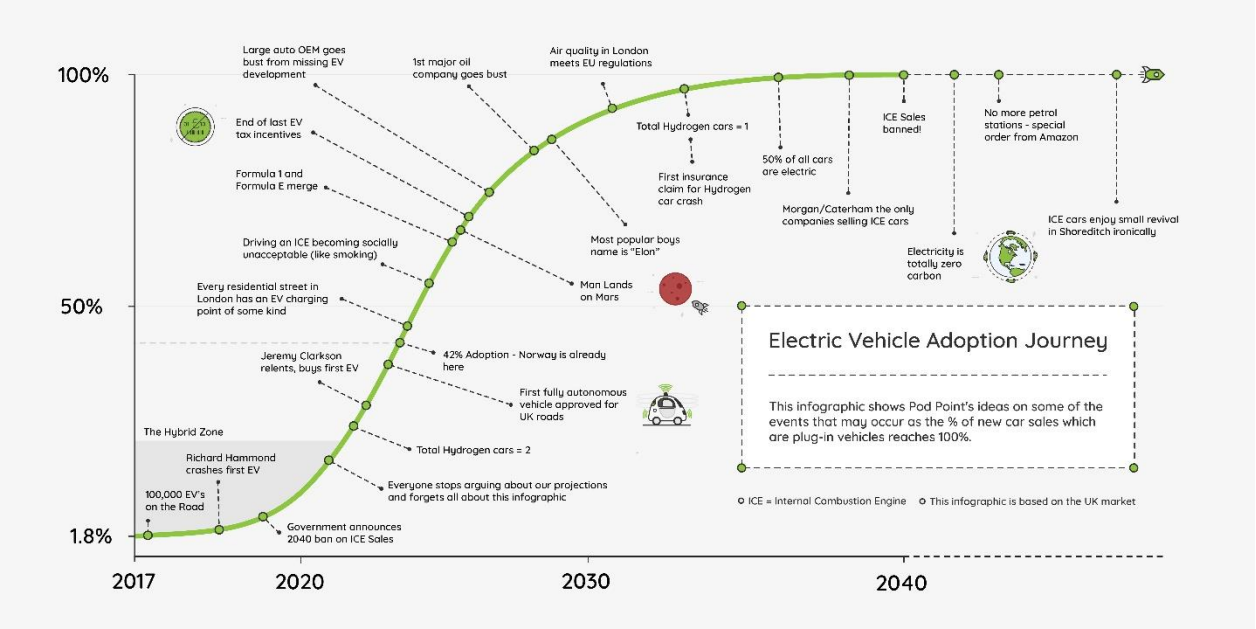

Figure 1.3. *Optimistic prevision on the emergence of the electrical vehicles along the years with a British touch of humor* [28].

To power electrical cars, the industrial companies seem to have made their choice on the Li-ion technology, because of its high energy storage capacity, its stability along the time and its relatively low cost when compared to other electrochemical storage systems. But other technologies are under serious investigation or already applied as for instance hydrogen fuel cells [29]. However, regarding the actual tendencies in the automotive market, the demand for efficient electrochemical storage systems will explode within the next decades. For the moment, electrical cars only represent 2% of the market. But taking in account that the electric cars will occupy the major part of the market by 2050, it will be difficult to implement the Li-ion chemistry in large industrial scales, because the actual technology still lays on cobalt-containing electrode materials [30]. Even though cobalt is the 33rd most abundant element in the Earth's crust, it is qualified as "critical" regarding the locations of its reserves, mainly situated in the Democratic Republic of Congo. Child and slave labor was frequently reported, expressing the need to find more ethical ways of extraction of cobalt-containing ores. Therefore, big improvements regarding the performances have to be done to develop this technology, but also materials which will end up with a lower cost together with a lower impact on the environment.

Therefore, the search for new active materials for NIBs and LIBs is essential for the good development of all the technologies laying on these storage systems. To this end, new classes of materials have to be explored and their chemical mechanisms have to be better understood. Especially, for the active materials at the positive electrode, which are now the bottleneck of the energy density improvement of the sodium and lithium-ion batteries.

2. Objectives and structuration of this thesis

Among the different classes of materials which could be used as positive electrode for alkali-ion systems, transition metal fluorides appear as one of the most promising. These compounds could be the solution to the lack of specific energy of the materials used nowadays as cathode in the first generation of LIBs, due to their ability to deliver more than one electron per formula unit during their charge/discharge processes. However, these materials suffer from low capacity retention and high hysteresis [31]. Those low performances are induced by the mechanisms taking place during their charge and discharge processes, mainly laying on conversion reactions when more than one electron is involved, which imply the crossing of high energy barriers and the total reorganization of the crystalline structure of the active material, as well as large volume changes. Furthermore, most of the fluoride materials studied as cathode for LIBs and NIBs do not present alkali species in their structures, where the cathode material should act as the reservoir of these latter [32]. Perovskite $AFeF_3$ ($A = Na^+, K^+$) compounds are one of the few structures containing alkali ions. Up to now, fluoride perovskites were only a little studied as active materials for LIBs and NIBs, and the mechanisms involved in their charge/discharge processes are still unclear. The synthetic methods reported in the literature to obtain these materials result in low performances, which do not allow the proper study of this class of compounds [33,34,35].

The aim of the following study is to implement new methods of synthesis for transition metal fluorides, in order to design materials with superior performances, as well as better understand the mechanisms involved in their charge/discharge processes. For this purpose, this thesis is organized following the different parts:

Chapter 2 provides the necessary background on LIBs and NIBs technologies, together with a presentation of the different materials used in these technologies and the possible candidates for the next generation of alkali-ion batteries. The description of the different active materials used as active materials for LIBs and NIBs allows the reader to place into context the active materials studied in the following chapters.

Chapter 3 briefly describes the different techniques used to synthesized the fluoride compounds and their precursors, as well as the characterization techniques employed to determine their morphologies, structures and performances.

In the chapter 4, CoF_2 is firstly described as a case study of metal difluorides used as positive electrode for LIBs. The influence on the morphology of the precursor used in the fluorolytic sol-gel synthesis is discussed, as well as their resulting electrochemical behavior, after grating the particles on graphene oxide (GO). The limitations of the use of this class of compounds is highlighted by the performances herein reported. In a second part, the synthesis of anhydrous iron(III) fluoride through "soft conditions" is described for the first time. The nanomaterial is then added either to carbon black (CB) through ball-milling or directly grafted onto GO during the synthesis process. The influence on the morphology and crystal structure of the different ways to prepare the composites is discussed. The composites materials are then used in different alkali systems through the reaction of one alkali ion per formula unit. This reaction does not imply the total conversion of the iron(III) fluoride, but rather the insertion/conversion reaction typically observed when this compound is discharged above 2.0 V vs. Li/Li^+. The mechanisms involved in the respective discharge/charge processes are studied by characterizing the structural changes via *ex situ* X-ray diffraction (XRD).

Chapter 5 refers to the synthesis of sodiated perovskite fluoride compounds, $NaMF_3$ (M = Mn, Fe and Co), adopting an orthorhombic unit cell, as well as their structural and morphological characterizations. Two different synthetic methods are used: one in two steps, using FeF_2 as precursor, and a second through only one step starting from $Fe(ac)_2$. The electrochemical behavior of these compounds towards lithium and sodium is reported. The structural changes of the $NaFeF_3$ crystalline framework involved in the extraction and the insertion of the alkali species is studied via *operando* and *ex situ* XRD. The conclusion arising from this structural study are supported by electronic structure calculations. The behavior of the crystalline structure towards lithium and sodium insertion is compared to the one of the anhydrous iron(III) fluoride reported in chapter 4.

The synthesis methods used in chapter 5 are implement in chapter 6 in order to synthesized cubic perovskite fluoride compounds, AMF_3 ($A = K^+$, NH_4^+; M = Mn, Fe, Co). The morphologies and crystalline structures of these compounds are characterized by transmission electronic microscopy (TEM) and XRD. The electrochemical behavior and the structural changes occurring in the crystal structure towards Li^+, Na^+ and K^+ are systematically studied

by galvanostatic and voltammetric techniques, as well as *ex situ* XRD. The results obtained are compared to the ones of the chapters 4 and 5.

The conclusion of this work discusses the difference in the pathways of reaction between the rhombohedral anhydrous iron(III) fluoride of the chapter 4 and the different perovskite compounds obtained in the chapters 5 and 6 towards different alkali-ion systems.

References

1. Andres, R. J.; Fielding, D. J.; Marland, G.; Boden, T. A.; Kumar, N.; Kearney, A. T., Carbon dioxide emissions from fossil-fuel use, 1751–1950. *Tellus B* **1999,** *51* (4), 759-765.
2. Huber, M. T., Energizing historical materialism: Fossil fuels, space and the capitalist mode of production. *Geoforum* **2009,** *40* (1), 105-115.
3. Pearson, P. J. G.; Foxon, T. J., A low carbon industrial revolution? Insights and challenges from past technological and economic transformations. *Energy Policy* **2012,** *50*, 117-127.
4. Hubbert, M. K., Energy from Fossil Fuels. *Science* **1949,** *109* (2823), 103-109.
5. Stephen, F. L., Fossil Fuels in the 21st Century. *Ambio* **2005,** *34* (8), 621-627.
6. Mohr, S. H.; Wang, J.; Ellem, G.; Ward, J.; Giurco, D., Projection of world fossil fuels by country. *Fuel* **2015,** *141*, 120-135.
7. Scott, V.; Haszeldine, R. S.; Tett, S. F. B.; Oschlies, A., Fossil fuels in a trillion tonne world. *Nature Climate Change* **2015,** *5*, 419.
8. Winters, A. Y. S., *Dancing with Giants*. The World Bank: 2007; p 288.
9. Bawa, K. S.; Koh, L. P.; Lee, T. M.; Liu, J.; Ramakrishnan, P. S.; Yu, D. W.; Zhang, Y.-p.; Raven, P. H., China, India, and the Environment. *Science* **2010,** *327* (5972), 1457.
10. Menyah, K.; Wolde-Rufael, Y., Energy consumption, pollutant emissions and economic growth in South Africa. *Energy Economics* **2010,** *32* (6), 1374-1382.
11. Adams, S.; Klobodu, E. K. M.; Opoku, E. E. O., Energy consumption, political regime and economic growth in sub-Saharan Africa. *Energy Policy* **2016,** *96*, 36-44.
12. Payne, J. E., On the dynamics of energy consumption and output in the US. *Applied Energy* **2009,** *86* (4), 575-577.
13. Apergis, N.; Payne, J. E., Renewable energy consumption and growth in Eurasia. *Energy Economics* **2010,** *32* (6), 1392-1397.
14. Fulkerson, W.; Judkins, R. R.; Sanghvi, M. K., Energy from Fossil Fuels. *Scientific American* **1990,** *263* (3), 128-135.
15. Mitchell, J. F. B., The "Greenhouse" effect and climate change. *Reviews of Geophysics* **1989,** *27* (1), 115-139.
16. Wigley, T. M. L., Could reducing fossil-fuel emissions cause global warming? *Nature* **1991,** *349* (6309), 503-506.
17. Wuebbles, D. J.; Jain, A. K., Concerns about climate change and the role of fossil fuel use. *Fuel Processing Technology* **2001,** *71* (1), 99-119.
18. Robbins, A., How to understand the results of the climate change summit: Conference of Parties21 (COP21) Paris 2015. *Journal of Public Health Policy* **2016,** *37* (2), 129-132.
19. Paardekooper, S. L., Rasmus Søgaard; Mathiesen, Brian Vad; Chang, Miguel;; Petersen, U. R. G., Lars; David, Andrei; Dahlbæk, Jonas; Kapetanakis, Ioannis; Aristeidis; Lund, H. B., Nis; Hansen, Kenneth; Drysdale, David William; Persson,; Urban, Heat Roadmap Europe 4: Quantifying the Impact of Low-Carbon Heating and Cooling Roadmaps. *Aalborg Universitetsforlag* **2018**.
20. Sánchez, I., Short-term prediction of wind energy production. *International Journal of Forecasting* **2006,** *22* (1), 43-56.
21. Boyle, G., Renewable Energy. *Renewable Energy* **2004**.
22. Rehman, S.; Bader, M. A.; Al-Moallem, S. A., Cost of solar energy generated using PV panels. *Renewable and Sustainable Energy Reviews* **2007,** *11* (8), 1843-1857.
23. Blakers, A. S., Matt; Lu, Bin; Cheng, Cheng and Stocks, Ryan, Hydroelectricity in Australia. *Energy News* **2019,** *37* (3), 11-13.
24. Kittner, N.; Lill, F.; Kammen, D. M., Energy storage deployment and innovation for the clean energy transition. *Nature Energy* **2017,** *2*, 17125.
25. Wikichesterdit, Simplified electrical grid with energy storage. In *https://en.wikipedia.org/wiki/Grid_energy_storage*, Wikipedia, **2009**.
26. Barbarossa, C.; De Pelsmacker, P.; Moons, I., Personal Values, Green Self-identity and Electric Car Adoption. *Ecological Economics* **2017,** *140*, 190-200.
27. Wang, Y.; Sperling, D.; Tal, G.; Fang, H., China's electric car surge. *Energy Policy* **2017,** *102*, 486-490.

28. Fairbairn, E., Electric Vehicle Journey Adoption. In *http://www.extrageographic.org/jeremy-clarkson-buys-an-electric-car*, **2018**.
29. Ibrahim, H.; Ilinca, A.; Perron, J., Energy storage systems—Characteristics and comparisons. *Renewable and Sustainable Energy Reviews* **2008,** *12* (5), 1221-1250.
30. Blomgren, G. E., The Development and Future of Lithium Ion Batteries. *Journal of The Electrochemical Society* **2017,** *164* (1), A5019-A5025.
31. Cabana, J.; Monconduit, L.; Larcher, D.; Palacín, M. R., Beyond Intercalation-Based Li-Ion Batteries: The State of the Art and Challenges of Electrode Materials Reacting Through Conversion Reactions. *Advanced Materials* **2010,** *22* (35), E170-E192.
32. Kim, S.-W.; Seo, D.-H.; Gwon, H.; Kim, J.; Kang, K., Fabrication of FeF_3 Nanoflowers on CNT Branches and Their Application to High Power Lithium Rechargeable Batteries. *Advanced Materials* **2010,** *22* (46), 5260-5264.
33. Dimov, N.; Nishimura, A.; Chihara, K.; Kitajou, A.; Gocheva, I. D.; Okada, S., Transition metal $NaMF_3$ compounds as model systems for studying the feasibility of ternary Li-M-F and Na-M-F single phases as cathodes for lithium–ion and sodium–ion batteries. *Electrochimica Acta* **2013,** *110*, 214-220.
34. Yamada, Y.; Doi, T.; Tanaka, I.; Okada, S.; Yamaki, J.-i., Liquid-phase synthesis of highly dispersed $NaFeF_3$ particles and their electrochemical properties for sodium-ion batteries. *Journal of Power Sources* **2011,** *196* (10), 4837-4841.
35. Cao, D.; Yin, C.; Shi, D.; Fu, Z.; Zhang, J.; Li, C., Cubic Perovskite Fluoride as Open Framework Cathode for Na-Ion Batteries. *Advanced Functional Materials* **2017,** *27* (28), 1701130.

Chapter 2

Background

1. Introduction

1.1. A little bit of history

Electrochemical devices could have been invented before our era, as shows the very controversial Bagdad battery [1,2]. The original contemporary description of such devices was done by Alessandro Volta (1745-1827). He realized that by connecting a frog's leg in series with two plates made of different metals a movement occurred. He invented in 1800 the first battery, nowadays called after his name, the voltaic pile, constituted of stacked discs made of copper and zinc separated by brine-soaked paper. This cell was not practical because of the hydrogen production at the surface of copper when the current was created, forming an insulating layer and resulting in a short lifetime of the electrochemical cell [3]. This problem was solved by John Frederic Daniell (1790-1845), who had the idea to use a second electrolyte within the cell, which had no hydrogen, in contact with copper to avoid the formation of gas bubbles. This assembly is known as the first efficient battery [4]. Over time, plenty of different primary cells, namely batteries which cannot be recharged with electricity, emerged, until the first secondary battery was invented by Gaston Planté (1834-1889) in 1859. This first secondary cell was made of metallic lead on the anodic side and lead dioxide on the cathodic side separated by sulfuric acid as an electrolyte. On each electrode of the cell, lead sulfate was generated by the reaction with the electrolyte, producing electrons on the anodic side and consuming electrons on the cathodic side, creating an electric flow when the two electrodes were short-circuited. By applying a current, the reverse reactions took place, thus providing a rechargeable battery secondary cell [5]. This technology has been improved with replacing the liquid electrolyte by a gel and is still largely used nowadays, for instance in car starters.

1.2. Storage and conversion devices

Up to now, a large variety of electrochemical devices for storage and conversion of energy has been designed, going from the simple electrostatic capacitor, to supercapacitors, LIBs and nickel-cadmium batteries (NiCd) or hydrogen fuel cell [6,7,8]. All these devices can be classified depending on how much energy they can store and how fast they can deliver it, often represented by the Ragone plot (**Figure 2.1**).

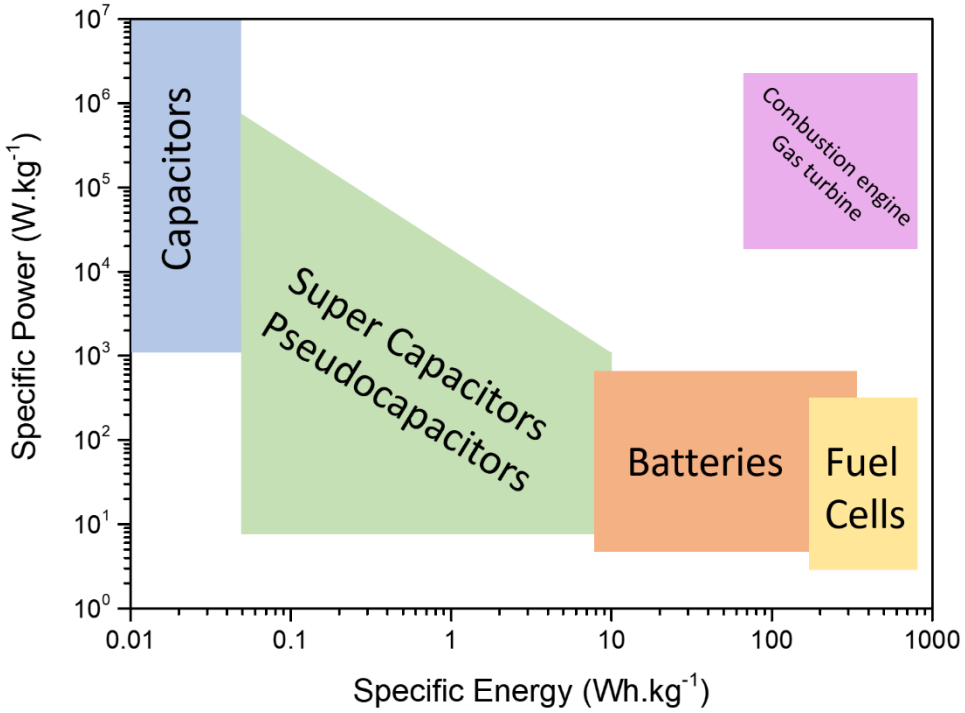

Figure 2.1. *Ragone plot: specific energy versus specific power of various storing and intern-combustion-engine devices. Adapted from Thomas Christen and Martin W. Carlen* [8].

Capacitors store energy from electrostatic charges accumulated on both electrode sides separated by an insulator. There are no redox reactions involved in the storage of energy. The amount of electricity that they can store is low, but they can deliver this electricity in a very short time [9]. Since these devices can store only a small amount of energy, they are mainly used as electronic components. To increase the amount of energy which electrostatic based devices can store, an electrolyte was introduced to replace the insulating part. Additionally, porous electrodes are able to store a large amount of electrostatic charges thanks to their high specific area, therefore they were preferred in contrast to the flat configuration of the metallic plate in normal capacitors. Those devices are called supercapacitor, because of their ability to store a higher amount of electricity compared to normal capacitors. Another kind of supercapacitors, called pseudocapacitors, combine a large specific surface with very fast electrochemical reactions to store an even higher amount of energy [10]. On the other side of the Ragone plot, fuel cells stand out for high specific energy devices due to conversion of small molecules, the fuel, into electrical current by the mean of a catalyst. These devices are built on the same schema as a secondary cell. Namely ionic species are carried through a membrane between two electrodes. At the anodic side, small molecules (i.e. the fuel) are converted into cationic species by a first catalyst and travel through the solid-based electrolyte, while the electronic counterpart flows within the external circuit. The charged components meet at the cathodic side to react onto a

second catalyst with a second small molecule, usually oxygen to create water and carbon dioxide. The various fuel cells differ between themselves according to the small molecules used as fuel, the type of electrolyte (proton exchange membranes, solid oxide fuel cells, etc.), the operating temperature, and the kind of catalyst used [11].

The overall amount of electrical energy that a storage device is able to accumulate, expressed as the specific energy, can be defined by $Wh.l^{-1}$ or $Wh.kg^{-1}$, which in the case of batteries, is the product of its capacity ($mAh.g^{-1}$) by its nominal voltage (V). This amount of electrical energy, or energy density, depends upon the active materials located in both positive and negative sides of the electrochemical cell, and the additional weight of all the other parts of the battery (formulating agents for the electrodes, current collectors, electrolyte, separator, casting part, etc.). In the case of capacitors, the energy density is defined by the product of the nominal voltage (limited by the stability window of the electrolyte) and its capacitance, which is defined by the amount of electrostatic charge stored at the surface of the electrodes. For devices involving electrochemical reactions, the nominal voltage is created by the difference in redox potential between the active materials at the positive and negative sides of a cell (high and low redox potential, respectively). Since the electrical energy comes from redox reactions that undergo the active materials at each side of the cell, the energy density that they bear is defined by their capacity, which represents the number of electrons that can deliver one gram of active material **(2.1)**:

$$\textbf{(2.1)} \qquad C_{th} = n_{e^-} \cdot F \,/\, M_w = [C.g^{-1}] \cdot \frac{1000}{3600} = [mAh.g^{-1}]$$

Where ***ne-*** is the number of electrons involved in the redox reaction of the active material, ***F*** is the Faraday constant, and M_w the molar mass of the active material.

The amount of active material has to be balanced in the two opposite electrodes in order to match the total reaction of the compounds on both sides of the cell during the charge/discharge. The main characteristics of the principal secondary cells are summarized in **Table 2.1** [12].

Secondary cell type	Nominal cell voltage (V)	Specific energy ($Wh.kg^{-1}$)	Main features
Lead-acid	2.1	40	Low cost, low energy density, heavy
Nickel-cadmium	1.2	60	Memory effect, low energy density, not environmentally friendly

Nickel-metal hybrid	1.2	120	Memory effect, low energy density
Lithium-ion	3.8	265	High energy density, light, expensive
Sodium-ion	3.6	115	Good energy density, possibly cheaper than Li-ion batteries

Table 2.1. *Main characteristics of the principal secondary cell technologies.*

2. Lithium-ion batteries

2.1. Generalities

Among all the different types of secondary cells, LIBs drew attention because of the physicochemical properties of lithium. Lithium is, from all the elements, the most electropositive (-3.0401 V vs. SHE at standard conditions) and the lightest metal (M_w = 6.941 $g.mol^{-1}$), making it an anode material of choice. This technology was first proposed by M. Stanley Whittingham, who used electrodes made of metallic lithium and titanium(IV) sulfide, while he was working at Exxon in the 1970s, the American multinational oil and gas corporation. Due to the high instability of titanium(IV) sulfide and its excessive price this technology was not very practicable, and the company renounced to work further on the project [13]. Ten years after, several groups working on this field found the reversible reactivity towards lithium of compounds having specific crystalline structures, as for instance the lamellar organized $LiCoO_2$ or the typical spinel structure of $LiMn_2O_4$ [14,15,16,17]. This discovery enabled first Asahi Kasei and later Sony to develop the first industrial prototype of Li-ion battery in 1991, a cell made of $LiCoO_2$ and metallic lithium. The use of metallic lithium as a negative electrode induced the well-known dendrite effect and the first self -catching-fire cells. To overcome this issue, metallic lithium was replaced by graphite, improving greatly the safety of this technology. This breakthrough permitted to the company the industrial-scale production of the LIBs for commercialization [18]. From this first commercialization on, the LIBs appeared as the storage system of choice for any portative devices, due to its high energy density, long cycle life, and good performances. Moreover, in contrast to the NiCd or NiMH batteries [19], this technology barely presents memory effect [20], which permits to interrupt the charge or discharge of the cell whenever it pleases the user. Indeed, for the NiCd or NiMH technologies, the sintering of the active material particles during non-complete charge/discharge processes leads to the loss of electrical contact, which decreases the overall potential of the cells, therefore reducing the energy which can be stored. The first generation of this technology, based on $LiCoO_2$ and graphite, was responsible for the worldwide commercial boom of wireless phones

and laptops. As society aims to lower CO_2 emissions, this kind of batteries appears as the best candidate to power our cars and to replace the well-established intern combustion engines partially responsible for the generation of greenhouse gases. At the moment, the first generation of LIBs is not performant enough to totally take over petrol engines, due to the high cost of battery systems and bad distance-range capabilities. In order to make the transition to electric cars possible, more efficient systems have to be found, presenting more powerful and cheaper active materials [21]. Up to now, the active materials at the positive side of the full-cell represent the bottleneck of the development of the LIBs, hence the need to find new classes of compounds suitable to enhance drastically their specific energy.

2.2. Working principles of a Li-ion battery

LIBs are closed electrochemical systems, which store and convert chemical potential to electrical energy through the mean of chemical Faradic reactions, occurring at their positive and negative electrodes. The electrodes are commonly called anode for the negative electrode and cathode for the positive one, where the oxidation and the reduction take place respectively during the discharge. The highly reversible character of the redox reactions occurring during the charge and discharge processes are based on disinsertion/insertion mechanisms for the first generation of LIBs. The crystalline framework does not collapse in the course of those reactions, ensuring a long lifetime towards cycling of the electrochemical cell. The two electrodes are separated by a membrane to prevent electric contact, in order to avoid short-circuits in the cell and then to create a potential across them. This membrane is impregnated by an electrolyte composed of a lithium salt dissolved in combination with carbonate solvents. The electrolyte ensures the ionic conductivity across the two electrodes by shuttling the positive charges of the lithium ions and does not present electrical conductivity. **Figure 2.2** displays a typical lithium-ion full cell, consisting of a graphite material as negative active material and a layered metal oxide as cathode material, where the charge and discharge processes are depicted.

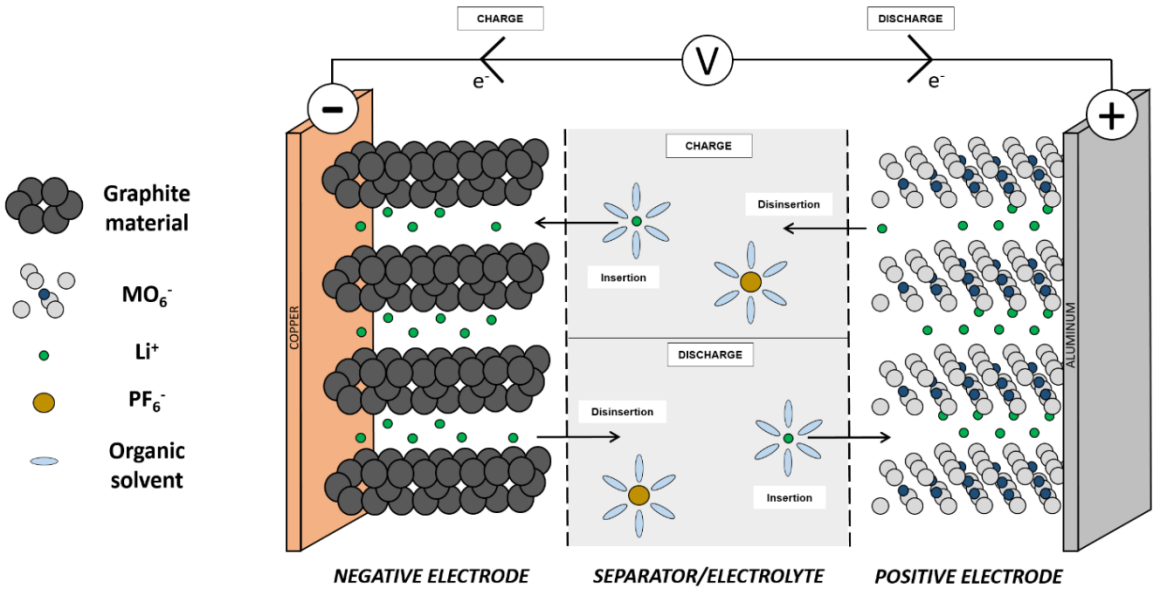

Figure 2.2. *Schematic representation of a lithium-ion full-cell during the charge/discharge process (sizes and charges of the atoms are not respected). Adapted from Reddy et al* [12].

During the charge process, lithium ions leave the active material located at the positive side of the cell through a disinsertion reaction, while electrons are injected within the external circuit. The transition metal of the layered structure undergoes an increase of its oxidation state to balance the charges. The reaction can be illustrated as follow **(2.2)**:

$$\textbf{(2.2)} \qquad LiM^{a}O_2 \leftrightarrow xLi^{+} + xe^{-} + Li_{1-x}M^{a+x}O_2$$

Where ***M*** is the transition metal, ***a*** is the initial oxidation state of the transition metal and ***x*** the number of electrons/lithium ions involved.

Thanks to the electrolyte, the positive charge (i.e. the lithium ions) are transported to the negative side and the lithium ions located at the proximity of the anode will be inserted into the carboneous material to be paired with electrons coming from the external circuit. The reaction can be illustrated as follow **(2.3)**:

$$\textbf{(2.3)} \qquad xLi^{+} + xe^{-} + C_6 \leftrightarrow Li_xC_6$$

Where the overall reaction of the full-cell is **(2.4)**:

$$\textbf{(2.4)} \qquad LiM^{a}O_2 + C_6 \leftrightarrow Li_{1-x}M^{a+x}O_2 + Li_xC_6$$

The charge and discharge processes of a full-cell, or a half-cell when a specific material is studied, are usually represented by galvanostatic curves. The profile of these curves is governed

by the redox reactions, occurring at the active materials in both electrodes and influenced by polarization phenomena as depicted in **Figure 2.3a**.

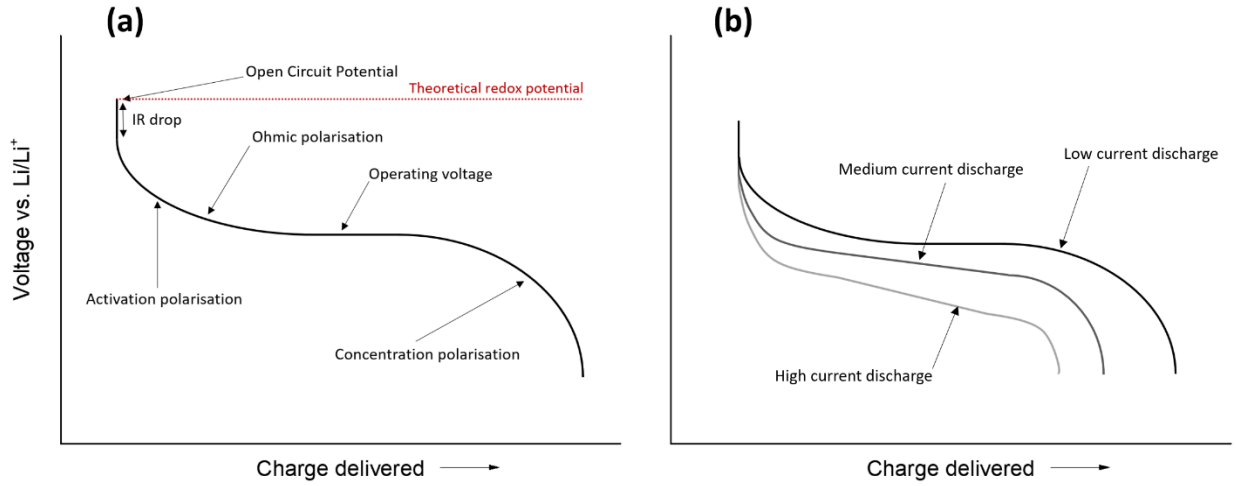

Figure 2.3. (a) *Influence of the different polarization phenomena on the discharge curve of a lithium-ion cell and* **(b)** *influence of the current density on the polarization. Adapted from Bhaskar Saha and Kai Goebel* [22].

Noticeably, the practicable potential of a compound is different from the one expected from thermodynamics (**Figure 2.3**). These differences are due to kinetics limitation. The first difference in potential is caused by the IR drop due to the internal resistance that faces the flowing current in the electrochemical cell. The second noticeable one is the activation polarization related to the kinetics of the electrochemical redox reaction occurring within the active material, for example, the energy barrier that the reaction has to overcome to be activated. As depicted in **Figure 2.3**, the Ohmic polarization is the impedance that presents an active material, which can influence the slope of the resulting operating potential. Hence, the concentration polarization takes into account the diffusion limitation of the ions transported across the electrolyte. All these factors influence the operating voltage of an electrochemical cell, namely by decreasing it during the discharge and increasing it during the charge. Exactly this difference of potential is called polarization. This polarization can be inherent to the kind of electrochemical redox reaction involved in the charge/discharge process, but the formulation of the active material can also reduce it. For example, by decreasing the size of the active material particles, the interface area in contact with the electrolyte will increase, improving the ionic transfer in the material, as well as shortening the ionic path for a redox reaction. The current density applied to an active material can also greatly influence the galvanostatic curves

depending on how fast/slow the kinetics of a specific electrochemical redox reaction is (**Figure 2.3b**) [22].

2.3. Anodic active material in LIBs

2.3.1. Generalities

As already mentioned, metallic lithium cannot be used practically as anode for LIBs. Upon recharge, the platting of the lithium ions occurs simultaneously through corrosion and "passivation" (formation of the solid electrolyte interface (SEI)), generating a very dispersed deposition. This deposition can be isolated by the SEI, partially electrochemically inactivating the anode. Furthermore, this highly dispersed deposition conducts to the formation of dendrites, able to pierce the membrane between the two electrodes, creating a short circuit. Therefore, the use of metallic lithium has only shown its commercial interest to primary systems, where it is still widely present in medical and military applications [23]. In order to make lithium secondary cells practical, the lithium ions have to be confined within materials presenting reversible reactions with the latter at a controlled low potential. Indeed, when the potential is too low, lithium plating can occur. This results in a "rocking-chair" cell, where lithium ions are easily de/intercalated in both electrodes during the charge/discharge processes [24]. The panel of compounds, which can be used at the negative side of lithium-ion cells, are classified into three groups depending on the type of electrochemical redox reactions that they undergo towards lithium. **Figure 2.4** displays the different compounds employed as anode for LIBs, reacting through insertion, conversion and alloying reactions with lithium [25].

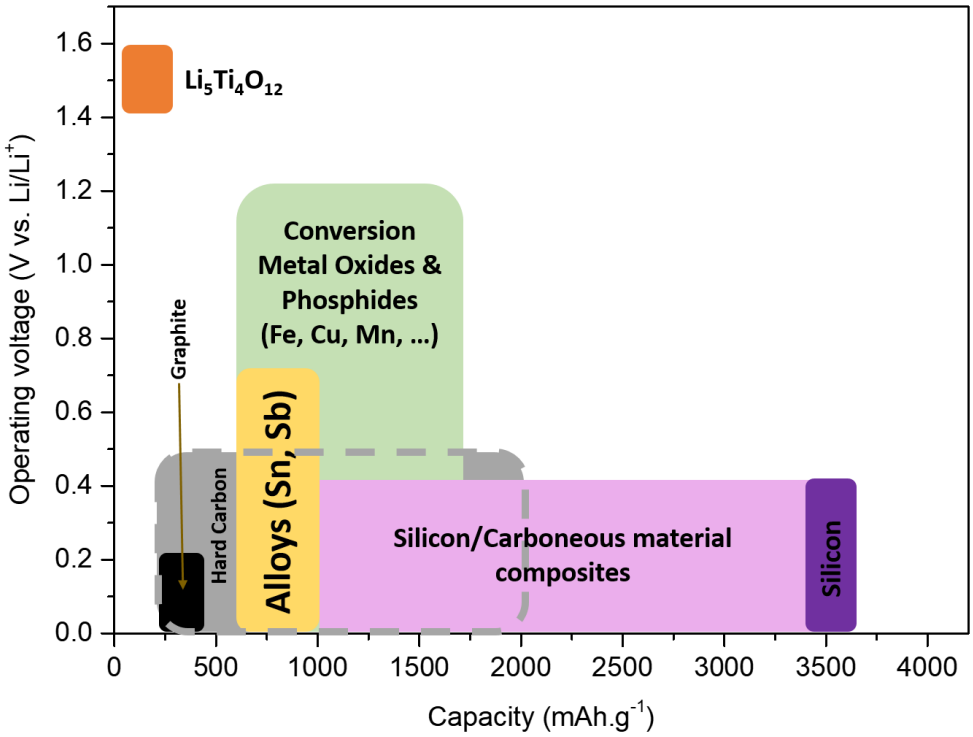

Figure 2.4. *Panel of different active materials used as anodes for LIBs.*

2.3.2 Insertion-reacting materials

Carboneous materials as host materials have been extensively studied. At the early stage of the lithium secondary cells, they presented the lowest electrochemical redox potential, superior stability compared to polymers, metal oxides and chalcogenides and especially considerable safety improvements in comparison with metallic lithium. Carboneous materials can be classified into three types; the soft carbons, hard carbons and graphite materials (**Figure 2.5**) [26,27]. These materials are obtained by varying the carbon precursor used for the synthesis and the temperature of calcination/graphitization. All these structures consist of the same building block: sheets of carbon atoms organized into honeycomb lattices. Each carbon atom is bonded to three other neighbor carbon atoms through three σ bonds oriented in the direction of the carbon sheets, and one π bond oriented out of this sheet plane. Within these planes, the sp^2 orbital hybridization allows the electron involved in the π bond to migrate through the plane, allowing electronic conductivity. The structure of these materials deviates more or less from the ideal graphitic framework, which greatly influences the resulting performances towards lithium. The weak Van der Waals interactions ensure bonding between two layers, enabling the reaction of lithium ions into the graphitized carbon host via intercalation, which is the insertion of the cations in between two layers. The highest concentration of lithium that can host graphitic materials has the stoichiometry of LiC_6, which represents 372 $mAh.g^{-1}$ [28]. Soft carbons have a

similar structure to the graphitic one, but they only exhibit crystalline nano-domains. Lithium reacts through insertion reactions in the low organized carbon layers. Soft carbons present good capacity and low capacity loss at the first discharge [29]. Hard carbons, on the contrary, are carbon structures carbonized at high temperature (T > 1500 °C) and present a very low stacking degree. This type of organization presents a rough structure, defects, and high surface of grain boundaries, which confers extra sites for the lithium accommodation in addition to intercalation. Therefore, these materials possess very high capacity, ranging from 250 to 2000 $mAh.g^{-1}$ (representing a stoichiometric of Li_xC_6 with x up to ~ 5) [30]. However, soft and hard carbons do not have flat working potential, varying the overall potential of the full-cell. Furthermore, their potential of reaction is very close to 0 V vs, Li/Li^+, engendering lithium plating on the top of the electrode material. Graphitic carboneous materials used as anode usually consist of aggregates of graphite polycrystalline particles ranging from nanoscale to microscale. In contrast to the soft and hard carbons, graphitic carboneous materials present flat discharge and charge profiles and their electrochemical redox potential is above the lithium platting. Additionally they show good conductivity due to the well-organized carbon sp^2 stacks. Therefore, they appeared as the best carboneous candidate to be used as anode for LIBs owing to their higher safety use, flat overall potential and capacity close to the ideal graphitic structure. Nevertheless, their capacity is still far from that of pure lithium (~ 3800 $mAh.g^{-1}$), hence the need to find better materials.

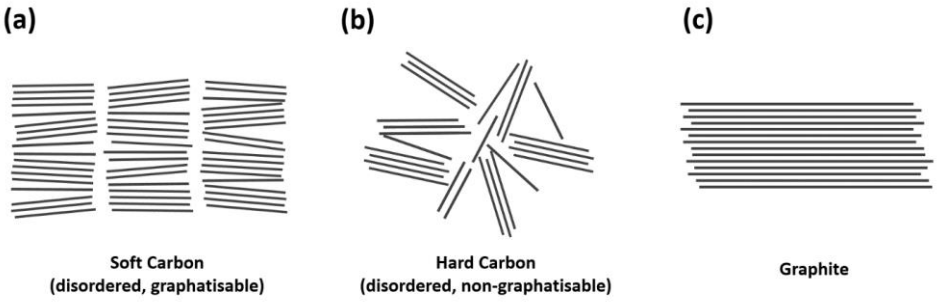

Figure 2.5. *Illustration of* ***(a)*** *soft carbon,* ***(b)*** *hard carbon and* ***(c)*** *graphite structures. Adapted from N. Loeffler et al* [31].

2.3.3. Li-alloying materials and conversion materials

Several elements from the third, fourth and fifth rows of the groups III, IV, and V (e.g. Sn, Pb, Al, Si, etc.) can be used to form alloys with lithium [32]. As the alloying reaction can be reversible and occurs at low potential (< 1 V vs. Li/Li^+), in addition with their high specific capacity (3600 $mAh.g^{-1}$ for $Li_{4.4}Si$, 800 $mAh.g^{-1}$ for $Li_{4.4}Sn$, 600 $mAh.g^{-1}$ for Li_3Sb or $mAh.g^{-1}$ 1650 in Li_3P

[33]), those materials are very interesting as anode for LIBs. The main difficulty to overcome is their large volume expansion and contraction during lithium insertion and disinsertion respectively compared to graphite (**figure 2.6**). This high volume expansion leads to the expansion of the whole electrode during lithium insertion together with the formation of a considerable amount of SEI. During lithium extraction, the active material size decreases and loses its integrity exposing new surface free for the formation of fresh SEI, as well as losing its contact with the agent which ensures the conductivity within the electrode. Repeated cycles of these processes lead to capacity losses coming from the formation of new SEI at each cycle and a decrease of the overall conductivity of the electrode [34].

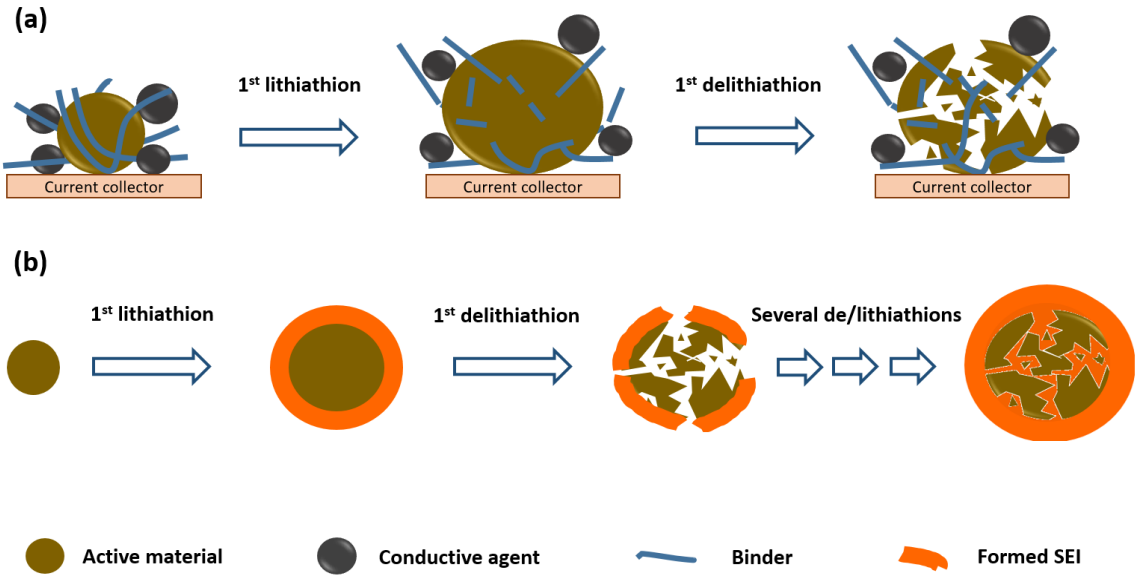

Figure 2.6. *Illustration of* **(a)** *the pulverization of a Si-electrode upon lithium insertion/extraction and* **(b)** *the resulting excessive SEI formation along with cycling.*

To compensate for this volume change, and to avoid mechanical stress and implement SEI stabilization, many strategies were investigated in terms of morphology and carbon coating, as well as using binder agents in the formulation of electrodes able to accept higher volume changes than the traditional PVdF. Among those elements, silicon attracted most of the attention because of its Earth abundance, low cost and specific capacity close to the one of metallic lithium. The amorphous character of the different lithiated phases generated by lithium insertion/disinsertion confers a single redox plateau at around 0.2-0.4 V vs. Li/Li^+. However, as mentioned before, the swelling of silicon towards lithium insertion is too high, about 320 %, leading to the pulverization of the electrode, when formulated as graphite would be. Up to now, synthesis strategies to avoid this problem are very expensive. But the introduction of a fraction of this compound in graphitic anodes is already commonly used. The first study on

silicon/graphitic composite materials was carried out by Yoshio *et al.* in 2002 and was firstly commercialized in 2014 by the company Amprius. Remarkably, those composites materials can present capacity values as high as 900 $mAh.g^{-1}$ with good capacity retention [35]. Tesla claimed that the use of this technology increased the range of their cars by 6 %.

In 2000, the reversible conversion reaction between metal oxides and lithium, also called displacement reaction, was reported for the first time by Poizot [36]. The reaction can be illustrated as follows **(2.5)**:

$$\textbf{(2.5)} \quad M_x^{y/2}O_y + 2yLi^+ + 2ye^- \leftrightarrow xM^0 + yLi_2O \quad (M = \text{transition metal})$$

As can be seen, in contrast with the insertion reaction, transition metal oxides can react with more than one lithium atom per formula unit, offering higher specific capacities than the usual graphitic materials (e.g. 1200 $mAh.g^{-1}$ for the MnO_2, 1000 $mAh.g^{-1}$ for the Fe_2O_3 or 700 $mAh.g^{-1}$ for the CoO) [37]. The metal oxide compound is then transformed into its metallic form and lithium oxide nano-domains. This kind of reaction was also observed for transition metal fluorides, sulfides, nitrides, and phosphides. Their electrochemical redox potentials are included between 0.5 and 1.0 V vs. Li/Li^+, avoiding the formation of lithium dendrites onto the electrodes, thus increasing safety in their use. In addition to their high specific capacity, their good corrosion resistance, relative abundance, and low cost make transition metal oxides interesting candidates to replace the graphitic material anodes. However, similarly to the Li-alloying metals, those materials suffer a high volume expansion towards lithium insertion, as well as low conductivity, together with kinetic limitations and thermodynamic restrictions. The high surface energy established by the formation of the nano-domains during the lithium reaction is mainly responsible for the high polarization between the discharge/charge processes [38].

2.4. Active materials at the positive side

Similarly to graphite, the active materials used at the positive side of the full lithium-ion cell are active through insertion reactions. These active materials are used as a lithium reservoir within the battery, hence the discharged state of the cell after assembly. Since the working potentials of active materials located on the negative side are included in a narrow window (0.1 V < $WP_{(\text{anode materials})}$ < 1 V vs. Li/Li^+), the redox potential of the positive active materials defines the overall potential of the battery. How high their working potential can be is delimited by the stability of the electrolyte towards decomposition reactions, which usually occur above 4.6 V vs. Li/Li^+ [39,40]. The active materials presenting all these mentioned specifications can be

organized in three main classes depending on their structure: $LiMO_2$ layered compounds (with M = Mn, Ni and Co), LiM_2O_4 spinel compounds (M = Mn, etc.) and $LiMPO_4$ olivine compounds (with M = Mn, Fe, Ni and Co) [41]. The intrinsic chemistry of the active materials defines their practical capacity and operating voltage. The ionic conductivity is defined by the configuration of the crystalline framework, which has an influence on the rate capability. Regarding the safety of those active materials, their redox potential should not be close to the limit of stability of the electrolyte, in order to avoid decomposition processes during rough cycling conditions, as well as decomposition of the active material itself which can generate gas by thermal decomposition (e.g. O_2 release in the case of $LiCoO_2$) [42,43]. The transition metal oxide structures benefit from high energy density due to the compact lattices they present, as well as good ion-diffusion pathways. However, not all lithium ions contained in the framework are active, due to large anisotropic changes towards lithium extraction as for instance in the case of layered compounds [44]. In contrast, more open frameworks such as vanadium oxides or olivine structures present lower specific capacities, but the dis/insertion of their lithium content is complete [45]. Recent researches are mainly focused on the improvement of these phases and of their derivatives including the $LiMBO_3$ borate compounds [46], Li_2MSiO_4 silicate compounds [47] and the Li_xMAO_4F tavorite and triplite compounds (with A = S or P and x = 1 or 2) [48,49]. At the early stage of the technology, $LiCoO_2$ imposed itself as the reference material; therefore, transition metal oxides exhibiting intercalation upon reaction caught the attention of the scientific community and found its application in most of the mobile devices. However, this material has a short life span, bad thermal stability and limited specific capacity. Because of the high price and toxicity of cobalt, battery manufacturers tried to reduce its amount within the layered compound by substituting it with other transition metals such as nickel or manganese, along with the wish to improve its cyclability and thermal stability. Within the panel of the layered compounds, the more commonly used in industry are NMC ($LiNi_xMn_yCo_{1-x-y}O_2$) [50] and NCA ($LiNi_yCo_{1-x-y}Al_xO_2$) [51]. Spinel LMO ($LiMn_2O_4$) has a lower specific energy than the best layered compounds, but presents good rate capability and is usually used in automotive mixed with layered compounds to improve the high current performance of the battery pack [52]. The third class of compounds comprising $LiFePO_4$ (LFP) was developed in the mid-90s. Its low conductivity hindered its commercial application, however with the emergence of nanotechnologies, reducing the particle size and the addition to this material of conductive matrix overcame the barrier for the application of the LFP electrodes, as it was proposed by the CNRS together with Hydro-Québec [53]. LFP presents lower specific capacity but improved specific energy compared to the other insertion materials. Furthermore, it has also

longer cycle life besides good thermal stability, resulting in safer use under harsh conditions [54]. The theoretical voltages of all these different active materials are plotted versus their theoretical capacities in **Figure 2.7**. As a major drawback nevertheless, it can be seen that their specific capacities of all these compounds, their ability to deliver and accept lithium ions regarding their mass, is rather low when compared to the upcoming new generation of Li-alloying metal or conversion materials used as anodes. This limitation comes from the fact that insertion reactions involve one lithium atom or less per formula unit, restricting the specific energy that the insertion-based compounds can present. Regarding the battery assembly, this will lead to an unbalance of the active materials on both sides of the battery, when materials with high specific capacities as silicon would be used as anodes. Indeed, if pure silicon anode materials are employed as anode against typical $LiCoO_2$, the mass of the cathode material should be more than twenty times the mass of the anode to match its theoretical capacity. This will result in a considerable thickness of the positive electrode, hindering the performances of the whole battery due to diffusion limitations in the thick positive electrode.

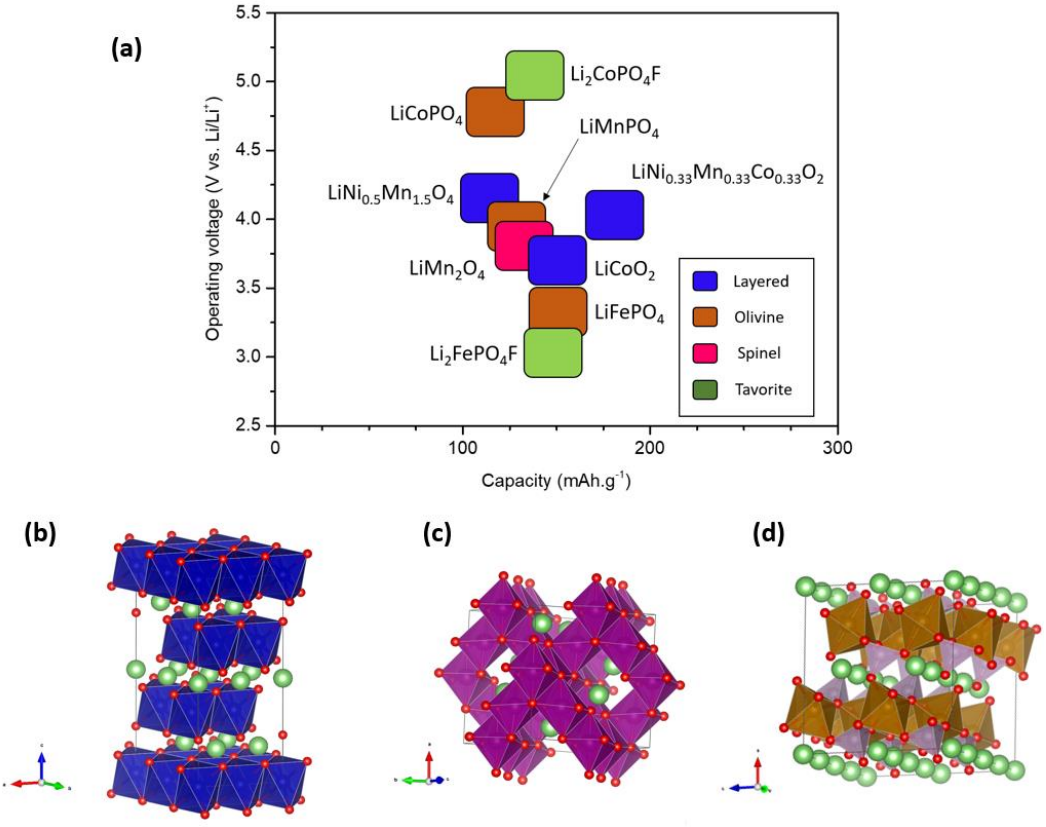

Figure 2.7. ***(a)*** *Principal insertion reacting materials used as positive electrode for LIBs displayed in function of the specific capacities and redox potentials, and crystal structures:* ***(b)*** ***l****ayered structure,* ***(c)*** ***s****pinel structure and* ***(d)*** ***o****livine structure.*

3. Sodium-ion batteries

3.1. Generalities

LIBs will be massively used in the upcoming times. They are already implemented in most of the mobiles devices and start to be used for large-scale application in electric vehicles and stationary facilities. However, concerns were engendered by the amount of lithium resources available [55,56]. Evidence showed that a shortage would be quite unlikely [57], but if our vehicle fleet is prompt to be mainly powered by batteries from 2040, lithium production and cost could be severely affected in the next years, hence the need to have other alternatives based on different concepts. Within the alkali metal group, sodium stands out as the lighter element after lithium and shares very similar chemical properties. It is, therefore, possible to set up an electrochemical cell with sodium based on analogous fundamental principles as LIBs, namely two electrode materials reacting at low and high potentials vs. Na/Na^+, separated by an electrolyte consisting of a sodium salt dissolved in organic solvents. As a matter of fact, this technology is not new and was discovered at the same time as the LIBs in the 70s-80s, but since the commercialization of the latter was rapidly successful, no further research was undertaken. The low performances of the $NaCoO_2$-like compound compared to $LiCoO_2$, and the lack of the anode active materials upon the reaction with sodium, caused this technology to almost disappear, before a revival interest in 2000 [58,59]. First Stevens and Dahn reported the reversible insertion of sodium in hard carbon materials [28]. A few years later, Okada *et al.* demonstrated the electrochemical activity of the $NaFeO_2$ phase through Fe^{3+}/Fe^{4+} redox couple, which was not the case for $LiFeO_2$, due to the not adapted crystal structure [60]. These important findings, together with the need for new storage technologies, made sodium-ion batteries appealing again. Sodium has a slightly higher electrochemical redox potential than lithium as well as a higher mass. Its cationic size is notably larger, which is translated into a lower specific energy value when used in its metallic form (see summary in **Table 2.2**) [61]. In term of price, sodium is significantly cheaper than lithium, however, the content of alkali metals is not the largest factor influencing the final price of the whole cell (alkali ions are present in the electrodes and the electrolyte). Additionally, the possibility to use aluminum current collectors on both sides of the battery presents an interesting point, as sodium does not alloy with aluminum, avoiding the use of costly and heavy copper metal at the negative side. The opportunity to transfer the knowledge of the LIBs to the application of NIBs is also a major advantage. In fact, up to now, the Na-intercalation chemistry was not as deeply investigated as it is in their lithium analogues

and due to their difference in size, structures which do not work with lithium can be active towards sodium as it was already demonstrated [62]. The larger size of sodium ions permits to stack layered metal oxides in different ways, creating more flexibility in the design of the active material framework. Moreover, the larger ionic radius of sodium permits also a weaker solvation energy within the electrolyte (made of polar solvent), improving the charge transfer kinetics at the interface of the electrode/electrolyte, as well as the ionic conductivity in the electrolyte [63].

	Sodium (Na)	**Lithium (Li)**
Redox potential (V vs. SHE)	-2.71	-3.04
Cationic radius (Å)	1.06	0.76
Atomic mass ($g.mol^{-1}$)	23.0	6.9
Cost as carbonate ($/ton)	150	17000
Specific energy ($mAh.g^{-1}$)	1165	3829
Coordination preference	Octahedral and prismatic	Octahedral and tetrahedral

Table 2.2. *General characteristics of sodium and lithium [61].*

3.2. Active materials at the negative side

As in the lithium-ion system, metallic sodium cannot be used as an anode because of safety reasons. Together with the high reactivity of sodium with organic electrolytes, dendrites can be formed along with cycling. Moreover, sodium has a low melting point (98 °C), creating real safety concerns if harsh conditions of cycling are used. Furthermore, the graphitic structure has a very low reactivity towards the insertion of sodium ions, due to thermodynamic issues. Only a small fraction of the alkali metal can be inserted into the graphitic structure compared to lithium (NaC_{64} compared to LiC_6), under vacuum atmosphere at elevated temperatures [64]. Nevertheless, other non-graphitic carboneous structures showed good reactivity with sodium, such as petroleum cokes, black carbon or pitch-based carbon fibers, demonstrating the possibility to design carbon-based anode for NIBs [65,66,67]. This reactivity was demonstrated to

originate from the high disorder present in those materials. Up to date, hard carbons presented the best performances in terms of specific capacity, with around 300 $mAh.g^{-1}$ and good cycling stability [68,69]. However, the cost of production of hard carbon is relatively high, which is an obstacle if the sodium ion technology wants to stand as a cheaper alternative to LIBs. In the case of insertion materials, the electrochemical redox potentials of sodium insertion within the crystalline framework are usually too high to be employed as anode materials. Titanate phases are known to show the lowest potentials reported so far, with about 180 $mAh.g^{-1}$ in the case of the $Na_2Ti_3O_7$ at 0.3V [70], or with amorphous TiO_2 nanotubes, directly grown on a titanium current collector, which are active based on pseudocapacitance mechanisms, delivering 140 $mAh.g^{-1}$ for an average potential of 1.5 vs. Na/Na^+ [71]. Towards alloying reactions, sodium does not adopt the same stoichiometry as lithium. For instance, silicon can only accommodate one atom of sodium per formula unit to produce the metallic alloy NaSi, which makes silicon much less interesting in terms of specific energy than in the lithium system. Moreover, the high diffusion barrier of sodium is too high for the cation to be transported within the lattice of silicon. Nonetheless, intermetallic species such as tin ($Na_{3.75}Sn$), antimony (Na_3Sb), or a mixture of both, as well as sodium phosphide (Na_3P) have more interesting specific energy values. Similarly to Li-alloying materials, Na-alloying materials present high volume expansion, even higher than in the case of silicon in LIBs. Comparable strategies are employed to avoid the total pulverization of the electrode, such as carbon confinement [72]. Concerning the conversion materials, only a few compounds show reactivity towards the displacement reaction with sodium.

3.3. Active materials at the positive side

At the very initial stage of the NIBs, the reversible intercalation of sodium ions in $NaCoO_2$ was successfully demonstrated, but the lower voltage profile defined by a multi-step plateau, as well as its lower specific capacity, limit its attractiveness compared to lithiated analogous phases [73]. The early work of Delmas and co-workers demonstrated that not only the cobalt-containing phase was active, but also other 3d transition metal compounds were active towards sodium, such as Na_xCrO_2, Na_xMnO_2 [74]. However, due to the small window of stability provided by the electrolyte in the sodium system, only a fraction of the potential was demonstrated at this time, keeping sodium-ion technology shunted aside until the beginning of 2000. In contrast to the active materials found in the negative side of the battery, a large choice of possible active materials for the cathode was developed in the two last decades. They can be classified into two major groups: layered metal oxides and polyanion

structures [75,76]. The large size of the sodium ion delivers high flexibility in the stacking order of the metal oxide layered compounds, allowing the design of a multitude of different active materials presenting their own specific electrochemical behavior. On the other hand, in polyanion structures, the large ionic radius of sodium allows the thermodynamic stabilization of phases which are not stable with lithium, making their synthesis possible, such as the Na_2FePO_4F phase while the generation of the analogous Li_2FePO_4F compound is possible only through electrochemical replacement of the alkali ion starting from the sodiated phase [77]. Other interesting types of materials proved to be interesting as well. For example, metal-organic frameworks represented by the Prussian blue analogs (PBAs) have large interstitial spaces suitable for the fast diffusion of sodium. Furthermore, those compounds are cheap to prepare and present excellent cycling life [78]. Some organic compounds show reactivity towards sodium such as $Na_2C_6O_6$ or $Na_4C_8H_2O_6$ [79], exhibiting specific capacities comparable to the inorganic materials, but with relatively low working potential. A selection of materials is displayed in **Figure 2.8**. This large array of materials presenting very distinctive performances in the function of their crystalline structure (high rate performance, high specific capacity, long span life) will allow the use of NIBs for all the applications where lithium ions batteries are currently in use.

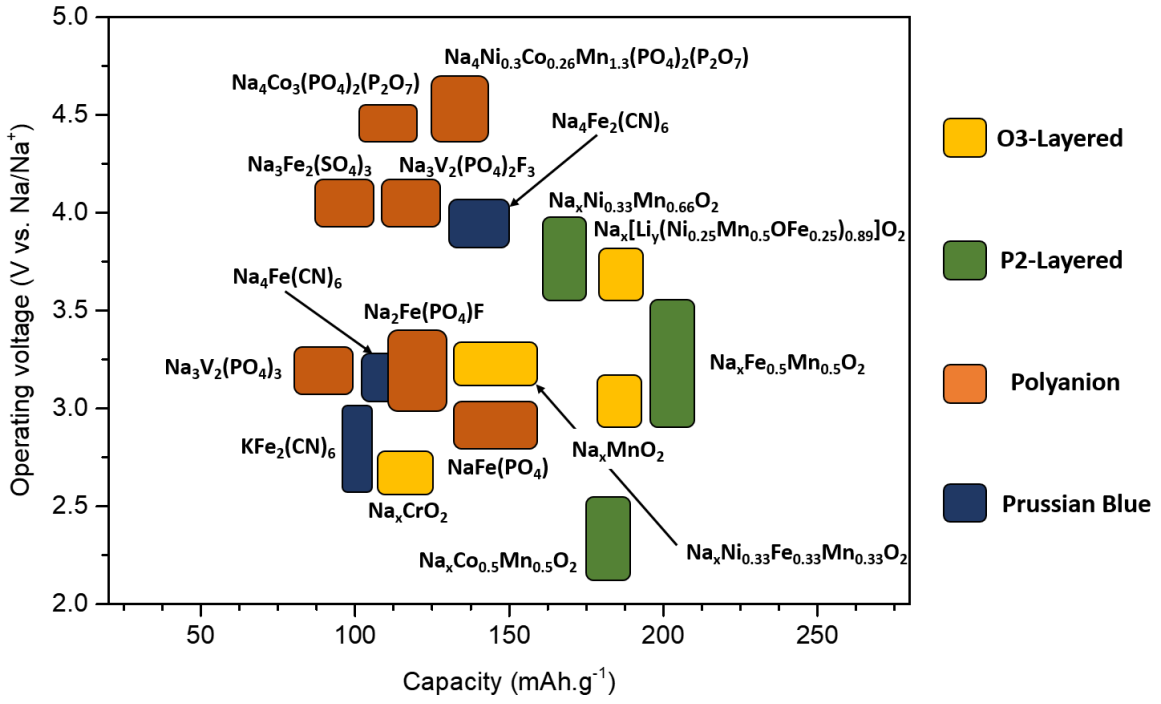

Figure 2.8. *Fraction of the different active materials used as cathodes for NIBs in function of their working potential against their specific capacity.*

4. Metal fluorides used as cathodes for Li-ion batteries

4.1. Generalities

Among the number of potential compounds to be used as cathode active materials for the next generation of LIBs, two classes appear to match with the needed requirements. First of all, they should present high specific capacities to match the ones of the future anode materials, such as silicon, but they should also be cost-effective, abundant and environmentally friendly. Sulfur compounds answer to most of these requirements, however, they present low working potential and issues regarding their cycling stability due to shuttling effects of the sulfur atoms owning to their reaction mechanisms [80]. The second class of compounds is metal fluorides. Those materials are already used for many applications such as optics, luminescence, dental composites, catalysis or uranium enrichment processes [81]. Very recently, these compounds attracted attention for energy storage and conversion [82]. Similarly to metal oxides, metal fluorides can react through a conversion reaction, delivering more than one electron per unit formula. Nonetheless, in contrast to metal oxides, fluoride materials have higher electrochemical redox potentials vs. Li/Li^+ [83], making them suitable active material for positive electrodes. Owning to the relatively low weight of the transition metals, such as iron, cobalt, nickel, copper, and manganese, and the fluorine atom, these materials present high capacities, as it can be seen in **Figure 2.9**. The use of metal fluorides for battery purposes began in the 60-70s when CuF_2, NiF_2, and BiF_3 were studied as positive electrodes in primary lithium batteries [84]. In 1997, Arai *et al.* were the first to report transition metal fluorides as cathodes for secondary lithium batteries. In their work, they described the insertion reaction of lithium within different trifluoride based compounds (FeF_3, VF_3, CoF_3, TiF_3, and MnF_3) [85]. As the potential window in this study was kept above 2.0 V vs. Li/Li^+, the conversion reaction of the fluoride compounds was not taking place. However, it was shown that this class of materials was also able to present similar behavior as the usual insertion compounds. Interesting results were described in the case of the rhombohedral iron(III) fluoride, which was able to deliver reversibly 140 $mAh.g^{-1}$ at a potential of 3.4 V. The pioneering work of Amatucci's group at the beginning of the 2000s showed that those materials could deliver even higher capacities when they were cycled at lower potential or higher temperature [83,86]. In their early research work, they described the use of composites made of iron(III) fluoride and different carbon compounds

mixed together by ball-milling. Within this study, the active materials showed specific capacities very close to the theoretical one (the theoretical capacity of iron(III) fluoride is 712 $mAh.g^{-1}$ through a three electrons reaction). From this primary study on, the scientific community started to study these materials extensively.

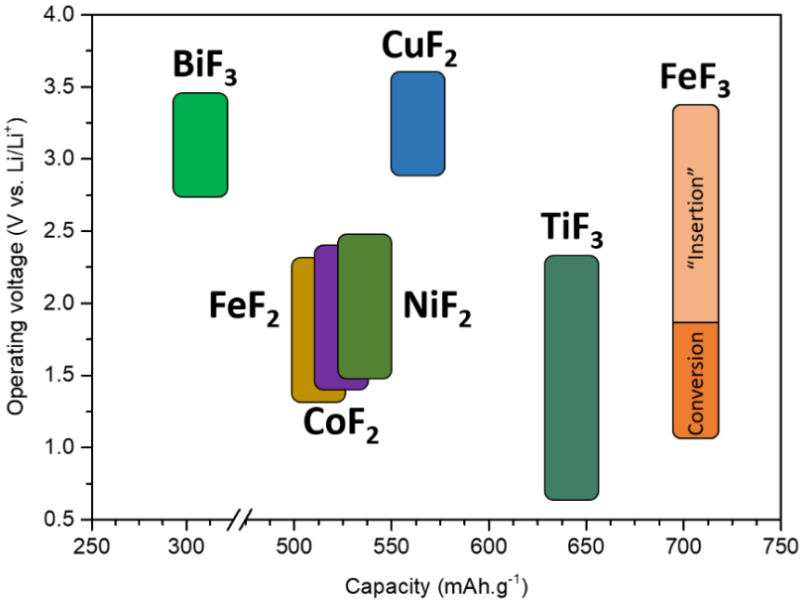

Figure 2.9. *Working voltage vs. Li/Li^+ of the different metal fluorides used as positive electrodes against their theoretical capacities.*

Together with their high working potential, their high capacities confer high energy densities to metal fluorides, making then promising candidates for the next generation of LIBs. However, slow reaction kinetics are induced due to the consequent structure changes that involves their conversion reaction, as well as the high insulating character of these compounds given the highly ionic character of the bond between fluorine and metal. Furthermore, during the conversion reaction, nano-sized domains of the reduced metallic species and the lithium fluoride are generated, creating a high-energy surface barrier to overcome in order to activate this reaction. These generated nano-domains lead as well to different reaction pathways during the discharge and charge processes [83,87]. All these phenomena taken into account make the metal transition fluorides having high hysteresis regarding their working potential, low rate capabilities, and poor cycling stabilities. Besides their performance issues, they present another inherent drawback: they do not contain lithium, whereas normally the positive electrode of a lithium-ion cell is used as a lithium reservoir. It is noteworthy to point out that, in contrast to the metal difluorides, which present only conversion reactivity towards lithium, trifluoride materials can have insertion against alkali ions, as it is the case for the different iron(III) phases, such as the FeF_3 R-*3c* and $FeF_3{\cdot}0.33H_2O$ phases [88] or the perovskite-type $NaFeF_3$ [89].

4.2. Metal difluorides as positive electrode for Na- & Li-ion batteries

The use of transition metal difluorides in LIBs is well described in the literature. FeF_2, CoF_2, NiF_2 and CuF_2, which have a rutile structure represented by $(MeF_6)^{-4}$ octahedrons connected to other octahedrons through two edges and four corners (**Figure 2.10**), present high enough theoretical reacting potentials to be used as positive electrode, whereas the pristine crystalline structure will collapse to generate the metallic species and two equivalents of lithium fluoride. MF_2 (M = Fe, Co and Ni) (**Figure 2.10a**) and CuF_2 (**Figure 2.10b**) compounds have very different electrochemical signatures, namely different working potentials and reaction pathways, although they adopt almost the same rutile structure. But as mentioned earlier, their high insulating character influences greatly the performances of these materials, hence their need to be used in practice in the presence of conductive matrices to improve their charge transfer kinetics and the need of nano-sized particles to shorten the pathway of the reacting species (electrons and lithium cations). Various nano-composites were designed in order to overcome this lack of conductivity [90,91,92]. The first application of cobalt and nickel difluorides was made under the formulation of thin films [93,94]. Interestingly, these materials were reported as suitable for anode purpose due to the low reaction potential that they showed within these studies (0.5 V vs. Li/Li^+) but however showed higher discharge capacity than their theoretical ones (more than 600 $mAh.g^{-1}$ c.f. **Figure 2.9**). The discharge mechanisms were proven to produce metallic Ni and Co, as well as lithium fluoride. Low capacity retention was also reported in the case of CoF_2, probably due to the relatively low cutoff potential for the reconversion of the material into the difluoride compound. NiF_2 showed a relatively good capacity retention within the 0.01-3.5 V vs. Li/Li^+ potential window, probably due to a topotactic reaction of lithium in the not complete converted nickel fluoride species, such as $LiNiF_4$. It has later been shown that CoF_2 and NiF_2 could be nano-formulated to obtain sensitively improved performances, but still having a lack of stability upon cycling and low working potential hindering their application as active materials for positive electrode applications [95,96]. The non-total reconversion during the charging process of these compounds could be one of the reasons for the low capacity retention they show. Further studies designing hierarchical composite structures demonstrated that the confining of the active material could greatly improve the capacity retention, avoiding the possible dissolution of the fluoride material in the electrolyte or the pulverization of the electrode during the volume expansion taking place during the discharge process [97]. The case of copper(II) fluoride is slightly different because its working potential is higher than for other metal difluorides materials (~ 3.0 V for CuF_2 compared to < 2 V vs. Li/Li^+ in the case of the other transition metal difluorides). This

difference in working potential is believed to arise from differences in the rutile organization structure, as well as its different reaction mechanism towards lithium [98]. Weng *et al.* demonstrated that the formation of the nanostructured material after the first discharge was mainly isolating the metallic copper in a lithium fluoride matrix, preventing the electrical conductivity during the subsequent charge/discharge processes [99]. The mechanism involving the irreversible CuF_2 conversion is different as in the case of the other transition metal fluorides, where the metallic species create a conductively connected network for the electrons, enabling the subsequent reconversion. Furthermore, the non-reconverted metallic copper is sensitive to oxidation if a potential higher than 3 V vs Li/Li^+ is applied [100]. Similarly to the case of the other metal difluorides, nano-sized materials embedded into carboneous matrix seems to be suitable to overcome these mechanistic and chemical-stability drawbacks [97]. More recently, several studies claimed that mixed transition metal fluoride compounds, such as $Fe_{0.5}Cu_{0.5}F_2$, could improve their performances by a synergistic effect [101], even if some other studies seem to be inconsistent with these findings [101,102]. Metal difluorides for sodium-ion batteries have been seldom studied due to their low activity, owning to thermodynamical limitations. The sodiation of these compounds occurs via disproportion reactions, in contrast of the one-step conversion towards lithium. This reaction pathway towards sodium limits the practicable capacity to less than half of the theoretical one [103]. For example, Hwang *et al.* designed a composite of NaF-FeF_2 and observed capacities lower than 100 $mAh.g^{-1}$ during the first charge/discharge process at low discharge potential (1.0 V vs Li/Li^+), speaking for a reaction only through insertion mechanisms [104].

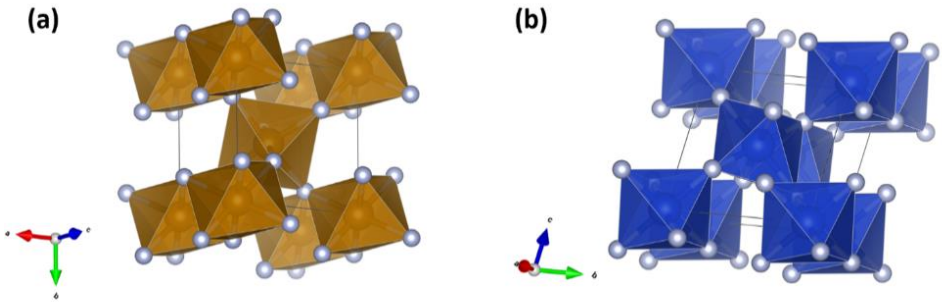

Figure 2.10. *Illustrations of the* **(a)** *tetragonal rutile crystal structure of FeF_2, CoF_2, NiF_2, and* **(b)** *monoclinic rutile crystal structure typical for CuF_2.*

4.3. Iron(III) fluoride as positive electrode for Na- & Li-ion batteries

Iron(III) fluoride has been the fluoride compound most extensively studied for battery applications during the last two decades due to its high abundance, environmentally friendly

character and for presenting the highest theoretical energy density among all other metal fluoride compounds [82]. Iron(III) fluoride can adopt several crystal structures depending upon the water content in its framework. Given its hygroscopic character, contact with water gradually leads to the formation of the trihydrated phase, $FeF_3 \cdot 3H_2O$. The building blocks of such structures are built up by $(FeF_6)^{3-}$ octahedrons connected by their corners, which differs from the typical rutile structure where octahedrons present also shared-edge connections. The crystalline phase of anhydrous iron(III) fluoride is close to the ReO_3 one, but with a Fe-F-Fe angle of ~150 ° resulting in a rhombohedral configuration, where the rhenium oxide structure conformation is the ideal cubic one.

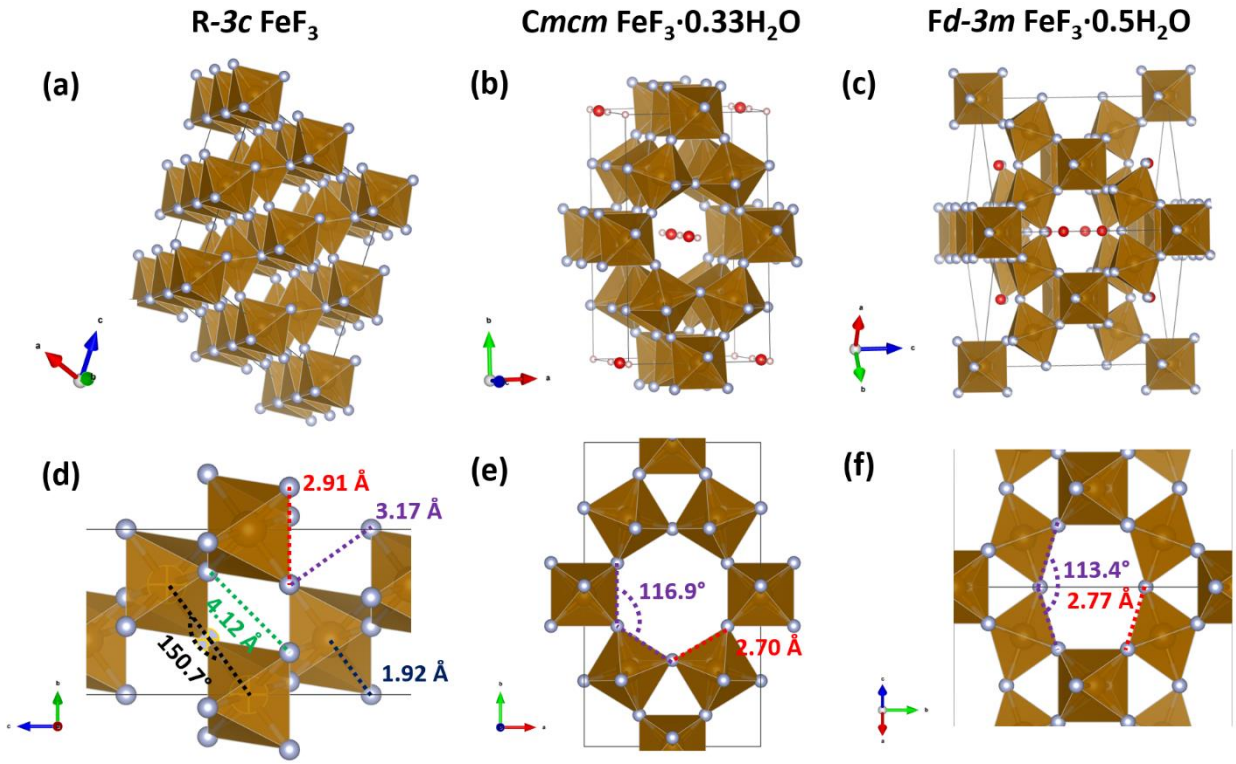

Figure 2.11. *Illustrations of the different phases that adopt iron(III) fluoride compound depending on their water content, namely* **(a)** *R3-c* FeF_3 *anhydrous,* **(b)** $FeF_3 \cdot 0.33H_2O$ *Hexagonal Tungsten Bronze and* **(c)** $FeF_3 \cdot 0.5H_2O$ *Pyrochlore phases and* **(d)**, **(e)**, **(f)** *focus on their cell parameters, respectively.*

The incorporation of 0.33 molecule parts of water per formula unit forces the structure to adopt the hexagonal tungsten bronze structure (HTB), which presents large channels in the crystallographic *c* direction. If, on the other hand, 0.5 molecules of water per formula unit are incorporated a pyrochlore framework is formed. The channels in the HTB and pyrochlore structures are stabilized by the incorporation of water and offer good diffusion pathways for lithium ions (**Figure 2.11**). These structures offer channels of different dimensions with 6.53

Å^2 for the R-3*c* anhydrous iron(III) fluoride, 19.21 Å^2 for HTB structure and 20.20 Å^2 for the pyrochlore structure. In contrast with the typical reaction of lithium with metal difluoride, the pure FeF_3 presents a two-step mechanism, which involves first the insertion of lithium ions in the framework as well as complex displacement reactions (**2.6**). Below 2.0 V vs. Li/Li$^+$, only the conversion of the lithiated iron fluoride structure occurs, which ends up by the formation of nano-domains of metallic iron and lithium fluoride (**2.7**).

(**2.6**) $Fe^{III}F_3 + Li^+ + e^- \rightarrow$ "$LiFe^{II}F_3$" (above 2.0 V vs. Li/Li$^+$)

(**2.7**) "$LiFe^{II}F_3$" + 2 Li^+ + 2 e^- → Fe^0 + 3 LiF (below 2.0 V vs. Li/Li$^+$)

The mechanism dominating the first part of the whole discharge is not quite clear, even though many studies were done in order to figure out the identity of the intermediate species before the conversion reaction below 2.0 V. The group of Ceder proposed that the lithium insertion occurs up to 0.25 Li atoms, followed by a phase transition of the framework to the trirutile phase up to 0.5 atoms of Li per formula unit. During this process, the connections of the $(FeF_6)^{3-}$ octahedrons pass from corner- to edge-shared, involving the collapse of the original structure and leading to conversion products with complicated stoichiometries ($Li_{3/4}Fe_{3/4}F_3$, $LiFe_{1/2}F_3$, $Li_{15/8}Fe_{3/8}F_3$, etc.). After the fluoride material is fully converted into metallic iron and lithium fluoride, particles of the two different compounds tend to agglomerate to lower the high surface energy created throughout the generation of nanoscopic domains. Then, upon the charge, different pathways of reaction are followed induced by this agglomeration, leading to high hysteresis. The obtained phase at the end of the charge is reported to not show long-range order and is ascribed to a deformed FeF_3 rutile structure [105,106]. Iron fluoride compounds are frequently studied in the potential range > 2.0 V since the one-electron reaction does not involve a dramatical electrode pulverization, as it is the case for the three-lithium reaction where lower potentials are applied (< 2.0 V) [107,108]. As iron(III) fluoride phases present different structures, their insertion behaviors towards lithium are slightly different above 2.0 V vs. Li/Li$^+$, but if the full conversion is achieved, they exhibit similar reactivity. Larger channels are beneficial for lithium diffusion while increasing the water content within the structures hinders good lithium transport. Iron(III) fluoride materials adopting the HTB structure have generally higher rate capability than the tighter R-*3c* polymorph. However, the fully hydrated $FeF_3{\cdot}3H_2O$ presents limited performances due to the high water content in the structure, affecting its specific capacity and rate capability [109]. Regarding the reactivity of these compounds towards sodium, only open structures are commonly adapted to host the larger ionic radius of sodium cations. Li *et al.* proposed for first time the use of the FeF_3 pyrochlore structure for this purpose and

showed how superior performances compared to the reported ones for anhydrous iron(III) fluoride phase [110].

4.4. Perovskite iron fluoride phases for alkali-ion batteries

As mentioned above, the major drawback of fluoride materials, used as cathodes in alkali-ion batteries, is the absence of alkali ions in their structure. Indeed, the positive electrode in alkali-ion systems is supposed to act as a reservoir of alkali ions. To use fluoride materials as practicable cathodes, composites made of metallic species (Fe or Co) mixed with two or three equivalents of lithium fluoride were proposed in order to incorporate lithium in the positive electrode. Even though these composites show similar behavior compared to their metal fluoride analogs, their performances are quite low [111,112]. Another possibility to pair transition metal fluoride-based cathodes with alkali-free anodes is the use of $AFeF_3$ structures (A = Li, Na, K). However, $LiFeF_3$ is not thermodynamically stable and its synthesis leads to the formation of a LiF and FeF_2 mix, or the trirutile $LiFe_2F_6$ phase [113]. Lithium has not a large enough atomic radius to occupy the 12-fold coordinated A-sites, thus making the perovskite structure thermodynamically unstable [114]. On the other hand, larger ions, such as sodium or potassium, are able to stabilize this kind of structure. Sodium iron(II) fluoride presents a perovskite structure, where the $(FeF_6)^{3-}$ octahedrons are corner-shared with a Fe-F-Fe angle of around 143 ° (**Figure 2.12.a-b**). This conformation is analog to the R-*3c* FeF_3. The incorporation of sodium atoms within the framework induces a larger channel dimension, namely 7.70 $Å^2$ for $NaFeF_3$ compared to 6.53 $Å^2$ for the R-3*c* FeF_3. This considerable difference in dimension creates an improve sodium diffusion within the 3D channel network oriented along the [10-1], [-10-1] and [010] crystallographic directions. Gocheva *et al.* proposed first the synthesis of $NaFeF_3$ by mechano-synthesis between NaF and FeF_2 through a ball-milling process [115]. The use of this material as positive electrodes for NIBs was described in this seminal study and the reversible electrochemical disinsertion of sodium was monitored by Mössbauer spectroscopy. Afterward, different synthesis approaches were described, such as liquid phase or rolling quench synthesis [89,116]. Yu *et al.* performed calculations on the structure and the electronic properties of $NaFeF_3$ towards sodium electrochemical dis/insertion [117]. They concluded that the charge/discharge processes should occur through a two-step mechanism with the dis/insertion of the first half sodium content out/in the unit cell at a redox potential of 2.62 V and the second half at 2.82 vs. Na/Na^+. This work highlights the possibility to disinsert sodium entirely from the structure. However, in practice, the mechanisms occurring during the charge/discharge processes of $NaFeF_3$ remain elusive, due to the low performances reported,

which imply a non-complete sodium extraction. The low performances of $NaFeF_3$, illustrated by poor capacity retention, low rate capability and high hysteresis, could be ascribed to the synthesis methods used to prepare this compound, where the morphology and the crystallinity degree cannot be controlled. Furthermore, other metal transition sodiated perovskites were also studied as positive electrodes for NIBs, namely $NaMnF_3$, $NaCoF_3$, $NaNiF_3$ and $NaCuF_3$. Several hypotheses about the failure of these compounds where formulated: thermodynamically limitations could avoid the extraction of sodium from their structure due to the instability of the formed sodium-free species, such as CuF_3 [114], additionally to their too high working potentials, above the stability of common electrolytes.

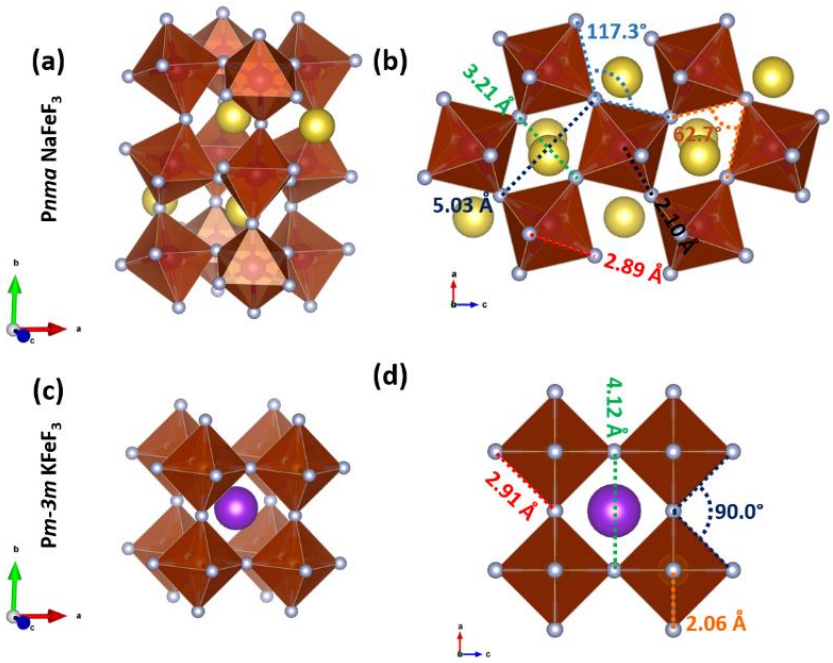

Figure 2.12. *Illustrations of the different perovskite structures:* **(a, b)** *orthorhombic Pnma and* **(c, d)** *cubic Pm-3m perovskites.*

Another interesting perovskite compound is $KFeF_3$, which adopts a cubic phase since potassium ions are larger compared to sodium. The channels in the three equivalent [100] crystallographic directions are larger than the ones in the P*nma* sodiated phase (8.49 $Å^2$ compared to 7.70 $Å^2$), allowing the diffusion of the large potassium ions (**Figure 2.12.c&d**). Although this compound was only little studied in the K-ion system [118], it can undergo the insertion of sodium ions after the partial or total disinsertion of the potassium ions from the A-sites of the perovskite structure. The open framework that this compound offers is believed to be adaptable to the dis/insertion processes of big ions such as sodium or potassium. Different synthetic methods for this compound are described in the literature as well as its

electrochemical properties [119,120]. Specific capacities of about half of its theoretical capacity were reported, making the study of its reaction mechanisms along potassium disinsertion and sodium dis/insertion incomplete. Only small volume changes of the unit cell were reported, although upon the full potassium disinsertion a significant decrease of the cell parameters is expected. On the basis of the study of Yu *et al.* , the adoption of the P*nma* perovskite structure would be expected, typical for $NaFeF_3$, after insertion of one sodium atom per formula unit [117]. Other potassium-containing phases analog to the hydrated phases of iron(III) fluoride were reported by Han *et al.* as active materials for LIBs and NIBs [120]. In their work, the frameworks adopt similar polymorphs than the hydrated iron(III) fluoride phase by replacing water molecules by potassium, albeit having very low activity upon alkali insertions. Other metal transition fluoride perovskites were studied as active materials for alkali-ion batteries, such as $KMnF_3$ or $KCoF_3$ [121]. Very low performances were reported in these studies, even when the K-ion system was used [118]. Other iron perovskite fluoride structures were already reported in the literature, such as $CsFeF_3$ or NH_4FeF_3, but never studied as actives material for battery purpose. In the case of the cesium containing structure, the alkali ions might be too heavy to diffuse at room temperature within the perovskite structure. However, the light weight of the ammonium ions could offer to these species good diffusion capability, even though so far, the activity of such molecule was never reported for alkali-ion systems.

References

1. Lu, X.; Anariba, F., Fostering Innovation through an Active Learning Activity Inspired by the Baghdad Battery. *Journal of Chemical Education* **2014,** *91* (11), 1929-1933.
2. Scrosati, B., History of lithium batteries. *J Solid State Electrochem* **2011,** *Volume 15* (Issue 7-8), pp 1623-1630.
3. Cecchini, R.; Pelosi, G., Alessandro Volta and his battery. *IEEE Antennas and Propagation Magazine* **1992,** *34* (2), 30-37.
4. O., D., The Constant Battery and the Daniell-Becquerel-Grove Controversy. *Ambix* **2001,** *48:1*, 25-40.
5. Dalard, F., Le Gorrec, B., Machat, J.Y. et al. , Nouveau type de piles Leclanché. II. Etude en regime fort intermittent. *J Appl Electrochem* **1976,** *6* (45), 1234-1236.
6. Poizot, P.; Dolhem, F., Clean energy new deal for a sustainable world: from non-CO_2 generating energy sources to greener electrochemical storage devices. *Energy & Environmental Science* **2011,** *4* (6), 2003-2019.
7. Whittingham, M. S., Materials Challenges Facing Electrical Energy Storage. *MRS Bulletin* **2008,** *33* (4), 411-419.
8. Dunn, B.; Kamath, H.; Tarascon, J.-M., Electrical Energy Storage for the Grid: A Battery of Choices. *Science* **2011,** *334* (6058), 928-935.
9. Westerlund, S.; Ekstam, L., Capacitor theory. *IEEE Transactions on Dielectrics and Electrical Insulation* **1994,** *1* (5), 826-839.

10. Zhang, Y.; Feng, H.; Wu, X.; Wang, L.; Zhang, A.; Xia, T.; Dong, H.; Li, X.; Zhang, L., Progress of electrochemical capacitor electrode materials: A review. *International Journal of Hydrogen Energy* **2009,** *34* (11), 4889-4899.
11. Steele, B. C. H.; Heinzel, A., Materials for fuel-cell technologies. In *Materials for Sustainable Energy*, pp 224-231.
12. Reddy T. D. , L. D., Handbook of batteries. *Storage Systems Tech* **2011,** *3*.
13. WHITTINGHAM, M. S., Electrical Energy Storage and Intercalation Chemistry. *Science* **1976,** *192* (4244), 1126-1127.
14. Mizushima, K.; Jones, P. C.; Wiseman, P. J.; Goodenough, J. B., Li_xCoO_2 ($0<x<-1$): A new cathode material for batteries of high energy density. *Materials Research Bulletin* **1980,** *15* (6), 783-789.
15. Godshall, N. A.; Raistrick, I. D.; Huggins, R. A., Thermodynamic investigations of ternary lithium-transition metal-oxygen cathode materials. *Materials Research Bulletin* **1980,** *15* (5), 561-570.
16. Thackeray, M. M.; David, W. I. F.; Bruce, P. G.; Goodenough, J. B., Lithium insertion into manganese spinels. *Materials Research Bulletin* **1983,** *18* (4), 461-472.
17. Qi, Z.; Koenig Jr., G. M., High-Performance $LiCoO_2$ Sub-Micrometer Materials from Scalable Microparticle Template Processing. *ChemistrySelect* **2016,** *1* (13), 3992-3999.
18. Hazama, T.; Miyabayashi, M.; Andoh, H.; Ishikawa, R.; Furuta, S.; Ishihara, H.; Shonaka, J., Lithium secondary batteries in Japan. *Journal of Power Sources* **1995,** *54* (2), 306-309.
19. Gonzalez, M.; Perez, M. A.; Diaz, J.; Ferrero, F. J. In *Ni-Cd and Ni-MH battery optimized fast-charge method for portable telecommunication applications*, Proceedings of Intelec'96 - International Telecommunications Energy Conference, 6-10 Oct. 1996; 1996; pp 522-529.
20. Sasaki, T.; Ukyo, Y.; Novák, P., Memory effect in a lithium-ion battery. *Nature Materials* **2013,** *12*, 569.
21. Peters, G. P.; Andrew, R. M.; Boden, T.; Canadell, J. G.; Ciais, P.; Le Quéré, C.; Marland, G.; Raupach, M. R.; Wilson, C., The challenge to keep global warming below 2 °C. *Nature Climate Change* **2012,** *3*, 4.
22. Goebel, K.; Saha, B.; Saxena, A.; Celaya, J. R.; Christophersen, J. P., Prognostics in Battery Health Management. *IEEE Instrumentation & Measurement Magazine* **2008,** *11* (4), 33-40.
23. Abraham, K. M., Recent developments in secondary lithium battery technology. *Journal of Power Sources* **1985,** *14* (1), 179-191.
24. Di Pietro, B.; Patriarca, M.; Scrosati, B., On the use of rocking chair configurations for cyclable lithium organic electrolyte batteries. *Journal of Power Sources* **1982,** *8* (2), 289-299.
25. Zhang, W.-J., A review of the electrochemical performance of alloy anodes for lithium-ion batteries. *Journal of Power Sources* **2011,** *196* (1), 13-24.
26. Dahn, J. R.; Zheng, T.; Liu, Y.; Xue, J. S., Mechanisms for Lithium Insertion in Carbonaceous Materials. *Science* **1995,** *270* (5236), 590-593.
27. Wu, Y. P.; Rahm, E.; Holze, R., Carbon anode materials for lithium ion batteries. *Journal of Power Sources* **2003,** *114* (2), 228-236.
28. Stevens, D. A.; Dahn, J. R., The Mechanisms of Lithium and Sodium Insertion in Carbon Materials. *Journal of The Electrochemical Society* **2001,** *148* (8), A803-A811.
29. Chen, Z.; Wang, Q.; Amine, K., Improving the performance of soft carbon for lithium-ion batteries. *Electrochimica Acta* **2006,** *51* (19), 3890-3894.
30. Buiel, E.; Dahn, J. R., Li-insertion in hard carbon anode materials for Li-ion batteries. *Electrochimica Acta* **1999,** *45* (1), 121-130.
31. Loeffler, B. N.; Bresser, D.; Passerini, S.; Copley, M., Secondary Lithium-Ion Battery Anodes: From First Commercial Batteries to Recent Research Activities. *Johnson Matthey Technology Review* **2015,** *59* (1), 34-44.
32. Obrovac, M. N.; Chevrier, V. L., Alloy Negative Electrodes for Li-Ion Batteries. *Chemical Reviews* **2014,** *114* (23), 11444-11502.
33. Nazri, G. A.; Conell, R. A.; Julien, C., Preparation and physical properties of lithium phosphide-lithium chloride, a solid electrolyte for solid state lithium batteries. *Solid State Ionics* **1996,** *86-88*, 99-105.
34. Li, X.; Gu, M.; Hu, S.; Kennard, R.; Yan, P.; Chen, X.; Wang, C.; Sailor, M. J.; Zhang, J.-G.; Liu, J., Mesoporous silicon sponge as an anti-pulverization structure for high-performance lithium-ion battery anodes. *Nature Communications* **2014,** *5*, 4105.

35. Wen, Z. S.; Yang, J.; Wang, B. F.; Wang, K.; Liu, Y., High capacity silicon/carbon composite anode materials for lithium ion batteries. *Electrochemistry Communications* **2003,** *5* (2), 165-168.
36. Poizot, P.; Laruelle, S.; Grugeon, S.; Dupont, L.; Tarascon, J. M., Nano-sized transition-metal oxides as negative-electrode materials for lithium-ion batteries. *Nature* **2000,** *407* (6803), 496-499.
37. Wu, H. B.; Chen, J. S.; Hng, H. H.; Wen Lou, X., Nanostructured metal oxide-based materials as advanced anodes for lithium-ion batteries. *Nanoscale* **2012,** *4* (8), 2526-2542.
38. Zhukovskii, Y. F.; Kotomin, E. A.; Balaya, P.; Maier, J., Enhanced interfacial lithium storage in nanocomposites of transition metals with LiF and Li_2O: Comparison of DFT calculations and experimental studies. *Solid State Sciences* **2008,** *10* (4), 491-495.
39. Aurbach, D.; Talyosef, Y.; Markovsky, B.; Markevich, E.; Zinigrad, E.; Asraf, L.; Gnanaraj, J. S.; Kim, H.-J., Design of electrolyte solutions for Li and Li-ion batteries: a review. *Electrochimica Acta* **2004,** *50* (2), 247-254.
40. Aurbach, D., Review of selected electrode–solution interactions which determine the performance of Li and Li ion batteries. *Journal of Power Sources* **2000,** *89* (2), 206-218.
41. Wang, Y.; Cao, G., Developments in Nanostructured Cathode Materials for High-Performance Lihium-Ion Batteries. *Advanced Materials* **2008,** *20* (12), 2251-2269.
42. Cho, J., Correlation between AlPO4 nanoparticle coating thickness on $LiCoO_2$ cathode and thermal stability. *Electrochimica Acta* **2003,** *48* (19), 2807-2811.
43. Sharifi-Asl, S.; Soto, F. A.; Nie, A.; Yuan, Y.; Asayesh-Ardakani, H.; Foroozan, T.; Yurkiv, V.; Song, B.; Mashayek, F.; Klie, R. F.; Amine, K.; Lu, J.; Balbuena, P. B.; Shahbazian-Yassar, R., Facet-Dependent Thermal Instability in $LiCoO_2$. *Nano Letters* **2017,** *17* (4), 2165-2171.
44. Diercks, D. R.; Musselman, M.; Morgenstern, A.; Wilson, T.; Kumar, M.; Smith, K.; Kawase, M.; Gorman, B. P.; Eberhart, M.; Packard, C. E., Evidence for Anisotropic Mechanical Behavior and Nanoscale Chemical Heterogeneity in Cycled $LiCoO_2$. *Journal of The Electrochemical Society* **2014,** *161* (11), F3039-F3045.
45. Huang, H.; Yin, S.-C.; Nazar, L. F., Approaching Theoretical Capacity of $LiFePO_4$ at Room Temperature at High Rates. *Electrochemical and Solid-State Letters* **2001,** *4* (10), A170-A172.
46. Legagneur, V.; An, Y.; Mosbah, A.; Portal, R.; Le Gal La Salle, A.; Verbaere, A.; Guyomard, D.; Piffard, Y., $LiMBO_3$ (M=Mn, Fe, Co):: synthesis, crystal structure and lithium deinsertion/insertion properties. *Solid State Ionics* **2001,** *139* (1), 37-46.
47. Dominko, R., Li_2MSiO_4 (M=Fe and/or Mn) cathode materials. *Journal of Power Sources* **2008,** *184* (2), 462-468.
48. Ramesh, T. N.; Lee, K. T.; Ellis, B. L.; Nazar, L. F., Tavorite Lithium Iron Fluorophosphate Cathode Materials: Phase Transition and Electrochemistry of $LiFePO_4F$ – Li_2FePO_4F. *Electrochemical and Solid-State Letters* **2010,** *13* (4), A43-A47.
49. Ati, M.; Melot, B. C.; Chotard, J. N.; Rousse, G.; Reynaud, M.; Tarascon, J. M., Synthesis and electrochemical properties of pure $LiFeSO_4F$ in the triplite structure. *Electrochemistry Communications* **2011,** *13* (11), 1280-1283.
50. Wutthiprom, J.; Phattharasupakun, N.; Sawangphruk, M., Turning Carbon Black to Hollow Carbon Nanospheres for Enhancing Charge Storage Capacities of $LiMn_2O_4$, $LiCoO_2$, $LiNiMnCoO_2$, and $LiFePO_4$ Lithium-Ion Batteries. *ACS Omega* **2017,** *2* (7), 3730-3738.
51. Chen, C. H.; Liu, J.; Stoll, M. E.; Henriksen, G.; Vissers, D. R.; Amine, K., Aluminum-doped lithium nickel cobalt oxide electrodes for high-power lithium-ion batteries. *Journal of Power Sources* **2004,** *128* (2), 278-285.
52. Yi, T.-F.; Hao, C.-L.; Yue, C.-B.; Zhu, R.-S.; Shu, J., A literature review and test: Structure and physicochemical properties of spinel $LiMn_2O_4$ synthesized by different temperatures for lithium ion battery. *Synthetic Metals* **2009,** *159* (13), 1255-1260.
53. Yamada, A.; Chung, S. C.; Hinokuma , K., Optimized $LiFePO_4$ for Lithium Battery Cathodes. *Journal of The Electrochemical Society* **2001,** *148* (3), A224-A229.
54. Susantyoko, R. A.; Alkindi, T. S.; Kanagaraj, A. B.; An, B.; Alshibli, H.; Choi, D.; AlDahmani, S.; Fadaq, H.; Almheiri, S., Performance optimization of freestanding MWCNT-$LiFePO_4$ sheets as cathodes for improved specific capacity of lithium-ion batteries. *RSC Advances* **2018,** *8* (30), 16566-16573.
55. Burke, A. F., Batteries and Ultracapacitors for Electric, Hybrid, and Fuel Cell Vehicles. *Proceedings of the IEEE* **2007,** *95* (4), 806-820.

56. Clement-Nyns, K.; Haesen, E.; Driesen, J., The Impact of Charging Plug-In Hybrid Electric Vehicles on a Residential Distribution Grid. *IEEE Transactions on Power Systems* **2010,** *25* (1), 371-380.
57. Tarascon, J.-M., Is lithium the new gold? *Nature Chemistry* **2010,** *2*, 510.
58. Kikkawa, S.; Miyazaki, S.; Koizumi, M., Deintercalated $NaCoO_2$ and $LiCoO_2$. *Journal of Solid State Chemistry* **1986,** *62* (1), 35-39.
59. Doeff, M. M.; Visco, S. J.; Yanping, M.; Peng, M.; Lei, D.; De Jonghe, L. C., Thin film solid state sodium batteries for electric vehicles. *Electrochimica Acta* **1995,** *40* (13), 2205-2210.
60. Okada, S.; Takahashi, Y.; Kiyabu, T.; Doi, T.; Yamaki, J.-I.; Nishida, T., Layered Transition Metal Oxides as Cathodes for Sodium Secondary Battery. *Meeting Abstracts* **2006,** *MA2006-02* (4), 201.
61. Yabuuchi, N.; Kubota, K.; Dahbi, M.; Komaba, S., Research Development on Sodium-Ion Batteries. *Chemical Reviews* **2014,** *114* (23), 11636-11682.
62. Han, M. H.; Gonzalo, E.; Singh, G.; Rojo, T., A comprehensive review of sodium layered oxides: powerful cathodes for Na-ion batteries. *Energy & Environmental Science* **2015,** *8* (1), 81-102.
63. Monti, D.; Jónsson, E.; Palacín, M. R.; Johansson, P., Ionic liquid based electrolytes for sodium-ion batteries: Na^+ solvation and ionic conductivity. *Journal of Power Sources* **2014,** *245*, 630-636.
64. Doeff, M. M.; Ma, Y.; Visco, S. J.; De Jonghe, L. C., Electrochemical Insertion of Sodium into Carbon. *Journal of The Electrochemical Society* **1993,** *140* (12), L169-L170.
65. Cao, Y.; Xiao, L.; Sushko, M. L.; Wang, W.; Schwenzer, B.; Xiao, J.; Nie, Z.; Saraf, L. V.; Yang, Z.; Liu, J., Sodium Ion Insertion in Hollow Carbon Nanowires for Battery Applications. *Nano Letters* **2012,** *12* (7), 3783-3787.
66. Qiu, S.; Xiao, L.; Sushko, M. L.; Han, K. S.; Shao, Y.; Yan, M.; Liang, X.; Mai, L.; Feng, J.; Cao, Y.; Ai, X.; Yang, H.; Liu, J., Manipulating Adsorption–Insertion Mechanisms in Nanostructured Carbon Materials for High-Efficiency Sodium Ion Storage. *Advanced Energy Materials* **2017,** *7* (17), 1700403.
67. Wenzel, S.; Hara, T.; Janek, J.; Adelhelm, P., Room-temperature sodium-ion batteries: Improving the rate capability of carbon anode materials by templating strategies. *Energy & Environmental Science* **2011,** *4* (9), 3342-3345.
68. Stevens, D. A.; Dahn, J. R., High Capacity Anode Materials for Rechargeable Sodium-Ion Batteries. *Journal of The Electrochemical Society* **2000,** *147* (4), 1271-1273.
69. Komaba, S.; Murata, W.; Ishikawa, T.; Yabuuchi, N.; Ozeki, T.; Nakayama, T.; Ogata, A.; Gotoh, K.; Fujiwara, K., Electrochemical Na Insertion and Solid Electrolyte Interphase for Hard-Carbon Electrodes and Application to Na-Ion Batteries. *Advanced Functional Materials* **2011,** *21* (20), 3859-3867.
70. Senguttuvan, P.; Rousse, G.; Seznec, V.; Tarascon, J.-M.; Palacín, M. R., $Na_2Ti_3O_7$: Lowest Voltage Ever Reported Oxide Insertion Electrode for Sodium Ion Batteries. *Chemistry of Materials* **2011,** *23* (18), 4109-4111.
71. Xiong, H.; Slater, M. D.; Balasubramanian, M.; Johnson, C. S.; Rajh, T., Amorphous TiO_2 Nanotube Anode for Rechargeable Sodium Ion Batteries. *The Journal of Physical Chemistry Letters* **2011,** *2* (20), 2560-2565.
72. Lao, M.; Zhang, Y.; Luo, W.; Yan, Q.; Sun, W.; Dou, S. X., Alloy-Based Anode Materials toward Advanced Sodium-Ion Batteries. *Advanced Materials* **2017,** *29* (48), 1700622.
73. Delmas, C.; Braconnier, J.-J.; Fouassier, C.; Hagenmuller, P., Electrochemical intercalation of sodium in Na_xCoO_2 bronzes. *Solid State Ionics* **1981,** *3-4*, 165-169.
74. Delmas, C., Alkali metal intercalation in layered oxides. *Materials Science and Engineering: B* **1989,** *3* (1), 97-101.
75. Delmas, C., Sodium and Sodium-Ion Batteries: 50 Years of Research. *Advanced Energy Materials* **2018,** *8* (17), 1703137.
76. Slater, M. D.; Kim, D.; Lee, E.; Johnson, C. S., Sodium-Ion Batteries. *Advanced Functional Materials* **2013,** *23* (8), 947-958.
77. Kosova, N. V.; Podugolnikov, V. R.; Bobrikov, I. A.; Balagurov, A. M., Crystal Structure and Electrochemistry of $Na_{2-x}Li_xFePO_4F$ ($0 \leq x \leq 1$) New Cathode Materials for Na- and Li-Ion Batteries. *ECS Transactions* **2014,** *62* (1), 67-78.
78. Lu, Y.; Wang, L.; Cheng, J.; Goodenough, J. B., Prussian blue: a new framework of electrode materials for sodium batteries. *Chemical Communications* **2012,** *48* (52), 6544-6546.

79. Wang, S.; Wang, L.; Zhu, Z.; Hu, Z.; Zhao, Q.; Chen, J., All Organic Sodium-Ion Batteries with Na4C8H2O6. *Angewandte Chemie International Edition* **2014,** *53* (23), 5892-5896.
80. Wang, D.-W.; Zeng, Q.; Zhou, G.; Yin, L.; Li, F.; Cheng, H.-M.; Gentle, I. R.; Lu, G. Q. M., Carbon–sulfur composites for Li–S batteries: status and prospects. *Journal of Materials Chemistry A* **2013,** *1* (33), 9382-9394.
81. Conte, D. E. P., A review on the application of iron(III) fluorides as positive electrodes for secondary cells. *N. Mater Renew Sustain Energy* **2014,** *3: 37*.
82. Badway, F.; Pereira, N.; Cosandey, F.; Amatucci, G. G., Carbon-Metal Fluoride Nanocomposites: Structure and Electrochemistry of FeF_3 : C. *Journal of The Electrochemical Society* **2003,** *150* (9), A1209-A1218.
83. Abraham, K. M., Status of rechargeable positive electrodes for ambient temperature lithium batteries. *Journal of Power Sources* **1981,** *7* (1), 1-43.
84. Arai, H.; Okada, S.; Sakurai, Y.; Yamaki, J.-i., Cathode performance and voltage estimation of metal trihalides. *Journal of Power Sources* **1997,** *68* (2), 716-719.
85. Plitz, I.; Badway, F.; Al-Sharab, J.; DuPasquier, A.; Cosandey, F.; Amatucci, G. G., Structure and Electrochemistry of Carbon-Metal Fluoride Nanocomposites Fabricated by Solid-State Redox Conversion Reaction. *Journal of The Electrochemical Society* **2005,** *152* (2), A307-A315.
86. Li, L.; Jacobs, R.; Gao, P.; Gan, L.; Wang, F.; Morgan, D.; Jin, S., Origins of Large Voltage Hysteresis in High-Energy-Density Metal Fluoride Lithium-Ion Battery Conversion Electrodes. *Journal of the American Chemical Society* **2016,** *138* (8), 2838-2848.
87. Carlo, L. D.; Conte, D. E.; Kemnitz, E.; Pinna, N., Microwave-assisted fluorolytic sol–gel route to iron fluoride nanoparticles for Li-Ion batteries. *Chemical Communications* **2014,** *50* (4), 460-462.
88. Yamada, Y.; Doi, T.; Tanaka, I.; Okada, S.; Yamaki, J.-i., Liquid-phase synthesis of highly dispersed $NaFeF_3$ particles and their electrochemical properties for sodium-ion batteries. *Journal of Power Sources* **2011,** *196* (10), 4837-4841.
89. Wang, X.; Gu, W.; Lee, J. T.; Nitta, N.; Benson, J.; Magasinski, A.; Schauer, M. W.; Yushin, G., Carbon Nanotube–CoF_2 Multifunctional Cathode for Lithium Ion Batteries: Effect of Electrolyte on Cycle Stability. *Small* **2015,** *11* (38), 5164-5173.
90. Song, H.; Cui, H.; Wang, C., Extremely high-rate capacity and stable cycling of a highly ordered nanostructured carbon–FeF_2 battery cathode. *Journal of Materials Chemistry A* **2015,** *3* (44), 22377-22384.
91. Parkinson, M. F.; Ko, J. K.; Halajko, A.; Sanghvi, S.; Amatucci, G. G., Effect of Vertically Structured Porosity on Electrochemical Performance of FeF_2 Films for Lithium Batteries. *Electrochimica Acta* **2014,** *125*, 71-82.
92. Zhang, H.; Zhou, Y.-N.; Sun, Q.; Fu, Z.-W., Nanostructured nickel fluoride thin film as a new Li storage material. *Solid State Sciences* **2008,** *10* (9), 1166-1172.
93. Fu, Z.-W.; Li, C.-L.; Liu, W.-Y.; Ma, J.; Wang, Y.; Qin, Q.-Z., Electrochemical Reaction of Lithium with Cobalt Fluoride Thin Film Electrode. *Journal of The Electrochemical Society* **2005,** *152* (2), E50-E55.
94. Teng, Y. T.; Pramana, S. S.; Ding, J.; Wu, T.; Yazami, R., Investigation of the conversion mechanism of nanosized CoF_2. *Electrochimica Acta* **2013,** *107*, 301-312.
95. Armstrong, M. J.; Panneerselvam, A.; O'Regan, C.; Morris, M. A.; Holmes, J. D., Supercritical-fluid synthesis of FeF_2 and CoF_2 Li-ion conversion materials. *Journal of Materials Chemistry A* **2013,** *1* (36), 10667-10676.
96. Chun, J.; Jo, C.; Sahgong, S.; Kim, M. G.; Lim, E.; Kim, D. H.; Hwang, J.; Kang, E.; Ryu, K. A.; Jung, Y. S.; Kim, Y.; Lee, J., Ammonium Fluoride Mediated Synthesis of Anhydrous Metal Fluoride–Mesoporous Carbon Nanocomposites for High-Performance Lithium Ion Battery Cathodes. *ACS Applied Materials & Interfaces* **2016,** *8* (51), 35180-35190.
97. Zheng, Y.; Zhang, P.; Wu, S. Q.; Wen, Y. H.; Zhu, Z. Z.; Yang, Y., First-principles studies on the structural and electronic properties of Li-ion battery cathode material CuF_2. *Solid State Communications* **2012,** *152* (17), 1703-1706.
98. Wang, F.; Robert, R.; Chernova, N. A.; Pereira, N.; Omenya, F.; Badway, F.; Hua, X.; Ruotolo, M.; Zhang, R.; Wu, L.; Volkov, V.; Su, D.; Key, B.; Whittingham, M. S.; Grey, C. P.; Amatucci, G. G.; Zhu, Y.; Graetz, J., Conversion Reaction Mechanisms in Lithium Ion Batteries: Study of the Binary Metal Fluoride Electrodes. *Journal of the American Chemical Society* **2011,** *133* (46), 18828-18836.

99. Seo, J. K.; Cho, H.-M.; Takahara, K.; Chapman, K. W.; Borkiewicz, O. J.; Sina, M.; Shirley Meng, Y., Revisiting the conversion reaction voltage and the reversibility of the CuF_2 electrode in Li-ion batteries. *Nano Research* **2017,** *10* (12), 4232-4244.
100. Wang, F.; Kim, S.-W.; Seo, D.-H.; Kang, K.; Wang, L.; Su, D.; Vajo, J. J.; Wang, J.; Graetz, J., Ternary metal fluorides as high-energy cathodes with low cycling hysteresis. *Nature Communications* **2015,** *6*, 6668.
101. Omenya, F.; Zagarella, N. J.; Rana, J.; Zhang, H.; Siu, C.; Zhou, H.; Wen, B.; Chernova, N. A.; Piper, L. F. J.; Zhou, G.; Whittingham, M. S., Intrinsic Challenges to the Electrochemical Reversibility of the High Energy Density Copper(II) Fluoride Cathode Material. *ACS Applied Energy Materials* **2019**.
102. He, K.; Zhou, Y.; Gao, P.; Wang, L.; Pereira, N.; Amatucci, G. G.; Nam, K.-W.; Yang, X.-Q.; Zhu, Y.; Wang, F.; Su, D., Sodiation via Heterogeneous Disproportionation in FeF_2 Electrodes for Sodium-Ion Batteries. *ACS Nano* **2014,** *8* (7), 7251-7259.
103. Hwang, I.; Jung, S.-K.; Jeong, E.-S.; Kim, H.; Cho, S.-P.; Ku, K.; Kim, H.; Yoon, W.-S.; Kang, K., NaF–FeF_2 nanocomposite: New type of Na-ion battery cathode material. *Nano Research* **2017,** *10* (12), 4388-4397.
104. Liu, P.; Vajo, J. J.; Wang, J. S.; Li, W.; Liu, J., Thermodynamics and Kinetics of the Li/FeF_3 Reaction by Electrochemical Analysis. *The Journal of Physical Chemistry C* **2012,** *116* (10), 6467-6473.
105. Ko, J. K.; Wiaderek, K. M.; Pereira, N.; Kinnibrugh, T. L.; Kim, J. R.; Chupas, P. J.; Chapman, K. W.; Amatucci, G. G., Transport, Phase Reactions, and Hysteresis of Iron Fluoride and Oxyfluoride Conversion Electrode Materials for Lithium Batteries. *ACS Applied Materials & Interfaces* **2014,** *6* (14), 10858-10869.
106. Murugesan, V.; Cho, J. S.; Govind, N.; Andersen, A.; Olszta, M. J.; Han, K. S.; Li, G.; Lee, H.; Reed, D. M.; Sprenkle, V. L.; Cho, S.; Nune, S. K.; Choi, D., Lithium Insertion Mechanism in Iron Fluoride Nanoparticles Prepared by Catalytic Decomposition of Fluoropolymer. *ACS Applied Energy Materials* **2019,** *2* (3), 1832-1843.
107. Zhai, J.; Lei, Z.; Rooney, D.; Sun, K., Top-down synthesis of iron fluoride/reduced graphene nanocomposite for high performance lithium-ion battery. *Electrochimica Acta* **2019,** *313*, 497-504.
108. Liu, L.; Guo, H.; Zhou, M.; Wei, Q.; Yang, Z.; Shu, H.; Yang, X.; Tan, J.; Yan, Z.; Wang, X., A comparison among $FeF_3 \cdot 3H_2O$, $FeF_3 \cdot 0.33H_2O$ and FeF_3 cathode materials for lithium ion batteries: Structural, electrochemical, and mechanism studies. *Journal of Power Sources* **2013,** *238*, 501-515.
109. Nishijima, M.; Gocheva, I. D.; Okada, S.; Doi, T.; Yamaki, J.-i.; Nishida, T., Cathode properties of metal trifluorides in Li and Na secondary batteries. *Journal of Power Sources* **2009,** *190* (2), 558-562.
110. Li, C.; Yin, C.; Gu, L.; Dinnebier, R. E.; Mu, X.; van Aken, P. A.; Maier, J., An $FeF_3 \cdot 0.5H_2O$ Polytype: A Microporous Framework Compound with Intersecting Tunnels for Li and Na Batteries. *Journal of the American Chemical Society* **2013,** *135* (31), 11425-11428.
111. Wall, C.; Prakash, R.; Kübel, C.; Hahn, H.; Fichtner, M., Synthesis of [Co/LiF/C] nanocomposite and its application as cathode in lithium-ion batteries. *Journal of Alloys and Compounds* **2012,** *530*, 121-126.
112. Prakash, R.; Wall, C.; Mishra, A. K.; Kübel, C.; Ghafari, M.; Hahn, H.; Fichtner, M., Modified synthesis of [Fe/LiF/C] nanocomposite, and its application as conversion cathode material in lithium batteries. *Journal of Power Sources* **2011,** *196* (14), 5936-5944.
113. Liao, P.; Li, J.; Dahn, J. R., Lithium Intercalation in $LiFe_2F_6$ and $LiMgFeF_6$ Disordered Trirutile-Type Phases. *Journal of The Electrochemical Society* **2010,** *157* (3), A355-A361.
114. Dimov, N.; Nishimura, A.; Chihara, K.; Kitajou, A.; Gocheva, I. D.; Okada, S., Transition metal $NaMF_3$ compounds as model systems for studying the feasibility of ternary Li-M-F and Na-M-F single phases as cathodes for lithium–ion and sodium–ion batteries. *Electrochimica Acta* **2013,** *110*, 214-220.
115. Gocheva, I. D.; Nishijima, M.; Doi, T.; Okada, S.; Yamaki, J.-i.; Nishida, T., Mechanochemical synthesis of $NaMF_3$ (M=Fe, Mn, Ni) and their electrochemical properties as positive electrode materials for sodium batteries. *Journal of Power Sources* **2009,** *187* (1), 247-252.
116. Kitajou, A.; Komatsu, H.; Chihara, K.; Gocheva, I. D.; Okada, S.; Yamaki, J.-i., Novel synthesis and electrochemical properties of perovskite-type $NaFeF_3$ for a sodium-ion battery. *Journal of Power Sources* **2012,** *198*, 389-392.

117. Yu, S.; Zhang, P.; Wu, S. Q.; Li, A. Y.; Zhu, Z. Z.; Yang, Y., Understanding the structural and electronic properties of the cathode material $NaFeF_3$ in a Na-ion battery. *Journal of Solid State Electrochemistry* **2014,** *18* (8), 2071-2075.
118. Cao, D.; Yin, C.; Shi, D.; Fu, Z.; Zhang, J.; Li, C., Cubic Perovskite Fluoride as Open Framework Cathode for Na-Ion Batteries. *Advanced Functional Materials* **2017,** *27* (28), 1701130.
119. Yi, T.; Chen, W.; Cheng, L.; Bayliss, R. D.; Lin, F.; Plews, M. R.; Nordlund, D.; Doeff, M. M.; Persson, K. A.; Cabana, J., Investigating the Intercalation Chemistry of Alkali Ions in Fluoride Perovskites. *Chemistry of Materials* **2017,** *29* (4), 1561-1568.
120. Han, Y.; Hu, J.; Yin, C.; Zhang, Y.; Xie, J.; Yin, D.; Li, C., Iron-based fluorides of tetragonal tungsten bronze structure as potential cathodes for Na-ion batteries. *Journal of Materials Chemistry A* **2016,** *4* (19), 7382-7389.
121. Wang, S.; Cui, B.; Zhuang, Q.; Shi, Y.; Zheng, H., Synthesis and Electrochemical Performance of Cobalt-Doped $KMnF_3$ as Cathode Materials for Potassium Ion Batteries. *Journal of The Electrochemical Society* **2019,** *166* (10), A1819-A182

Chapter 3

Experimental setup

1. Preparation methods

1.1. Synthesis

Most of the synthesis routes used in this thesis were carried out in the liquid phase. The preparation of the $Co(OH)_2$ precursor, described in chapter 4, was done by a simple co-precipitation reaction, while the iron oxide precursors were prepared through a hydrothermal synthesis for the hematite phase and a sol-gel route for the magnetite particles. The synthesis of the transition metal fluoride materials in liquid phase followed the so-called fluorolytic sol-gel route (explained below in more details). After the formation of the nanoparticles, the solid materials were precipitated by centrifugation, and afterwards purified by repeated precipitation/dispersion in ethanol and/or acetone. In the case of the perovskite materials, all syntheses and characterizations were carried out under inert atmosphere using conventional Schlenk techniques or handling in a glovebox, to avoid oxidation processes. Anhydrous iron(III) fluoride was synthesized via a gas-solid phase reaction. To overcome the insulating character of the fluoride materials, the nanoparticles were either grafted onto graphene oxide (GO) through different techniques, or mixed with carbon black (CB) by the mean of a ball-milling apparatus (planetary mill PULVERISETTE 7). The preparation details of the material are described in the respective chapters.

1.2. Different sol-gel routes

Many different approaches allow the synthesis of nanomaterials by soft chemistry, such as colloidal methods or hydrothermal syntheses [1,2]. Among them, the sol-gel process is one of the most known synthesis routes for the generation of metal oxide nanostructured materials [3]. Since the appearance of this method at the beginning of the 80s, it has been widely developed and used even today for many applications, such as the production of well-designed active materials for battery purposes [4]. The relatively low temperatures used during this process and the excellent control over the morphology and purity of the products made this method very popular. Additionally, not only inorganic compounds can be obtained by this approach but also polymers [5]. The precursors used to synthesize metal oxides are generally metal alkoxides, but other reactants can also be used, such as chlorides, nitrates or sulfates. The process can be split into two steps. First, a sol defined by a colloidal suspension is formed, which evolves gradually in a second step to form a gel. This gel is a bi-phasic media constituted of a liquid and a solid

phase, in which the particles can be bonded chemically or physically. By varying the reaction conditions, the products obtained can range from discrete particles to a continuous gel network. The synthesis process can be classified in two classes, namely the hydrolytic and the non-aqueous sol-gel process. In the case of the hydrolytic sol-gel process, the hydrolysis of the precursor first takes place to allow then the condensation reaction to occur. When alkoxides are used, the hydrolysis step is defined by the coordination of the metal center by water molecules, generating M—OH bonds (**3.1**). The condensation process occurs between hydroxylated and alcohol species to form M—O—M bonds (**3.2**) and (**3.3**). Due to simultaneous occurrence of hydrolysis and the condensation in the reaction media, the morphology of obtained materials depends upon the reaction rates of these processes, which are influenced by several factors, such as temperature, pH, etc. [6].

(**3.1**) —M—OR + H_2O → —M—OH + ROH

(**3.2**) —M—OH + HO—M— → —M—O—M— + H_2O

(**3.3**) —M—OR + HO— → —M—O— + ROH

M = metal ion, R = organic groups

In contrast, the non-aqueous sol-gel route does not involve a hydrolysis step, which needs the presence of the water [7]. The formation of the M—O—M bonds results from the direct reaction of the precursors, where the oxygen atoms are provided by the cleavage of carbon-oxygen bonds contained in alkoxides, alcohol or ethers precursors (**3.4**). The metal precursor can also react in a first step with the organic solvent to react then with another molecule of precursor (**3.5**). In this method, the reproducibility and crystallization limitations present in the complex hydrolytic route can be overcome.

(**3.4**) —M—O—R + R—O—M— → —M—O—M— + R—O—R

(**3.5**) —M—X + R—O—M— → —M—O—M— + R—X

X = solvent reacted group

For the generation of fluoride materials with high surface area, nano-sized metal oxides are generally treated by fluorinating agents at high temperatures, but these processes result in a decrease of the specific surface of the product [8]. Similarly to the formation of nano-sized metal oxide materials, the sol-gel route can be also applied in the case of the metal fluorides. In this case, hydrogen fluoride plays an analog role to water during the fluorination of alkoxide precursors (**3.6**) [9].

(**3.6**) —M—OR + HF → —M—F + HOR

The formation of the M—F bond is driven by the higher donor ability of the fluorine ions compared to alcohol molecules. Depending on the metal precursor used, the reaction can directly form precipitates without forming a gel. However, the real mechanism involved during this reaction has not yet been totally elucidated.

1.3. Reactants

Cobalt(II) nitrate hexahydrated 98 % ($Co(NO_3)_2 \cdot 6H_2O$), sodium ethoxide 98 % (NaOEt), iron(III) nitrate nonahydrated 98 % ($Fe(NO_3)_3 \cdot 9H_2O$), iron(II) chloride 98 % ($FeCl_2$), anhydrous iron(II) acetate 97 % (Fe(ac)2), anhydrous manganese(II) acetate 98+ % (Mn(ac)2), anhydrous cobalt(II) acetate 98+ % (Co(ac)2), anhydrous potassium ethoxide 98 % (KOEt) were purchased from ABCR. Ammonium fluoride 99,99 % (NH_4F), ammonium hydroxide 28–30 % NH_3 basis (NH_4OH), oleylamine 70 %, commercial Fe_2O_3 NPs, anhydrous methanol 90 % and benzyl alcohol 99,8 % (BnOH) were purchased from Sigma-Aldrich. The solution of anhydrous HF in methanol was prepared by bubbling a gaseous HF/argon mixture through the solvent in an fluorinated ethylene propylene (FEP) bottle under cooling. HF is a hazardous agent and has to be used under restricted conditions only!

2. Characterization methods

2.1. X-ray powder diffraction

In order to determine the crystalline phases and the purities of the synthesized products, powder X-ray diffraction (XRD) was used. In this experiment, X-rays produced by a metal source interact with the electronic density of the crystal atoms of the sample to probe. The sample is tilted in respect with the source, as well as the detector (depending on the apparatus configuration). When the X-rays interact with the crystalline framework at specific scattering angles (Θ) fulfilling the Bragg's law (**3.7**), diffracted constructive interferences are created and can be detected by the diffractometer apparatus, resulting in a diffraction pattern which can be recorded.

(**3.7**) $n \cdot \lambda = 2d \cdot \sin(\Theta)$

Where ***n*** is a positive integer, ***λ*** is the wavelength of the incident X-ray beam, ***d*** is the interplanar distance between two diffraction planes, and ***Θ*** the scattering angle.

This diffraction pattern is defined by reflections, which are the result of the previously cited constructive interferences. The pattern of reflections that a crystalline phase presents can be seen as its fingerprint. These reflections are defined by their set of shape, intensities and

location within the array of scattering angles, and can belong to one or several different crystalline phases within the compound to probe. The analysis of a diffraction pattern allows the determination of the crystalline phase to which the compound belongs, but also the average size of the crystallites through the Scherrer equation (**3.8**) [10], the cell parameters through Le Bail refinement or even the specific atomic positions through Rietveld refinement [11]. The crystalline phases can be assigned to specific space groups related to the organization of the atoms within the unit cell.

$$(\mathbf{3.8}) \quad \tau = \frac{K \cdot \lambda}{\beta \cdot cos(\Theta)}$$

Where $\boldsymbol{\tau}$ is the mean size of the crystalline domains, $\boldsymbol{K}$ the dimensional shape factor (taken as 0.8 during the crystallite size calculation, relative to spherical particles), $\boldsymbol{\lambda}$ is the wavelength of the incident X-ray beam, $\boldsymbol{\beta}$ the broadening at the half-maximum intensity (FWHM), and $\boldsymbol{\Theta}$ the specific scattering angle.

All the XRD measurements in this work were carried out in an STOE Stadi MP diffractometer equipped with a Dectris Mythen 1K linear silicon strip detector and a Ge(111) double-crystal monochromator (Mo $K_{\alpha 1}$ radiation). The X-ray generation is provided by a molybdenum tube in order to avoid any fluorescence noise for the measurement of samples containing cobalt or iron. The routine data collection for the powder materials and *ex situ* electrodes were conducted in transmission geometry, while the data collection for refinement and *operando* measurements was carried out in reflection geometry. The refinements of the obtained data were realized with the Fullprof software.

2.2. Transmission electronic microscopy and Energy-dispersive X-ray spectroscopy

Transmission electronic microscopy (TEM) is used to observe the features of objects ranging from the micro to the nano size. For this purpose, an accelerated beam of electrons is projected through a column under vacuum on the material to study. The electron beam is blocked depending on the thickness and the atomic composition of the sample and is later recovered on a phosphorescent screen. The contrast of the collected resulting beam allows to obtain a 2D representation of the probed material.

While the TEM experiment uses the primary electron beam, energy dispersive X-ray spectroscopy (EDX) is able to determine the atomic ratio within a material by the X-rays induced by the excitation of the sample by the primary beam. When the primary beam is focused on the surface sample, electrons belonging to the shell relative to ground states can be

excited. These excitations can eject electrons from inner shells and create holes within those atomic shells, which are then filled by electrons from higher shell levels. These electron transitions from higher to lower energy levels thus generate X-ray radiations, which have discrete energies relative to the involved electron transitions. From the different energy of the emitted X-rays, the composition of the sample can be determined.

In this work, these techniques were used in order to determine the size, the morphology and the atomic ratios of the synthesized nano-sized materials. The TEM images and EDX measurement were recorded on a Philips CM 200 microscope equipped with a LaB_6 cathode and operated at 200 kV equipped with an EDAX camera. The samples were prepared by depositing homogeneous dispersion of the nanomaterials in ethanol onto copper grids with a 300 µm carbon film.

2.3. Fourier-transform infrared spectroscopy

Fourier-transform infrared spectroscopy (FTIR) is a spectrometric technique allowing the obtention of infrared spectra of absorption or emission of solid, liquid or gas. The technique consists of a measurement of how much light a material can absorb at different wavelengths. Typical absorption wavelengths can be assigned to the vibrations of specific chemical bonds. Therefore, different chemical bonds can be detected through this characterization method.

In this work, this technique is mainly used to see the chemical interaction between the synthesized nanoparticles and their graphene oxide (GO) substrate. The IR spectra were recorded on a Digilab FTIR 3000, Excalibur series in ATR configuration in the range 3000-400 cm^{-1}.

3. Electrochemical characterization methods

3.1. Electrode preparation and cell assembly

The active material powders were blended with poly(vinylidenedifluoride) (PVdF, Alfa Aesar) in N-methylpyrrolidone (NMP, Sigma-Aldrich, anhydrous 99.5%). The final mass ratios between the active materials, PVdF, and the different conductive matrices were 68:17:5:10 (active material/ GO/CB/PVdF) in chapter 4 and 70:20:10 (active material/CB/PVdF) in the chapters 5 and 6. The homogeneous slurries wee spread on aluminum foils with a razor blade in order to obtain a thickness of 300 µm and left more than two days to allow the NMP to be evaporated. Then, disks of 18 mm of diameter were cut to be used as electrodes. The active material mass loadings range from 2 to 5 mg per electrode, which represents 0.68 to 1.72 $mg \cdot cm^{-2}$. For the *operando* XRD measurement in chapter 5, the milled materials with CB were used directly after the milling process without additional CB and PVdF. The mass loading of

active material for the *operando* cell is ~15 mg.cm^{-2}. The electrochemical performances were evaluated via half-cell tests using glass fiber as separators (Whatman), 1 M KPF_6 (ABCR, 99.9% battery grade) in nonaqueous propylene carbonate (ABCR, 99%) against metallic potassium (Sigma) as electrolyte for the K-ion system, 1 M $NaClO_4$ (ABCR, 99.9% battery grade) in a nonaqueous mixture of propylene carbonate (ABCR, 99%), fluoroethylene carbonate (Sigma, 99%) as the electrolyte (95:5) against metallic sodium (Sigma) for the Na-ion system when no other specifications are given, and 1 M $LiPF_6$ (ABCR, 99.9% battery grade) in a mix of ethylene carbonate (ABCR, 99.9%), propylene carbonate (ABCR, 99.9%) dimethyl carbonate (ABCR, 99.9%) as the electrolyte (1:1:1) against metallic lithium (Sigma) for the Li-ion system. For the full-cell setup in chapter 4, the same electrolyte as in the normal sodium system has been used, taking hard carbon (HC) as reference. All these steps were carried out in an argon glovebox atmosphere, with O_2 and H_2O values below 1 ppm.

3.2. Cyclic voltammetry

Cyclic voltammetry (CV) is a technique where the potential of the working electrode (WE) is ramped linearly versus time to a V_1 value, starting from the open circuit potential (OCP) of the WE. Once the desired voltage is reached the WE's potential is ramped to the opposite direction to reach a potential V_2, and then goes back to the initial value of the OCP. During this process, the CV experiment proceeds one cycle. During this cycle, the sweep in potential creates a positive current response along the anodic direction and a negative current response along the cathodic direction. This technique allows the identification of the potentials (vs. Li/Li^+, Na/Na^+ or K/K^+) of the different redox reactions occurring in the material during the charge and discharge processes. These experiments were carried out on a Bio-Logic VMP3 at a scan speed of 0.1 mV.s^{-1}.

3.3. Galvanostatic cycling

Cycling of the electrochemical cells was done realized via galvanostatic experiments. In these experiments, a constant current is applied to the cell and the evolution of its potential is monitored, versus the amount of electrons reacted with the active material. For the calculations of the current densities used, only the masses of the active materials were taken into consideration. The cycling experiments were conducted with a LAND CT2000A battery testing system.

References

1. Daou, T. J.; Pourroy, G.; Bégin-Colin, S.; Grenèche, J. M.; Ulhaq-Bouillet, C.; Legaré, P.; Bernhardt, P.; Leuvrey, C.; Rogez, G., Hydrothermal Synthesis of Monodisperse Magnetite Nanoparticles. *Chemistry of Materials* **2006,** *18* (18), 4399-4404.
2. Sau, T. K.; Rogach, A. L., Nonspherical Noble Metal Nanoparticles: Colloid-Chemical Synthesis and Morphology Control. *Advanced Materials* **2010,** *22* (16), 1781-1804.
3. Hench, L. L.; West, J. K., The sol-gel process. *Chemical Reviews* **1990,** *90* (1), 33-72.
4. Choi, D.; Kumta, P. N., Surfactant based sol–gel approach to nanostructured $LiFePO_4$ for high rate Li-ion batteries. *Journal of Power Sources* **2007,** *163* (2), 1064-1069.
5. Wu, D.; Fu, R.; Dresselhaus, M. S.; Dresselhaus, G., Fabrication and nano-structure control of carbon aerogels via a microemulsion-templated sol–gel polymerization method. *Carbon* **2006,** *44* (4), 675-681.
6. Livage, J.; Henry, M.; Sanchez, C., Sol-gel chemistry of transition metal oxides. *Progress in Solid State Chemistry* **1988,** *18* (4), 259-341.
7. Niederberger, M., Nonaqueous Sol–Gel Routes to Metal Oxide Nanoparticles. *Accounts of Chemical Research* **2007,** *40* (9), 793-800.
8. Kemnitz, E.; Noack, J., The non-aqueous fluorolytic sol–gel synthesis of nanoscaled metal fluorides. *Dalton Transactions* **2015,** *44* (45), 19411-19431.
9. Rüdiger, S.; Kemnitz, E., The fluorolytic sol–gel route to metal fluorides—a versatile process opening a variety of application fields. *Dalton Transactions* **2008,** (9), 1117-1127.
10. Patterson, A. L., The Scherrer Formula for X-Ray Particle Size Determination. *Physical Review* **1939,** *56* (10), 978-982.
11. McCusker, L.; Von Dreele, R.; Cox, D.; Louër, D.; Scardi, P., Rietveld refinement guidelines. *Journal of Applied Crystallography* **1999,** *32* (1), 36-50.

Chapter 4

Synthesis and electrochemical behavior of metal di- and trifluorides

1. Introduction

In this chapter, the syntheses, characterizations and electrochemical properties of transition metal di- and trifluorides are described. As already mentioned, metal fluoride compounds present very low conductivity. In order to overcome this insulating character, synthesis routes allowing the obtention of nanoscale materials are needed, as well as their combination with conductive matrices. The downsizing of the particles to the nanoscale improves drastically the diffusion of the charged species by shortening their pathways within the active material, while the formulation of the nanoscale active material with conductive matrices is carried out to improve the charge transfer of the charged species. The influence of the synthesis parameters on the final compounds is here described, as well as the electrochemical behavior of the active materials depending on the formulation. Cobalt(II) fluoride will be used as a case study of the metal difluoride as cathode material for lithium-ion batteries. The difluoride materials will be used in Chapter 5 as precursors for the syntheses of the perovskite structure. Whereas the anhydrous iron(III) fluoride produced by the fluorination of iron oxide will be used as reference material for electrochemical reactions towards different alkali ions of these perovskite structures.

2. Cobalt(II) fluoride

2.1. Synthesis of cobalt(II) fluoride compounds & composites and their structural and morphological characterization

In the literature, the synthesis routes used for the production of cobalt(II) fluoride usually follow a decomposition of cobalt precursors, such as $CoSiF_6$ [1], at temperatures ranging from 200 to 400°C, or hydrothermal synthesis involving a surfactant, to obtain nano-sized materials, followed by heat treatment for proper crystallization [2]. So far, no simple synthesis method able to control the morphology of the synthesized compounds has been described. In this chapter, the fluorolytic sol-gel route is used to produce metal difluoride nanoparticles in benzyl alcohol under microwave irradiation. This approach was already reported for the synthesis of iron(III) fluoride starting from the dehydrated and partially hydrolyzed $Fe(NO_3)_3 \cdot 9H_2O$ for catalysis and battery application [3,4]. The heat treatment under vacuum of hydrated transition metal nitrates

implies the formation of $M^{x+}(NO_3)_{1-x}(OH)_x$ species, with different compositions as a function of the heating, following their fluorination after their dissolution in an organic solvent. Herein, the influence on the composition of the precursors was studied by varying the parameters of the decomposition of $Co(NO_3)_2{\cdot}6H_2O$, as well as using pristine metal nitrate and $Co(OH)_2$ as starting materials. The synthesis takes place as follow. First, when decomposed metal nitrates precursors are used, 3 mmol of the compound are introduced in a Schlenk tube where vacuum is applied at different temperatures, namely 50 °C, 100 °C, 150 °C and 200 °C. The different temperatures used for the decomposition of the precursor will influence the nitrate/hydroxyl ratio within the staring material, influencing the subsequent fluorination step. Then, benzyl alcohol is introduced as a liquid medium to dissolve the decomposed precursor under inert atmosphere. When metal nitrate or $Co(OH)_2$ are used directly, they are introduced in benzyl under an inert atmosphere. The synthesis of the $Co(OH)_2$ precursor involves the facile reaction between the hydrated cobalt nitrate and two equivalents of sodium hydroxide in water and its purification and separation by filtration. After total dissolution of the precursor, a concentrated methanolic solution of hydrogen fluoride is added stoichiometrically in the reaction media and the mixture is directly transferred in a vial for microwave treatment at 150 °C for 5 min. Here, the use of microwave irradiation permits a fast heating of the liquid media.

Name of the sample	Precursor	T of decomposition treatment (C°)	N atomic % compared to Co calculated from EA
CoF_2-1	$Co(NO_3)_2{\cdot}6H_2O$	x	x
CoF_2-2	$Co(NO_3)_2{\cdot}6H_2O$	50	95.2%
CoF_2-3	$Co(NO_3)_2{\cdot}6H_2O$	100	86.4%
CoF_2-4	$Co(NO_3)_2{\cdot}6H_2O$	150	50.9%
CoF_2-5	$Co(NO_3)_2{\cdot}6H_2O$	200	31.7%
CoF_2-6	$Co(OH)_2$	x	x

Table 4.1. *Summary of the synthesis parameter of the CoF_2 materials and nitrate remaining content of the precursor calculated from elemental analysis results (***Table A4.1***).*

To study the influence of the decomposition of the nitrate precursors on the final products, elemental analysis was carried out to quantify the remaining amount of nitrate in the decomposed precursors. **Table 4.1** summarizes the synthesis parameters of the CoF_2 materials, as well as the calculated nitrate contents of the decomposed precursors. During the decomposition step, water molecules can hydrolyze the precursor and replace the nitrate groups by OH^-. The compositions obtained by Elementary Analysis could be a consequence of the temperature treatment used: the higher the temperature is, more hydroxyl groups could be coordinated to the cobalt center. **Figure A4.1** illustrates the linear trend which appears by

plotting the composition of the decomposed precursor as function of the treatment temperature. It can be seen that at a treatment temperature of 50 °C, a slightly higher hydrogen content is present, probably due to remaining water molecules.

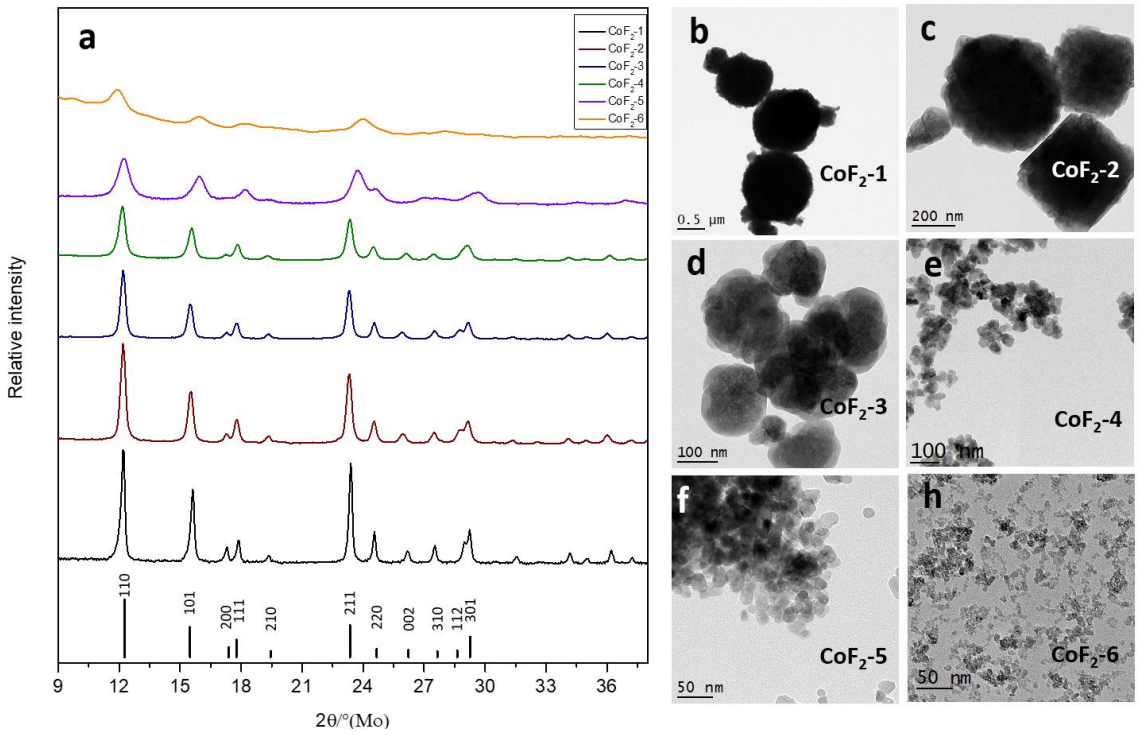

Figure 4.1. (a) *Diffraction patterns of the different CoF_2 materials and reference pattern of the rutile structure, and* **(b)**, **(c)**, **(d)**, **(e)**, **(f)** *and* **(h)** *respective TEM images.*

Figure 4.1.a depicts the XRD patterns of the CoF_2 compounds synthesized using different cobalt precursors. All the obtained products have reflection patterns fitting the reference of rutile cobalt difluoride belonging to the space group $P4_2/mnm$. The patterns do not present additional reflections, confirming the purity of the synthesized compounds. A broadening of the reflections can be observed alongside with the diminution of the nitrate content in the precursor. The reflections relative to the plane (110) do not change in position, but an obvious shift of a few reflections can be appreciated, such as the ones representing the planes (211), (220), (112) and (301). These phenomena can be ascribed to the low crystallinity degree of the nanomaterials. The TEM images of these synthesized compounds can be found in **Figures 4.1.b-h** and display small aggregates of spherical nanoparticles of different sizes. In agreement with the XRD patterns, a similar trend in the diminution of the particle sizes can be observed along with the decrease of the nitrate content in the precursor, ranging from particle sizes of 7 nm for the CoF_2 compound synthesized from the $Co(OH)_2$ precursor, up to 800 nm when untreated $Co(NO_3)_2{\cdot}6H_2O$ is used. **Table A4.2** displays a comparison of the crystallite sizes

calculated by the Scherrer equation and the sizes of the particles observed by electron microscopy. The sizes obtained by the two methods for the samples CoF_2-4, CoF_2-5 and CoF_2-6 are in good agreement, pointing to single crystalline particles, whereas the crystallite sizes slightly increase for the sample CoF_2-1, CoF_2-2, and CoF_2-3. Those observations are in contrast with the sizes of the particles determined by TEM. In addition, the bigger nanoparticles present a texture, which represents several nano-domains within a single particle. These results suggest that the particle formation is slower when the precursor contains more nitrate groups, compared when more hydroxyl groups are present in the precursor. The fluorination by hydrogen fluoride occurs faster in the case of the hydroxylated precursor, therefore more nucleation centers of the nanoparticles are created in the reaction media, favoring the formation of smaller particles. In the case of the untreated $Co(NO_3)_2{\cdot}6H_2O$, the water molecules involved in the solvation sphere of the cobalt center hinder the kinetics of the reaction, which ends up in the generation of very large particles. It is noteworthy to mention that the fluoride materials are usually quite hygroscopic and absorb water. After one month of storage in ambient atmosphere, the fluoride material converts to $CoF_2{\cdot}2H_2O$, the fully hydrated phase (**Figure A4.2**).

a

	Atomic % of Co	Atomic % of F	Overall atomic % of O
CoF_2-1	32.7	67.3	3.8
CoF_2-2	32.1	67.9	2.7
CoF_2-3	30.3	69.7	4.1
CoF_2-4	28.9	81.1	2.1
CoF_2-5	27.5	72.5	3.2
CoF_2-6	24.3	75.7	1.5

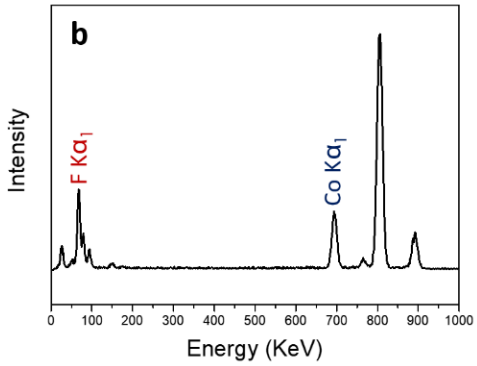

Table 4.2. (a) *Composition of the different CoF_2 synthesized compounds determined by EDX and* **(b)** *typical profile of an EDX graphic measurement (here, measurement of the CoF_2-6 sample)*

The atomic ratios of the cobalt and fluorine atoms are displayed in **Table A4.2**. The compositions of the fluoride compounds match well with the stoichiometry of the cobalt difluoride for the materials presenting bigger particles. However, the lower the particle sizes are, the higher the fluorine content becomes. This is probably due to the presence of chemisorbed HF molecules at the surface of the particles. Indeed, as the specific surface increases, due to the decrease of the size of the particles, the amount of chemisorbed HF increases.

In order to increase the overall conductivity of the materials, grafting the particles onto graphene oxide (GO) has been carried out. GO appears as a very suitable conductive matrix, because of its large surface area, useful for the particle grafting, and its lightweight. GO was prepared from graphite using a modified Hummers' method [5], which consists of an exfoliation step, followed by the oxidation of the graphene sheets. This oxidation will create organic functional groups at the surface of those graphene sheets, such as carboxylic acids or alcohols, which will serve as anchoring points for the particles to be grafted onto it. The grafting of the particles does not only improve the electrochemical performance of the fluoride material but also prevents the formation of particle aggregates, which could hinder the electronic conductivity of the electrode materials. Here, the grafting process is carried out by dispersing GO in presence of CoF_2 particles in BnOH and after a complete dispersion of the two components, microwave treatment at 150 °C for 10 min is applied. The use of BnOH in this grafting process will partially reduce the organic functional groups not involved as anchoring point. The partial reduction of the GO will make the carbon structure closer than the one of the graphene and then improve the conductivity of the oxidized carbon sheets [6,7].

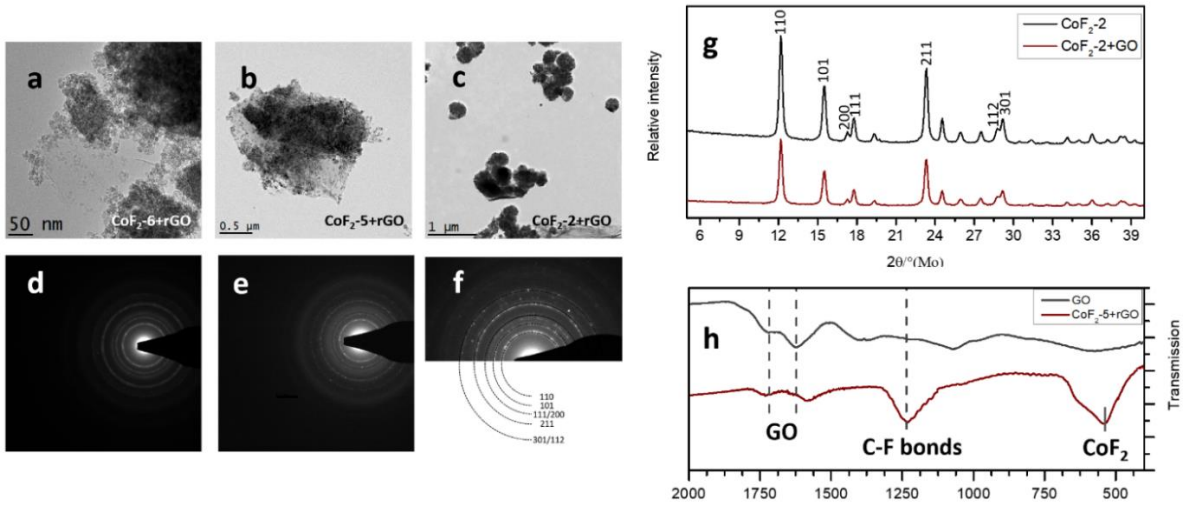

Figure 4.2. *TEM images of the* **(a)** *CoF_2-6+rGO,* **(b)** *CoF_2-5+rGO, **(c)** CoF_2-2+rGO samples and* **(d)**, **(e)**, **(f)** *their SAED measurement, respectively.* **(h)** *Comparison of the XRD patterns of the CoF_2-2 sample, before and after graphene oxide grafting.*

For the grafting processes, samples CoF_2-2, CoF_2-5 and CoF_2-6 were chosen due to their specific particle sizes. The weight ratio between the particles and the GO was chosen as 4/1. **Figure 4.2a-f** display the TEM images of the composite materials obtained by grafting the particles onto GO and their respective SAED measurements. Homogeneous distributions of the particles can be observed in the case of the samples CoF_2-5&6, whereas GO seems to wrap the

large particles of the sample CoF_2-2. No particles can be observed outside GO, translating the efficient grafting of the particles onto the oxidized graphene sheets. The X-ray diffraction patterns of CoF_2-2 before and after the grafting process (**Figure 4.2g**) are unchanged, showing that no alteration of the crystalline structure occurs during this process. Furthermore, no typical (020) reflection of the graphene sheet stacks can be observed, which means that the graphene sheets are well exfoliated, offering the highest specific surface they are able to provide. By FT-IR, a band appears at ~1200 cm^{-1} characteristic to C-F bonds, which represents the chemical linkage between the particles and the carbon material [8]. Additionally, a shift of the band corresponding to GO can be observed, which could be due to its partial reduction during the MW treatment in presence of BnOH (**Figure 4.2h**). Other composite materials can be produced using different carbon matrices, such as carbon nanotubes for instance. For the grafting of the particles onto carbon materials, anchoring points are necessary. For this purpose, carbon nanotubes (CNTs) were pretreated with nitric acid, in order to functionalize their surface. Then, $Co(OH)_2$ was synthesized in presence of these functionalized carbon nanotubes and used as precursor for fluorination.

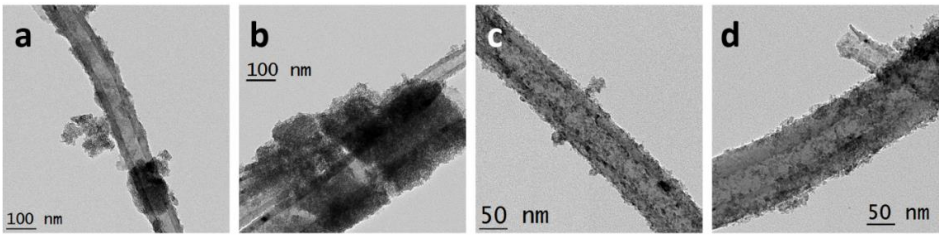

Figure 4.3. *TEM images of* **(a)-(b)** *the $Co(OH)_2$ precursor synthesized in presence of carbon nanotubes and* **(c)-(d)** *of the resulting CoF_2 composite compound (CoF_2-7+fCNTs).*

TEM images of the synthesized precursor and the target compound can be found in **Figure 4.3**. Before the fluorination, $Co(OH)_2$ seems to be formed on the surface of the functionalized carbon nanotubes (fCNTs). After fluorination, a homogeneous coating of very small nanoparticles onto and into the fCNTs can be observed. The size of the particles is smaller than when $Co(OH)_2$ is used in the absence of FCNTs, probably due to the large amount of organic functional groups at the surface of the fCNTs.

2.2. Electrochemical behavior of cobalt(II) fluoride compounds & composite materials

The high theoretical redox potential of cobalt fluoride (vs. Li/Li^+), in addition to its high theoretical capacity, make it a promising cathode material. Composite materials presenting different sizes are expected to present different electrochemical signatures. Indeed, the size reduction of the particles will increase the electrode/electrolyte interface area, improving the

charge transfer in the active material. Furthermore, smaller particles offer also shorter pathways for the active species to react. Therefore, downsizing the particles should be very useful to overcome the insulating character of fluoride materials. Nano-sized material can also accommodate more easily the volume expansion generated during the conversion reactions, partially preventing the pulverization of the electrode formulation.

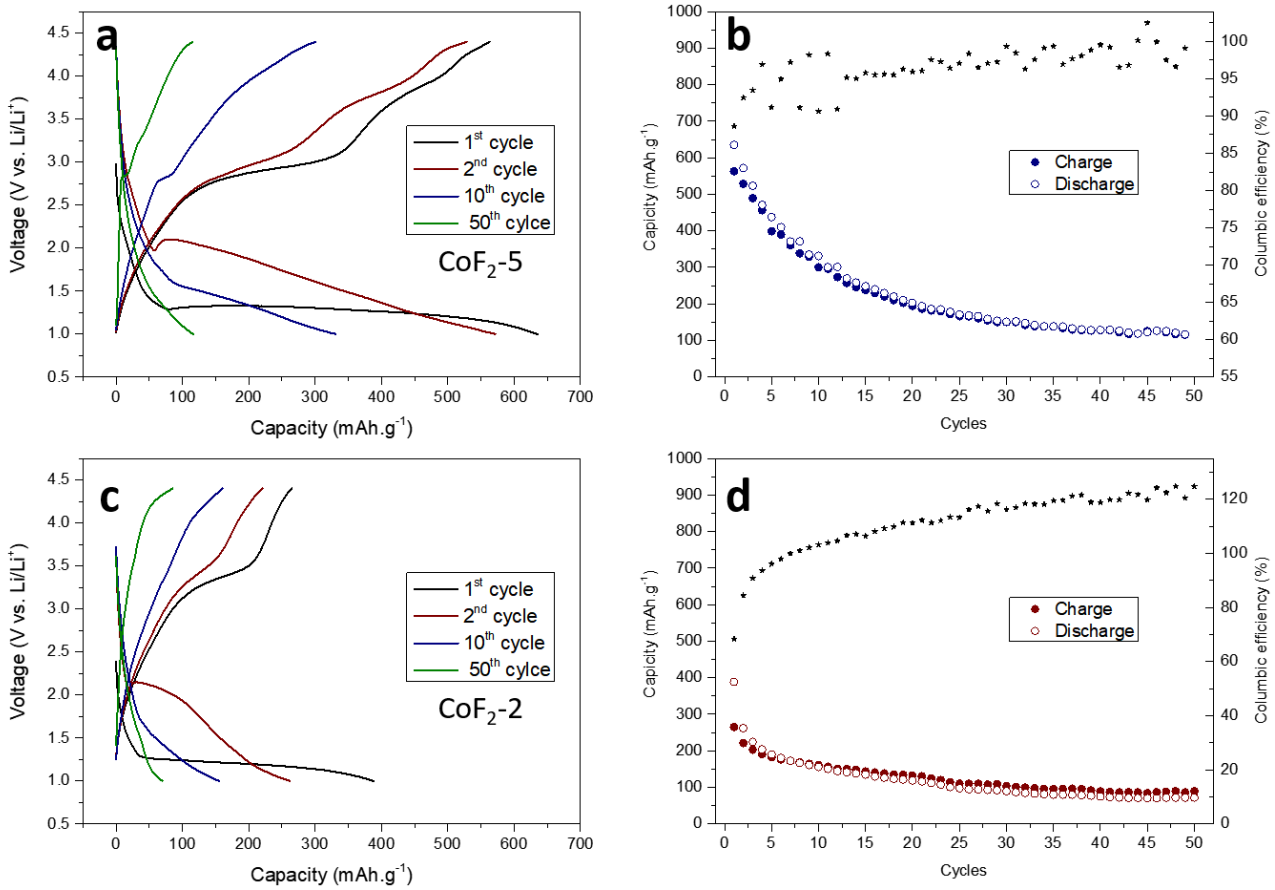

Figure 4.4. (a)-(c) *Galvanostatic profiles of the CoF_2-5+rGO and CoF_2-2+rGO cycled at C/10 towards lithium, and* **(b)-(d)** *corresponding capacity retention plots, respectively.*

The battery tests were carried out under a half-cell configuration using lithium as a counter and reference electrode in a liquid electrolyte. **Figure 4.4** displays the electrochemical behavior of the sample CoF_2-5+rGO and CoF_2-2+rGO when they are cycled at a constant current of C/10 (55.3 $mA.g^{-1}$). The two electrode materials show similar first discharge profiles at around 1.2 V vs Li/Li^+. This potential is lower than the theoretically expected one. This lower value comes from the fact that high-energy barriers have to be overcome in order to generate the resulting nano-domains within the particles induced by the conversion reaction, namely metallic cobalt and lithium fluoride. Additionally, the insulating character of the fluoride compounds slows the kinetics of the conversion reaction. During the reconversion of the materials, a plateau can be

observed at around 2.9 V for CoF_2-5+rGO and 3.3 V for CoF_2-2+rGO vs. Li/Li^+. These plateaus represent the reconversion of metallic cobalt and lithium fluoride into starting CoF_2. The subsequent discharges occur at higher potential, namely ~ 2.2 V vs. Li/Li^+. These higher discharge potential could be due to the not total reconversion of the material during the 1st charge process, generating CoF_x species more conductive than the starting materials, and improving the kinetics of the conversion reaction, as it has been reported before [2]. This trend is also observed during a cyclic voltammetry experiment (**Figure 4.5**). The capacities of the two samples along the cycles decrease rapidly after ten cycles, probably due to the not total reconversion of the compounds during the charge processes, in addition to side reactions from which the active materials could suffer, such as decomposition of the electrolyte on the fluoride material or the dissolution of the converted material upon the charge process, as it has already been observed for CuF_2 [9,10]. A summary of the capacity retention of all the tested materials can be found in **Figure A4.3**.

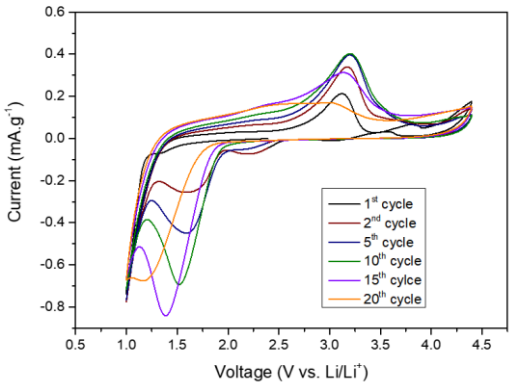

Figure 4.5. *Cyclic voltammetry experiment of the CoF_2-5+rGO sample carried out at 0.1 mV.s^{-1} in the 2-4.4 V window potential vs. Li/Li^+.*

A clear difference in capacity can be observed during cycling, namely, the bigger particles (CoF_2-2) do not reach the theoretical capacity, whereas the smaller particles (CoF_2-5) show higher capacity than the theoretical one during the first discharge process. This could be assigned to the size of the large particles, which does not allow the total conversion of the material. The extra capacity observed in the case of the smaller particles comes from the participation of the solid electrolyte interface (SEI) in electrochemical reduction reactions occurring during the discharge process. This trend is even more apparent when smaller particles are used as active material, such as for CoF_2-6+rGO and CoF_2+fCNT (**Figure A4.3**). The high surface area that the electrode-electrolyte interface present in materials with small particles, implies a higher amount of SEI formed, therefore creating additional irreversible capacity.

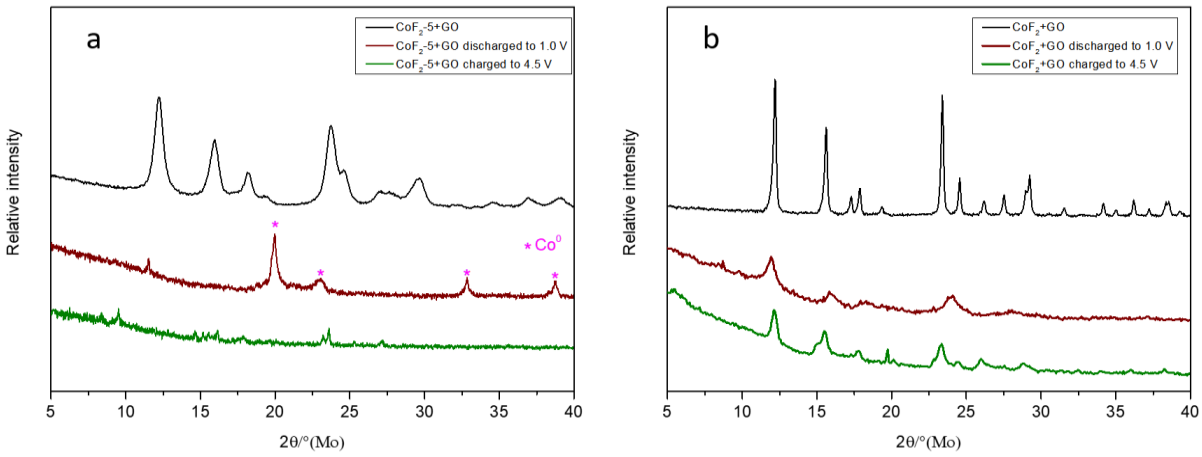

Figure 4.6. *Ex-situ XRD patterns of the electrodes materials after discharge and charge for the* **(a)** *CoF_2-5+rGO and* **(b)** *CoF_2-2+rGO.*

In order to probe the structural changes within the active materials after the first discharge and charge processes, *ex-situ* XRD measurements were carried out on the electrode materials (**Figure 4.6**). In the case of the small particles (CoF_2-5+rGO), the total disappearance of the reflections belonging to the rutile structure is observed and clear reflections from metallic cobalt appear. These phenomena depict the total conversion of cobalt(II) fluoride. Curiously, no reflection from lithium fluoride can be identified, probably due to the short-range order of the generated compound. During the following charge, no clear reflections can be observed, pointing to the amorphization of the active material. For the larger particles, after the first discharge, broad reflections, which can be assigned to the rutile structure, are still present. The absence of reflections belonging to metallic cobalt or lithium fluoride could be due to the formation of a CoF_x species during the discharge, or to a low crystallinity of the converted material, making LiF and metallic cobalt nano-domains not detectable by conventional X-ray diffraction. During the next charge, the reflections become more pronounced, pointing to a partial reconversion of the material to the initial CoF_2 material. In order to determine the morphology of the composite materials after cycling, ex-situ TEM was performed on the CoF_2-5+rGO sample after the 1st and 10th discharge (**Figure 4.7**). After the first discharge, the particles grafted onto GO, which have a larger diameter compared to the pristine ones can be observed; no particles are observed outside the sheets of graphene. The larger size of the particles can be ascribed to the volume expansion that endorses the material during its reaction with lithium (volume expansion = ~ 48%)[1]. The formation of a film can be observed around the fluoride particles after the first discharge process which represents the formed SEI (**Figure 4.7a&b**). After ten cycles, almost no material can be seen on the graphene sheets of GO, where a thick film seems to be formed. Furthermore, the original spherical morphology of the fluoride

material is completely lost. A SAED measurement does not show any crystalline compound present in this material (**Figure 4.7c&d**). From those images, it can be assumed that the repeated conversion/reconversion reaction leads to the transport of the active material away from the conductive GO sheets, together with the pulverization of the electrode material. Additionally, a high amount of SEI can be observed, which can prevent a good conduction of the active species to the reaction points.

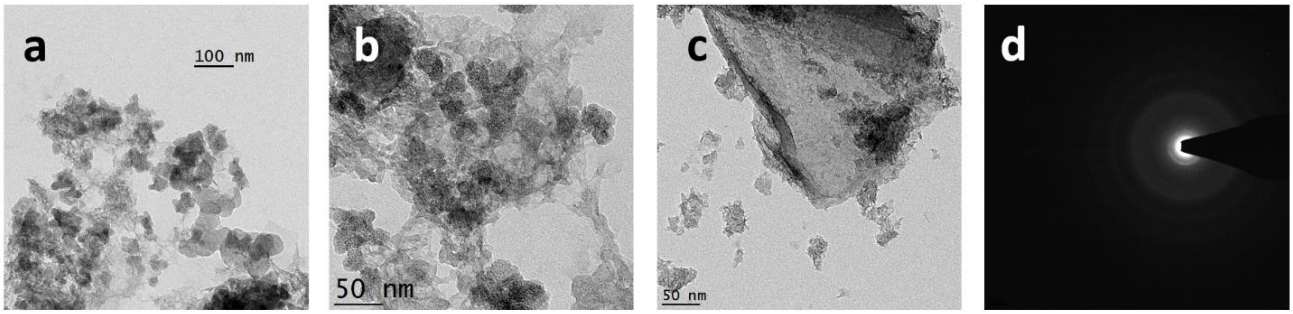

Figure 4.7. *Ex-situ TEM images of the CoF_2-5+rGO electrode material* **(a)-(b)** *after the 1st discharge and* **(c)** *after the 10th cycle,* **(d)** *corresponding SAED measurement.*

3. Iron di- & trifluoride

3.1. Synthesis and characterization of iron(II) fluoride

In this part of the thesis, the synthesis of colloidal FeF_2 nanoparticles of very small size stabilized by oleylamine is described. These particles are used as precursor for the formation of perovskite structure in chapter 5 and have to present a high surface area in order to allow a complete sodiation/fluorination occurring via a solid/liquid interface. Due to the non-existence of iron(II) nitrate species, and the low stability that compounds such as $Fe(OH)_2$ present to oxidation, another approach was implemented for the production of nano-sized iron difluoride, different to the one used for the synthesis of cobalt(II) fluoride. For this, several precursors were used in the attempt to synthesize iron(II) fluoride, namely $Fe(ClO_4)_2$, $Fe(acac)_2$, $Fe(ac)_2$ and $Fe(Cl)_2$. The standard synthesis conditions imply first the dissolution of the precursor in BnOH at room temperature under argon, followed by the addition of two equivalents of concentrated methanolic hydrogen fluoride solution and the treatment in an oil bath at 150°C for 30 min. The solution is finally cooled down to room temperature and then centrifugated to facilitate the precipitate of the formed nanoparticles. Syntheses using $Fe(ClO_4)_2$ and $Fe(acac)_2$ do not form any precipitate after the thermal treatment, caused by the non-reactivity of these

precursors towards the fluorination of the Fe^{2+}. In the case of the chloride precursor, it is not soluble in BnOH, so a heating step at 80°C was added before the fluorination step.

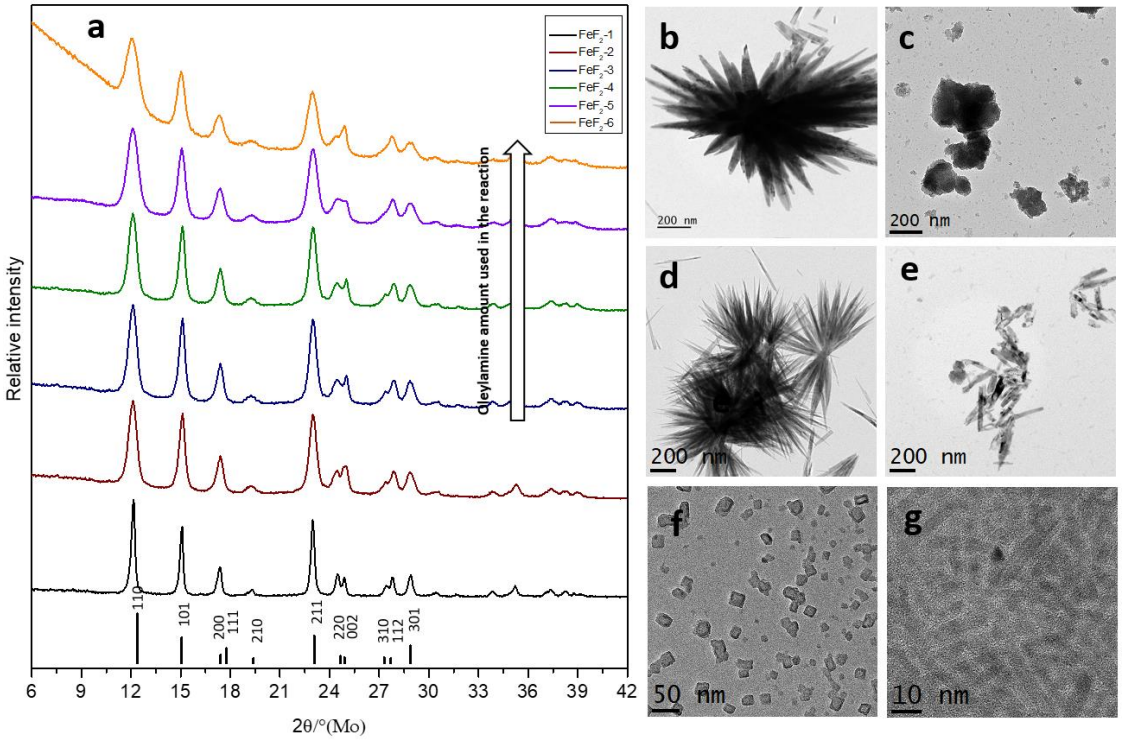

Figure 4.8. (a) *XRD patterns of the iron(II) fluoride compounds synthesized from* $Fe(Cl)_2$ *varying the synthesis parameters and* **(b)**, **(c)**, **(d)**, **(e)**, **(f)** *and* **(g)** *relative TEM images*.

Figure 4.8a displays the XRD patterns of the iron(II) fluoride synthesized from the chloride precursor, by varying the synthesis conditions. All the synthesized fluoride compounds have diffraction patterns fitting with the $P4_2/mnm$ space group relative to the rutile FeF_2 structure. Following the synthesis conditions stated previously, high particles sizes are obtained adopting an urchin-like morphology (**Figure 4.8b**). In an attempt to decrease the size of the particles, high energy stirring was tested. The high speed of the stirring, ~ 12000 rpm compared to 800 rpm for the previous conditions, gave a better dispersion and accessibility of the precursor in reaction media, allowing the generation of smaller particles [11]. Following this method, the decrease of the crystallite sizes could be confirmed by XRD from the broader reflections observed (crystallites ranging from 45 nm to 20 nm as calculated from the Scherrer equation, **Table 4.3**). Nevertheless, the particles synthesized by high energy stirring have a broad distribution size centered around 200 nm as shown in **Figure 4.8c**. The urchin-like structure is lost due to the high-energy stirring, hindering the growth of the particles in the desired direction and creating agglomerates of small crystallites. Another strategy to control the size of the particles consists in adding a surfactant to the reaction media, such as oleylamine, to decrease

the particle size by blocking their growth. After the nucleation of the particles, the surfactant will hinder further growth processes by creating a micelle around the particles and lowering the free energy of the particle surface, therefore its reactivity [12]. Different molar equivalents of oleylamine precursor were used here in respect with the iron. The surfactant was added to the reaction after the total dissolution of the chloride precursor, and then identical synthesis conditions followed. The XRD patterns of the nanoparticles obtained by this method show broader reflections with increasing amount of oleylamine, which represent the decreasing of the crystallite sizes (**Table 4.3**). With 0.2 equivalents of oleylamine to iron, the urchin-like structure is maintained but takes the form of needles with smaller sizes. From 0.5 equivalents of oleylamine, the urchin-like structure is lost and only separated needles are obtained of similar size compared to sample FeF_2-3. With an ever-higher amount of surfactant, the sizes of the particles decrease, forming cubic particles in the case of 1 equivalent and very small needles in the case of the 2 equivalents. It is noteworthy to point out that in the case of the urchin/needle-like structures, the reflections relative to the plane (002) have very narrow shapes. The narrower shapes of these reflections indicate a higher order along this crystalline direction and represent the orientation that the needles of those structures take to grow. The sample FeF_2-2 and FeF_2-5, which do not have such structures, do not present this characteristic. The atomic ratios calculated by EDX measurements are in accordance with the crystalline structure measured by XRD. These phenomena can be ascribed to the stabilization of the surface by the oleylamine precursor, preventing hydrogen fluoride molecules to be adsorbed at the surface of the nanoparticles.

	Eq. Oleylamine used compared to Eq. Fe	F atomic %	Fe atomic %	Calculated crystallite size (nm)
FeF_2-1	0	65.2	34.8	45
FeF_2-2	0 (high-energy stirring)	62.1	37.9	20
FeF_2-3	0.2	66.1	33.9	21
FeF_2-4	0.5	66.3	33.7	19
FeF_2-5	1	65.9	34.1	15
FeF_2-6	2	66.3	33.7	8

Table 4.3. *Different atomic ratios measured by EDX experiment, as well as crystallite sizes of the FeF_2 synthesized from the chloride precursor calculated by the Scherrer equation.*

Regarding the use of the acetate precursor, its solubility in BnOH at room temperature circumvents the additional heating step prior to the fluorinating step. Nevertheless, similar to the chloride precursor, particles presenting large sizes are obtained in normal conditions and by using high-energy stirring. Here, the particles do not demonstrate an urchin-like structure,

but rather a cubic morphology. Using one equivalent of oleylamine decreases significantly the size of the particles. However, after separation of the product by centrifugation and multiple purifications with ethanol and acetone, a viscous mixture is obtained. Hexane and benzene were tested in order to further purify the product of the reaction, but due to the high colloidal stabilization of the particles within these solvents, the precipitation of the particles by centrifugation was not possible. On **Figure 4.9**, big agglomerates of very small particles can be observed, embedded in a tight matrix, probably formed of oleylamine and its derivate induced by the precursor. This viscous character does not allow to use this material as precursor for the synthesis of perovskite compounds.

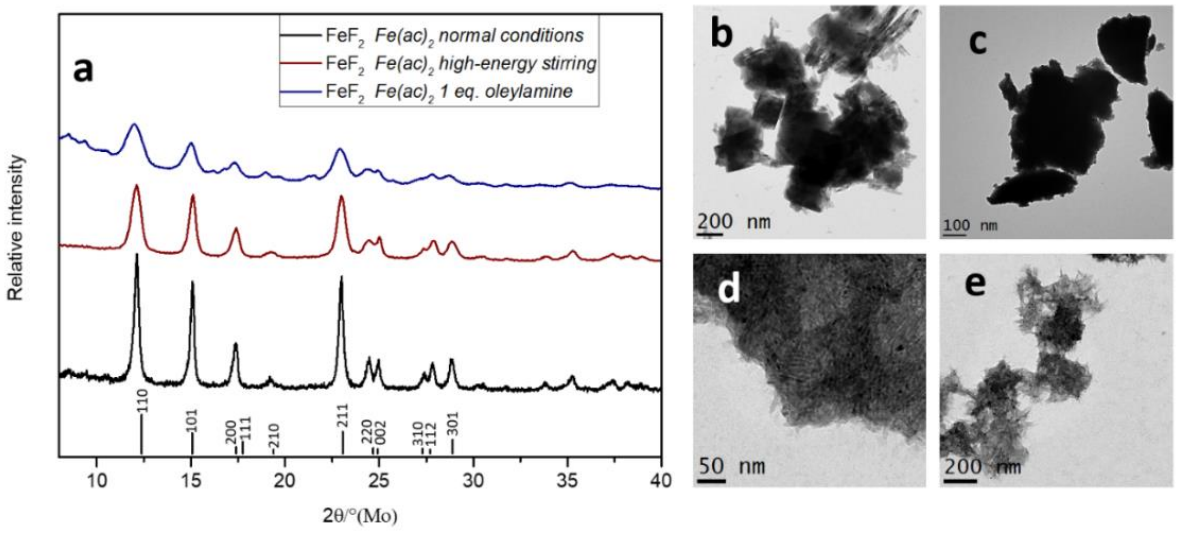

Figure 4.9. (a) *XRD patterns of the iron(II) fluoride compounds synthesized from* $Fe(ac)_2$ *varying the synthesis parameters and* **(b)**, **(c)**, **(d)** *and* **(e)** *relative TEM images*.

3.2. Synthesis and characterization of anhydrous iron(III) fluoride compounds and composites

Because of the high insulating character of the iron(III) fluoride, small particles are the best formulation to improve the diffusion of the active species in the material when used as electrode material for Li-ion batteries. Many synthesis methods were implemented to obtain nano-sized iron(III) fluoride materials, such as solvothermal or ionic liquid reactions [9,10]. These methods lead to the production of hydrated phases with different water contents depending upon their synthesis parameters, due to the generation of water during the fluorinating processes. Iron(III) fluoride structures, in particular HTB $FeF_3 \cdot 0.33H_2O$, pyrochlore $FeF_3 \cdot 0.5H_2O$ and fully hydrated $FeF_3 \cdot 3H_2O$, have water molecules which induce the stabilization of large channels beneficial for the diffusion of ionic species [11]. However, these molecules, also limit the cation insertion rate for the electrochemical reduction of iron(III), by occupying the locations where

those cations are supposed to be inserted. In the case of anhydrous iron(III) fluoride, the channels of the crystalline framework are free of additional species, allowing the active material to reach its full capacity at its one-electron reaction (237.5 $mAh.g^{-1}$), but the channels of this structure are quite small compared to the ones of the hydrated structures (cf. Chapter I section 5.3). In the literature only a few studies describe the synthesis of anhydrous iron(III) fluoride, mostly using dehydration processes or the decomposition of fluorosilicate or trifluoroacetates [12,13,14]. Those methods imply a high-temperature treatment and do not allow a control of the particle size. Furthermore, it is difficult to create an intimate contact between carbon matrices and these particles after their syntheses without involving methods detrimental for the crystallinity of the material, such as ball-milling for instance. In this work, the synthesis of anhydrous iron(III) fluoride is carried out by the fluorination of different iron oxide species and their composite formation with GO and carbon black. These composite active materials are then used for different alkali-ion battery systems (Li-, Na- and K-ion batteries) and their reactivity towards these different alkali species is discussed as follows, as well as the mechanisms involved in the electrochemical reactions.

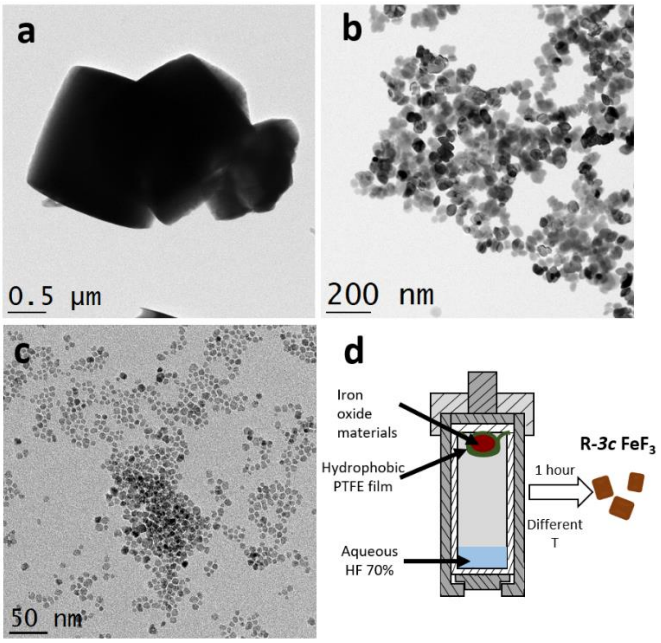

Figure 4.10. (a), **(b)**, **(c)** *TEM images of the iron oxide precursors, namely commercial hematite and nanosized hematite and magnetite, and* **(d)** *scheme of the anhydrous* FeF_3 *synthesis design.*

Iron(III) fluoride materials were prepared from a fluorination of iron oxide precursors. Three different kinds of iron oxide precursors were chosen, relatively large hematite particles purchased from a company, as well as hematite and magnetite nanoparticles, which were

synthesized during this study (**Figure 4.10a-c**). The hematite nano-material was synthesized through a simple well-known hydrothermal process starting from hydrated iron(III) nitrate in aqueous basic media [15]. Treating the mixture at 180 °C for 16 hours in an autoclave produces nanoparticles with sizes ranging from 30 to 50 nm. For the synthesis of the magnetite particles, the BnOH microwave route was chosen for its simplicity and its relatively short reaction times. Stoichiometric amounts of $Fe(ac)_2$ and $Fe(acac)_3$ were introduced into a microwave reactor in BnOH in order to obtain a nominal Fe_3O_4 composition. The solution made of the iron precursors dissolved in BnOH was treated under microwave irradiation at 230 °C for 20 min. The obtained nanoparticles are very small, ranging from 2 to 6 nm. Whereas the commercial particles have sizes in the microscale range. The fluorinations of the iron oxide precursors were carried out in an autoclave (scheme of the designed autoclave displayed in **Figure 4.10d**). To avoid the direct contact between the components of the reaction, the precursor was positioned at the top of the autoclave in a hydrophobic mesoporous PTFE film dried at 100 °C under vacuum prior to its introduction in the reactor, whereas the aqueous HF solution lays in the bottom of the autoclave. If the precursor was in direct contact with the hydrofluoric acid mixed phase hydrated iron(III) fluoride is formed, due to the water molecule present in the HF aqueous solution (**Figure A4.4**). The so-prepared autoclave is then treated at 100°C for 1 hour and cooled down at room temperature. As the boiling point of hydrogen fluoride is 18°C, the reaction occurs via a gas/solid interface. The hydrophobic PTFE film prevents the water from the aqueous HF solution to reach the precursor and avoids the insertion of the water molecules generated during the fluorination within the formed hygroscopic iron(III) fluoride by expelling them. **Figure 4.11** displays the XRD patterns of the different iron oxide precursors and the products of their fluorination, as well as the TEM images of the fluoride compounds. It can be seen from XRD that the fluorination of the commercial particles after one hour ends in a partial generation of an anhydrous iron(III) fluoride phase. This phenomenon can be observed in the TEM image at the particles surface partially etched during the reaction. In contrast, the hematite nanoparticles show full conversion after the fluorination process. Cubic nanoparticles of anhydrous iron(III) fluoride are obtained, with similar size compared to the relative precursor. The crystalline phase can be assigned by XRD to the hexagonal R-*3c* FeF_3. It is noteworthy to point out that it is the first time that this crystalline phase is obtained using soft reaction. In the case of the magnetite nanoparticles, a fluoride compound presenting the same mixed oxidation state of iron as the precursor is obtained, specifically $Fe^{(II)}Fe^{(III)}{}_2F_8$, adopting particles with a not very well defined morphology. Due to its crystal structure, this compound does not show activity towards lithium cycling. Regarding the purity and the appropriate size of the anhydrous iron(III) fluoride

nanoparticles obtained via the fluorination of hematite iron oxide synthesized by hydrothermal way, this material was chosen for electrochemical tests. However, as the metal fluorides present a high insulating character, this compound was coupled with carbon matrices prior to the electrochemical tests. For this purpose, ball-milling with carbon black was used, as well as the fluorination of a Fe_2O_3/GO composite obtained by liquid synthesis.

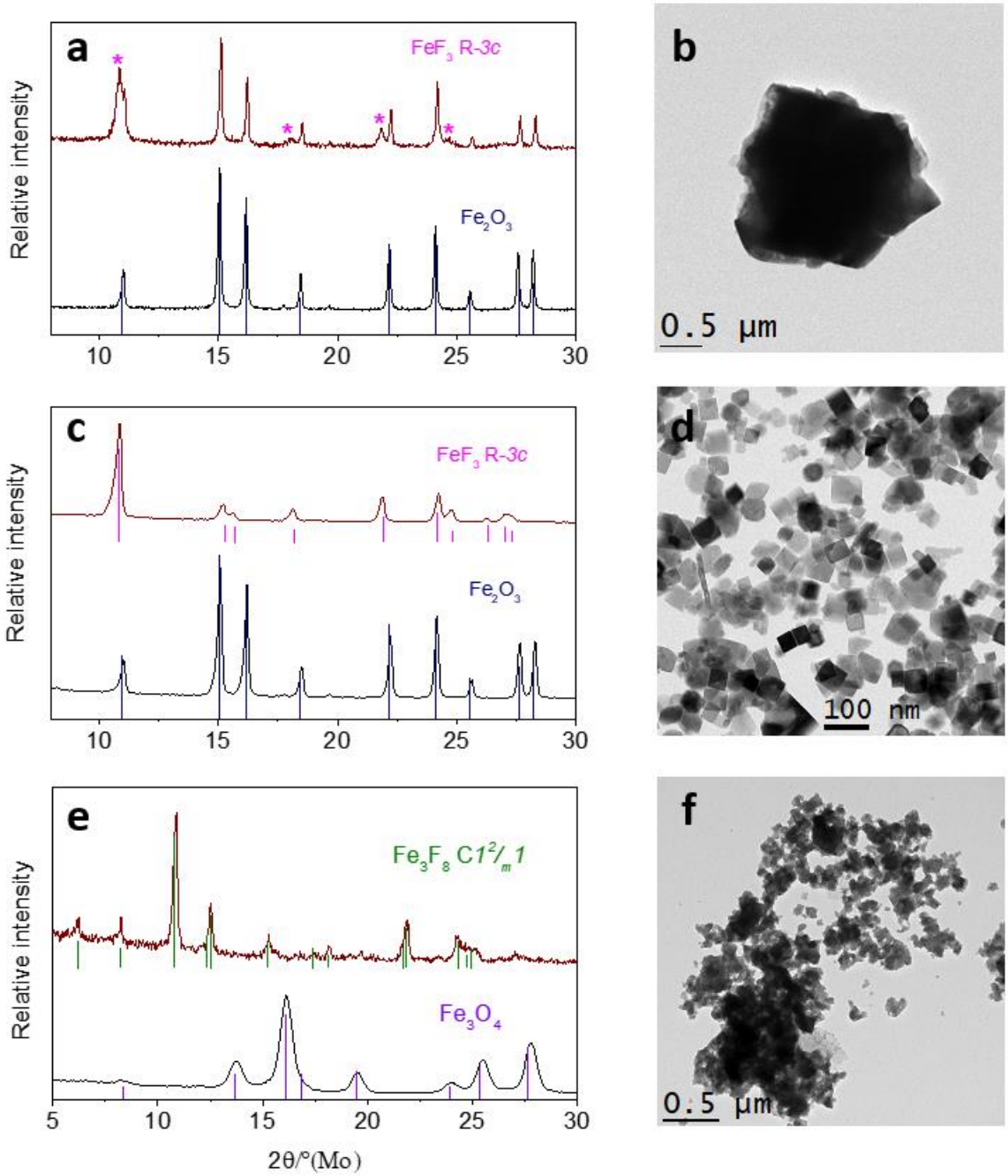

Figure 4.11. (a), **(c)**, **(e)** *XRD patterns of the different iron oxide precursor (**black**) and their fluorinated products (**red**) and* **(b)**, **(d)**, **(f)** *the TEM images related to the fluorinated products, respectively.*

In order to obtain a conductive electrode material, ball-milling of iron(III) fluoride particles with carbon black was carried out. This strategy has been previously employed to overcome the insulating character of metal fluoride materials by Badway *et al.*, who were the first to report the electrochemical conversion of iron fluoride compounds [16]. This process can reduce the sizes and change the morphology of the introduced materials and can also deteriorates their crystalline structure. At some extent, the ball-milling process can totally make crystalline compounds amorphous [17].

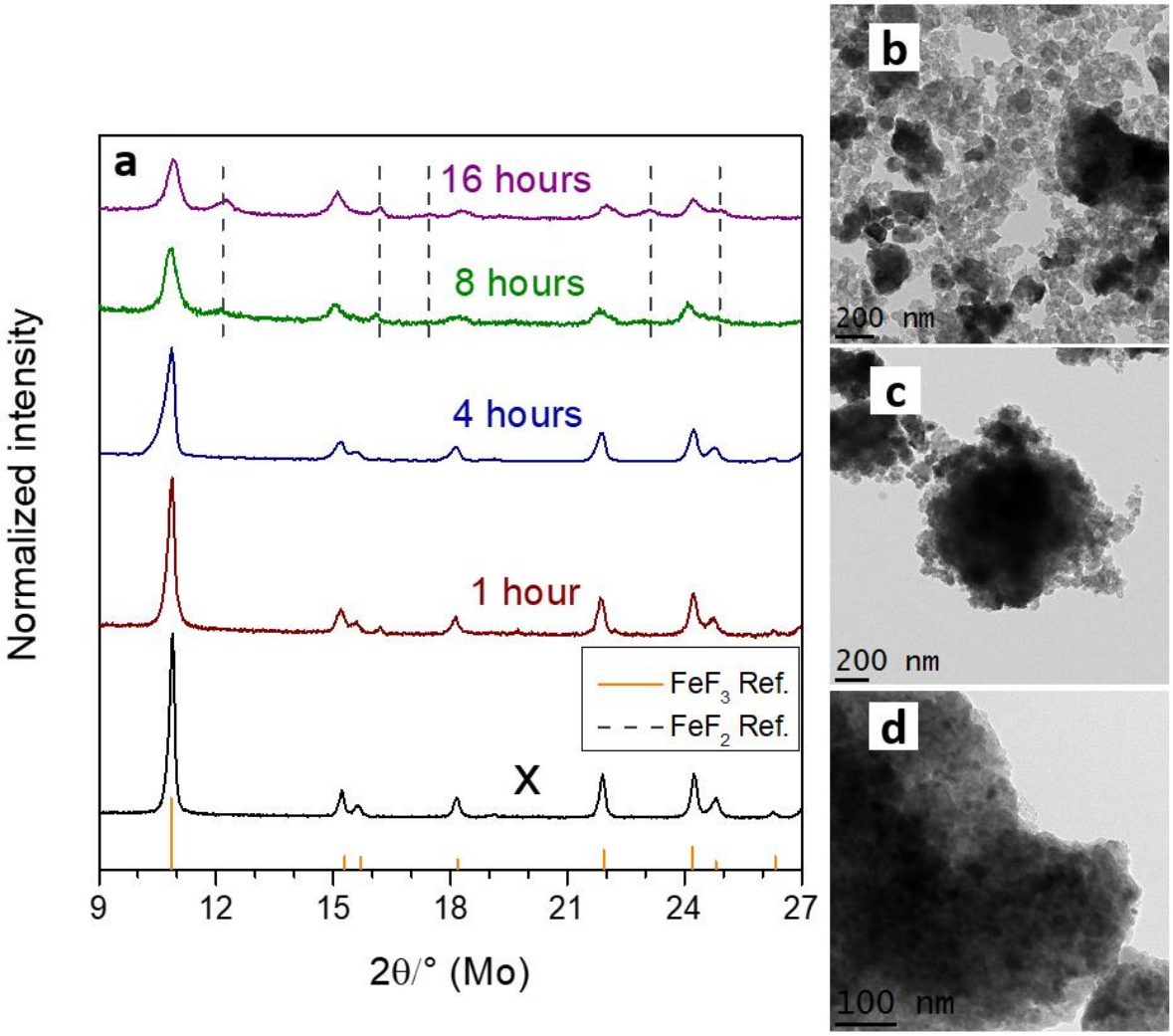

Figure.4.12. (a) *XRD pattern of the bare iron(III) fluoride nanoparticles ball-milled with carbon black for 1, 4, 8, 16 hours and the pristine sample.* **(b)**, **(c)**, **(d)** *TEM images of the ball-milled samples for 1, 4 and 16 hours, respectively.*

The mass ratio used for the milling process is 7:3 between the FeF_3 nanoparticles and the carbon black, respectively. The mechanochemical reaction was conducted for varying periods of time

ranging from 1 to 16 hours. The resulting XRD patterns of the milled composites confirm that the crystalline framework of the hexagonal structure is maintained throughout the milling (**Figure 4.12.a**). A systematic broadening of the reflections can be observed with extended milling times, which is associated with the decrease of the crystallite sizes. Calculations of the crystallite sizes by the Scherrer equation show that the original crystallite size (40 nm) decrease already after 1 hour of milling, after 4 hours is reduced by the half and end up down to 8 nm after 16 hours (**Table 4.4**). A slight shift to higher angles can also be noticed, denoting a minor decrease in size of the unit cell. These phenomena altogether speak for the deformation of the structure during the milling process. Starting after 8 hours of milling, reflections belonging to the rutile FeF_2 phase start to appear. The formation of this compound is caused by the hot spots created along the mechano-synthesis, inducing the dehalogenation of the FeF_3 due to the reducing character of the carbon black. There is no evidence of the formation of CF_x by XRD measurement. No reduction of the fluoride compound up to the metallic iron can be detected, even after 16 hours of milling. TEM images displayed in **Figure 4.12b-d** show the morphology of the milled composite materials. After 1 hour, an intimate mix between the two components can be observed where the nanoparticles of FeF_3 already lost their cubic shape. After 4 hours, agglomerates of the two components are formed where the pristine nanoparticles are almost no longer visible. After 16 hours, compact particles of large size are observed in which small darker spheres ranging between 5 and 10 nm can be discerned. Those small particles can be assigned to the fluoride material embedded within the carbon matrix. These results slightly differ from those reported by Badway *et al.*, where the formation of the rutile phase was detected after 2 hours of milling and metallic iron after 8 hours. Differences arise from the variant of carbon matrix used, which depending on its composition buffers the collisions induced by the process and the lower rotation speed employed during the milling in this study. By decreasing the size of the particles, the reaction path of the charged species within the material will be shortened, improving the kinetics of the active material reactions. However, the harsh conditions of the milling process deteriorate the crystalline framework where cationic species are supposed to diffuse, which could as well alter the kinetics of reaction of insertion of these species within the structure. Furthermore, it has been reported that ball-milling process of crystalline structures could create strain within the framework, which could hinder the cationic insertion during electrochemical cycling [18,19].

Milling time (hour)	2Θ of the (012) (°)	Size by the Sherrer equation (nm)
X	10.86	40
1	10.86	33
4	10.85	20
8	10.88	15
16	10.93	8

Table.4.4. *2Θ position of the reflection (012) and size of the crystallites of the crystallite belonging to the R-3c phase of the materials milled during different times.*

To find alternative to the use of high-energy milling, the active material nanoparticles were also synthesized in the presence of GO. For this purpose, the hematite nanoparticles were firstly grafted onto the carboneous material. Similarly to the grafting of the cobalt fluoride nanoparticles, the organic functional groups at the surface of the GO sheets will serve as anchor points for the iron oxide nanoparticles to be chemically bonded. A scheme of the process is displayed on **Figure 4.13a**. The GO is then totally dispersed in water in a sonic bath to obtain a black homogenous dispersion. Once the GO is dispersed, a second solution of the iron oxide nanoparticles in water is added and quickly shaken to promote the mixing of the two solutions. An ocher precipitate appears immediately after the addition of the iron material, the typical color of the iron oxide hematite. The grafting of the iron oxide particles onto the graphene oxide breaks the colloidal stability of the carbon sheets and causes the precipitation of the composite material (**Figure 4.13e-f**). The synthesis route of the GO following the Hummer's method induces the acidification of the carboneous sheets due to the acidic medium used along the process [20] , therefore, carboxylic functional groups are expected at the surface of the GO. Carboxylic functional groups are known to interact with the surface of iron oxide materials via chelation [21]. Furthermore, the basic media used for the synthesis of the iron oxide nanoparticles should enhance the presence of hydroxyl functional groups, allowing condensation reactions to occur with the carboxylic functional groups. The chemical surface compositions of both components lead to a high chemical affinity between the iron oxide nanoparticles and the GO, without any other treatment than their physical mixing. This high affinity is further confirmed by TEM where a homogenous deposition of the hematite nanoparticles onto the GO can be observed (**Figure 4.13b-c**).

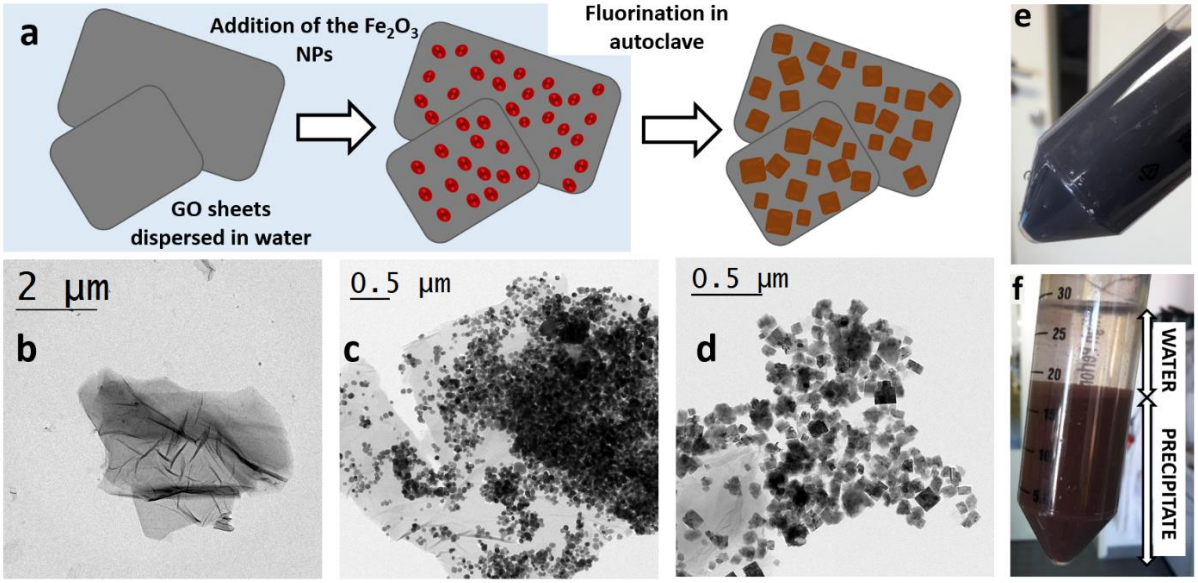

Figure 4.13. (a) *Scheme of the synthesis process of the FeF_3+GO composite. TEM images of* **(b)** *the GO,* **(c)** *Fe_2O_3 nanoparticles grafted onto GO and* **(d)** *product of the fluorination.* **(e)** *and* **(f)** *pictures of before and after addition of the Fe_2O_3 solution in the GO dispersion.*

Finally, the fluorination step was carried out in a similar way than with the bare Fe_2O_3 nanoparticles. From TEM images (**Figure 4.13d**), it can be seen that cubic iron(III) fluoride nanoparticles were effectively generated on the surface of the GO. No particles can be seen out of the GO, speaking for the retention of the composite structure. The XRD pattern of the fluorinated composite material (**Figure 4.14a**) confirms its structure as hexagonal relative to the R-*3c* space group, similar to the synthesis from bare iron oxide nanoparticles. **Figure 4.14b** displays the FT-IR spectra of each intermediate of the synthesis process. The signature of the hematite iron oxide nanoparticles can be seen by an absorption located around ~500 cm^{-1} with two maxima, whereas the GO has several bands of absorption located at 1075 and 1230 cm^{-1} for the vibration of the C-OH bond, 1620 cm^{-1} for the C=C bond and 1710 cm^{-1} for the C=O bond [22]. After grafting the iron oxide nanoparticles, the intensities of the absorption related to the vibration of the C-OH slightly decreased, since these organic functional groups are the anchor points for the iron oxide. After the fluorination step, the absorption characteristic to the iron oxide in the 500 cm^{-1} region disappeared to be replaced only by one maximum at 535 cm^{-1} typical for the Fe-F vibration [4], confirming the total fluorination of the precursor. No absorption related to the C-OH vibrations can be observed, while a band related to the C-F vibration appears at 1230 cm^{-1}. The bands associated with the C=C and C=O vibrations shifted at a higher and lower wavelength, namely 1740 and 1580 cm^{-1}, probably due to a change in the carbon network within the sheets of the GO.

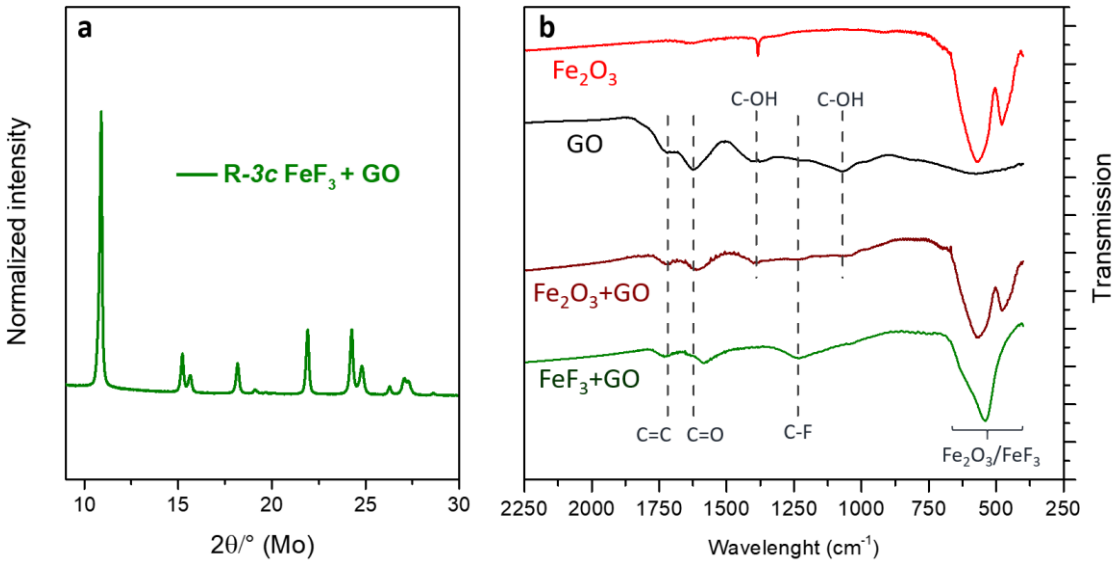

Figure 4.14. (a) *XRD pattern of the synthesized FeF_3+GO composite and* **(b)** *FT-IR spectra of the different intermediate of the composite synthesis process.*

To study the influence of the fluorination process on the GO, different reaction times at 100 °C were tested, namely 1 hour, 4 hours and 16 hours. **Figure 4.15a-f** depicts the TEM images of the different products obtained with variable fluorination time. It can be seen that the longer the fluorination step is carried out, the more the GO structure is affected. After 4 hours, the particles are not only longer grafted onto the surface of the GO but embedded within the carbon matrix, while the nanoparticles adopt a more spherical morphology. When the fluorination is conducted for 16 hours, the 2D carbon sheets are no longer visible and are transformed into a not well-defined carbon structure completely coating the iron fluoride material. The FT-IR measurements of the fluorinated products are shown on the **Figure 4.15g**. An increase of the absorption of the band relative to the C-F and the Fe-F can be observed as well as the coalescence of the band relative to the C=C and C=O bond vibrations. Those differences in the FT-IR spectra translate into an alteration of the starting GO structure. Likewise observed on TEM images, the GO material is slowly transformed into a fluorinated carbon matrix embedding the iron fluoride material, while the size of the particles slightly increases. Compared to the ball milling process, the crystalline structure of the iron fluoride here is not altered and no side products are formed. With a longer time of fluorination, the particles can also be embedded into a carbon matrix, as it is the case from 8 hours of ball-milling process. On the other hand, the process involving the grafting of the nanoparticles with GO does not imply a decrease in the size of the nanoparticles, which will influence the conductivity and the diffusion of the reactive species.

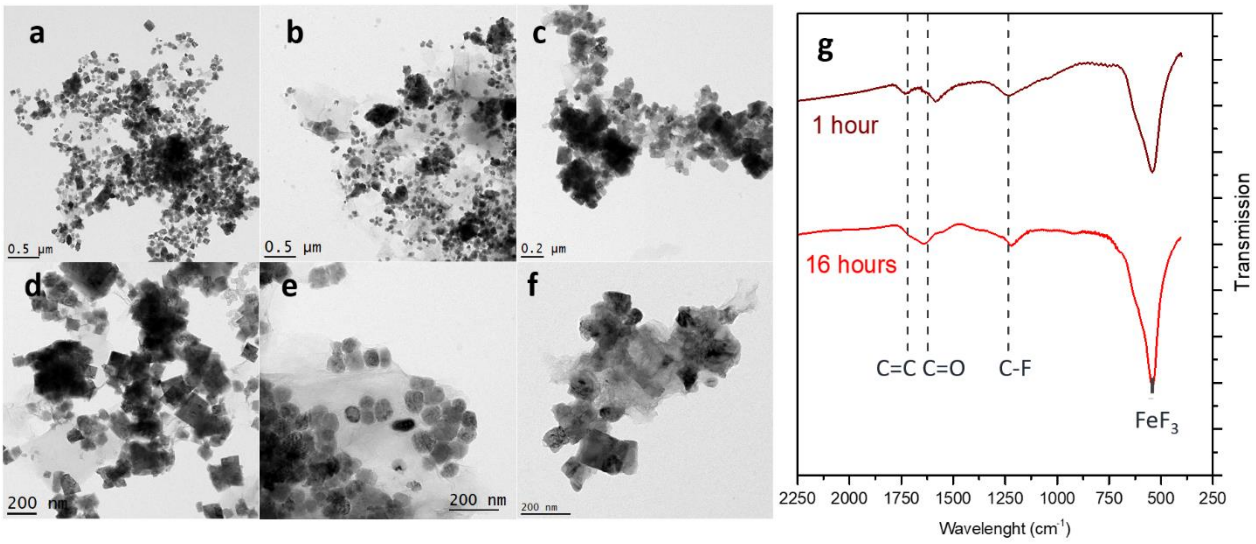

Figure 4.15. *TEM images of the fluorinated products* **(a)** *and* **(d)** *after 1 hour,* **(b)** *and* **(e)** *after 4 hours and* **(c)** *and* **(f)** *after 16 hours.* **(g)** *FT-IR measurements of the product of fluorination after 1 hour and 16 hours.*

3.3. Electrochemical behavior of the anhydrous iron(III) fluoride composites

To test the electrochemical properties of the fluoride composites as a cathode, the materials were used in half-cells with metallic lithium as a reference and a mixture of $LiPF_6$ and organic solvents as an electrolyte. As mentioned earlier (Chapter 2, section 4.3), the discharge of iron(III) fluoride phases can be separated in two potential regions where they react through different mechanisms. Above 2 V vs. Li/Li^+, the reaction is related to the insertion of one atom of lithium per unit formula, whereas below 2 V, the fluoride material is converted into metallic iron and lithium fluoride by the reaction of two more atoms of lithium. This electrochemical investigation will be mainly focused on the first reactive region of the iron(III) fluoride, in order to study the mechanisms involved during the insertion of one atom of lithium within hexagonal FeF_3.

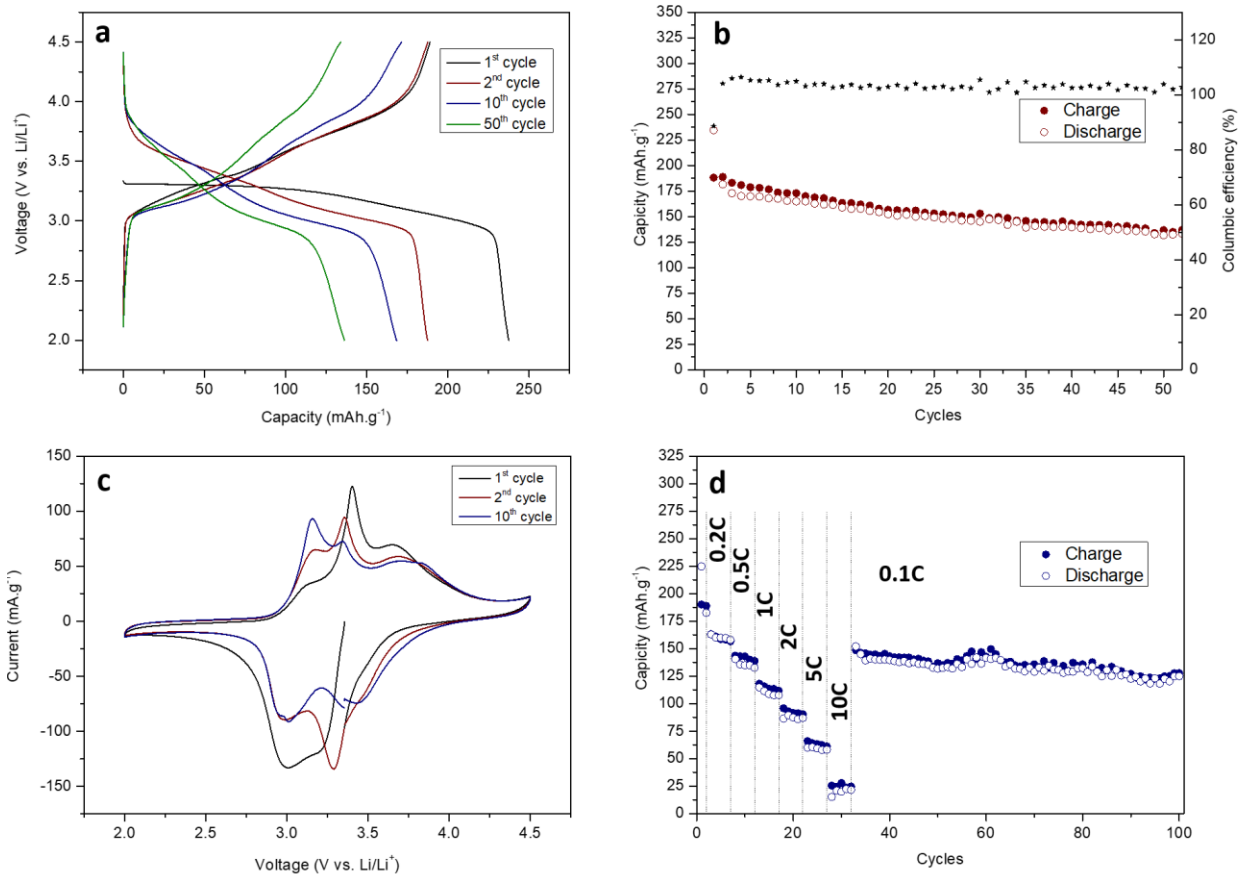

Figure 4.16. (a) *Galvanostatic curves of the FeF_3+GO-1h cycled towards Li at C/10 and* **(b)** *related capacity retention.* **(c)** *Cyclic voltammetry experiment of the FeF_3+GO-1h at the scan rate of 0.1 $mV.s^{-1}$ towards Li.* **(d)** *Capacity retention of the FeF_3+GO-1h at different current densities.*

Figure 4.16a shows the galvanostatic profiles of the discharge and charge processes at different cycles of the sample synthesized by fluorination of the composite precursor for one hour. The first discharge can be divided into two distinct regions. A flat plateau can be observed around 3.3 V vs. Li/Li^+ up to 120 $mAh.g^{-1}$, which represents roughly 0.5 lithium per formula unit inserted within the crystal structure. In a second step, a steep plateau appears which can be assigned to the reaction of another 0.5 lithium per formula unit. The first plateau is included in a window potential of 50 mV, while the second one is in a window potential of 400 mV, pointing to different phenomena occurring during the reaction between the active material and the lithium during these two steps. At the end of the first discharge, the theoretical capacity of 240 $mAh.g^{-1}$ is obtained, representing the reaction of one atom of lithium with the fluoride structure. During the following charge, two slopped plateaus can be seen, between 3.0-3.5 V for the first one and 3.5- 4.0 V for the second one. The second discharge shows a different profile compared to the first one, with two slopped plateaus. The subsequent discharge/charge

processes stay similar to the second cycle, however showing decreasing capacities with for example 130 mAh.g^{-1} at the 50th cycles, which represents roughly half of the first discharge (**Figure 4.16b**). The cyclic voltammetry experiment of the materials presents the same trend, with a different profile of the first cycle compared to the subsequent ones (**Figure 4.16c**). A sharp peak located around 3.3 V can be clearly seen, while two less pronounced redox waves are present between 3.0-3.5 V, and 3.5-4.0 V. This sharp peak disappears from the 10th cycle. The composite material demonstrates relatively poor rate capability with 130 mAh.g^{-1} delivered when cycled at 1C and up to 25 mAh.g^{-1} when cycled at 10C.

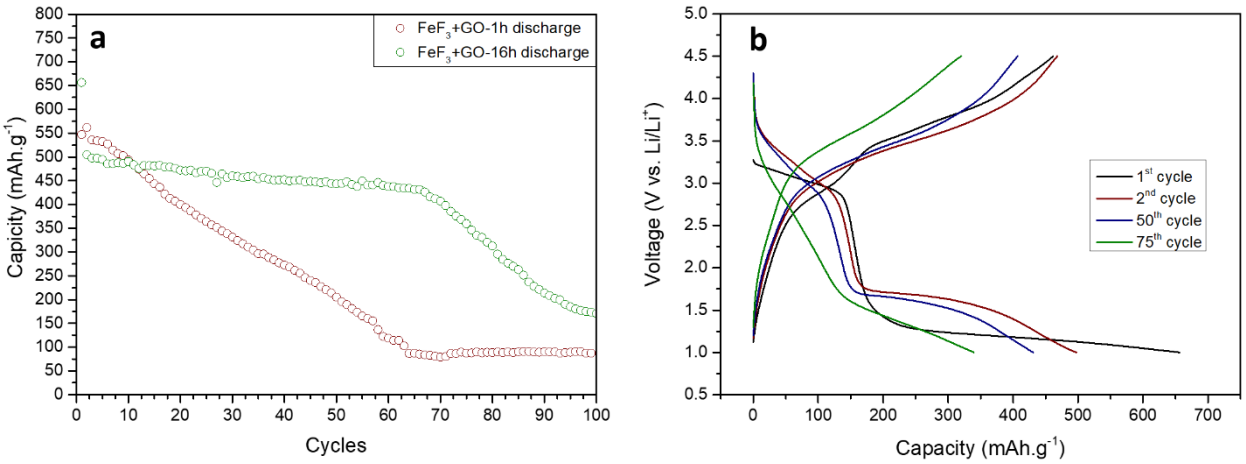

Figure 4.17. (a) *Capacity retention of FeF_3+GO-1h and FeF_3+GO-16h at C/5 towards Li in the 1-4.5 V window potential and* **(b)** *related galvanostatic profile of FeF_3+GO-16h.*

The samples with longer times of fluorination, 4 and 16 hours, have very similar electrochemical behavior in the potential window involving the reaction of only one atom of lithium (**Figure A4.4**). However, when the discharge is conducted down to 1.0 V, some differences can be observed (**Figure 4.17**). The first capacities delivered by the compounds with 1 hour and 16 hours of fluorination are different. The capacity of the FeF_3+GO-1h gradually decreases to be close to zero at the ~ 60th cycle, while FeF_3+GO-16h presents a drop in capacity after the first cycle, followed by good capacity retention up to the 70th cycle. Those disparities come from the fact that these two composite materials do not present the same morphology. From the previous section, it was shown that after 1 hour of fluorination, the iron(III) fluoride particles were only grafted onto the GO sheets. On the contrary, after 16 hours of fluorination, the GO was undergoing a chemical transformation induced by the longer fluorination time. This chemical transformation allows the carbon matrix to embed the iron fluoride. The discharge down to such potential induces the conversion of the composite materials into metallic iron and lithium fluoride, causing a large expansion of the electrode

material and structural deformations. When the particles are simply grafted onto the carbon sheets, the conversion will lead to the break of the chemical bonds between the GO and the particles. Therefore, the capacity continuously decreases in the case of the FeF_3+GO-1h, as it has been previously described in the case of the cobalt fluoride composite material. In contrast, as the material in the FeF_3+GO-16h sample is embedded with the carbon matrix, the structure of the composite is able to buffer the volume expansion after the first discharge, ensuring the electronic conductivity and the cohesion of the electrode material. As the morphology of the material is kept, the material is able to undergo cycling with a good capacity retention. Such behavior was already reported for iron fluoride material embedded in conductive matrices [23,24]. However, the drop in capacity at the 70th cycle can be ascribed to the break of the composite structure in this case, caused by the repeated discharge and charge processes.

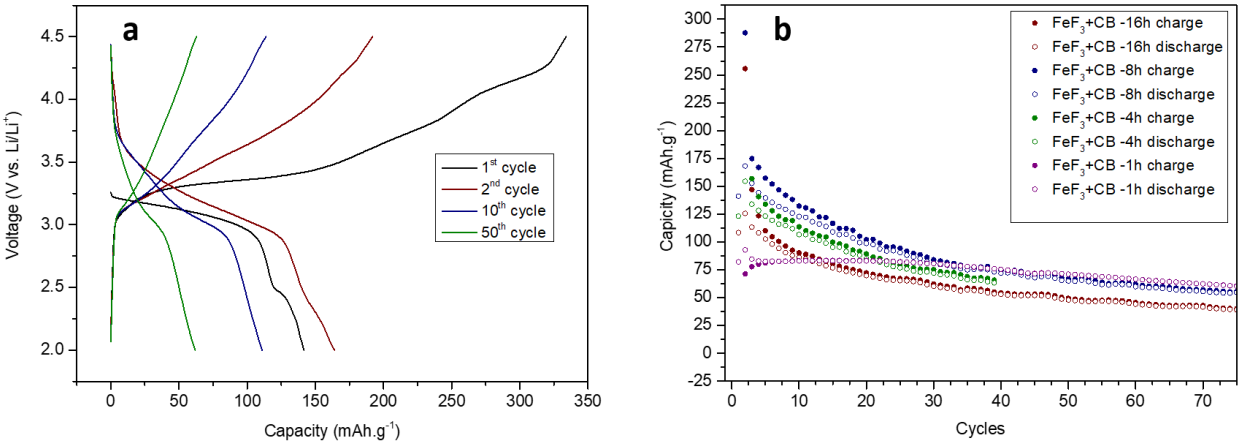

Figure 4.18. (a) *Galvanostatic curves of FeF_3+CB-8h cycled towards Li at C/10 and* **(b)** *capacity retention of the different FeF_3+CB materials.*

For comparison, the composite materials prepared by ball-milling were also tested as cathode material for LIBs. **Figure 4.18** displays the capacity retentions of those composite materials cycled at C/10, as well as the galvanostatic profiles of the sample ball-milled for 8 hours. The capacities achieved by those ball-milled composites are lower than the GO composites, as well as their capacity retentions. The compound ball-milled only for 1 hour shows low discharge capacities, which can be caused by the not enough intimate contact between the iron(III) fluoride material and the carbon black (c.f. **Figure 4.12b-d**). The first discharge curve of the material ball-milled for 8 hours only presents one slopped plateau in the 3 V region and a second one at around 2.5 V. The next charge is higher than the expected theoretical capacity, probably due to a side reaction occurring during this initial process. During the subsequent cycles, only one slopped plateau can be observed between 2.8 and 4.0 V. Those differences in

electrochemical responses can be attributed to the deterioration of the crystalline structure during the high energy milling process, partially caused by the reductive effect of the carbon black. Furthermore, the size of the particles decreases along this process and the organization of the channels where the ionic species diffuse is disturbed, creating, for example, more grain boundaries.

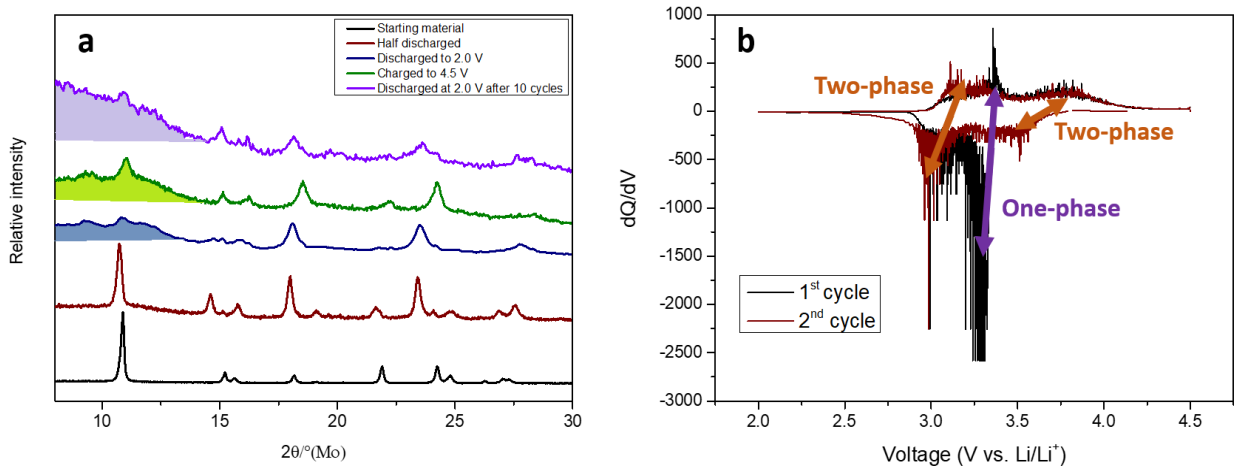

Figure 4.19. (a) *Ex-situ XRD pattern of FeF_3+GO-1h at different state of charge and* **(b)** *dQ/dV profile of the galvanostatic plot cycled at C/10 towards Li.*

To investigate the structural changes occurring within the material prepared by the grafting of the iron(III) fluoride material onto GO, XRD measurements were conducted on the electrode materials at different states of charge (**Figure 4.19a**). The discharge is first stopped after the insertion of 0.5 lithium atom per formula unit. The position of the reflection (012) shifts to smaller angles, which can be ascribed to the enlargement of the crystalline lattice structure. The intensities and positions of reflections at high angles change drastically, with the appearance of two reflections of high intensities at 2Θ = 18 ° and 23.5 °. This resulting XRD pattern can be attributed to the formation of Li_xFeF_3 through a single-phase solid solution reaction (with $x <$ 0.5) together with the beginning of the formation of a second phase, which can be ascribed to the appearance of the reflections at 2Θ = 18 ° and 23.5 °. The discharge conducted down to 2.0 V completes the reaction of one lithium atom per formula unit. The major reflection related to the (012) diffraction plane almost disappears, together with the appearance of an amorphous background at small 2Θ values. The two reflections at 2Θ = 18 ° and 23.5 ° do not decrease in intensity, but present larger FWHM. After the charge of the compound to 4.5 V, the intensity of the reflection located at 2Θ = 11 ° slightly increases, while the two broad reflections shift to higher angles. After 10 cycles at the end of the discharge, the amorphous background at small angles increases. The two reflections located at 18 ° and 23.5 ° are still present, but with lower

intensities. It was shown that the hexagonal framework of anhydrous iron(III) fluoride was not thermodynamically able to host one atom of lithium per unit cell [25,26]. From 0.25-0.5 lithium atom per formula unit inserted within the structure, the framework would form a material related to a trirutile compound ($LiFe_2F_6$) and other phases with complicated stoichiometries ($Li_{3/4}Fe_{3/4}F_3$, $LiFe_{1/2}F_3$, $Li_{15/8}Fe_{3/8}F_3$, etc.). The structure of the starting material is made of $(FeF_6)^{-3}$ octahedra connected by corners, while in the trirutile-like structure the $(FeF_6)^{-4}$ octahedrons share also two edges. The transformation of the pristine structure to the trirule-like structure involves reorganization of the crystal framework. This is confirmed by the results obtained by *ex-situ* experiments: the material reacts through a single-phase insertion of lithium, with the simultaneous start of the conversion of the active material to the trirutile-like phase, followed by only a two-phase conversion reaction at lower potential generating products, with a more amorphous character. This amorphous character could be assigned to the short-range order of the generated compounds with very different stoichiometries [27]. The phase related to the single-phase reaction of the starting hexagonal crystal structure is still partially present, as shows the low-intensity reflection at 2Θ = 11 °. The intensities of the two reflections at 2Θ = 18 ° and 23.5 ° become broader, due to the decrease of the crystallite size induced by the conversion reaction. Upon the charge, the intensity of the reflection at 11 ° slightly increases, probably due to the partial reformation of this crystalline phase induced by a reconversion reaction. The two reflections at 2Θ = 18 ° and 23.5 °, however, shift to higher angles, which could be due to the contraction of the formed trirutile phase caused by the departure of the lithium atoms. After repeated cycles of discharge/charge, the amorphous background increases, while the intensities of the remaining reflections decrease, which is probably due the partial reconversion of the amorphous $Li_aFe_bF_3$ phases. **Figure 4.19b** displays the dQ/dV plot related to the two first cycles of the FeF_3+GO-1h material cycled at C/10 towards lithium. Those two cycles present different electrochemical signatures. A peak is present at 3.3 V during the first discharge process, which can be assigned to the single-phase insertion of $x < 0.5$ lithium per formula unit in the crystal framework to obtain Li_xFeF_3. A peak related to the reverse process of this insertion can be observed during the charging process, due to the partial remaining of the Li_xFeF_3 phase at the end of the discharge. During the second cycle, only the signature of the two-phase reaction can be seen, characterized by a high hysteresis. Between the first and second cycles, the FeF_3+GO-1h material exhibits a drop of capacity, which can be assigned to the irreversible conversion mechanism following the lithium insertion. The charge process does not allow the reformation of the hexagonal pristine phase and leads to the delithiation of the trirutile and amorphous phases. During the subsequent discharge and charge processes, the

active material reacts through a two-phase mechanism. This two-phase mechanism generates drastic changes in the crystal organization, leading to poor capacity retention.

When this material is used towards sodium, it suffers of a poor performance (**Figure 4.20a-b**). The capacity obtained during the first discharge process is around 40 $mAh.g^{-1}$, while the first charge goes up to 100 $mAh.g^{-1}$. The subsequent cycles present higher capacities, with better columbic efficiencies, but still lower than the ones reported for the lithium system. The ex-situ experiment of the first discharge at very low current shows that the reflections of the hexagonal pristine structure are still present after the first partial sodium insertion, although the apparition of a small signal can be observed for instance at $2\Theta = 18$ ° (**Figure 4.20c-d**). These low performances can be explained by the tight crystalline framework of the pristine material. Sodium ions have larger ionic radii compared to lithium, so they are too large to be effectively inserted within this crystalline structure, causing a low rate of sodium insertion. Furthermore, no trirutile structure was reported for the sodiated phase, preventing the anhydrous iron(III) fluoride to react through a conversion reaction. In the case of the cycling within the K-ion system (**Figure A4.5**), the active material shows low activity, which could be partially assigned to electrostatic processes. As the size of the potassium ions is even larger than the one of the sodium ions, this low activity is not surprising. The crystalline framework is not open enough to host such a large alkali species.

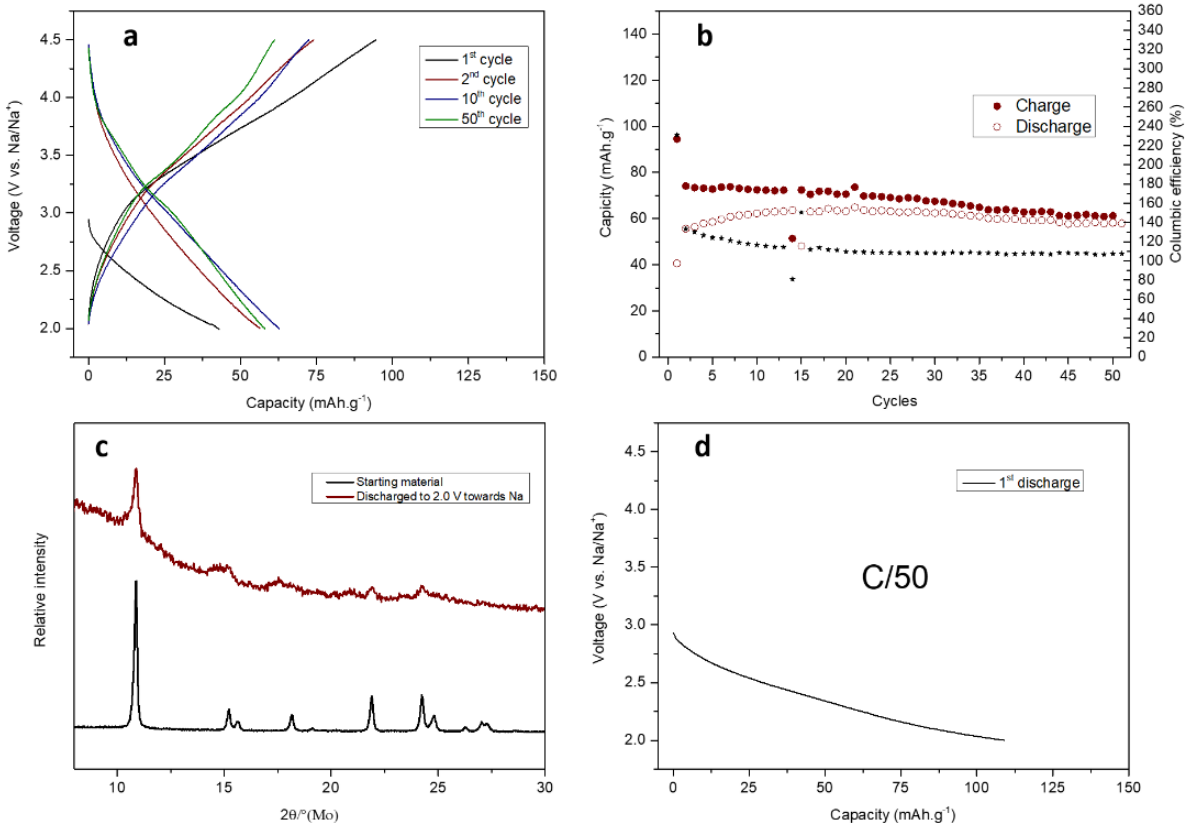

Figure 4.20. (a) *Galvanostatic curves of FeF_3+GO-1h cycled towards Na at C/10 and* **(b)** *related capacity retention.* **(c)** *Ex-situ XRD pattern of FeF_3+GO-1h after the first discharged at C/50 towards Na and* **(d)** *related galvanostatic.*

4. Conclusion

In the first part, cobalt(II) fluoride nanoparticles were synthesized through the fluorolytic sol-gel route with cobalt precursors presenting different ratio of hydroxyl and nitrate anions. The benzyl alcohol mediated reaction produces smaller particles when the precursors contain fewer nitrate anions compared to hydroxide. By varying the composition of the precursor, nanoparticles ranging from few nanometers to the microscale can be prepared with very high purity and narrow size distribution. Those particles can then be added to a conductive matrix to be used as active materials for Li-ion half-cells. High capacities can be achieved during the first cycles, but the capacity retention of these composite materials is quite low. Furthermore, the working potential is lower than the theoretical expected one, decreasing greatly their specific energy and ability to be used as cathode material. The downsizing of the particles to ~50 nm allows the full electrochemical conversion of the material, delivering its full capacity. Their low capacity retention could be attributed to the incomplete reconversion during the

charge processes, additionally to the repeated conversion reaction, which induces the pulverization of the electrode materials, as well as the formation of a high amount of SEI, preventing the good diffusion of the active species.

In the second section, iron fluoride compounds were studied. The fluorination of iron(II) chloride in the presence of oleylamine permits the generation of stabilized FeF_2 rutile nanoparticles. In contrast, anhydrous iron(III) fluoride was synthesized through a gas-solid mediated technique, by the fluorination of hematite iron oxide. The separation of the metal oxide precursor within a PTFE hydrophobic film from the HF aqueous solution, prevents the hydration of the fluoride phase and avoids the formation of iron(III) fluoride hydrated phases. The use of micrometric-sized particles leads only to their partial fluorination, while the fluorination of magnetite precursor generates the Fe_3F_8 phase, not suitable for the insertion of lithium. High energy milling is used in order to produce composite materials made of iron(III) fluoride synthesized from the iron oxide hematite nanoparticles and carbon black. This process tends to form FeF_2 due to the reductive effect of the carbon and to decrease the size of the pristine particles, which greatly influence the electrochemical behavior. In contrast, the grafting of the iron(III) fluoride nanoparticles onto GO does not influence the morphology, neither the crystalline phase of the synthesized compounds. Those FeF_3/GO composite materials can be produced by grafting the precursor directly onto the GO. The time of fluorination of this composite precursor shapes the GO to gradually form a fluorinated carbon coating around the nanoparticles. The morphology of the composite does not change drastically the electrochemical behaviors of fluoride material in the 2-4.5 V vs. Li/Li^+ region. During the first discharge, the insertion of 0.5 lithium per formula unit generates the Li_xFeF_3 phase ($x < 0.5$) by a solid solution reaction, together with the start of a trirutile-like phase generation. The reaction of 0.5 more lithium leads to the conversion of the crystalline framework into phases with an amorphous character. During the subsequent cycles, the active material reacts through the re/conversion of the trirutile and amorphous phases. The low rate capability and capacity retention of the hexagonal phase is attributed to the conversion reactions, which generates severe reorganization within the crystal structure, and induces slow kinetics of the reactions. In the case of the cycling towards larger alkali ions, the active material demonstrates poor performances, probably since its crystal framework is not open enough.

5. Experimental section

Synthesis of $Co(OH)_2$. Solution 1 was made by dissolving of 3 mmol of $Co(NO_3)_2 \cdot 6H_2O$ into 10 mL of water, while solution 2 was made by dissolving 6 mmol of NaOH in 10 mL of water. After both 1 and 2 completely dissolved, solution 2 was added to solution 1 under stirring. The purplish mix of the two solutions turns brown after a few seconds and a precipitate can be observed. After 10 min, the resulting precipitate was collected by centrifugation and purified 3 times with water, and finally dried overnight at 70 °C.

Graphene oxide (GO) preparation. Pre-oxidation of graphite. 2 g of graphite powder were added to 40 mL of concentrated H_2SO_4. Then, 3 g of $K_2S_2O_8$ were added to the mixture under stirring followed by the slow addition of 3 g of P_2O_5. The mixture was stirred at 80 ºC for 5 h, cooled down, repeatedly centrifuged and washed with water until neutral pH was reached and finally dried at 65 ºC.

Graphene oxide (GO) preparation. Oxidation-step. 2 g of prepared pre-oxidized graphite was introduced in 90 mL of concentrated H_2SO_4 and stirred in an ice bath. Then, 2 g of $NaNO_3$ were slowly added under stirring. 12 g of $KMnO_4$ were very slowly added under vigorous stirring, in order that the temperature does not go above 10 ºC (the mixture becomes green). The mixture was then stirred for 1 h in the ice bath and stirred for 5 days at room temperature (at the end the mixture becomes pinkish). 250 mL of water were slowly added under vigorous stirring and the mixture was then transferred to a round bottom flask and heated at 98 ºC for 1 h. 20 mL of H_2O_2 (30 wt%) were slowly added to the hot mixture (which becomes yellow-orange). The warm suspension was finally filtered and purified with a solution made of 250 mL of water and 50 mL of concentrated HCl. The solid was transferred to a beaker, suspended in water, and repeatedly centrifuged and washed to obtain a pH of 6-7. Finally, the solid was dried at 70 ºC.

Synthesis of CoF_2. 3 mmol of $Co(NO_3)_2 \cdot 6H_2O$ were introduced in a Schlenk tube. In order to decompose/dehydrate this reactant, vacuum was applied under different temperature values (50 °C, 100 °C, 150 °C and 200 °C) for 2 hours. Once the decomposition step was done, 30 mL of benzyl alcohol (BnOH) were added under argon atmosphere and the mix was stirred in order to dissolved the obtain precursors. In the case of non-decomposed $Co(NO_3)_2 \bullet 6H_2O$ and $Co(OH)_2$, the precursors were added directly into the Schlenk tube only under argon. Once the dissolution of the precursor was completed, 6 mmol of concentrated methanolic solution were added to the reaction media under stirring. The resulting solution was then transferred into

microwave reactors and treated under microwave radiation for 5 min at a temperature of 150 °C. After the microwave treatment completed, the reactor containing the pinkish solution was cooled down to room temperature and the solution was transferred to a centrifuge vial. After centrifugation, the precipitate was collected, dispersed in ethanol and centrifuged again. This process is repeated three times to purify the final compound. Finally, the obtained powder was dried overnight at 70 °C. To avoid a reaction of the material with water or oxygen, the products were kept in a glovebox.

Grafting of the CoF_2 NPs onto GO. 120 mg of the CoF_2 obtained powder and 45 mg of GO were dispersed into 20 mL of BnOH for at least 2 hours. Once both components were completely dispersed, microwave treatment for 5 min at 150 °C was carried out. The obtained black composite was then purified following the same procedure than the CoF_2 nanoparticles.

Synthesis of FeF_2. 10 mmol of $Fe(Cl)_2$ or $Fe(ac)_2$ were introduced in 60 mL of BnOH contained in a PTFE reactor under argon atmosphere. The solution was then heated to 80 °C in order to dissolve the iron precursor in the solvent. Once the dissolution completed, different amounts of oleylamine were introduced (0 eq, 0.2 eq, 0.5 eq, 1 eq and 2 eq compared to iron) under magnetic stirring (800 rpm) or high energy stirring (12000 rpm). 20 mmol of concentrated methanolic HF solution were introduced in the reaction media under stirring and kept 30 min at 150 °C. The solution was then cooled down to room temperature and precipitated via centrifugation. The precipitate was dispersed first in acetone and precipitated via centrifugation, and then similar processes was repeated twice with ethanol, in order to purify the product. Finally, the powder was dried overnight in an oven at 70 °C and stored in glovebox to avoid water absorption.

Synthesis of the hematite Fe_2O_3 NPs and grafting with GO. 3 mmol of $Fe(NO_3)_3{\cdot}9H_2O$ were dissolved into 15 mL of water at pH = 9 controlled with NH_4OH. The solution was transferred to a Teflon-lined stainless-steel autoclave and treated at 180 °C for 16 h. The hematite iron oxide nanoparticles were collected by centrifugation and purified three times by redispersion in water. Finally, the obtained powder was dried overnight at 70 °C. In the case of the grafting with GO, a solution of dispersed Fe_2O_3 in water was mixed to a solution of dispersed GO. An ocher precipitate was observed directly after mixing both solutions. The solution was precipitated by centrifugation and dried overnight at 70 °C without any further purification.

Synthesis of the magnetite Fe_3O_4 NPs. 1 mmol of $Fe(ac)_2$ and 2 mmol of $Fe(acac)_3$ were dissolved into 20 mL of BnOH. After total dissolution the solution was transferred into a

microwave reactor and treated up to 230 °C under microwave radiations for 20 min. The magnetite iron oxide nanoparticles were collected by centrifugation and purified three times by redispersion in ethanol. Finally, the obtained powder was dried overnight at 70 °C.

Synthesis of the anhydrous FeF_3 NPs. 200 mg of different iron oxide precursors were placed in a Teflon paper and introduced at the top of a Teflon-lined stainless-steel autoclave filled with 5 mL of aqueous 70% HF solution. The nanoparticles were treated at 100 °C for 1 h in the case of the bare FeF_3 NPs, and along different times (1, 4 and 16 hours) in the case of the FeF_3+GO composites. The materials were collected without further purification. The ball milling of these compounds was carried out with 30% w/w of CB at 750 rpm for different times

Annexe

Name of the sample	T of decomposition treatment (C°)	H atomic %	N atomic %	O atomic %	N atomic % compared to Co calculated from EA
CoF_2-2	50	0.2	11.2	39.1	95.2
CoF_2-3	100	0.1	10.5	38.0	86.4
CoF_2-4	150	0.5	7.2	32.7	50.9
CoF_2-5	200	0.7	4.9	30.0	31.7

Table A4.1. *Atomic percentage composition obtained by Elemental Analysis and calculated nitrogen contents for the different decomposed precursors.*

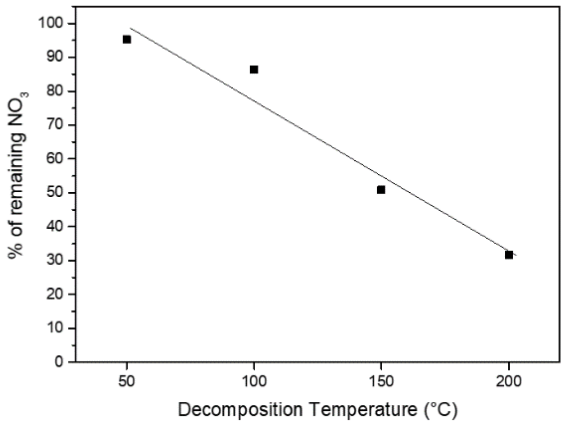

Figure A4.1. *The linear relation between the temperature used for the decomposition of the precursor and the remaining content of -NO_3 in the decomposed precursor.*

Sample name	Calculated sizes of the crystallites (nm)	Sizes of the particles observed by TEM (nm)
CoF_2-1	51	~800
CoF_2-2	45	~300
CoF_2-3	40	~150
CoF_2-4	32	30-50
CoF_2-5	15	10-25
CoF_2-6	8	3-10

Table A4.2. *Crystallite sizes of the different CoF_2 synthesized compounds calculated by the Scherrer equation (as the particles are spherical, the shape factor has been taken as K = 0.87) and particle sizes observed by TEM.*

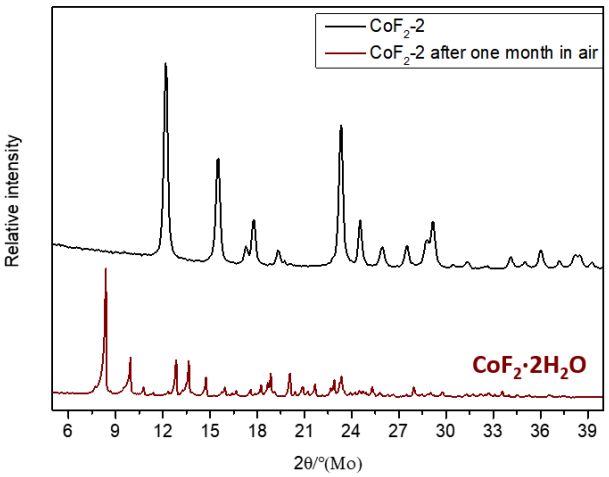

Figure A4.2. *XRD patterns of CoF_2-2 after synthesis and after 1 month of storage in ambient atmosphere.*

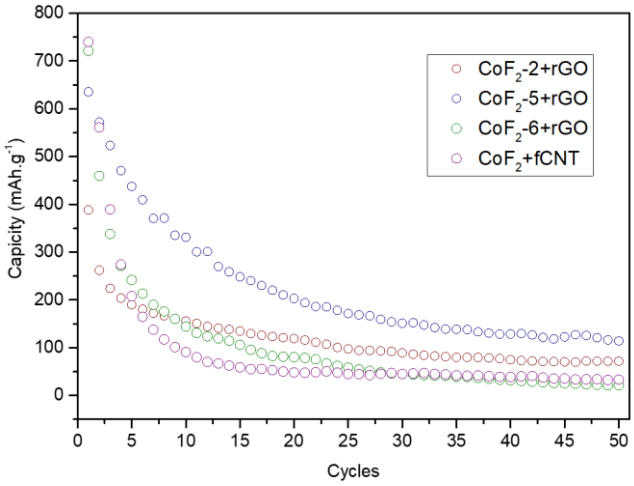

Figure A4.3. *Capacity retention of the different cobalt(III) fluoride composites materials cycled at C/10 towards Li in the window potential 1-4.4 V (vs. Li/Li^+).*

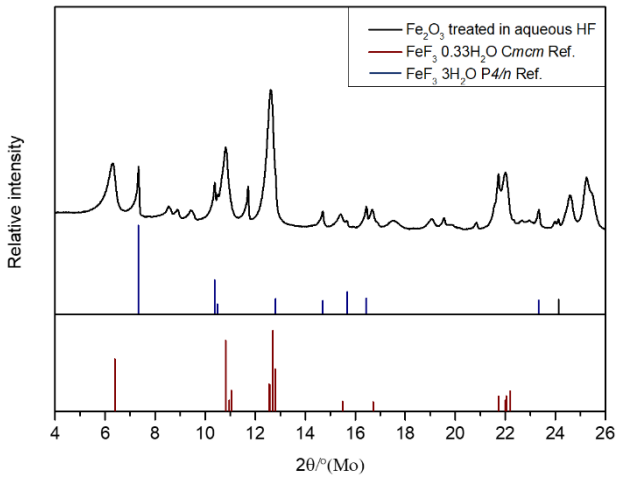

Figure A4.4. *XRD patterns of product of synthesis when the Fe_2O_3 precursor is in direct contact with the aqueous HF solution.*

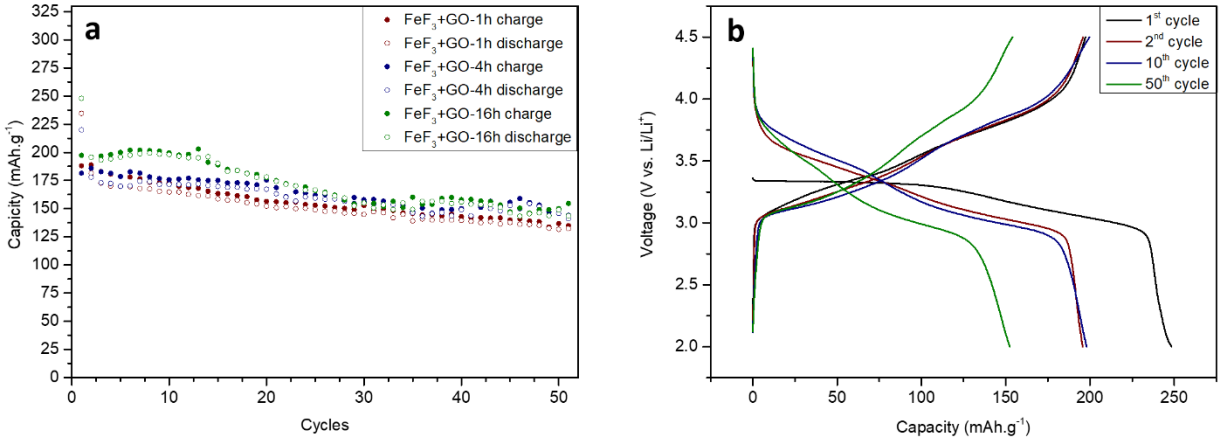

Figure A4.5. (a) *Capacity retention of the different iron(III) fluoride composites materials with GO at C/10 towards Li and* **(b)** *related galvanostatic profile of FeF_3+GO-16h .*

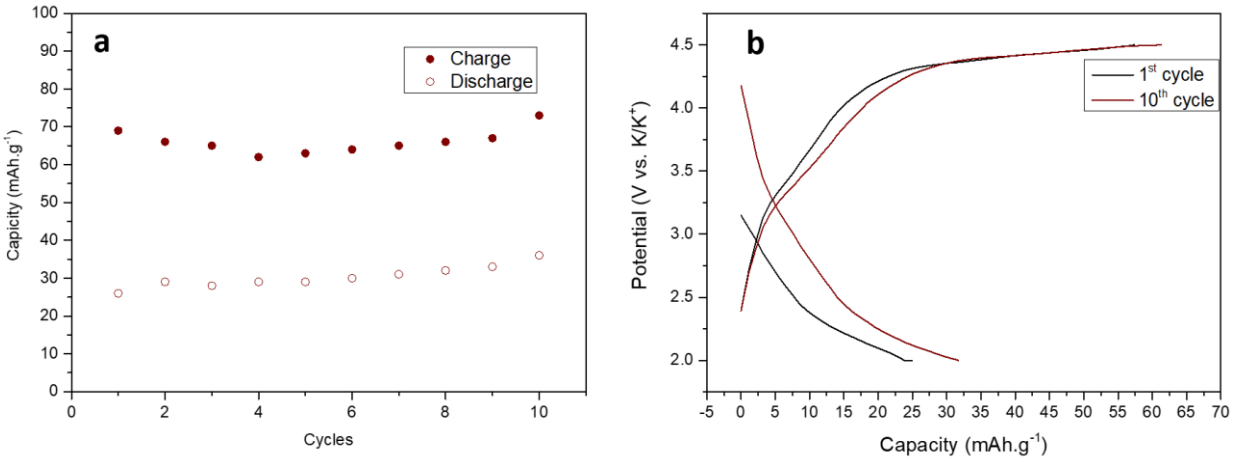

Figure A4.6. (a) *Capacity retention of FeF_3+GO-16h at C/10 towards potassium and* **(b)** *its related galvanostatic profile.*

References

1. Wang, X.; Gu, W.; Lee, J. T.; Nitta, N.; Benson, J.; Magasinski, A.; Schauer, M. W.; Yushin, G., Carbon Nanotube–CoF_2 Multifunctional Cathode for Lithium Ion Batteries: Effect of Electrolyte on Cycle Stability. *Small* **2015,** *11* (38), 5164-5173.
2. Teng, Y. T.; Pramana, S. S.; Ding, J.; Wu, T.; Yazami, R., Investigation of the conversion mechanism of nanosized CoF_2. *Electrochimica Acta* **2013,** *107*, 301-312.
3. Guo, Y.; Gaczyński, P.; Becker, K.-D.; Kemnitz, E., Sol–Gel Synthesis and Characterisation of Nanoscopic FeF_3-MgF_2 Heterogeneous Catalysts with Bi-Acidic Properties. *ChemCatChem* **2013,** *5* (8), 2223-2232.
4. Carlo, L. D.; Conte, D. E.; Kemnitz, E.; Pinna, N., Microwave-assisted fluorolytic sol–gel route to iron fluoride nanoparticles for Li-Ion batteries. *Chemical Communications* **2014,** *50* (4), 460-462.
5. Hummers, W. S.; Offeman, R. E., Preparation of Graphitic Oxide. *Journal of the American Chemical Society* **1958,** *80* (6), 1339-1339.
6. Russo, P. A.; Donato, N.; Leonardi, S. G.; Baek, S.; Conte, D. E.; Neri, G.; Pinna, N., Room-Temperature Hydrogen Sensing with Heteronanostructures Based on Reduced Graphene Oxide and Tin oxide. *Angewandte Chemie International Edition* **2012,** *51* (44), 11053-11057.
7. McAllister, M. J.; Li, J.-L.; Adamson, D. H.; Schniepp, H. C.; Abdala, A. A.; Liu, J.; Herrera-Alonso, M.; Milius, D. L.; Car, R.; Prud'homme, R. K.; Aksay, I. A., Single Sheet Functionalized Graphene by Oxidation and Thermal Expansion of Graphite. *Chemistry of Materials* **2007,** *19* (18), 4396-4404.
8. Wang, X.; Dai, Y.; Gao, J.; Huang, J.; Li, B.; Fan, C.; Yang, J.; Liu, X., High-Yield Production of Highly Fluorinated Graphene by Direct Heating Fluorination of Graphene-oxide. *ACS Applied Materials & Interfaces* **2013,** *5* (17), 8294-8299.
8. Rane, A. V.; Kanny, K.; Abitha, V. K.; Thomas, S., Chapter 5 - Methods for Synthesis of Nanoparticles and Fabrication of Nanocomposites. In *Synthesis of Inorganic Nanomaterials*, Mohan Bhagyaraj, S.; Oluwafemi, O. S.; Kalarikkal, N.; Thomas, S., Eds. Woodhead Publishing: 2018; pp 121-139.
3. Cabana, J.; Monconduit, L.; Larcher, D.; Palacín, M. R., Beyond Intercalation-Based Li-Ion Batteries: The State of the Art and Challenges of Electrode Materials Reacting Through Conversion Reactions. *Advanced Materials* **2010,** *22* (35), E170-E192.
4. Seo, J. K.; Cho, H.-M.; Takahara, K.; Chapman, K. W.; Borkiewicz, O. J.; Sina, M.; Shirley Meng, Y., Revisiting the conversion reaction voltage and the reversibility of the CuF_2 electrode in Li-ion batteries. *Nano Research* **2017,** *10* (12), 4232-4244.
9. Mourdikoudis, S.; Liz-Marzán, L. M., Oleylamine in Nanoparticle Synthesis. *Chemistry of Materials* **2013,** *25* (9), 1465-1476.
10. Li, T.; Li, L.; Cao, Y. L.; Ai, X. P.; Yang, H. X., Reversible Three-Electron Redox Behaviors of FeF_3 Nanocrystals as High-Capacity Cathode-Active Materials for Li-Ion Batteries. *The Journal of Physical Chemistry C* **2010,** *114* (7), 3190-3195.
11. Li, C.; Gu, L.; Tsukimoto, S.; van Aken, P. A.; Maier, J., Low-Temperature Ionic-Liquid-Based Synthesis of Nanostructured Iron-Based Fluoride Cathodes for Lithium Batteries. *Advanced Materials* **2010,** *22* (33), 3650-3654.
12. Liu, L.; Guo, H.; Zhou, M.; Wei, Q.; Yang, Z.; Shu, H.; Yang, X.; Tan, J.; Yan, Z.; Wang, X., A comparison among $FeF_3{\cdot}3H_2O$, $FeF_3{\cdot}0.33H_2O$ and FeF_3 cathode materials for lithium ion batteries: Structural, electrochemical, and mechanism studies. *Journal of Power Sources* **2013,** *238*, 501-515.
13. Murugesan, V.; Cho, J. S.; Govind, N.; Andersen, A.; Olszta, M. J.; Han, K. S.; Li, G.; Lee, H.; Reed, D. M.; Sprenkle, V. L.; Cho, S.; Nune, S. K.; Choi, D., Lithium Insertion Mechanism in Iron Fluoride Nanoparticles Prepared by Catalytic Decomposition of Fluoropolymer. *ACS Applied Energy Materials* **2019,** *2* (3), 1832-1843.
14. Sun, H.; Zhou, H.; Xu, Z.; Ding, J.; Yang, J.; Zhou, X., Preparation of anhydrous iron fluoride with porous fusiform structure and its application for Li-ion batteries. *Microporous and Mesoporous Materials* **2017,** *253*, 10-17.
15. Guntlin, C. P.; Zünd, T.; Kravchyk, K. V.; Wörle, M.; Bodnarchuk, M. I.; Kovalenko, M. V., Nanocrystalline FeF_3 and MF_2 (M = Fe, Co, and Mn) from metal trifluoroacetates and their Li(Na)-ion storage properties. *Journal of Materials Chemistry A* **2017,** *5* (16), 7383-7393.

16. Li, Y.; Liao, H.; Qian, Y., Hydrothermal Synthesis of Ultrafine α-Fe_2O_3 and Fe_3O_4 Powders. *Materials Research Bulletin* **1998,** *33* (6), 841-844.
17. Badway, F.; Pereira, N.; Cosandey, F.; Amatucci, G. G., Carbon-Metal Fluoride Nanocomposites: Structure and Electrochemistry of FeF_3 : C. *Journal of The Electrochemical Society* **2003,** *150* (9), A1209-A1218.
18. Fecht, H. J.; Hellstern, E.; Fu, Z.; Johnson, W. L., Nanocrystalline metals prepared by high-energy ball milling. *Metallurgical Transactions A* **1990,** *21* (9), 2333.
19. Weeber, A. W.; Bakker, H., Amorphization by ball milling. A review. *Physica B: Condensed Matter* **1988,** *153* (1), 93-135.
20. Dimiev, A. M.; Alemany, L. B.; Tour, J. M., Graphene Oxide. Origin of Acidity, Its Instability in Water, and a New Dynamic Structural Model. *ACS Nano* **2013,** *7* (1), 576-588.
21. Panias, D.; Taxiarchou, M.; Paspaliaris, I.; Kontopoulos, A., Mechanisms of dissolution of iron oxides in aqueous oxalic acid solutions. *Hydrometallurgy* **1996,** *42* (2), 257-265.
22. Chaiyakun, S.; Witit-Anun, N.; Nuntawong, N.; Chindaudom, P.; Oaew, S.; Kedkeaw, C.; Limsuwan, P., Preparation and characterization of graphene oxide nanosheets. *Procedia Engineering* **2012,** *32*, 759-764.
23. Li, J.; Fu, L.; Xu, Z.; Zhu, J.; Yang, W.; Li, D.; Zhou, L., Electrochemical properties of carbon-wrapped FeF_3 nanocomposite as cathode material for lithium ion battery. *Electrochimica Acta* **2018,** *281*, 88-98.
24. Huang, Q.; Turcheniuk, K.; Ren, X.; Magasinski, A.; Song, A.-Y.; Xiao, Y.; Kim, D.; Yushin, G., Cycle stability of conversion-type iron fluoride lithium battery cathode at elevated temperatures in polymer electrolyte composites. *Nature Materials* **2019**.
25. Dimov, N.; Nishimura, A.; Chihara, K.; Kitajou, A.; Gocheva, I. D.; Okada, S., Transition metal $NaMF_3$ compounds as model systems for studying the feasibility of ternary Li-M-F and Na-M-F single phases as cathodes for lithium–ion and sodium–ion batteries. *Electrochimica Acta* **2013,** *110*, 214-220.
26. Doe, R. E.; Persson, K. A.; Meng, Y. S.; Ceder, G., First-Principles Investigation of the Li−Fe−F Phase Diagram and Equilibrium and Nonequilibrium Conversion Reactions of Iron Fluorides with Lithium. *Chemistry of Materials* **2008,** *20* (16), 5274-5283.
27. Yamakawa, N.; Jiang, M.; Key, B.; Grey, C. P., Identifying the Local Structures Formed during Lithiation of the Conversion Material, Iron Fluoride, in a Li Ion Battery: A Solid-State NMR, X-ray Diffraction, and Pair Distribution Function Analysis Study. *Journal of the American Chemical Society* **2009,** *131* (30), 10525-10536.

Chapter 5

Synthesis, electrochemical behavior and structural changes of orthorhombic $NaMF_3$

1. Introduction

In the LIBs and NIBs systems used nowadays, the positive electrode acts as the reservoir of alkali ions, making potential technologies based on transition metal fluorides or on sulfur chemistry very challenging. In the case of sulfur used as a cathode for the LIBs, one possible solution is the prelithiation of the electrode material [1,2]. Nevertheless, this technique would involve additional costs in the material preparation, hindering its implementation towards an industrial scale. As discussed in the previous chapter, the electrochemical reaction of lithium with anhydrous iron(III) fluoride leads to the conversion of the crystalline framework, preventing the insertion of one lithium atom within the structure in order to obtain the electrochemically-prepared $LiFeF_3$ perovskite. On the other hand, attempts to synthesize the lithiated perovskite iron(III) fluoride leads to the generation of a FeF_2 and LiF mixture, or the trirutile $LiFe_2F_6$ phase [3]. The thermodynamical instability of this phase is due to the too-small size of lithium, which produces a collapse of the crystalline framework [4]. In contrast, due to the larger size of sodium, the $NaFeF_3$ phase has been already described in the literature, as well as its electrochemical activity towards sodium. However, so far, a combination of poor reversibility and low capacity put a limit over the performances of batteries based on this compound [5,6]. In this chapter, two routes are presented to obtain $NaFeF_3$ as a perovskite: a two-step synthesis by fluorination/sodiation of iron(II) fluoride, and a one-step synthesis through NH_4F fluorination. These versatile routes allow the generation of sodiated transition metal fluorides, which adopt an orthorhombic conformation. The $NaFeF_3$ prepared here can be used as an active material for NIBs and LIBs. Special interest was devoted to understanding the structural changes involved in the charge/discharge processes of $NaFeF_3$ towards lithium and sodium. These structural changes are characterized by ex-situ and *operando* XRD experiments, and supported by electronic structure calculations.

2. Synthesis of orthorhombic perovskite fluorides

In this study, sodiated perovskite structures were synthesized following two approaches, namely one involving a two-step synthesis and a second one through only one step. The two-step route implies the syntheses of the metal difluoride firstly (details are described in chapter

4), followed by a second step, a fluorination via the fluorolytic sol-gel process using as fluorinating agent ammonium fluoride in the presence of sodium ethoxide, after the dispersion of all the components of the reaction in BnOH through sonication. If the precursor particles are too large, only the surface of the material is converted into the target compound and reflections belonging to the rutile phase of the precursor and $NaFeF_3$ can be detected via XRD measurements (**Figure A5.1**). A nanoscale MF_2 precursor is a prerequisite for the full conversion of all the reactants into the perovskite phase. **Figure 5.1** displays the XRD patterns of the compounds obtained from fluorination/sodiation of CoF_2 and FeF_2 (more specifically, the samples CoF_2-6 and FeF_2-5, cf. chapter 4) and **Figure A5.2a** shows the Rietveld refinement of the $NaFeF_3$ phase with calculated lattice parameters and atomic positions.

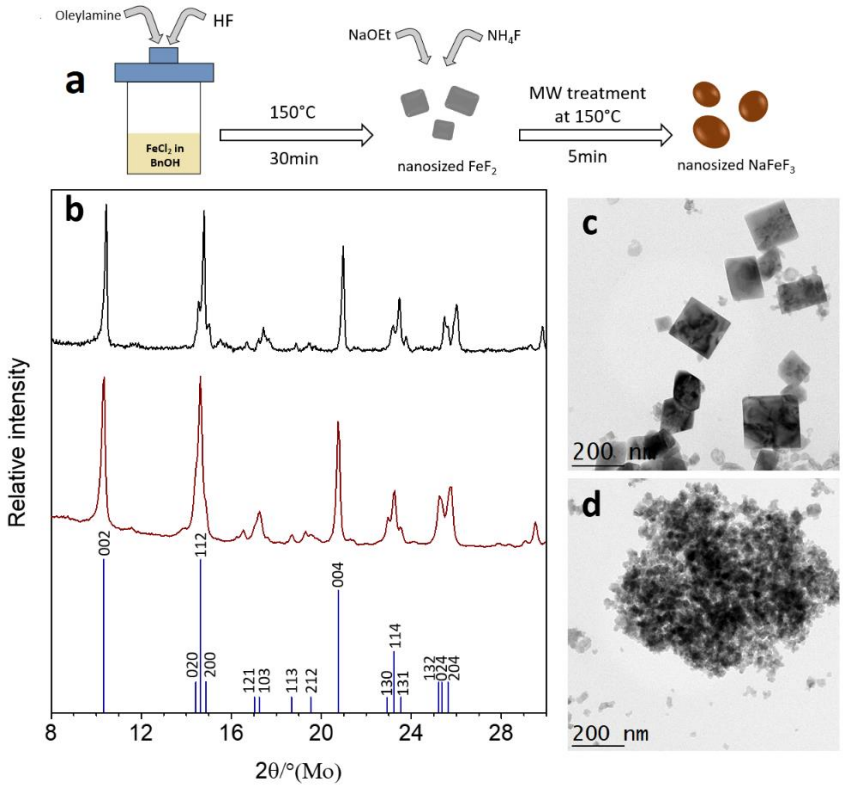

Figure 5.1. (a) *Schematic reaction pathway of the two-step synthesis of $NaFeF_3$.* **(b)** *XRD patterns of $NaCoF_3$ and $NaFeF_3$, and* **(c)** *&* **(d)** *relative TEM images of the products, respectively.*

Both compounds present XRD patterns corresponding to the orthorhombic perovskite structure relative to the P*nma* space group. The $NaFeF_3$ pattern exhibits broader reflections compared to $NaCoF_3$, which can be ascribed to a smaller crystallite size. To confirm this observation, TEM images were taken and show that the $NaCoF_3$ particles are lager and adopt cubic shapes with a size around 150 nm, in contrast to $NaFeF_3$, which forms particles between 30 and 50 nm with

not very well-defined shapes. These differences in size and morphology arise from the difference in the precursor morphology, but as well from the fact that the small size FeF_2 precursor particles are stabilized by oleylamine. Oleylamine is used as a surfactant in the synthesis and is still present in the reaction media, participating in the formation of the nanoparticles, generating nanoparticles of lower sizes. A visualization of the crystal structure of $NaFeF_3$ can be obtained from the Rietveld refinement, with the atomic positions and cell parameters, showing clear channels along the [010] and [-101]/[101] crystallographic directions, useful for ionic diffusion within the material (**Figure A5.2b**). If the synthesis of a $LiFeF_3$ phase is attempted following the same synthesis route and using lithium methoxide as a lithium source, a mixture of FeF_2 and LiF is obtained (**Figure A5.3**). Furthermore, to confirm the existence of these products, DFT calculations were carried out, which agree with the observed outcome. The $NaFeF_3$ phase presents a more stable energy than NaF + FeF_2 (ΔE = + 140 meV.FU^{-1}), while the isostructural $LiFeF_3$ is unstable compared to LiF + FeF_2 (ΔE = - 240 meV.FU^{-1}).

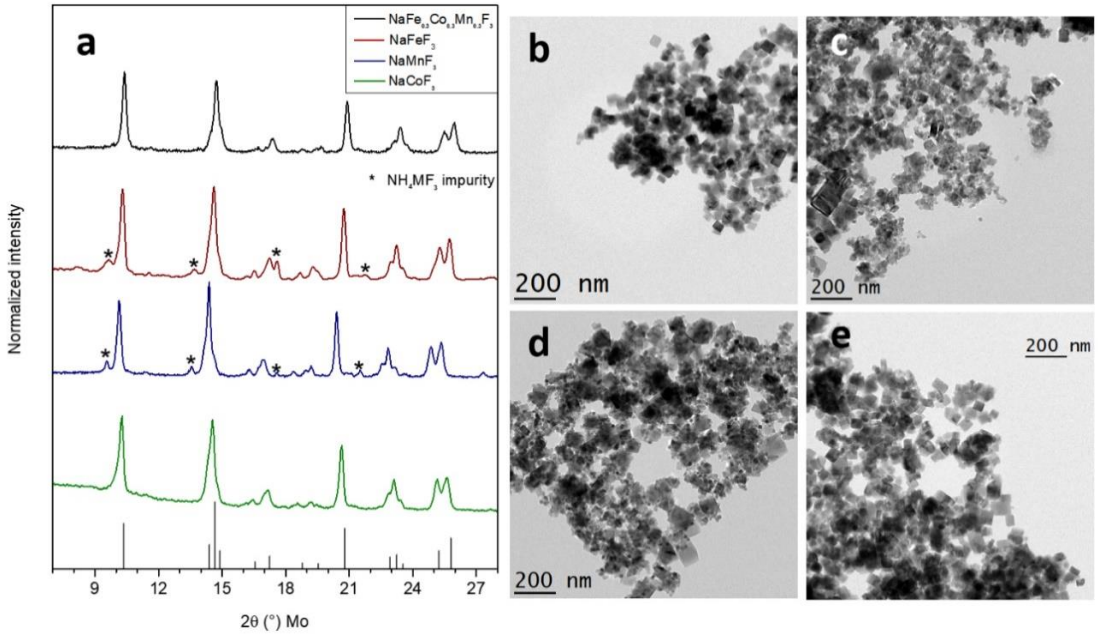

Figure 5.2. (a) *XRD patterns of $NaCoF_3$, $NaFeF_3$, $NaMnF_3$, and $NaCo_{1/3}Mn_{1/3}Fe_{1/3}F_3$ and* **(b)**, **(c)**, **(d)** *&* **(e)** *relative TEM images of the compounds, respectively.*

The one-step reaction route involves the use of transition metal acetates and sodium ethoxide in BnOH, in the presence of ammonium fluoride as single fluorine source. After the total dispersion/dissolution of the three components of the reaction, the mixture is heated at 150 °C in an oil bath. The decomposition of the fluorine-containing reactant into HF and NH_3 above 100 °C induces the fluorolytic sol-gel formation of the perovskite nanoparticles. The availability of the different transition metal acetate species ($Co(ac)_2$, $Mn(ac)_2$ and $Fe(ac)_2$)

allows the formation of likewise different transition metal fluoride structures through this synthesis method. **Figure 5.2a** displays the XRD patterns of the different transition metal fluorides. Similarly to the two-step synthesis, the main phase obtained through this route can be ascribed to the orthorhombic perovskite structure. A shift of the reflection pattern to higher angles can be noticed along with the increase of the atomic number of the metal, pointing to a contraction of the crystalline lattice, as expected. However, small reflections belonging to the cubic NH_4MF_3 compound can be observed with variable intensity depending on the synthesized material. The presence of this side-product is due to the competition of the formation of the sodiated phase with the NH_4MF_3 phase, induced by the use of three equivalents of ammonium fluoride in the case of the one-step reaction, whereas only one is used in the two-step reaction. The generation of mix transition metal fluorides with this technique is also possible as illustrated by the synthesis of the $NaFe_{1/3}Mn_{1/3}Co_{1/3}F_3$ phase, which demonstrates an orthorhombic structure as well. The TEM images of these different compounds show very similar morphologies, namely cubic-shaped nanoparticles ranging from 20 to 50 nm. Small spherical nanoparticles can also be observed, which can be attributed to the NH_4MF_3 side product. These spherical nanoparticles are more apparent for samples having higher reflection intensities related to the NH_4MF_3 compound.

The instabilities of these compounds towards oxidation are noticeable. When exposed to air, $NaFeF_3$ is quickly transformed to Na_3FeF_6 in cryolite phase, where iron(II) is oxidized to iron(III). This oxidized material presents inactive sodium atoms due to the oxidation state of the iron atoms, additionally to the not adapted crystal structure towards alkali insertion that demonstrates the compound [7,8]. Hence, all syntheses and subsequent manipulations of these compounds need to be done under an inert atmosphere. These materials are also sensitive to oxidation when mixed together with materials containing surface oxygen species such as GO or fCNTs (**Figure A5.4**).

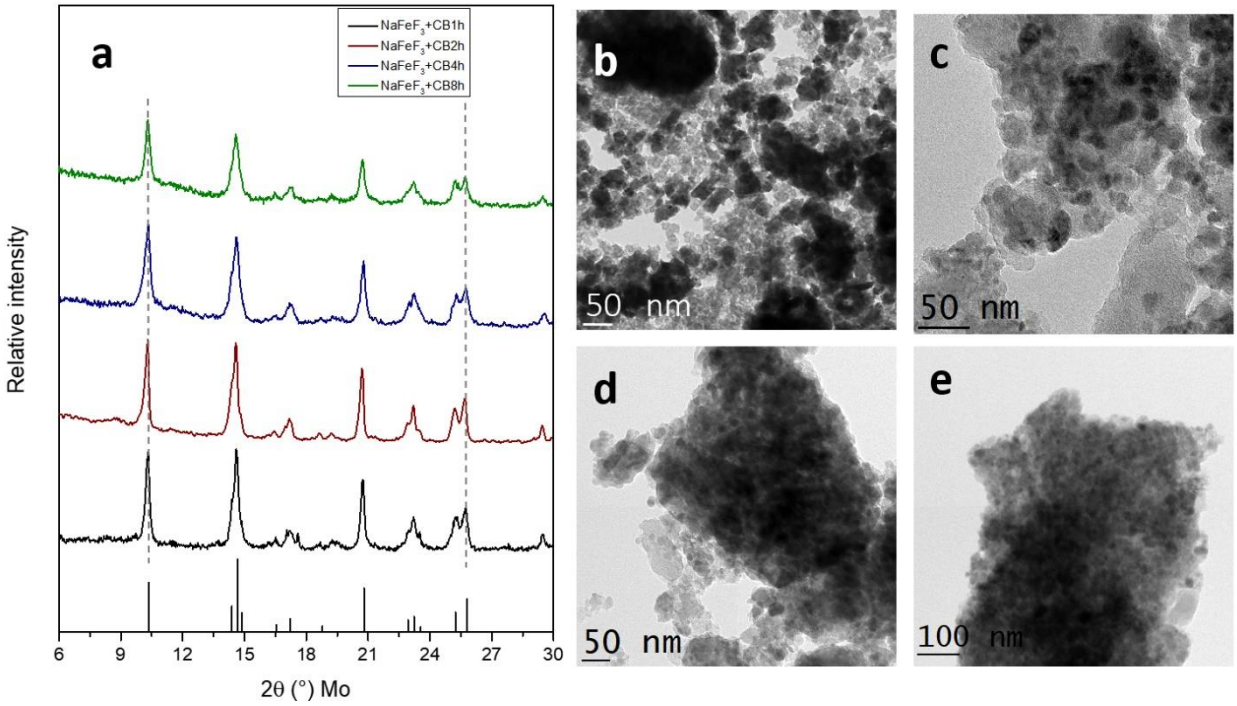

Figure 5.3. (a) *XRD patterns of $NaFeF_3$ obtained from FeF_2 ball-milled with CB for 1 h, 2 h, 4 h & 8 h and* **(b)**, **(c)**, **(d)** & **(e)** *relative TEM images of the compounds, respectively.*

To overcome the insulating character of the fluoride perovskite, ball-milling of the active materials was performed with CB. **Figure 5.3a** displays the XRD patterns of $NaFeF_3$ synthesized from FeF_2 milled for different times. It can be seen that the FWMHs of the reflections do not change drastically with extended times of milling. In contrast to the milling process of anhydrous iron(III) fluoride in the previous chapter (cf. chapter 4 section 3.2), no shift of the reflections can be observed (dashed gray line on **Figure 5.3a**). Additionally, no new reflections appear, which would point to the partial conversion of the active material into side products along with the milling. As the iron content is already at its 2+ oxidation state, no further reduction induced by carbon can occur. Similar to the case of the anhydrous FeF_3, milling for 1 hour leads to a mixing of the two components, while from 2 hours, the active material starts to be embedded within the carbon black matrix. After 8 hours of milling, only large agglomerates of carbon black and active material particles can be observed, where the fluoride compound appears in the shape of darker dots ranging from 10 to 25 nm (**Figure 5.3b-e**). Unlike the iron(III) material, the crystal structure of the perovskite compound does not suffer too much from the ball-milling, but still beneficiates from the intimate mixing promoted by this technique.

3. Electrochemical behavior of the orthorhombic perovskite fluoride compounds

The synthesized materials mixed with carbon black were used as positive electrodes for NIB half-cells, using metallic sodium as a reference and a counter electrode, and sodium perchlorate dissolved in ethylene carbonate and fluoroethylene carbonate as an electrolyte. To determine the optimal milling time with the conductive matrix, the composite materials based on iron prepared by different milling times were subjected to galvano-cycling (**Figure A5.5**). The low capacities obtained from the materials ball-milled for 1 and 2 hours show that the active material is not enough homogeneously mixed with the carbon matrix to overcome the $NaFeF_3$ insulating character. The low conductivities of these composites induce poor charge transfer abilities of the active materials, leading to poor reaction kinetics. In contrast, a milling treatment of 4 hours seems to be sufficient to allow the active material to reach good performances, due to a good mixing between the two components as seen on the TEM images shown on the previous section. Therefore, this sample (herein called $NaFeF_3$+CB4h) was chosen to conduct further experiments.

This sample was cycled at different current rates and within different potential windows to study the electrochemical behavior of $NaFeF_3$. Through galvano-cycling, at a current density of C/10 (19.6 $mA.g^{-1}$), the first charge achieves up to 200 $mAh.g^{-1}$, which represents the total disinsertion of the sodium ions out of the crystal framework (**Figure 5.4a**). The following discharge provides 150 $mAh.g^{-1}$, to slightly increase up to 166 $mAh.g^{-1}$ after the 10^{th} cycle. The value of the charge is comparable, demonstrating a good columbic efficiency of the material (between 97 % and 100 % after the first cycle). No appreciable plateaus are observed during the first cycle. However, clear plateaus can be seen at 3.0 V and 3.3 V vs. Na/Na^+ from the second cycle on. The cyclic voltammetry experiment conducted at a low scan rate shows the same tendency (**Figure 5.4b**). During the first cycle, no pronounced redox waves are apparent, while from the second cycle, obvious signals are present. The maximum values of the anodic waves are located at 3.10 V and 3.55 V, while the cathodic waves have lower values, namely 2.86 and 3.33 V. The appearance of two different signals during the charge and the discharge demonstrates a two-step dis/insertion of one sodium atom per formula unit, as predicted by calculations [9]. The composite material shows a good rate capability with 130 $mAh.g^{-1}$ at C/3 and 108 $mAh.g^{-1}$ at 1 C. When higher cutoff potentials are applied during the charge, the material presents high initial capacities, but worse capacity retentions caused by the occurrence

of side reactions, such as the decomposition of the electrolyte at the surface of the fluoride nanoparticles (**Figure 5.4c-d**).

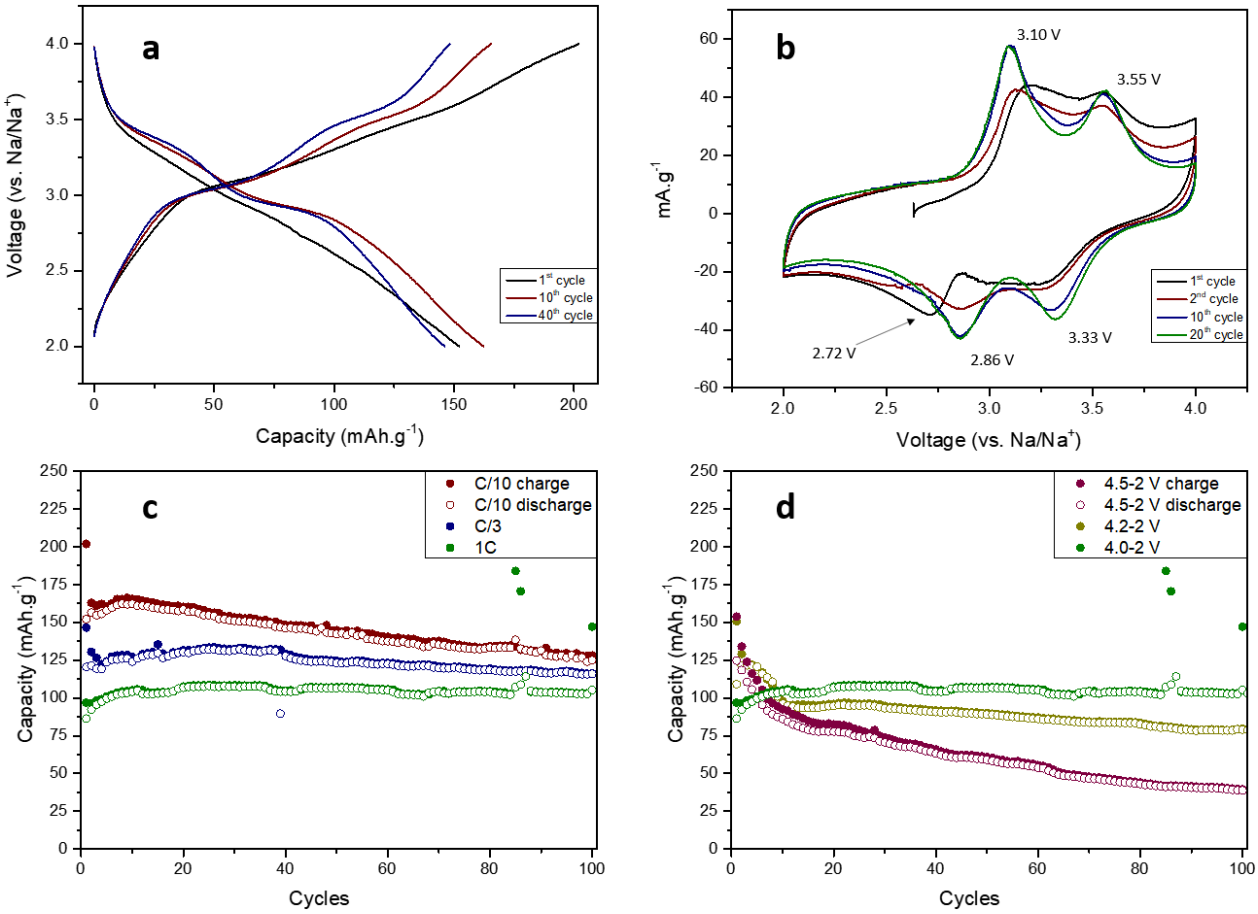

Figure 5.4. (a) *Galvanostatic profile of $NaFeF_3$+CB4h compound cycled at C/10 towards sodium and* **(b)** *cyclic voltammetry experiment towards sodium at a scan rate of 0.1 $mV.s^{-1}$.* **(c)** *Capacity retentions of the compound cycled at different current densities and* **(d)** *within different potential windows.*

In the literature, other transition metal perovskites compounds are reported to have higher redox potentials than $NaFeF_3$, namely 4.3 V for $NaCoF_3$ and 3.9 V for $NaMnF_3$ [10]. Therefore, these compounds synthesized through a one-step synthesis were tested as cathode materials at a higher cutoff potential (2-4.5 V vs. Na/Na^+). In contrast to $NaFeF_3$, the cobalt compound shows low performances. Its initial charge is about 100 $mAh.g^{-1}$ with a flat plateau around 4.2 V (**Figure 5.5**). The next discharge goes up to 25 $mAh.g^{-1}$ without presenting obvious plateaus. During the following cycles, the charge processes present high capacities, while the discharges do not go above 40 $mAh.g^{-1}$. The plateau appearing during the charge can be attributed to the decomposition of the electrolyte at the surface of the active material. The redox potential of the cobalt being too close to the limit of the potential window, the hysteresis of the material hinders

the charge process, while the instability of the electrolyte towards the material prevents to use of higher cutoff potentials. The performances of the manganese phase are slightly better. The first charge shows a similar plateau as the cobalt phase, but at a lower voltage. During the first discharge, a plateau around 3.7 V can be appreciated for a discharge capacity of 60 $mAh.g^{-1}$, but with decreasing values along the cycles. As the theoretical potential of the $NaMnF_3$ is lower than $NaCoF_3$, the compound is able to perform higher rate of sodium dis/insertion, but still at a low rate compared to $NaFeF_3$.

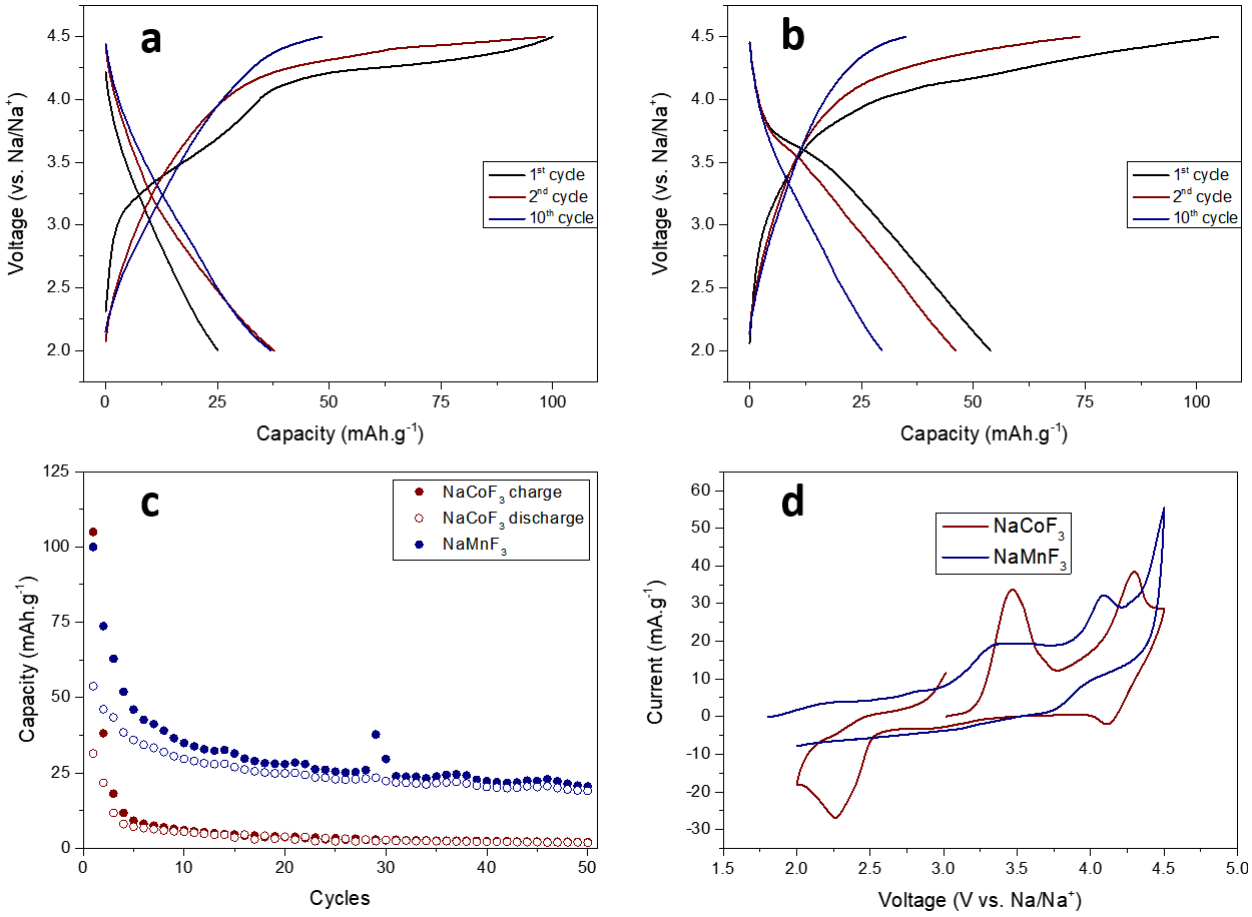

Figure 5.5. (a) *and* **(b)** *Galvanostatic profiles of $NaCoF_3$ and $NaMnF_3$ ball-milled with CB cycled at C/10 towards sodium, respectively.* **(c)** *Capacity retentions of the compound cycled at different C/10.* **(d)** *Cyclic voltammetry experiments of $NaCoF_3$ and $NaMnF_3$ ball-milled with CB at a scan rate of 0.1 $mV.s^{-1}$.*

After the first sodium disinsertion, the $NaFeF_3$ crystalline framework is able to undertake the insertion of alkali ions through electrochemical processes. As lithium exhibits a smaller ionic radius compared to sodium, the cycling of the iron phase towards lithium is made possible. **Figure 5.6a** displays the galvanostatic plot of the active material cycled at C/3. As the average potential of the redox lithium couple is ~ 0.3 V higher than the one of the Na/Na^+ redox couple,

a higher potential cutoff has been used in order to obtain the full disinsertion of the sodium ions out of the structure, and for comparison, the specific capacities have been calculated on the basis of the FeF_3 mass. The first charge achieves 230 $mAh.g^{-1}$, which represents the full extraction of the sodium ions. During the following discharge, 200 $mAh.g^{-1}$ are obtained, with a slopped plateau. The subsequent cycles present more pronounced plateaus, as it was the case towards sodium. The specific capacity of the compound increases up to the 30th cycle to endorse a slight decrease afterward.

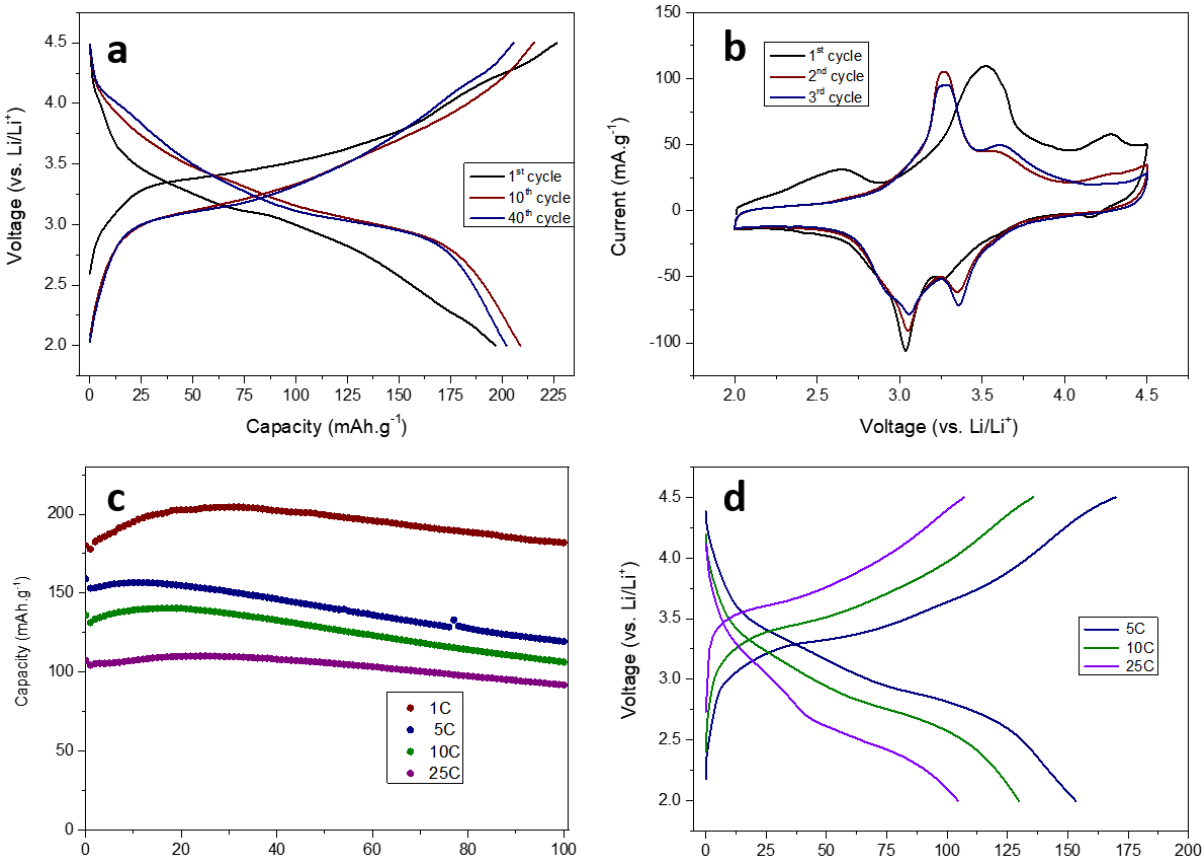

Figure 5.6. (a) *Galvanostatic profile of $NaFeF_3$+cb4h compound cycled at C/3 towards lithium and* **(b)** *cyclic voltammetry experiment towards lithium at a scan rate of 0.1 $mV.s^{-1}$.* **(c)** *Capacity retentions of the compound cycled at different high current densities and* **(d)** *relative galvanostatic profiles of the second cycles.*

The cyclic voltammetry experiment exhibits an intense anodic wave during the first cycle (**Figure 5.6b**), which represents the first sodium disinsertion. During the following cycles, two waves can be observed at 3.2 V and 3.6 V towards the anodic direction, at 3.0 V and 3.4 V towards the cathodic direction. No change in the shape of the voltammetry profiles can be observed along the cycles, demonstrating the reversible lithium dis/insertion after the initial sodium disinsertion, as it is the case for the compound cycled towards sodium. In the lithium system, the active material demonstrates outstanding rate capabilities. The cycling at 1C shows

good capacities, while the increase in current density at very high rates does not prevent the fluoride framework to undergo lithium dis/insertion with very good values, namely up to 160 $mAh.g^{-1}$ at 5C, 145 $mAh.g^{-1}$ at 10C and 120 $mAh.g^{-1}$ at 25C. The galvanostatic profiles at high current densities show relatively low hysteresis, with appreciable plateaus (**Figure 5.6c-d**). The ability of the active material to react with lithium in such cycling conditions indicates that fast reaction kinetics are involved in the charge/discharge mechanisms. Those performances are extremely high compared to the as-synthesized anhydrous iron(III) fluoride, which have hindered performances due to the conversion reactions involved in its charge/discharge mechanisms.

As $NaFeF_3$ can act as the reservoir of alkali ions, this active material was used within a full-cell configuration. For this purpose, hard carbon (HC) is used as a negative electrode, by dissolving glucose in a solution of dispersed GO in water (GO 5 % w/w compared to glucose). The carbonization of this mixture at high temperature (1200 °C) will create low-range organized graphene sheets, induced by the GO [11]. HC prepared this way possesses low enough working potential to deliver a good practicable voltage against $NaFeF_3$. Its expected theoretical capacity is higher than the fluoride material, hence the need to balance the weight of the active material (**Figure 5.7a**). The mass of the negative electrode material matching with the capacity of $NaFeF_3$ was chosen as 1.2 higher to prevent that HC becomes the limiting factor of the cycling. **Figure 5.6a-b** depicts the galvanostatic profile and the capacity retention of the $NaFeF_3$//HC full-cell. Due to the irreversible reactions occurring at the HC electrode, the first cycle presents low columbic efficiency. The sodium ions extracted from the fluoride material, namely ~200 $mAh.g^{-1}$ representing the full disinsertion of the sodium ions out of the fluoride material, are involved in these irreversible reactions, such as the formation of the SEI, and cannot participate in the cycling during the subsequent cycles. Along the following cycles, the columbic efficiency increases, but is still far from 100%. This low columbic efficiency leads to the shrinking of the capacity, with 30 $mAh.g^{-1}$ of remaining capacity after 10 cycles. The low performances of the considered full-cell can be partially ascribed to the low columbic efficiency of the carbon material, hence the need to employ materials with high columbic efficiency when $NaFeF_3$ is used as a positive electrode.

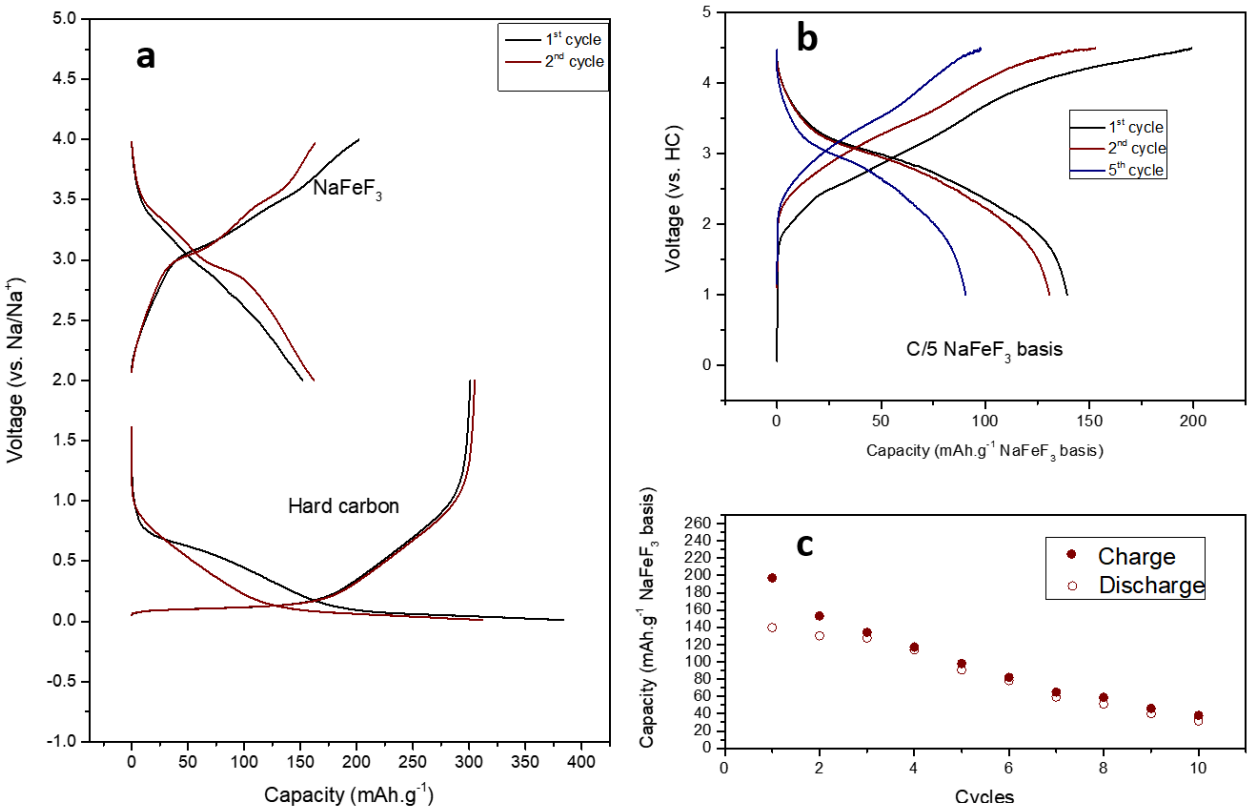

Figure 5.7. (a) *Galvanostatic profile of the half-cells, $NaFeF_3$//Na and HC//Na cycled at C/10.* **(b)** *Galvanostatic profile of the $NaFeF_3$//HC full cell cycled at C/5 ($NaFeF_3$) and* **(c)** *the relative capacity retention.*

4. Mechanistic study of $NaFeF_3$ cycling towards sodium and lithium

To investigate the structural changes occurring during the charge and discharge processes of $NaFeF_3$ towards sodium and lithium, *ex-situ* and *operando* experiments were performed. Based on the electrochemical behavior of $NaFeF_3$, a two-step insertion mechanism should take place. To characterize possible intermediates such as $Na_{0.5}FeF_3$ and the crystalline phases that the framework adopts after full charge and discharge, the cells were stopped at different states of charge and characterized by XRD (**Figure 5.8**).

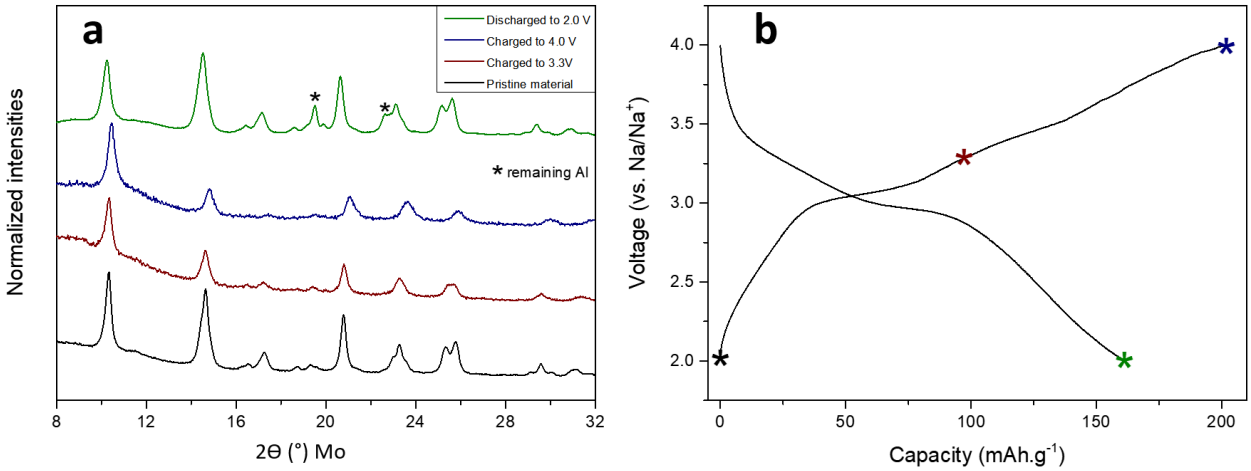

Figure 5.8. **(a)** *Ex-situ XRD experiment of $NaFeF_3$ at different states of charge, cycled at C/20 towards sodium and* **(b)** *relative galvanostatic plot.*

The ex-situ patterns acquired after the charge of the compound at 3.3 V and 4.0 V vs. Na/Na^+ do not present an intermediate of insertion and neither phase transitions, which could be ascribed, for example, to the trirutile $NaFe_2F_6$. The full extraction of sodium out of the crystalline framework follows a solid solution reaction, where the orthorhombic P*nma* structure is transformed into the cubic P*m-3m* FeF_3. The cubic adoption of the crystalline framework is very surprising because this iron(III) fluoride polymorph was reported as unstable under 400 °C. The hexagonal FeF_3, which is the stable polymorph of iron(III) fluoride, is a structure with an organization relative to the R-*3c* space group, where the crystalline framework is denser, due to the twisted bridging Fe-F-Fe bond angles of ~ 150 °, compared to 180 ° of the cubic conformation. As described in the previous chapter, this rhombohedral structure presents narrow channels, allowing the sodium insertion only at a low rate. The adoption of the cubic conformation of $NaFeF_3$ after the full sodium extraction is further confirmed by refinement (**Figure A5.6**). DFT calculations also confirm the high probability of this crystalline framework at the charge state, due to the equivalent thermodynamic stabilities for both polymorphs, namely R-*3c* and P*m-3m* (**Table A5.1**). Additionally, this transformation leads to smaller volume contraction, with only 6.5 % of volume change for the adoption of a structure relative to the *Pm-3m* space group, against 11.5 % in the case of the R-*3c*. During the following discharge, which represents the sodium insertion back in the structure, the perovskite orthorhombic structure is recovered, pointing to reversible dis/insertion processes. To appreciate the structural transformation in more details, and to be sure that no additional mechanisms are involved during the charge and discharge processes, an *operando* measurement

was conducted (**Figure 5.9**, **Figure A5.8** picture of the setup and **Figure A5.8a** full range measurement) [11].

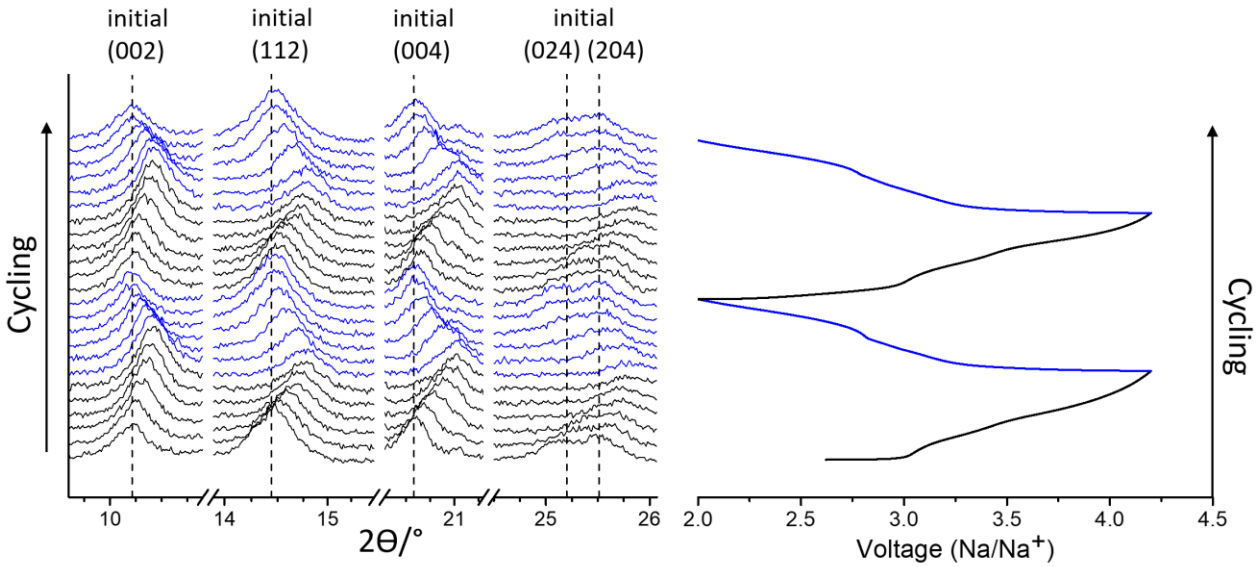

Figure 5.9. *Operando XRD experiment of $NaFeF_3$ conducted at C/20 towards sodium and corresponding galvanostatic plot.*

For the *operando* measurement, a special electrochemical half-cell has been used, with a beryllium plate acting as the current collector for the active material and an X-ray window. In order to obtain appropriate reflection intensities, around 15 $mg.cm^{-2}$ of active material is introduced in the cell. Therefore, a higher potential cutoff was used to buffer the hysteresis created between charge/discharge processes generated by the high mass loading of the active material. Cycling is carried out at C/20 to obtain one diffraction pattern for every 0.05 sodium atoms inserted. During cycling, an obvious increase in the intensity of the reflection related to the plane (002) of the perovskite structure can be noticed, while the reflections related to the planes (112) and (004) have smaller intensities. All the reflections related to the structure shift towards higher diffraction angles. This shift, attributed to the contraction of the structure, is consistent with the volume change between the P*nma* and R-*3c* calculated from the refinement (cf. **Figure A5.2a** and **Figure A5.6**). At higher angles, the reflections related to the planes (024) and (204) around 25.5 ° disappear, whereas a reflection at ~ 26 ° emerges, related to the plane (211) of the P*m-3m* phase, demonstrating a progressive transition between the two crystalline phases. During the reverse step, the patterns related to the discharge process show exactly the same behavior than during the charge. All the reflections shift back to lower diffraction angles, while the intensities of the reflections regain gradually their initial values. During the second cycle, no change in this trend can be observed, confirming a reversible mechanism along the

cycles. Furthermore, the initial pattern of the compound overlaps perfectly with the one corresponding to the crystalline phase state after two cycles, demonstrating a highly reversible process (**Figure A6.8b-c**). The high specific capacities provided during cycling of $NaFeF_3$ could come from the adoption of the cubic conformation, leaving enough room for the sodium ions to be inserted and to diffuse within the crystalline structure. The insertion of sodium, without additional reaction, results in good capacity retentions, due to the high reversibility of this reaction.

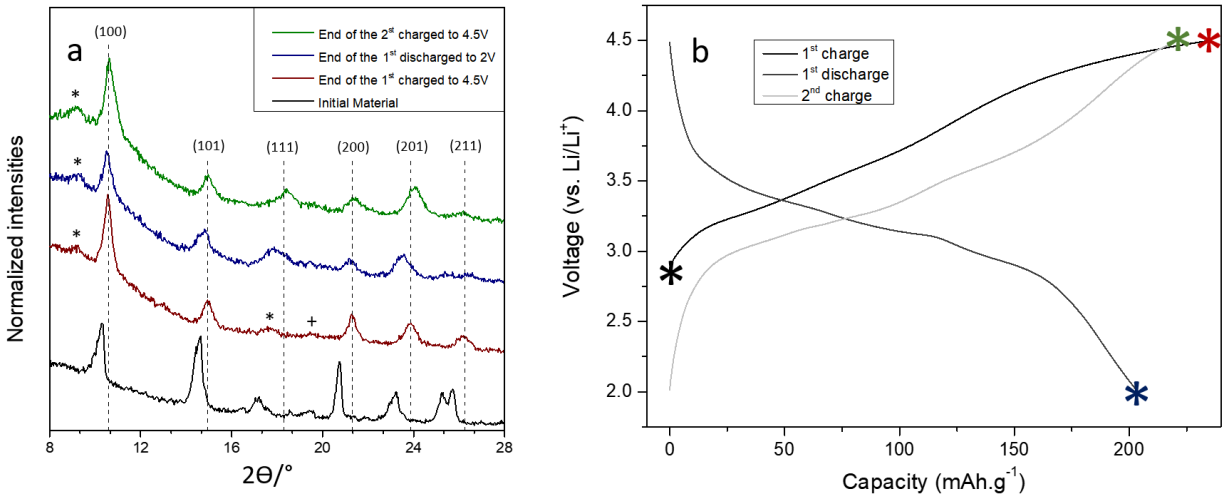

Figure 5.10. (a) *Ex-situ XRD experiment of $NaFeF_3$ at different states of charge, cycled at C/10 towards lithium (* : PVdF ; + : carbon black) and* **(b)** *relative galvanostatic plot.*

As shown in the previous section, $NaFeF_3$ can be cycled at very high current density towards lithium. To understand why this compound demonstrated such an exceptional rate capability, *ex-situ* XRD experiments were performed at the end of different charge/discharge processes (**Figure 5.10**). Similarly to the sodium system, the crystalline framework can endorse the full extraction of sodium, which is not surprising taking in account the relatively low difference of redox potential between the Li/Li^+ and Na/Na^+ couples. The resulting crystalline framework is also ascribed to the cubic P*m-3m* iron(III) fluoride, meaning that the counter electrode has no influence on the initial desodiation process (metallic lithium instead of metallic sodium). During the following discharge, the crystalline framework does not present any conversion, as expected, taking into account the study presented in the previous chapter and the reports in the literature [12]. After the total sodium disinsertion, the reflection related to the plane (100) of the cubic framework does not shift and keeps relatively the same intensity, while the reflections related to the planes (110) and (201) shift slightly to lower diffraction angles along the lithium insertion. The capacity achieved at a current density equals to C/10 is very close to the

theoretical capacity of the compound, representing the full insertion of lithium within the crystalline framework, namely the $LiFeF_3$ composition. Regarding the changes within the XRD pattern of the electrochemically prepared $LiFeF_3$, it can be assumed that the structure adopts a slightly distorted cubic-perovskite framework. During the subsequent lithium extraction, no drastic changes in the XRD pattern can be observed. The peculiar shape, size, and morphology of the as-prepared material drive the crystalline framework to react by a memory effect and induce structural conformation stabilization promoted by specific reaction kinetics. This memory effect enables the prevention of the collapse of the framework through conversion into the trirutile phase, as it should be expected from a thermodynamic point of view. The extraordinary rate capability of $NaFeF_3$ towards lithium can be ascribed to the reaction pathway, which only involves the insertion of lithium within the crystalline framework, induced by a kinetically controlled mechanism. The relatively small size of the lithium ions implies a highly favored diffusivity, which allows extremely fast reaction kinetics. Furthermore, the very small volume changes along the charge/discharge processes provide to the active material a very good capacity retention. These phenomena are summarized and illustrated in **Figure 5.11**. The contrast between the thermodynamic reaction pathway against the kinetically controlled reaction is displayed on the stability diagrams of Na_xFeF_3 and Li_xFeF_3 ($0 < x < 1$). Within these diagrams, the probability that the compound adopts different polymorphs is given depending on the alkali system (**Figure 5.11a**). It can be seen that if thermodynamically pathway would be favored, the $P4_2/mnm$ trirutile phase would be adopted, involving important reorganization of the crystalline structure, whereas the kinetically pathway adopts polymorphs with lower stability. However, the adoption of these polymorphs does not imply drastic reorganization of the crystalline framework. The transition involving small structural changes does not require overcoming high-energy activation barriers, which is not the case for the thermodynamically favored pathway, as illustrated in **Figure 5.11b**. Together with the experimental results, the computational study of the different polymorphs that can adopt the iron(III) fluoride structure along the cycling demonstrates that a kinetic pathway is promoted rather than a thermodynamic one.

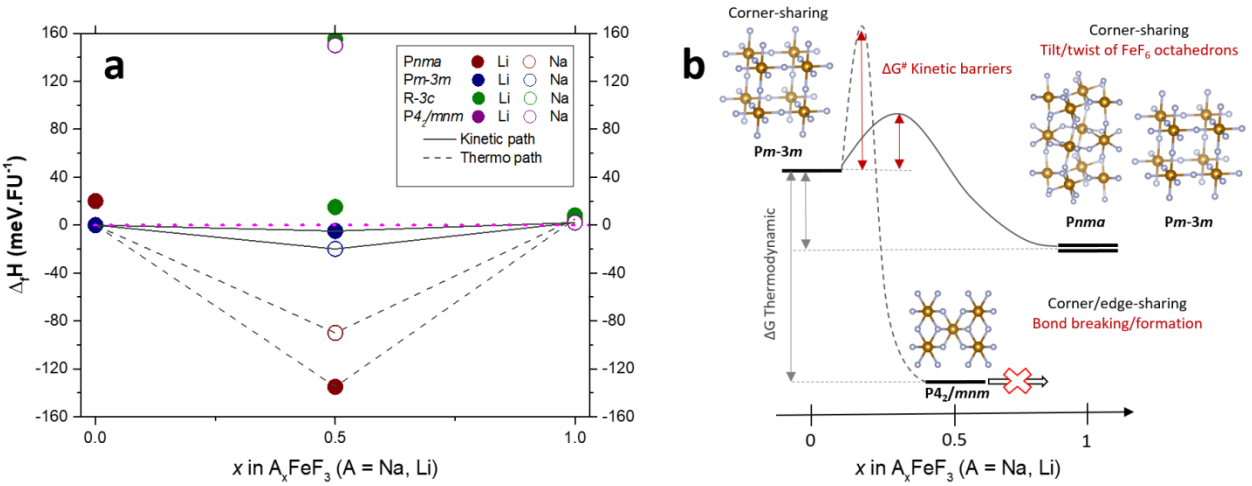

Figure 5.11. *Polymorphism theoretical analysis.* **(a)** *Phase stability diagram of Li_xNaFe_3 (empty circles) and Na_xFeF_3 (filled circles) as computed with spin-polarized DFT+U calculations (U_Fe = 5.3 eV). The formation energies Δ_fH (meV) = $E(A_xFeF_3) - xE(AFeF_3) + (1-x)E(FeF_3)$ are computed with respect to the proportional mixture of the most stable FeF_3 (Pm-3m) and $AFeF_3$ (Pnma) set as the reference energy (horizontal magenta line at zero energy). The initial structures considered in the calculations are $NaFeF_3$ (Pnma), $Li_{0.5}FeF_3$ ($P4_2/mnm$), and FeF_3 (R-3cH, R-3cR, and Pm-3m) from which Li and Na have been removed/added. Only the stable ($\Delta_fH < 0$) and metastable ($0 < \Delta_fH < 160$ meV FU^{-1}) A_xFeF_3 have been reported.* **(b)** *Schematic representation of the kinetic barriers associated with the thermodynamically (dotted lines) and kinetically (full line) controlled electrochemical transformations, together with the local structures of the polymorph stabilized during the reaction (Li and Na are not represented for a sake of clarity) showing that the kinetic path involves "easy" tilt and twist of corner-shared FeF_6 octahedrons all along the reaction, whereas the thermodynamic path involves bond breaking/formation and changes in FeF_6 connectivities.*

5. Conclusion

Different orthorhombic perovskite fluoride compounds were successfully synthesized through the sol-gel fluorolytic method. The one-step reaction of these materials described in this chapter appears as a very versatile route, where the use of transition metal acetates allows the formation of different metal-containing compound ($NaCoF_3$, $NaMnF_3$, $NaFeF_3$, and $NaCo_{1/3}Mn_{1/3}Fe_{1/3}F_3$). However, as this synthesis method involves the reaction of three equivalents of NH_4F with one equivalent of sodium ethoxide and metal acetate, the high concentration of the ammonium ions in the reaction media leads to the formation of the NH_4MF_3 side product. In contrast, the use of nanosized metal difluorides allows the introduction of only one equivalent of ammonium

fluoride, and enables the synthesis of pure $NaFeF_3$ nanoparticles. The obtained nanoparticles show very good reversibility, low hysteresis and high capacities, when used as cathode active material towards sodium. Towards lithium, $NaFeF_3$ achieves outstanding rate capabilities, as well as good capacity retentions. Two distinct plateaus are visible in both systems, even if no specific intermediate of alkali insertion is detected by XRD experiments. The exceptional performances of this compound towards sodium and lithium are due to the cubic conformation that the crystalline framework adopts after the initial sodium extraction. The transition to the cubic conformation, in contrast to the rhombohedral room temperature stable conformation, induces low volume changes, which is beneficial for the reversibility of this process. Furthermore, upon alkali insertion, this crystalline framework host alkali ionic species without dramatic reorganization of the structure, which is not the case when R-*3c* iron(III) fluoride is used as a starting material. From a thermodynamically point of view, the connectivity of the $[FeF_6]$ octahedrons in the crystalline framework should partially change from corner-shared to edge-shared, when $x > 0.5$ in A_xFeF_3 (A = Na, Li). However, due to the high energy barrier that represent these transformations, the reaction of the alkali species only goes through reversible dis/insertion mechanisms, which allows the retention of the crystalline framework. This points to a kinetically promoted reaction pathway rather than a thermodynamically one, resulting in excellent capacity retention and high rate capability of the material.

6. Experimental section

Synthesis of $NaMF_3$ two-step. For the two-step synthesis of the cubic perovskite, nanosized FeF_2 or CoF_2 synthesized in chapter 4 were used as precursors. 6 mmol of the material were dispersed in 30 ml of BnOH in presence of 6 mmol of NaOEt and 6 mmol of NH_4F in a Schlenk tube. After total dispersion/dissolution of the three components, 10 mL of this solution were treated under microwave irradiation at 150 °C for 5 min. After cooling down of the reaction

6. Experimental section

Synthesis of $NaMF_3$ two-step. For the two-step synthesis of the cubic perovskite, nanosized FeF_2 or CoF_2 synthesized in chapter 4 were used as precursors. 6 mmol of the material were dispersed in 30 ml of BnOH in presence of 6 mmol of NaOEt and 6 mmol of NH_4F in a Schlenk tube. After total dispersion/dissolution of the three components, 10 mL of this solution were treated under microwave irradiation at 150 °C for 5 min. After cooling down of the reaction media to room temperature, the particles were precipitated via centrifugation and purified twice in degassed methanol using the same method.

Synthesis of $NaMF_3$ one-step. $Fe(ac)_2$ (6mmol) and NaOEt (6 mmol) were dissolved in the presence of NH_4F (18 mmol) in 30 mL of BnOH in a Schlenk tube. The three components were dispersed using an ultrasonic bath for at least 2 hours. After total dispersion, 10 ml of this solution were treated under microwave irradiation at 150 °C for 5 min. A collection and purification methods similar to the previous synthesis are used. For the preparation of other transition-metal perovskites, the same synthesis was used by replacing the appropriate precursors [$Mn(ac)_2$, and $Co(ac)_2$].

Ball-Milling Process. The collected powders were mixed together with carbon black (CB) by ball milling (planetary mill PULVERISETTE 7) for different times (1 hour, 2 hours, 4 hours and 8 hours) at 750 rpm using zirconia beakers and beads under argon atmosphere. 0.5 g of the powder mix were used for each milling, with a ball to powder ratio of 14:1.

Annexe

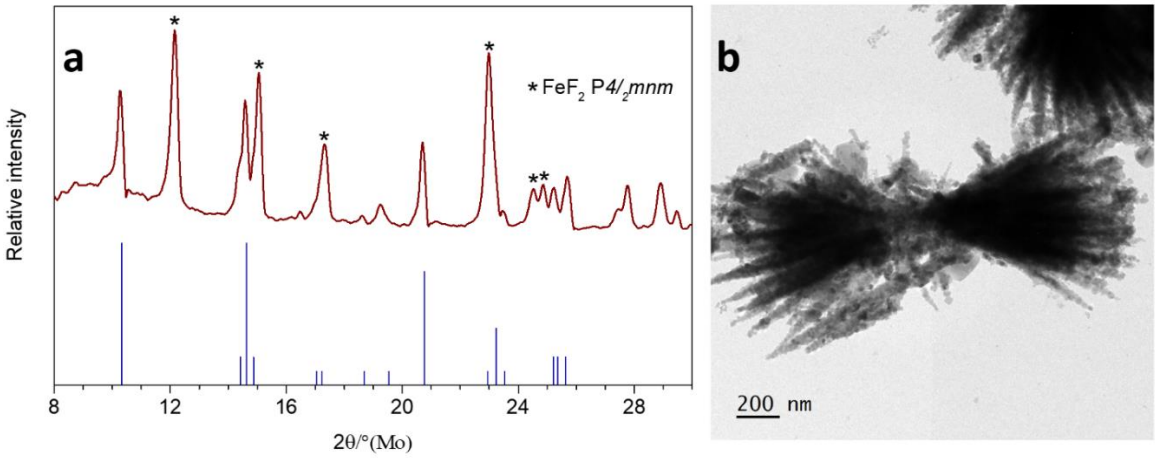

Figure A5.1. (a) *XRD pattern of the compound after fluorination/sodiation of the FeF_2-1 precursor and* **(b)** *respective TEM image.*

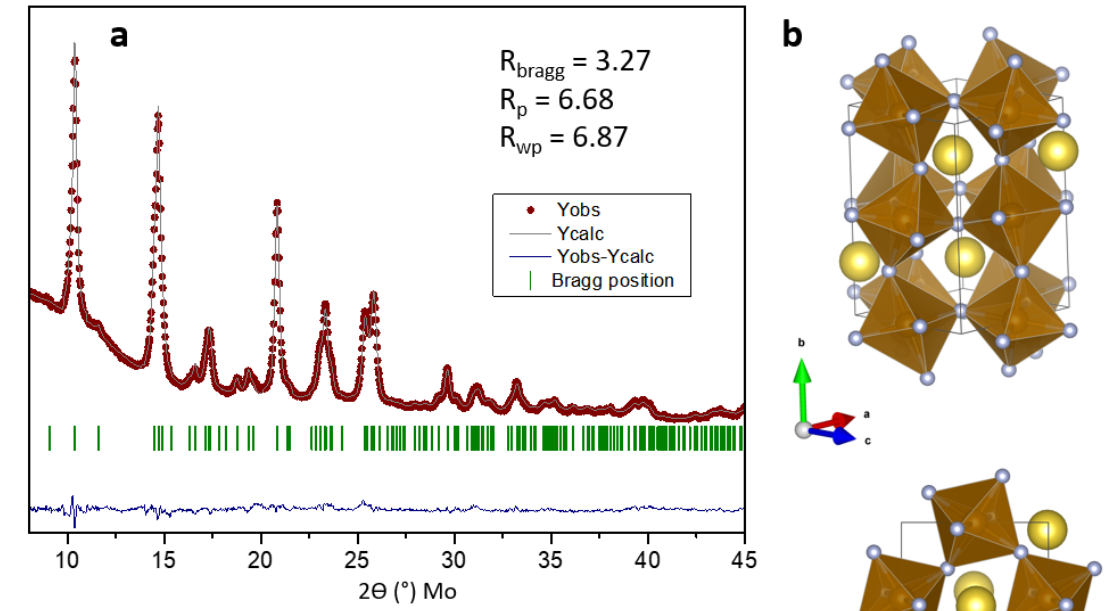

atom	Wyckoff	x	y	z	B_{iso}	occ.
Fe	4b	0.5	0.5	0	0.63	1
Na	4c	0.049	0.25	-0.012	0.98	1
F1	4c	0.457	0.25	0.116	0.98	1
F2	8d	0.196	0.544	0.192	0.98	1

Space group Pmna. Lattice parameters: a = 5.629 Å, b = 7.848 Å, c = 5.465 Å, V = 241.424 Å³

Figure A5.2 (a) *Rietveld refinement of the $NaFeF_3$ compound with refinement parameters and* **(b)** *crystal model with refinement parameters.*

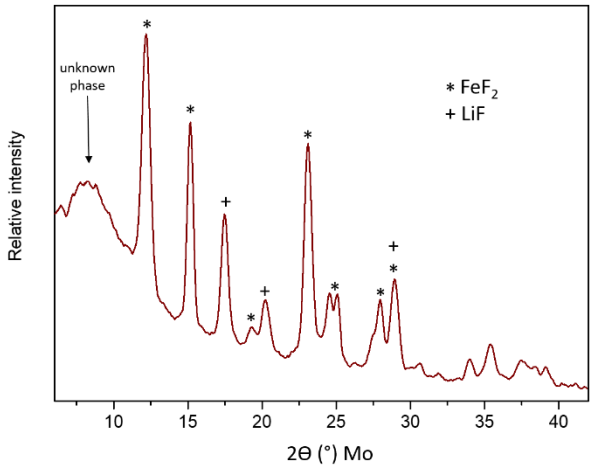

Figure A5.3. *XRD pattern of the compound after fluorination/lithiation of the FeF_2-5 precursor.*

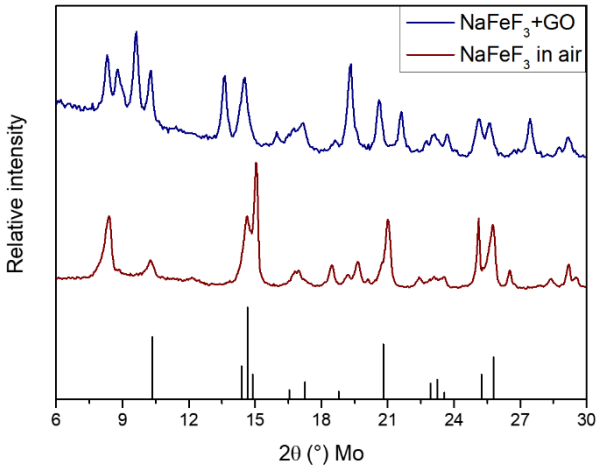

Figure A5.4. *XRD patterns of oxidized compounds of $NaFeF_3$.*

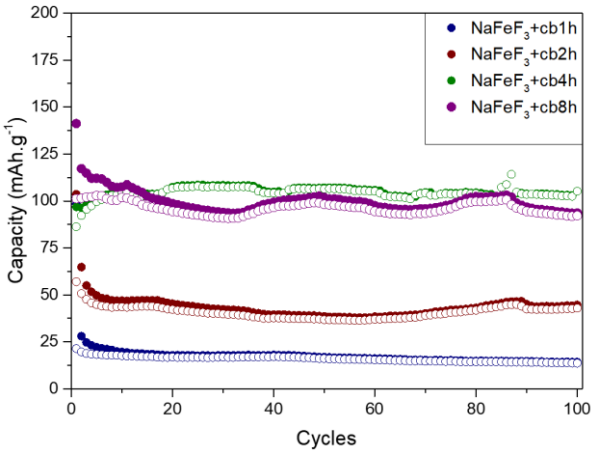

Figure A5.5. *Capacity retentions of $NaFeF_3$ ball-milled with CB for different milling times.*

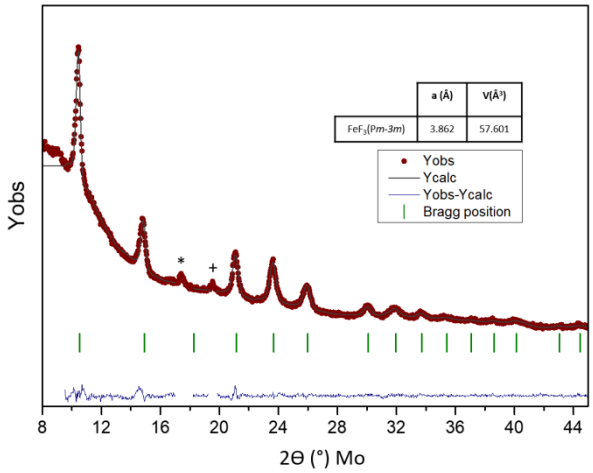

Figure A5.6. *Lebail refinement of the resulting phase of $NaFeF_3$ charged state.*

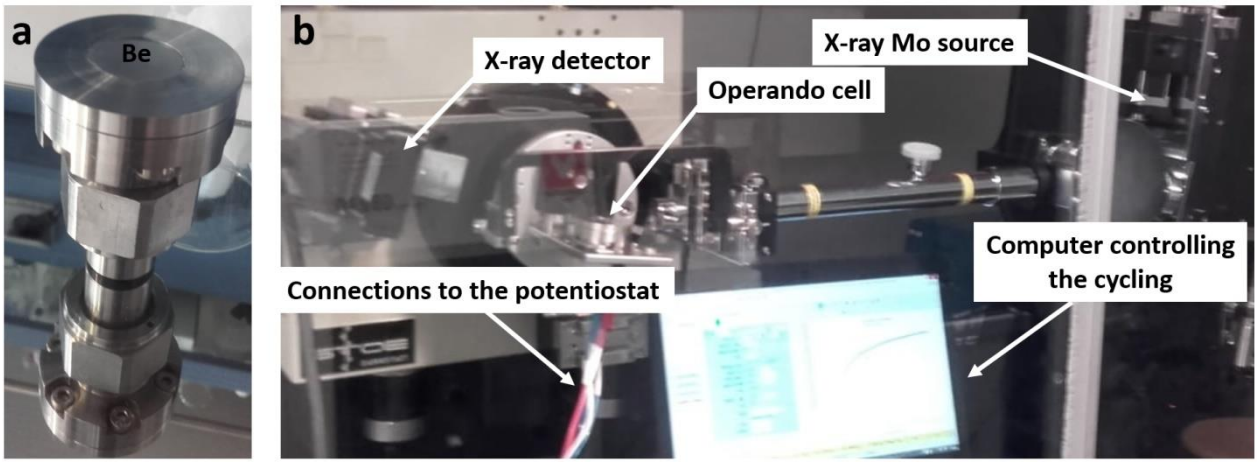

Figure A5.7. *Picture of* **(a)** *the operando half-cell and* **(b)** *the operando set up involving the X-ray diffractometer.*

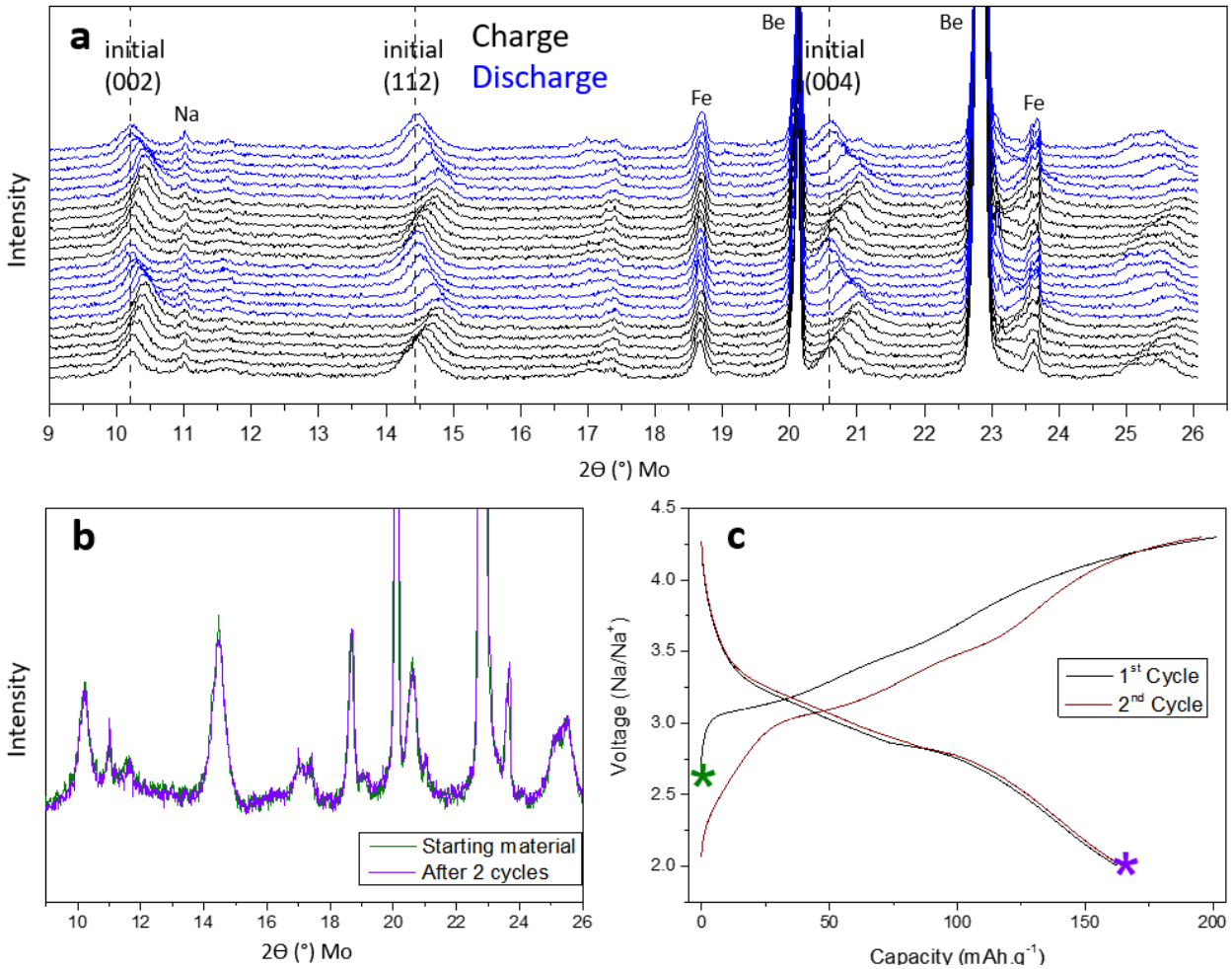

Figure A5.8. (a) *Full range patterns operando measurement.* **(b)** *Initial and final XRD patterns of $NaFeF_3$ after two cycles in operando cell towards sodium and* **(c)** *relative galvanostatic plot.*

	Structure-type	Mag	E - E_{ref} (meV)	Vol (Å^3)
FeF3	**Pm-3m**	**AFM**	**0**	**58.20**
	R-*3cH* ICSD240402	AFM	6.8314	55.35
	R-*3cH* ICSD240394	AFM	8.2780	53.59
	R-*3cR*	AFM	4.7299	53.73
	From P4_2/*mnm* - Li0.5FeF3	AFM	165.4241	52.31
Li0.5FeF3	From P*m-3m* FeF3	AFM	607.1851	63.12
	From P*nma* NaFeF3	AFM	132.6931	54.95
	From R-*3cH* FeF3	AFM	148.3824	55.00
	From R-*3cR* FeF3	AFM	293.5200	59.99
	P4_2/*mnm*	**AFM**	**0.0000**	**52.44**
LiFeF3	From P*m-3m* FeF3	AFM	unstable	
	From P*nma* NaFeF3	**AFM**	**0**	**55.23**
	From R-*3cH* FeF3		unstable	
	From R-*3cR* FeF3		unstable	
	From P4_2/*mnm* Li0.5FeF3	AFM	23.6700	55.56
Na0.5FeF3	From P*m-3m* FeF3	AFM	251.0768	63.14
	From P*nma* NaFeF3	AFM	78.6767	59.33
	From R-*3cH* FeF3	AFM	unstable	
	From R-*3cR* FeF3	AFM	unstable	
	P4_2/*mnm*	**AFM**	**0.0000**	**57.17**
NaFeF3	From P*m-3m* FeF3	AFM		
	P*nma* NaFeF3	**AFM**	**0.0000**	**62.24**
	From R-*3cH* FeF3		unstable	
	From R-*3cR* FeF3		unstable	
	From P4_2/*mnm* Li0.5FeF3	AFM	unstable	

Table A5.1. *Relative energies ($E - E_{ref}$ in meV/FU) and volumes (Å^3) of the A_xFeF_3 phase (A = Li, Na; x = 0, 0.5, 1) as obtained from full structural relaxation in spin-polarized DFT+U calculations. For each composition, the phase associated with the lowest energy is indicated in bold and the phase having converged towards another crystal-type are noted unstable. All structures were found more stable in the antiferromagnetic (AFM) state.*

References

1. Elazari, R.; Salitra, G.; Gershinsky, G.; Garsuch, A.; Panchenko, A.; Aurbach, D., Rechargeable lithiated silicon–sulfur (SLS) battery prototypes. *Electrochemistry Communications* **2012,** *14* (1), 21-24.
2. Rosenman, A.; Markevich, E.; Salitra, G.; Aurbach, D.; Garsuch, A.; Chesneau, F. F., Review on Li-Sulfur Battery Systems: an Integral Perspective. *Advanced Energy Materials* **2015,** *5* (16), 1500212.
3. Liao, P.; Li, J.; Dahn, J. R., Lithium Intercalation in $LiFe_2F_6$ and $LiMgFeF_6$ Disordered Trirutile-Type Phases. *Journal of The Electrochemical Society* **2010,** *157* (3), A355-A361.
4. Dimov, N.; Nishimura, A.; Chihara, K.; Kitajou, A.; Gocheva, I. D.; Okada, S., Transition metal $NaMF_3$ compounds as model systems for studying the feasibility of ternary Li-M-F and Na-M-F single phases as cathodes for lithium–ion and sodium–ion batteries. *Electrochimica Acta* **2013,** *110*, 214-220.
5. Yamada, Y.; Doi, T.; Tanaka, I.; Okada, S.; Yamaki, J.-i., Liquid-phase synthesis of highly dispersed $NaFeF_3$ particles and their electrochemical properties for sodium-ion batteries. *Journal of Power Sources* **2011,** *196* (10), 4837-4841.
6. Kitajou, A.; Komatsu, H.; Chihara, K.; Gocheva, I. D.; Okada, S.; Yamaki, J.-i., Novel synthesis and electrochemical properties of perovskite-type $NaFeF_3$ for a sodium-ion battery. *Journal of Power Sources* **2012,** *198*, 389-392.
7. Sun, S.; Shi, Y.; Bian, S.; Zhuang, Q.; Liu, M.; Cui, Y., Enhanced charge storage of Na_3FeF_6 with carbon nanotubes for lithium-ion batteries. *Solid State Ionics* **2017,** *312*, 61-66.
8. Shakoor, R. A.; Lim, S. Y.; Kim, H.; Nam, K.-W.; Kang, J. K.; Kang, K.; Choi, J. W., Mechanochemical synthesis and electrochemical behavior of Na_3FeF_6 in sodium and lithium batteries. *Solid State Ionics* **2012,** *218*, 35-40.
9. Yu, S.; Zhang, P.; Wu, S. Q.; Li, A. Y.; Zhu, Z. Z.; Yang, Y., Understanding the structural and electronic properties of the cathode material $NaFeF_3$ in a Na-ion battery. *Journal of Solid State Electrochemistry* **2014,** *18* (8), 2071-2075.
10. Kitajou, A.; Ishado, Y.; Yamashita, T.; Momida, H.; Oguchi, T.; Okada, S., Cathode Properties of Perovskite-type $NaMF_3$ (M=Fe, Mn, and Co) Prepared by Mechanical Ball Milling for Sodium-ion Battery. *Electrochimica Acta* **2017,** *245*, 424-429.
11. Sun, N.; Guan, Y.; Liu, Y.-T.; Zhu, Q.; Shen, J.; Liu, H.; Zhou, S.; Xu, B., Facile synthesis of free-standing, flexible hard carbon anode for high-performance sodium ion batteries using graphene as a multi-functional binder. *Carbon* **2018,** *137*, 475-483.
12. Jumas, J.-C.; Sougrati, M. T.; Perea, A.; Aldon, L.; Olivier-Fourcade, J., Combined operando studies of new electrode materials for Li-ion batteries. *Hyperfine Interactions* **2013,** *217* (1), 107-115.
13. Doe, R. E.; Persson, K. A.; Meng, Y. S.; Ceder, G., First-Principles Investigation of the Li−Fe−F Phase Diagram and Equilibrium and Nonequilibrium Conversion Reactions of Iron Fluorides with Lithium. *Chemistry of Materials* **2008,** *20* (16), 5274-5283.

Chapter 6

Synthesis, electrochemical behavior and structural changes of cubic fluoride perovskites

1. Introduction

In the search of new materials for NIBs, the possibility to adapt the positive electrode compounds of LIBs was explored in previous works by several authors [1,2]. However, the close-packed structure of the layered oxides leads to low capacity retentions, due to the low diffusion and the deformation of the inter-layered framework caused by the large size of sodium ions [3]. On the other hand, Na superionic conductor structures (NaSICON) demonstrate extremely high rate capabilities and excellent capacity retentions, but however low specific capacities due to the high molar mass of their polyanionic groups [4]. A third class of compounds active in NIBs is characterized by open structures, such as Prussian Blue analogues (PBAs), belonging to the metal-organic frameworks (MOFs) material class [5]. The specific large channel volumes of these structures permit fast diffusion and dis/insertion processes, conferring high stability and rate capability to these active materials, together with the possibility to use them for KIBs (potassium-ion batteries) [6]. Open structure frameworks frequently contain large size cationic species within the channels of their framework to stabilize it [7]. For instance, ammonium ions have been used in different active materials to expand the crystalline structure, increasing the channel sizes [8]. In the case of $NaFeF_3$, the tilt of around 140 ° of the Fe-F-Fe bridges causes a contraction of the channels [9]. Towards alkali cycling, the crystalline framework adopts a cubic conformation to make the ionic diffusion possible. As described in the previous section, this cubic conformation results in high performances of the material. The incorporation of a larger ion at the A-sites of the perovskite framework stabilizes the cubic conformation, which could be defined as open structure, while smaller ions lead to thermodynamically unstable phases (i.e. $LiFeF_3$). $KFeF_3$, having its crystalline structure relative to the P*m*-3*m* space group, was studied as positive active material and shows good performances, but not as good as the ones reported for $NaFeF_3$ recently [10,11]. These lower performances could be caused by the ball-milling of the micro-sized material under harsh conditions, which creates mechanical strain and decreasing the atomic organization of the crystalline framework. On the other hand, the use of ammonium within fluoride frameworks has not been yet introduced. This chapter focuses on the syntheses of two cubic perovskite fluorides ($KFeF_3$ and NH_4FeF_3) and their electrochemical behavior in

different alkali-ion systems, together with the description of their structural changes during cycling.

2. Synthesis of the cubic perovskite fluorides ($KFeF_3$ and NH_4FeF_3)

In the previous chapter, two different synthetic methods were used in order to obtain $NaMF_3$ compounds, namely a two-step synthesis involving the reaction of an MF_2 precursor in presence of NH_4F and sodium ethoxide, and a one-step synthesis starting from the $Fe(ac)_2$ precursor. The latter was performed by dispersing three equivalents of ammonium fluoride as fluorine source, together with one equivalent of iron(II) acetate and sodium ethoxide. The high concentration of ammonium cations in the synthesis media was leading to the partial generation of NH_4MF_3 as side product. The same synthesis route has been applied to the production of $KFeF_3$, by replacing the sodium ethoxide by potassium ethoxide. When one equivalent of potassium ethoxide to the iron precursor is used, the $KFeF_3$ crystalline structure can be assigned to the P*m*-3*m* cubic perovskite by XRD measurement. However, when energy-dispersive X-ray (EDX) is conducted, the atomic ratios obtained are not in accordance with the stoichiometry of the compound, with a deficit in potassium (**Figure 6.1**). This phenomenon can be explained by the competition between the formation of the phase containing potassium and the phase containing ammonium ions within the A-site of the perovskite structure. Indeed, as the two compounds adopt the same polymorph, the two cationic species seem to be present in the crystal structure forming a solid solution and do not present two distinctive phases. This solid solution between the ammonium and the potassium within the channels of the fluoride framework can be even more easily appreciated when less potassium is used in the synthesis. A clear shift of the reflections to smaller angles is visible, while the reflections related to the planes passing through the A-sites decrease in intensity (examples of the diffraction planes passing through the A-site are displayed on **Figure A6.1**). Those observations are the result of the substitution of the potassium cations by larger ammonium cations, which have a lower atomic form factor. An excess of the KOEt precursor in the synthesis media can shift the balance in favor of the pure potassium phase, as confirmed by EDX. Additional amount of potassium precursor does not lead to the formation of side products. In the case of $NaFeF_3$, a non-stoichiometric amount of NaOEt generates the formation of sodium fluoride. Therefore, in regard of the cubic perovskite fluoride, this synthesis technique is suitable for the production of a potential active material for positive electrodes.

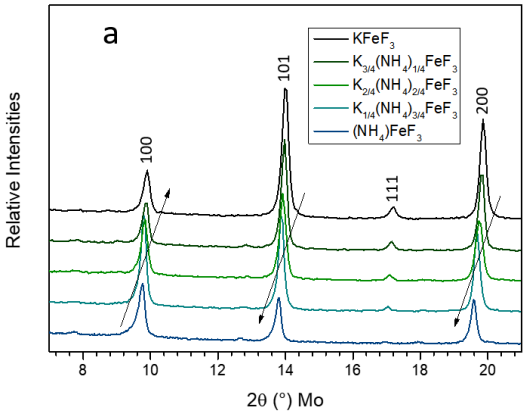

b

	K/Fe reactant molar ratio	K atomic % (EDX)	Fe atomic % (EDX)
NH_4FeF_3	/	0	100
$(NH_4)_{3/4}K_{1/4}FeF_3$	0.25	19.5	80.5
$(NH_4)_{1/2}K_{1/2}FeF_3$	0.5	31.8	68.2
$(NH_4)_{1/4}K_{3/4}FeF_3$	0.75	41.9	57.1
$KFeF_3$	1	45.8	54.2
$KFeF_3$ KOEt excess	1.17	49.6	50.4

Figure 6.1. (a) *XRD patterns of the $K_x(NH_4)_yFeF_3$ compounds and* **(b)** *relative atomic ratios obtained by EDX.*

Similarly to the case of the orthorhombic perovskite compounds, this synthesis can be applied to the formation of other transition metal fluoride perovskites, namely $KMnF_3$ and $KCoF_3$. **Figure 6.2** displays the XRD patterns of these different compounds, as well as their respective TEM images. All these compounds exhibit a crystal structure belonging to the P*m-3m* group. A small shift of the reflections to higher angles can be observed with the increase of the atomic number of the species located within the B-site of the structure. This is due to the contraction of the electronic cloud of the metal along with the increase of its atomic weight. The XRD patterns adopt reflections with similar broadness, which is in accordance with the TEM images of these different compounds. All the materials synthesized through this route present spherical particles with a size ranging between 20 and 40 nm. The manganese compound forms big aggregates of not very defined nanoparticles, while the iron and cobalt compounds exhibit very distinct particles. These compounds could be also synthesized from the two-step synthesis described in the previous chapter, as it is the case for the $KFeF_3$ (**Figure A6.2**). The XRD pattern of the particles presents very broad reflections. The TEM images display very small particles ranging from 5 to 30 nm. This size distribution centered on a small value could be due to the remaining amount of oleylamine on the surface of the FeF_2 precursor. Similarly to $NaFeF_3$, the cubic perovskite compounds demonstrate high sensibility to oxidation and are converted to A_3MF_6 (A= K^+ and NH_4^+, M = Mn^{2+}, Fe^{2+} and Co^{2+}) when they are exposed to air or to oxygen containing species. Therefore, the composite formation of these active materials with carbon structures such as GO is not possible. However, the small sizes of these compounds allow their ball-milling with carbon black under relatively soft conditions, enabling the retention of a good crystalline network and the absence of mechanical strain within the crystal structure. $KFeF_3$ synthesized from $Fe(ac)_2$ was chosen due to the size of the particles, where

the channels of the crystalline structure are more ordered than the smaller particles obtained from FeF_2. The ball-milling process with carbon black does not affect the crystalline phase of the active material and does not drastically decrease the size of the pristine particles, as shown by XRD and TEM measurements (**Figure A6.2**).

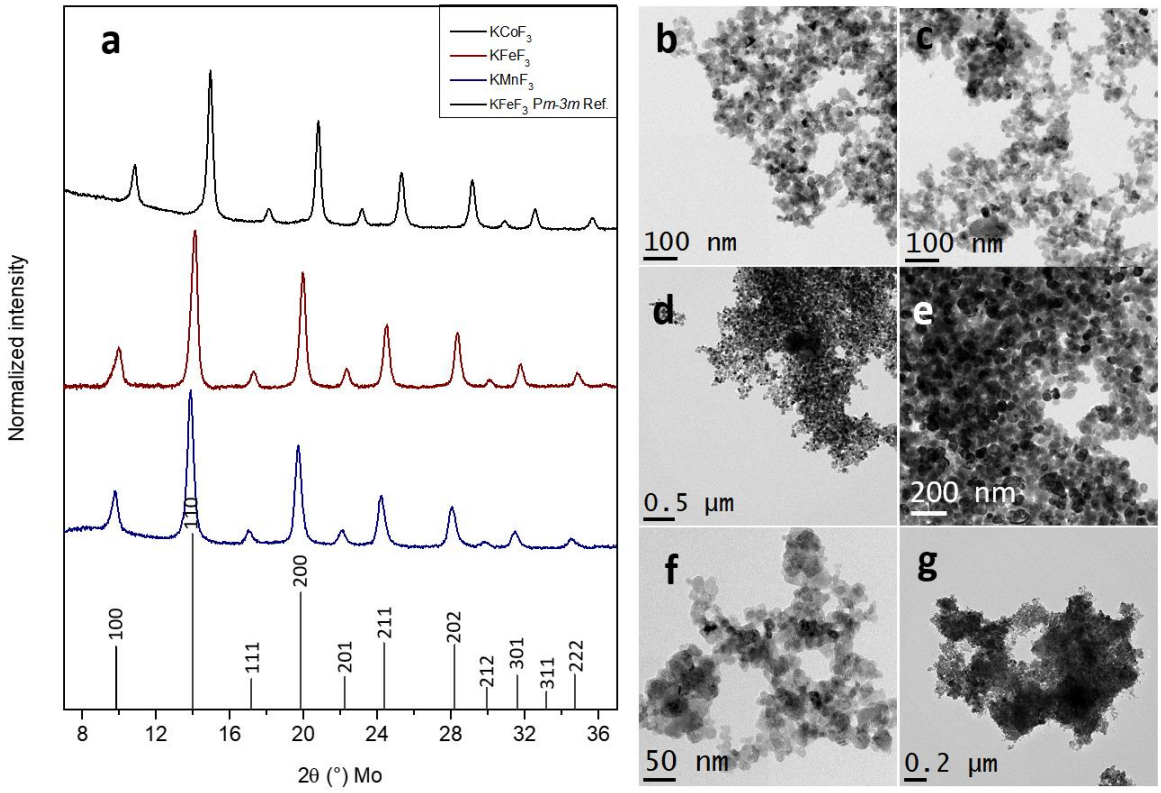

Figure 6.2. (a) *XRD patterns of the $KMnF_3$, $KFeF_3$, $KCoF_3$ cubic perovskite fluoride compounds, and* **(b)-(g)** *respective TEM images.*

When no potassium precursor is present in the synthesis, the product is pure NH_4FeF_3. This compound has the same crystalline structure than $KFeF_3$, but with reflections located at smaller angles due to the higher values of the cell parameters, and differences in intensity. Those different intensities are due to the smaller atomic form factor of the ammonium ions compared to the potassium ions (the atomic form factor, which represents the spatial distribution of an atom, is determined by its atomic number (Z)). This phase can be obtained by using either a one-step or a two-step route. **Figure 6.3** shows the XRD patterns of the products following the two different methods, as well as their corresponding TEM images.

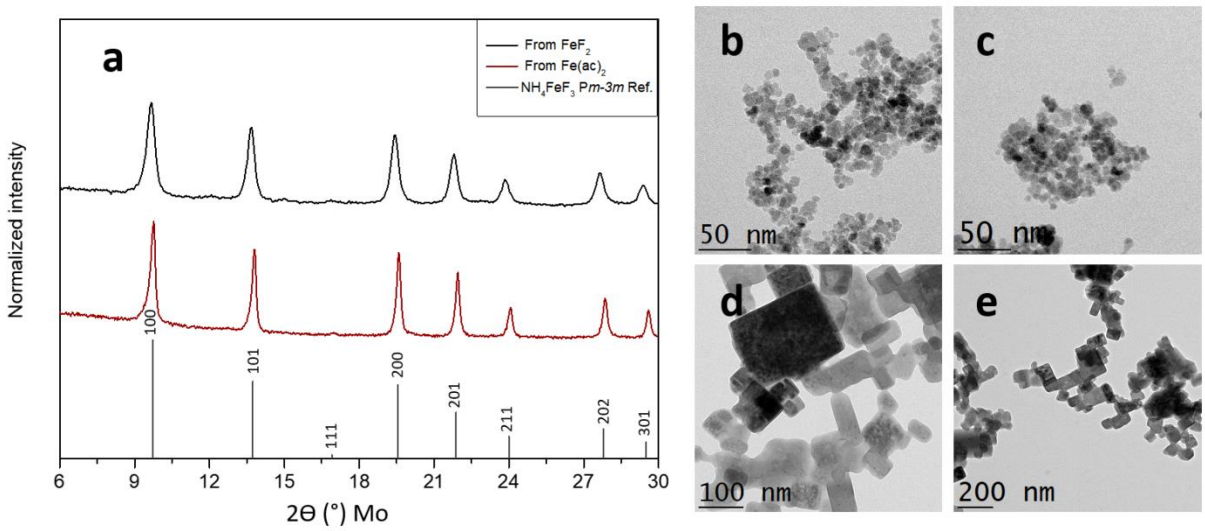

Figure 6.3. (a) *XRD patterns of the $(NH_4)FeF_3$ cubic perovskite fluoride compounds synthesized from FeF_2 nanoparticles and $Fe(ac)_2$, and* **(b)-(e)** *respective TEM images.*

No impurities can be observed from XRD experiments. Comparably, the nanoparticles, obtained by the conversion of the FeF_2 material to the perovskite material by means of ammonium fluoride, show smaller size compared to the product obtained by one-step synthesis, with a value between 5 and 15 nm. Again, the presence of oleylamine in the reaction media is responsible for the small size of these particles. In contrast, when NH_4FeF_3 is obtained from the fluorination of $Fe(ac)_2$ in presence of three equivalents of ammonium fluoride, the particles are noticeably larger, with an average size centered around 50 nm and present a cubic morphology. The XRD pattern of NH_4FeF_3 shows narrower reflections, which suggest that the particles are single crystalline. Similarly to all the perovskite fluoride compounds reported in this thesis, this phase demonstrates oxidation when it is exposed to oxygen or oxygen-containing organic species. Therefore, the active materials synthesized from $Fe(ac)_2$ were ball-milled with carbon black following the same conditions as $KFeF_3$.

3. Electrochemical behavior of the cubic perovskite fluorides ($KFeF_3$ and NH_4FeF_3)

In order to evaluate the performances of the cubic perovskite fluoride compounds, the composites obtained after ball-milling with CB were used as positive active materials in different alkali metal-ion half-cell setups at room temperature. **Figure 6.4a** displays the galvanostatic profile of $KFeF_3$ cycled at a current density of C/10 (17.6 $mA.g^{-1}$) towards sodium. The first charge of this compound shows a different behavior compared to the subsequent ones because of the different nature of the initial cation extraction. This initial process represents the disinsertion of the potassium ions out of the crystalline framework and is illustrated by a sloped curve showing flatter potential at high voltage, demonstrating a higher capacity than the expected theoretical one. This high redox potential compared to the sodium disinsertion within $NaFeF_3$ can be explained by the larger atomic radius of potassium, inducing higher energy activation for this process. The extra capacity observed when the half-cell is cycled up to 4.5 V vs. Na/Na^+ is related to the decomposition of the electrolyte onto the surface of the fluoride nanoparticles. The following discharge shows a sloped plateau between 3.5 V and 2.5 V for a capacity of around 180 $mAh.g^{-1}$. As no side reaction is expected during the discharge of $KFeF_3$ down to 2.0 V, the obtained discharge capacity represents the full insertion of sodium ions within the fluoride framework. Similarly to $NaFeF_3$, from the second cycle, clear plateaus can be observed at 3.0 V and 3.3 V with a net capacity decrease. Those pronounced plateaus are still visible after the 50^{th} cycle, but the remaining capacity is only 60%, caused by low columbic efficiency between the charge and discharge processes. The cyclic voltammetry displays a similar trend with a first anodic wave represented by an increasing current signal close to the cutoff potential. During the subsequent cycles, clear waves can be observed at 3.3 V and 2.8 V towards the cathodic direction and at 3.0 V and 3.5 V towards the anodic direction. It can be noticed that the cathodic peak located at 3.3 V is less pronounced than the one at 2.8 V (**Figure 6.4b**). From those results, it can be assumed that the sodium dis/insertion occurs in a similar way than starting from $NaFeF_3$. The larger hysteresis observed here could come from the back insertion of the potassium ions present in the electrolyte after the first charge. This compound demonstrates very good rate capabilities towards sodium, with up to 140 $mAh.g^{-1}$ at 1C (~ 80 % of the theoretical capacity) and 120 $mAh.g^{-1}$ at 5C (~ 70 %). These high rate capabilities can be ascribed to the large channels that the $KFeF_3$ cubic perovskite structure presents. However, the material has low capacity retention, with about only half of the capacity remaining after 100 cycles, independent of the current density used. The low capacity retentions that this compound exhibits is due to the high cutoff potential used

during the charge inducing the decomposition of the electrolyte. When lower charge cutoff potentials are employed, the material demonstrates lower discharge capacities caused by the incomplete disinsertion of the potassium ions (**Figure A6.3**). Varying the composition of the electrolyte used in the half-cells would influence the side reactions related to the decomposition of the electrolyte on the fluoride material. **Figure 6.4d** displays the capacity retentions of the active material cycled within different electrolyte compositions. Changing the organic solvents of the electrolyte does not influence too much the capacity retention, while exchanging the salt from $NaClO_4$ to $NaPF_6$ improves it slightly. However, lower capacities are achieved with these electrolyte compositions compared to one normally used for the electrochemical test in the sodium system.

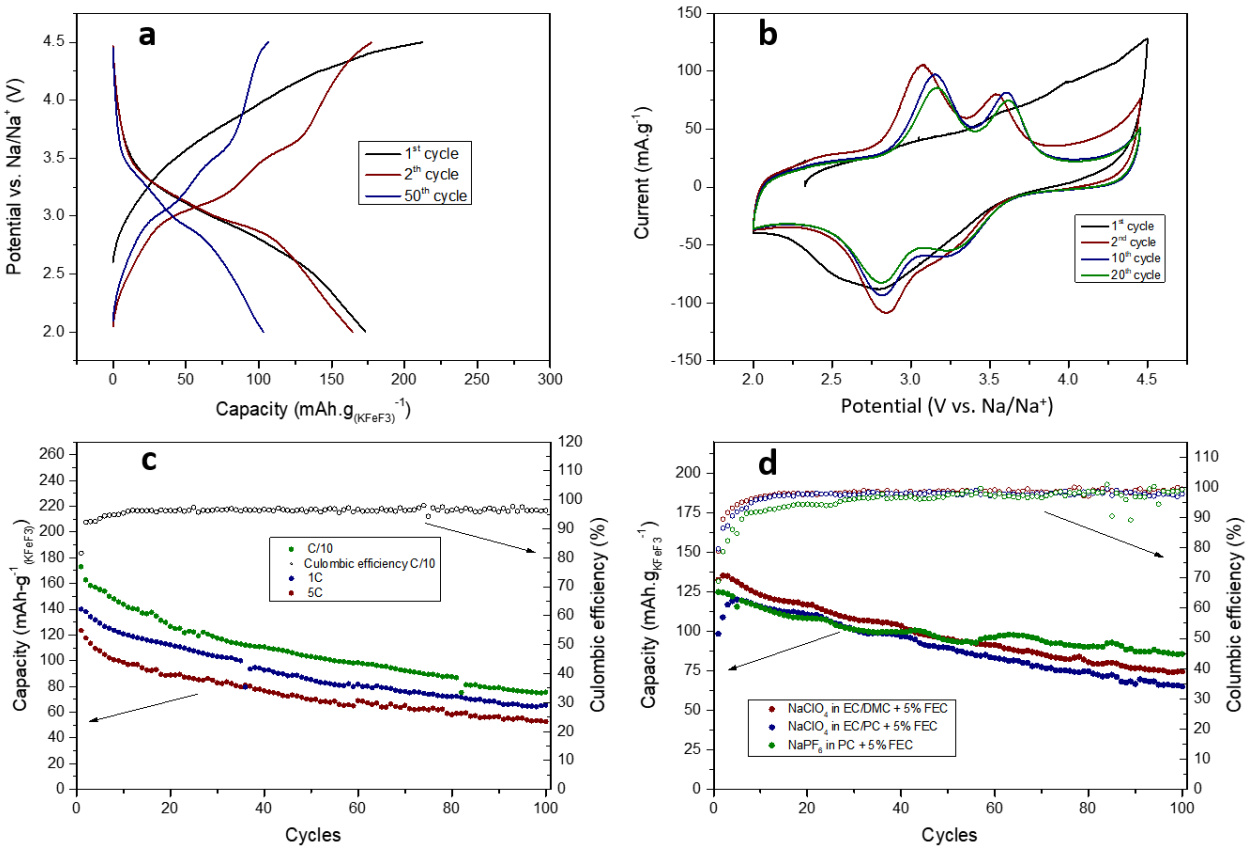

Figure 6.4. (a) *Galvanostatic plot of $KFeF_3$ cycled at C/10 towards sodium.* **(b)** *Cyclic voltammetry experiment of $KFeF_3$ at a scan rate of 0.1 $mV.s^{-1}$ towards sodium.* **(c)** *&* **(d)** *Capacity retentions of $KFeF_3$ at different current densities and using different electrolyte systems.*

$KFeF_3$ can be successfully cycled towards lithium as well. Similarly to the sodium system, the first charge process represents the disinsertion of the potassium ions from the crystalline framework and displays a higher redox potential than the first sodium extraction of $NaFeF_3$

when cycled towards lithium (**Figure 6.5a**). Additional capacity is also observed in this case, due to the decomposition of the electrolyte induced by the high cutoff potential used. In contrast to the cycling towards sodium, the following discharge/charge processes are very similar. Namely, from the first discharge, a plateau can be observed between 3.5 V and 3.0 V vs. Li/Li^+ for a capacity representing the full insertion of one lithium atom per formula unit (~176 $mAh.g^{-1}$). During the charge, a similar plateau can be seen in the same region, exhibiting very low hysteresis between the two processes. The cyclic voltammetry experiment exhibits a first anodic wave with maximums at ~ 3.5 V and 4.3 V, which represent the disinsertion of the potassium ions and the decomposition of the electrolyte, respectively (**Figure 6.5b**). During the subsequent cycles, only one peak can be observed along the cathodic and anodic direction, respectively at 2.8 V and 3.3 V. The presence of only one redox peak translates into that the dis/insertion of lithium after the initial potassium extraction occurs through one single insertion reaction. The large channels of the cubic structure can easily accommodate the small-size alkali ions, in comparison with cycling towards sodium where two redox processes are observed. Small peaks at high potential are noticed, which represent the decomposition of the electrolyte. As the redox potential of sodium and lithium are different from ~ 0.2 V vs. SHE, the potential applied during the charge in the lithium system is lower than in the sodium system. Therefore, when $KFeF_3$ is cycled towards lithium, the decomposition of the electrolyte occurs at higher potential. Indeed, the active material demonstrates slightly better capacity retention in the lithium system, with 75 % of the initial capacity after 100 cycles at C/10 against 50 % towards sodium cycled at the same current density, even though the columbic efficiency of the active material is around 95% after the 10 first cycles (**Figure 6.5c**). In this system, $KFeF_3$ exhibits outstanding rate capability, with up to 75 % of the theoretical capacity at a current density of 5C and 33 % at 40C. These values are higher than the ones achieved by $NaFeF_3$ cycled under the same conditions. These superior performances are ascribed to the open structure that presents $KFeF_3$ after the initial extraction of potassium out of the crystalline framework.

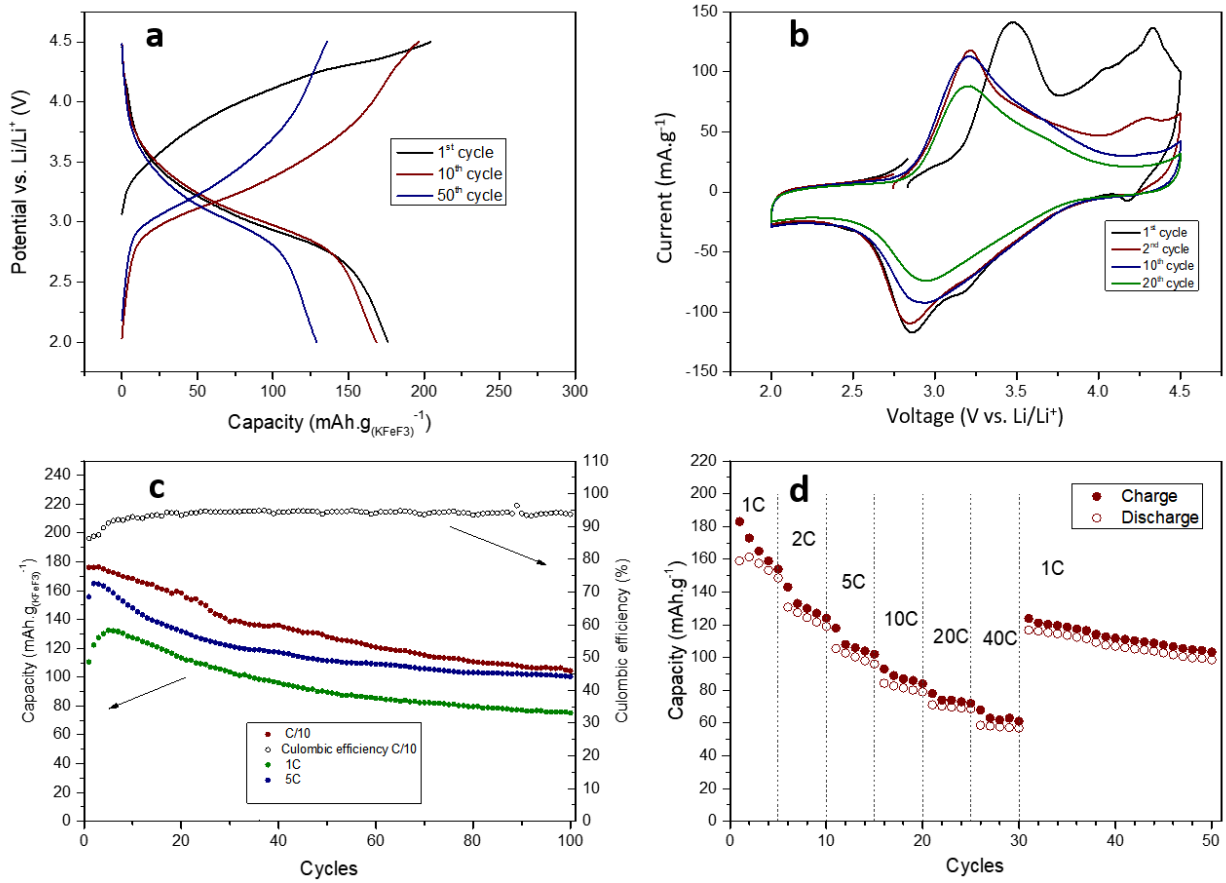

Figure 6.5. (a) *Galvanostatic plot of $KFeF_3$ cycled at C/10 towards lithium.* **(b)** *Cyclic voltammetry experiment of $KFeF_3$ at a scan rate of 0.1 $mV.s^{-1}$ towards lithium.* **(c)** *&* **(d)** *Capacity retention of $KFeF_3$ at different current densities.*

In contrast to $KFeF_3$, NH_4FeF_3 has only been reported as negative electrode material reacting through a conversion reaction at low potentials, as it is the case for the metal difluorides or iron trifluoride [12]. So far, its activity towards alkali insertion has never been described. The compound needs to undergo first the extraction of the ammonium ions out of its crystalline framework to accept the alkali ions. Recently, Wu *et al.* reported the possibility of implementing a rocking-chair system working on the shuttle of ammonium between layered structured materials, such as PBAs [13]. However, in the literature, the dis/insertion of this cation was never studied in alkali-ion systems. Here is described for the first time the disinsertion mechanisms of ammonium ions from a crystalline structure in different alkali-ion systems. **Figure 6.6a** shows the galvanostatic profile of the cubic ammonium iron trifluoride cycled at C/10 (20.6 $mAh.g^{-1}$) towards sodium. As observed in the case of $KFeF_3$, the disinsertion of the ammonium ions is represented by a sloped curve between 3.5 V and 4.5 V vs. Na/Na^+ with higher capacity than the theoretical one (206 $mAh.g^{-1}$). Similarly to the previous cases, this extra capacity comes from the decomposition of the electrolyte at high cutoff potential, but in

a less pronounced way with this active material. It is worth noting that it is the first time that the extraction of this cation is demonstrated for a non-aqueous alkali-ion system. After the initial ammonium disinsertion, the first discharge displays up to 182 $mAh.g^{-1}$, which represents ~ 0.9 sodium atom inserted per formula unit. The discharge processes seem to start from 3.5 V, but do not present any pronounced plateau. Similarly to the discharges, sloped curves can be observed for the charges. At a higher current density, the active material demonstrates similar profiles (**Figure 6.6b**).

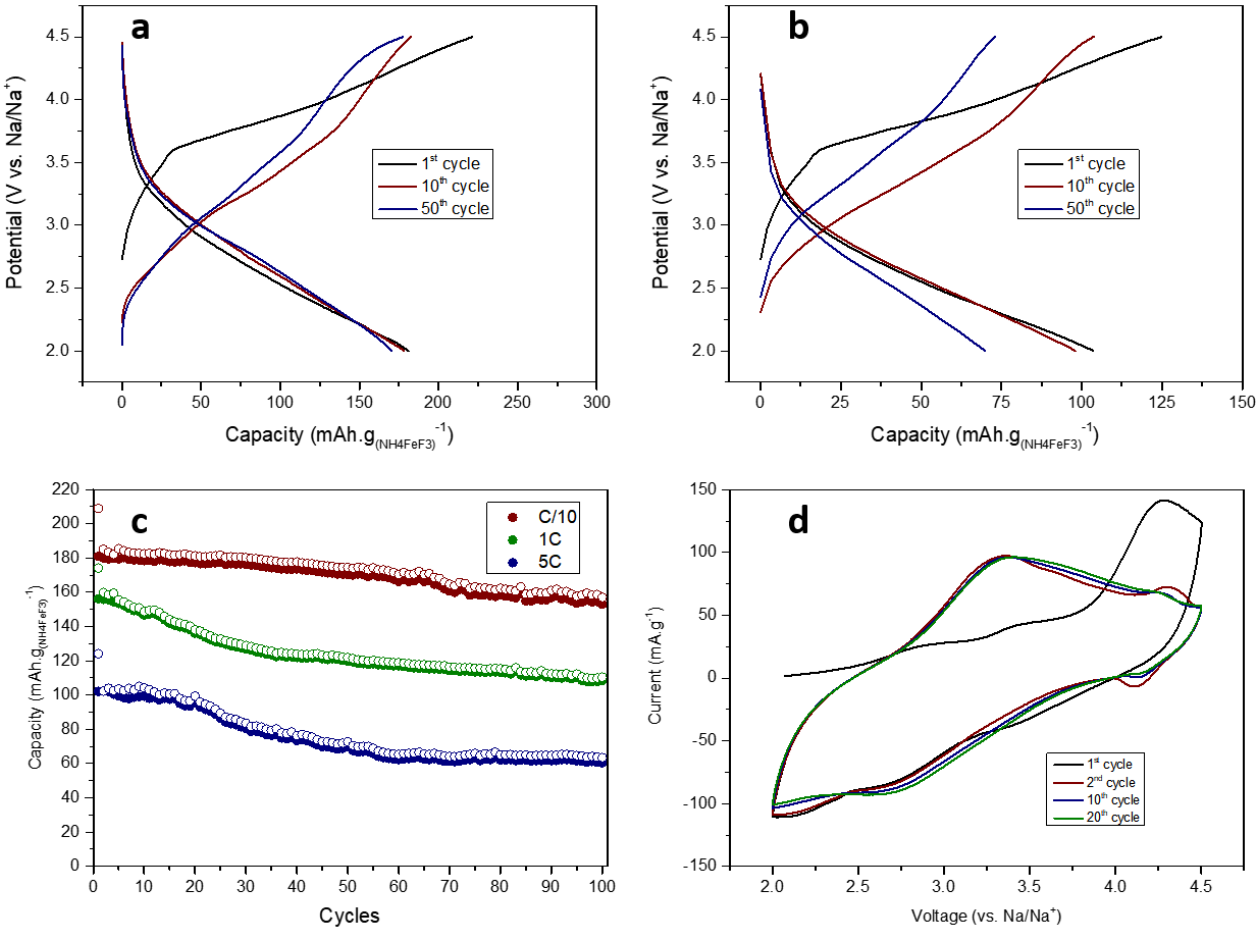

Figure 6.6. (a) *Galvanostatic plot of NH_4FeF_3 cycled at C/10 and* **(b)** *at 5C towards sodium.* **(c)** *Capacity retentions of NH_4FeF_3 at different current densities.* **(d)** *Cyclic voltammetry experiment of NH_4FeF_3 at a scan rate of 0.1 $mV.s^{-1}$ towards sodium.*

NH_4FeF_3 presents good capacity retention when cycled at C/10 with 90 % of capacity remaining after 100 cycles, but worse capacity retention when cycled at higher current, with 64 % at 1C and 60 % when cycled at 5C (**Figure 6.6c**). The initial wave observed along the anodic direction of the cyclic voltammetry shows a peak with a maximum at 4.2 V, while during the subsequent cycles, no clear peaks can be observed along the cathodic direction and a broad

wave at 3.3 V along the anodic direction can be seen, which is relevant with the observation from the galvanostatic profile (**Figure 6.6d**).

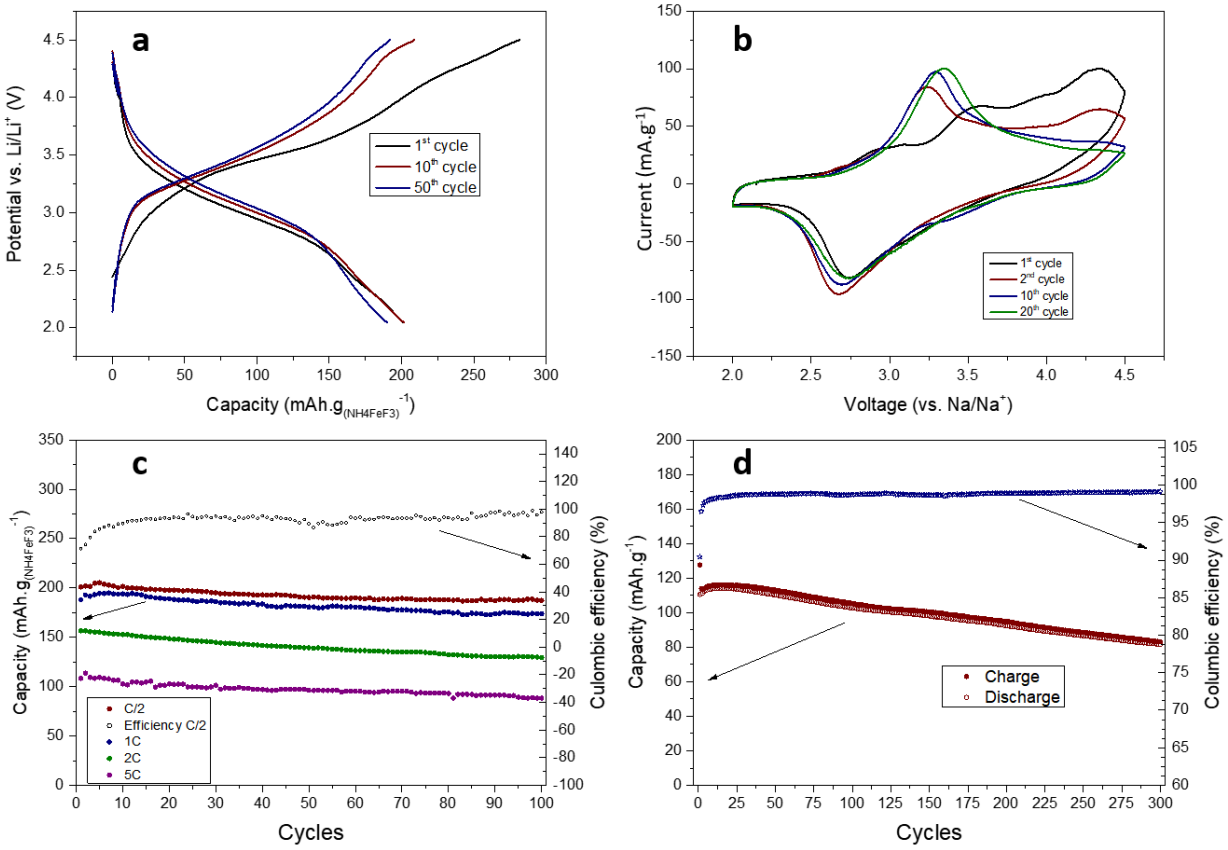

Figure 6.7. (a) *Galvanostatic plot of NH_4FeF_3 cycled at C/10 towards lithium.* **(b)** *Cyclic voltammetry experiment of NH_4FeF_3 at a scan rate of 0.1 mV.s^{-1} towards lithium.* **(c)** *Capacity retentions of NH_4FeF_3 at different current densities and* **(d)** *at 5C during extended cycling.*

Towards lithium, this material shows higher capacity than towards sodium, with a first columbic efficiency of ~ 70 % at a current density of C/10. The redox plateau of the ammonium extraction is also more pronounced with a noticeable flat region between 3.3 V and 3.7 V vs. Li/Li^+. The following discharge exhibits 210 mAh.g^{-1}, which represents the full lithium insertion within the structure. In contrast to the sodium system, a clear plateau can be observed between 3.4 V and 2.9 V for the discharge processes, while the plateau is located between 3.1 V and 3.7 V during the charge, without drastic changes of the profile along the cycles. The cyclic voltammetry experiment is depicted in **Figure 6.7b**. During the first anodic process, a wave of small intensity can be seen around 3.0 V, followed by more pronounced peaks at 3.5 V and 4.2 V, which represent the extraction of the ammonium cation from the fluoride framework. As it has been seen on the galvanostatic profile, only one redox peak is present during the subsequent cycles, pointing to a single reaction of lithium with the fluoride material.

No obvious peaks related to the decomposition of the electrolyte can be observed at high potential, probably due to the higher stability of the electrolyte towards NH_4FeF_3. The material presents good rate capability and delivers 160 mAh.g^{-1} at 2C and up to 110 mAh.g^{-1} at 5C, with a capacity retention of 94 % when cycled at C/10 after 100 cycles and 74 % when cycled at 5C after 300 cycles.

These cubic iron perovskite fluorides can be effectively cycled towards potassium, as shows **Figure 6.8**. The large channels that these structures present can allow the diffusion of the larger potassium ions. The $KFeF_3$ composite delivers 126 mAh.g^{-1} when cycled at a current density of C/10 and demonstrates a capacity retention of around 50 % after 50 cycles. Similarly to the cycling of the different perovskite compounds towards sodium, the charge/discharge profile exhibits two regions, with one first sloped plateau centered at 3.3 V and a second one more pronounced starting from 2.7 V vs. K/K^+. The large hysteresis between the charge and discharge processes leads to low columbic efficiency, partially responsible for the low capacity retention. A comparable galvanostatic profile is observed in the case of NH_4FeF_3, with two specific regions in the 4.4-2.0 V potential window. Nevertheless, a flat potential can be seen at high potential during the charge, which is commonly related to side reactions involving the decomposition of the electrolyte. This flat plateau decreases slightly along the cycles, inducing a columbic efficiency of ~70 % at the first cycle and ~ 90 % at the 20th cycle. Hysteresis is here even more pronounced than the potassium-containing phase. These phenomena lead to very low capacity retention for this compound in the potassium system. It is worthy to stress that the rhombohedral iron(III) fluoride material was not active at all towards potassium, due to the tight channels that such structure possesses.

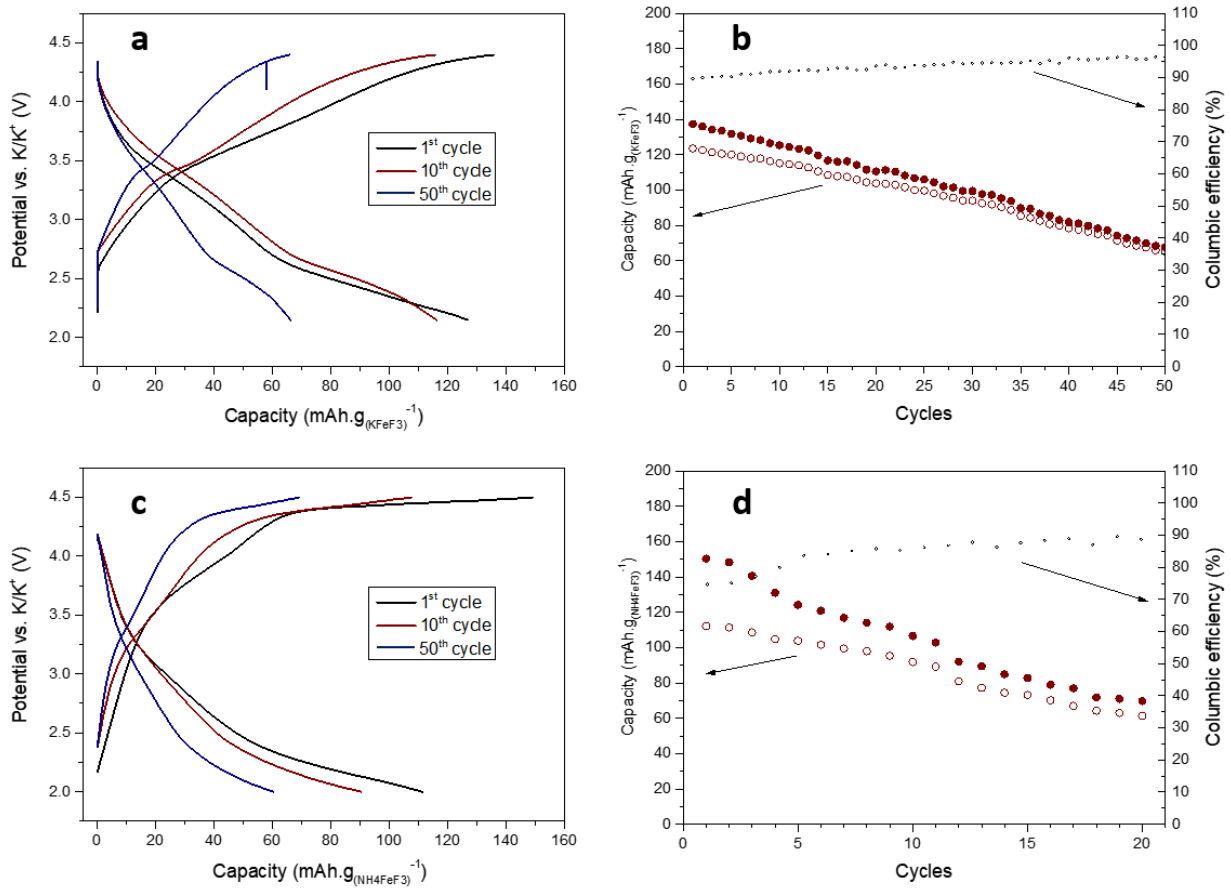

Figure 6.8. (a) *and* **(c)** *Galvanostatic profiles of $KFeF_3$ and NH_4FeF_3 cycled at C/10 towards potassium,* **(b)** *and* **(d)** *relative capacity retentions, respectively.*

4. Structural changes during the dis/insertion processes of alkali ions in cubic perovskite fluorides

In order to better understand the mechanisms responsible for the performances of the cubic perovskite fluorides, a systematic *ex situ* XRD study was conducted on the electrode materials at different states of charge. **Figure 6.9a** shows the *ex situ* XRD patterns relative to $KFeF_3$ cycled in the sodium systems. Towards sodium, the material in its charge state has a very similar crystal structure compared to the starting compound. Upon the extraction of the potassium ions, the crystalline framework is preserved and the intensities related to the planes passing through the A-site decrease, namely the reflections (101), (111), (200) and (211) (**Table A6.1a**). Those reflections decrease due to the removal of potassium from the A-sites of the perovskite structure. A slight shift of the pattern to high angles can be observed, pointing to a small contraction of the unit cell (V = 68.01 $Å^3$ compared to V = 69.02 $Å^3$). After the full extraction of potassium from the $KFeF_3$ structure, the composition of the electrode material is FeF_3. However, as mentioned in chapter 4 of this thesis, the stable conformation of iron(III)

fluoride at room temperature is the rhombohedral one. This cubic conformation is similar to one reported in the previous chapter when sodium ions were totally extracted from $NaFeF_3$. If the structure would adopt the rhombohedral structure at the end of the charge, the insertion of alkali species would either pass through conversion reactions (in the case of lithium), or not be possible in view of the too large size of the cationic radii (in the case of sodium and potassium). It is worth noting that the cubic FeF_3 obtained from the potassium-containing compound presents larger unit cell than in the case of $NaFeF_3$. The diffractogram corresponding to the end of the following discharge adopts a pattern analog to the $NaFeF_3$ P*nma* structure. The active material adopts this conformation directly after the insertion of 0.5 sodium atoms per formula unit (**Figure A6.4**), which supports the typical two-step plateaus present during the charge/discharge processes of the material towards sodium. However, the reflections observed from the sodiated state of $KFeF_3$ are located at smaller angles compared to the reference of the $NaFeF_3$ phase, which points to a larger unit cell. The larger cell volume is attributed to the back insertion of potassium ions present in the electrolyte after the first charge or remaining potassium atoms in the crystalline structure ($V(\text{sodiated } KFeF_3) = 275$ Å^3 vs. $V(NaFeF_3) = 241$ Å^3). A clear broadening of the reflections can be seen after sodium insertion, which represents the decrease of the size of the crystallites. In the lithium system (**Figure 6.9b** and **Table A6.1b**), upon the extraction of potassium ions from the crystalline framework, the structure behaves similarly as during the first charge towards sodium, namely the cubic conformation is adopted together with a slight contraction of the structure. The diffractogram corresponding to the lithiated $KFeF_3$ presents minor changes in reflection intensities, probably due to the low atomic scattering factor of lithium compared to potassium. During these processes, all the reflections also undergo a clear broadening, demonstrating a decrease of the size of the crystallites upon potassium extraction and lithium insertion. A slight expansion of the framework can also be observed ($a = 4.081$ Å compared to $a = 4.061$ Å). As discussed previously, the adoption of this cubic conformation prevents the collapse of the crystalline structure, avoiding the conversion between the crystal framework and lithium. The excellent rate capabilities demonstrated by this compound in both sodium and lithium system are attributed to the maintaining of the crystalline framework along the charge/discharge processes, avoiding big volume changes and offering large channels for the sodium and lithium ions to diffuse.

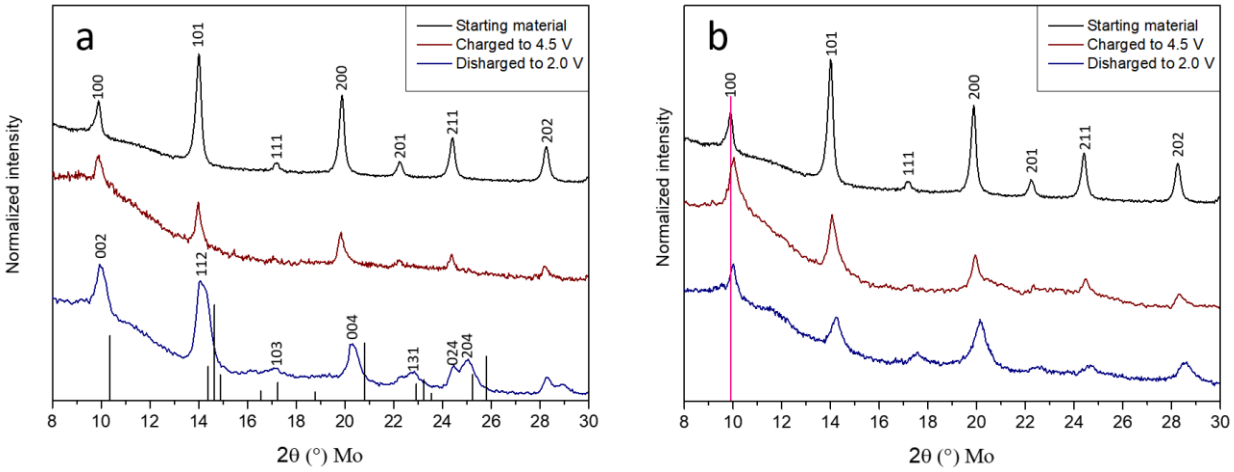

Figure 6.9. *Ex situ XRD patterns of $KFeF_3$ cycled at C/20* **(a)** *towards sodium and* **(b)** *towards lithium.*

When $KFeF_3$ is cycled towards potassium at low current density (C/20), 147 $mAh.g^{-1}$ of reversible capacity can be obtained at the first cycle with a columbic efficiency of 93 %, which represents the reaction of 0.8 atoms of potassium per formula unit. The two-step redox mechanism involved during the potassium insertion does not induce the formation of an intermediate phase, as suggested by the *ex situ* XRD patterns, but rather a solid-solution reaction, similarly to the sodium and lithium systems. At the end of the charge, the unit cell presents a small volume contraction due to the removal of the potassium ions (V = 67.23 $Å^3$ compared to V = 69.02 $Å^3$) (**Figure 6.10** and **Table A6.1c**). Similarly to the previous case, the intensities related to the planes passing through the A-site of the perovskite structure decrease upon potassium extraction, while they increase after the reinsertion of the potassium ions. After the reinsertion of potassium, the pattern goes back to its initial position, which implies the high reversibility of the dis/insertion of potassium within the cubic structure. However, $KFeF_3$ suffers from low capacity retention at higher current densities, which can be attributed to large hysteresis between the charge and discharge processes, as well as the instability of the electrolyte towards the fluorine material when high cutoff potentials are applied.

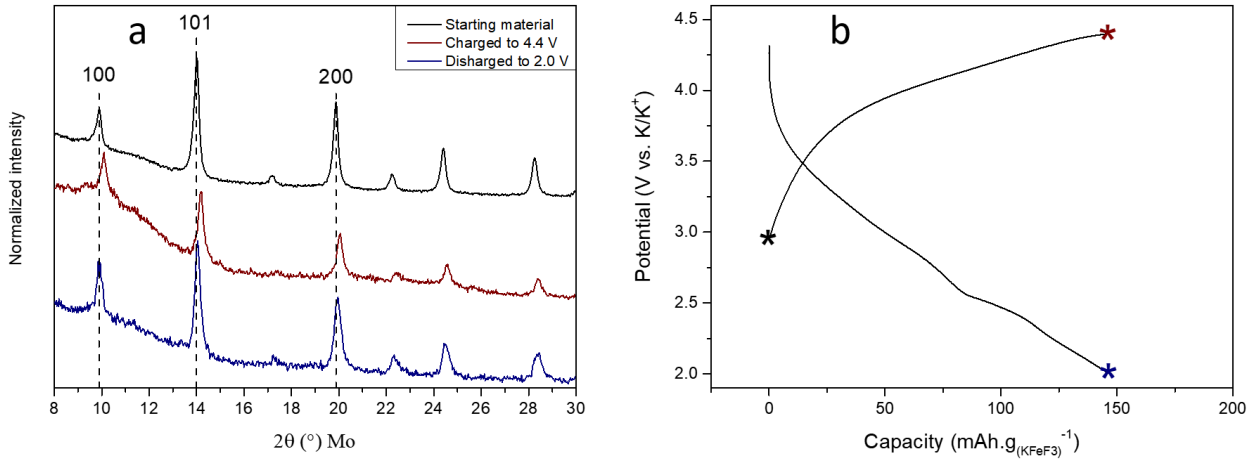

Figure 6.10. (a) *Ex situ XRD patterns of $KFeF_3$ cycled at C/20 towards potassium and* **(b)** *relative galvanostatic profile.*

In the lithium system, the crystalline structure of NH_4FeF_3 undergoes high amorphization after the first charge (**Figure 6.11a** and **Table A6.1d**). The whole reflection pattern shifts to higher angles, which points to the contraction of the unit cell caused by the extraction of the NH_4^+ ions ($V = 69.62$ Å^3 compared to $V = 74.72$ Å^3). This contraction is larger than the ones observed for $KFeF_3$, mainly due to the larger ionic radii of the ammonium ions. Upon lithium insertion, a slight increase of the cell parameters can be noticed, but no additional reflections appear and no change in intensity can be seen, demonstrating the insertion of lithium within the crystalline framework without supplementary reactions. However, the extraction of the large ammonium ions could be responsible for the crystallinity decrease of the structure by generating amorphization in the crystalline framework and as well grain boundaries in the particles of the starting electrode material. The inferior rate capability of this material compared to the $KFeF_3$ can be assigned to the lower-range order generated after the first ammonium extraction. Indeed, the amorphization of the crystal structure hinders the good diffusion of the ionic species given the discontinuous channels within the electrode material forming barriers for the ionic diffusion. On the other hand, after the initial diminution of the crystallinity in NH_4FeF_3, the degree of crystallinity is kept constant during the subsequent cycles, while in the case of $KFeF_3$, the reflections on the pattern almost completely disappear after 50 cycles (**Figure 6.11b**). The good retention of the capacity of NH_4FeF_3 can be assigned to the conservation of the crystal framework after the first ammonium extraction, although the crystallinity dramatically decreases. In contrast, the repeated lithium dis/insertion processes in the $KFeF_3$ cubic perovskite structure generate a loss of crystallinity along the cycles, which can explain the worse capacity retention of this compound in the lithium and sodium systems, as it has already been reported by other authors [14].

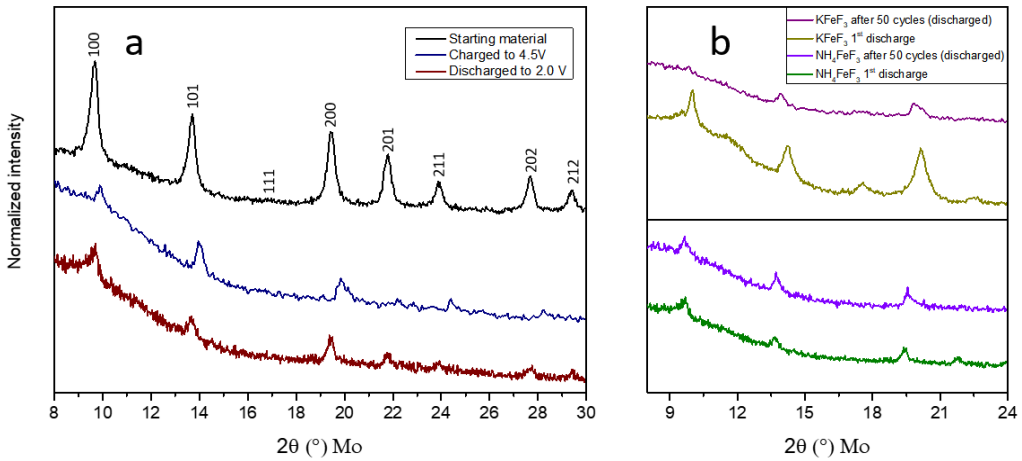

Figure 6.11. (a) *Ex situ XRD patterns of NH_4FeF_3 cycled at C/20 towards lithium and* **(b)** *comparison between the NH_4FeF_3 and $KFeF_3$ at the 1st and 50th cycles towards lithium.*

5. Conclusion

Cubic iron perovskite fluorides containing potassium and ammonium in their A-sites were synthesized by simple one-step and two-step methods, i.e. starting from $Fe(ac)_2$ and FeF_2 precursors, respectively. These synthesis routes allow the control of the size and the morphology of the nanoparticles, as well as the preparation of other transition metal cubic perovskite fluorides, such as $KMnF_3$ and $KCoF_3$. Those materials can be combined with carbon black through ball-milling under mild conditions, without dramatically influencing the crystallinity of the compounds. The iron fluoride structures show activity towards the reaction with different alkali species, namely lithium, sodium and potassium. $KFeF_3$ demonstrates a full potassium extraction during the initial charge process in the sodium and lithium systems, which allows the following full insertion of these alkali ions. This active material shows outstanding rate capability with up to 120 $mAh.g^{-1}$ at 5C towards sodium and 135 $mAh.g^{-1}$ at 5C towards lithium. The active electrode material can even be cycled up to 40C in the lithium system, delivering decent capacity (60 $mAh.g^{-1}$). However, only poor capacity retention is observed for both systems, since the electrolyte is unstable towards the fluoride material when cycled at high cutoff potential. The ammonium-containing phase can go through a full extraction of the cation located within the A-site of the perovskite structure. The reactivity of such molecules had never been reported so far in non-aqueous alkali-ion systems until now. After the initial charge process, the insertion of alkali ions can be carried out at good rates, with 0.9 sodium and 1.0 lithium per formula unit at a current density of C/10. This compound demonstrates also good rate capability with half of its theoretical capacity delivered at 5C during the initial discharge (~ 100 $mAh.g^{-1}$). Those two cubic perovskite fluoride compounds can efficiently be cycled

towards potassium with 74 % for $KFeF_3$ and 56 % for NH_4FeF_3 of their theoretical capacities obtained during the first discharge. Nevertheless, a large hysteresis between the charge/discharge processes and the instability of the electrolyte lead to low capacity retentions for both materials. *Ex situ* XRD experiments demonstrate that the potassium dis/insertion occurs through a highly reversible solid-solution reaction, which confirms that the low capacity retention comes from instability of the electrolyte and the high hysteresis between the charge/discharge processes. Within the other systems, during the initial charge, $KFeF_3$ undergoes the full extraction of the potassium ions, which leads to the formation of a cubic FeF_3 framework. This conformation is analogous of the one reported for $NaFeF_3$ in the previous chapter, but with larger cell parameters and allows the reversible insertion of alkali ions during the following discharge, without the generation of conversion reactions. Upon sodium insertion, a phase similar to $NaFeF_3$ is created, but with a higher volume cell, while upon lithium insertion the cubic conformation is kept, leading to a $LiFeF_3$ cubic polymorph. During these processes, the crystallinity of the compound decreases. The excellent rate capability of $KFeF_3$ can be rationalized by the retention of the perovskite structure along the charge/discharge processes and the large channels that this structure presents. On the other hand, the crystallinity of NH_4FeF_3 dramatically decreases during the first ammonium extraction, probably due to the large radii of the cation located in the A-site of the perovskite structure. However, the structure can still accept the reversible insertion of alkali ions, but presenting lower rate capability compared to $KFeF_3$, due to the lower-range order of the diffusion channels. The low crystallinity obtained after the initial charge is kept after repeated cycles. All in all, the maintenance of the crystallinity of the NH_4FeF_3 system ensures good capacity retention, while the crystallinity of $KFeF_3$ decreases continuously along the cycles. The continuous decrease of the crystallinity of the $KFeF_3$ system along the cycles, together with the instability of the electrolyte at high cutoff potentials, results in worse capacity retentions.

6. Experimental section

Synthesis of $KFeF_3$ one-step. $Fe(ac)_2$ (6mmol) and KOEt (7 mmol) were dissolved in the presence of NH_4F (18 mmol) in 30 mL of BnOH in a Schlenk tube. The three components were dispersed using an ultrasonic bath for at least 2 h. Then, the Schlenk tube was introduced into an oil bath for heat treatment at 150 °C for 10 min. Then the reaction media is naturally cooled down to room temperature and the particles are precipitated via centrifugation and purified twice in degassed methanol using the same method. For the preparation of other transition-

metal perovskites, the same synthesis was used by replacing the appropriate precursors [i.e. $Mn(ac)_2$, and $Co(ac)_2$].

Synthesis of $KFeF_3$ two-step. For the two-step synthesis of the cubic perovskite, nanosized FeF_2 synthesized in chapter 4 is used as precursor. 6 mmol of the material are dispersed in 30 ml of BnOH in presence of 7 mmol of KOEt and 6 mmol of NH_4F in a Schlenk tube. After total dispersion/dissolution of the three components, the reaction media is heated up to 150 °C for 10 min. The grey solution turns yellowish. A collection and purification method similar to the previous synthesis is used.

Syntheses of $(NH_4)FeF_3$ and $K_{(1-x)}(NH_4)_xFeF_3$. The above described methods are repeated using specific equivalents of KOEt to obtain the desired composition of the target compound, namely, $(NH_4)FeF_3$, $K_{3/4}(NH_4)_{1/4}FeF_3$, $K_{1/2}(NH_4)_{1/2}FeF_3$, and $K_{1/4}(NH4)_{3/4}FeF_3$, using the one-step and two-step reaction methods.

Ball-Milling Process. The collected powders were mixed together with carbon black (CB) by ball milling (planetary mill PULVERISETTE 7) for 4 h at 750 rpm using zirconia beakers and beads under the argon atmosphere. 0.5 of the mixed powder are used for each ball milling, and the weight ratio of this powder related to the zirconia beads is 1:14.

Annexe

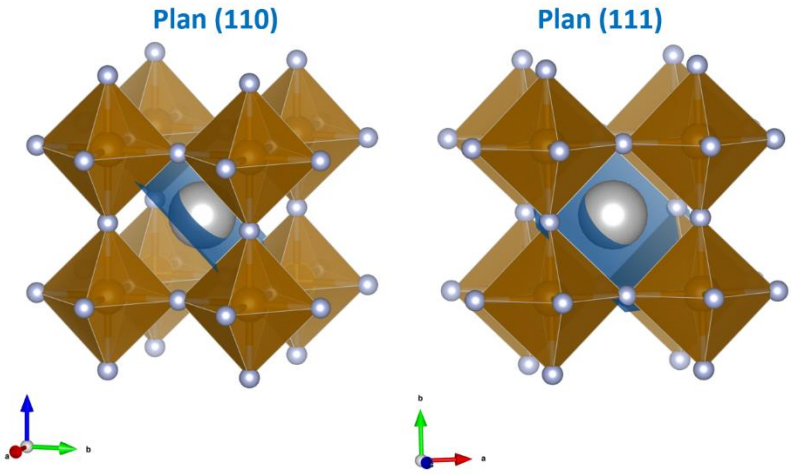

Figure A6.1. *Examples of crystalline plans passing through the middle of the A-site of the cubic perovskite structure, namely here the plan (110) and (111).*

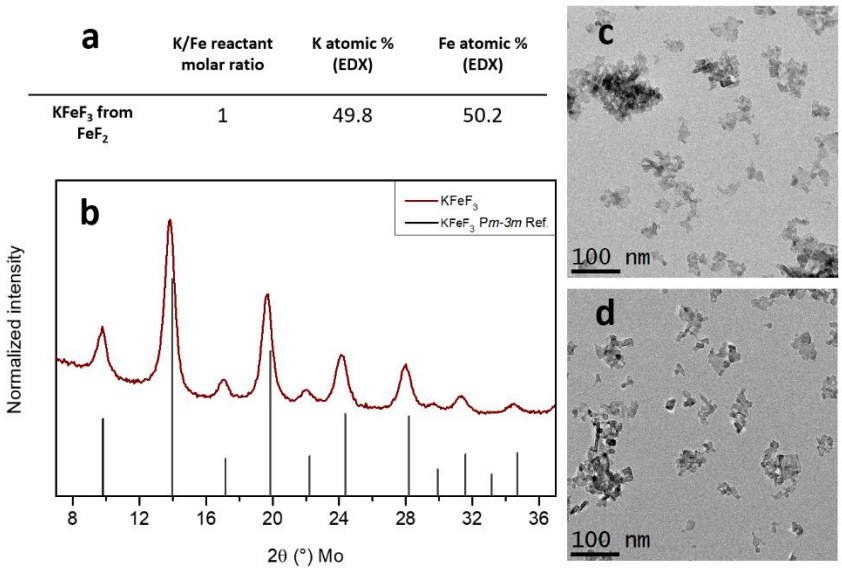

Figure A6.2. (a) *EDX measurement,* **(b)** *XRD pattern and* **(c)** *TEM images of* $KFeF_3$ *synthesized from* FeF_2.

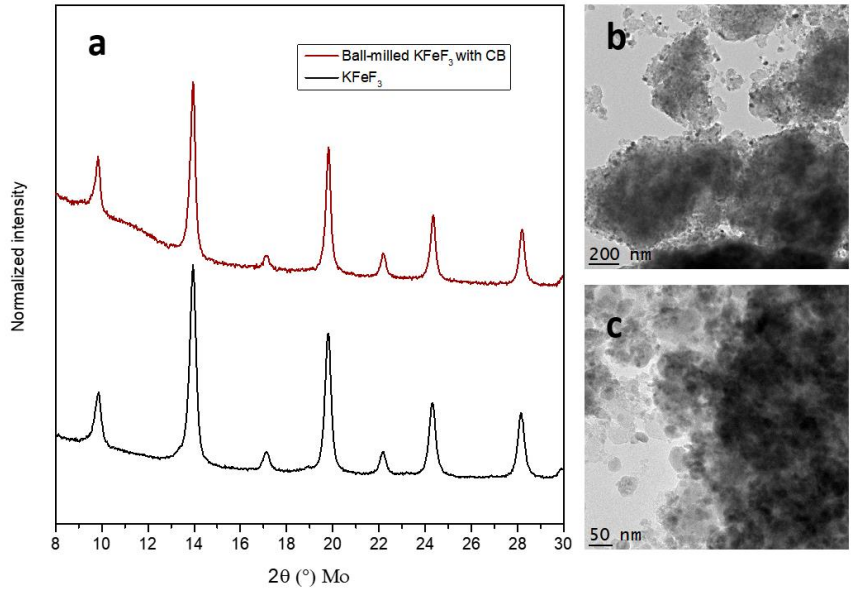

Figure A6.3. (a) *XRD patterns of* $KFeF_3$ *synthesized from* $Fe(ac)_2$ *before and after ball-milling with CB, and* **(b)** *&* **(c)** *TEM images of* $KFeF_3$ *after ball-milling with CB.*

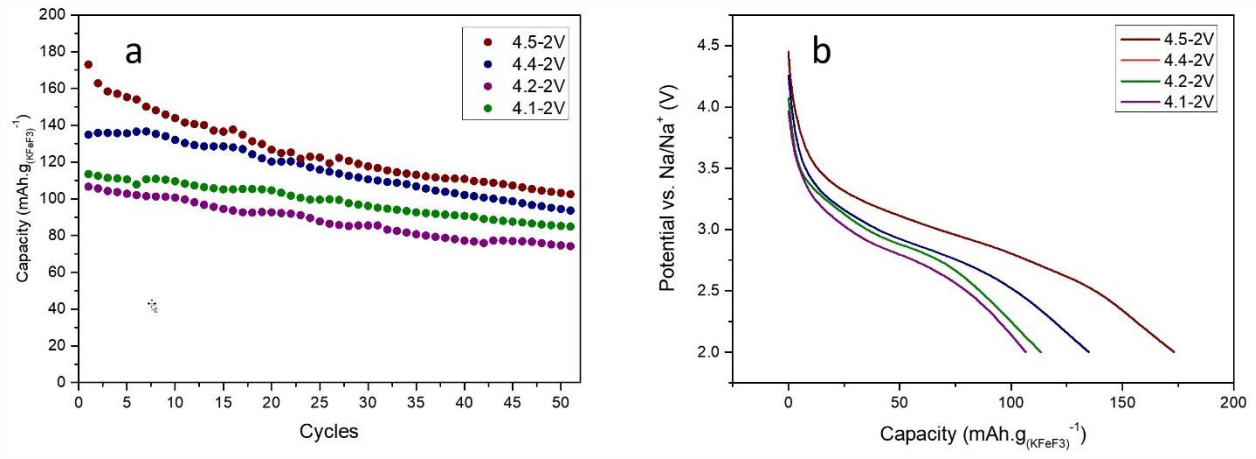

Figure A6.4. (a) *Capacity retentions of $KFeF_3$ cycled at C/10 with different cutoff potentials and* **(b)** *respective first galvanostatic discharge profiles.*

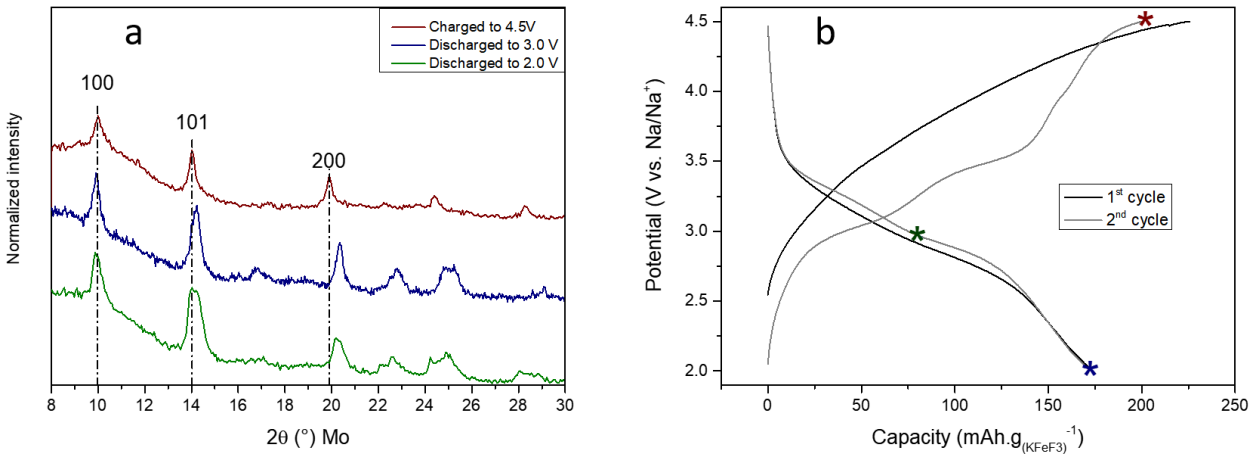

Figure A6.5. (a) *Ex situ XRD patterns of $KFeF_3$ cycled at C/20 towards sodium and* **(b)** *respective galvanostatic profile.*

$KFeF_3$ in the Na-ion system

(a) Reflections of the *Pm-3m*	Synthesized $KFeF_3$	Electrode FeF_3
(100)	26	27
(101)	100	38
(111)	6	3
(200)	57	28
(201)	11	9
(211)	29	14
(220)	24	17

Reflections of the *Pnma*	Ref $NaFeF_3$	Electrode $NaFeF_3$
(002)	76	59
(112)	100	100
(103)	18	9
(004)	71	48
(114)	17	14
(024)	27	25
(204)	45	38

$KFeF_3$ in the Li-ion system

(b) Reflections of the *Pm-3m*	Synthesized $KFeF_3$	Electrode FeF_3	Electrode $LiFeF_3$
(100)	26	39	21
(101)	100	30	18
(111)	6	~0	5
(200)	57	17	21
(201)	11	4	2
(211)	29	14	6
(220)	24	8	10

$KFeF_3$ in the K-ion system

(c) Reflections of the *Pm-3m*	Synthesized $KFeF_3$	Electrode FeF_3	Electrode $KFeF_3$
(100)	26	21	27
(101)	100	43	95
(111)	6	3	8
(200)	57	30	36
(201)	11	10	12
(211)	29	11	16
(220)	24	14	14

NH_4FeF_3 in the Li-ion system

(d) Reflections of the *Pm-3m*	Synthesized NH_4FeF_3	Electrode FeF_3	Electrode $LiFeF_3$
(100)	100	21	34
(101)	82	36	17
(111)	~1	~0	~0
(200)	81	22	26
(201)	62	4	14
(211)	29	8	11
(220)	38	5	10

Table A6.1. *Relative intensities of the ex situ XRD patterns of* **(a)** *$KFeF_3$ towards sodium and the $NaFeF_3$ reference and* **(b)** *towards lithium and* **(c)** *towards potassium.* **(d)** *Relative intensities of the ex situ XRD patterns of NH_4FeF_3 cycles towards lithium. Plan highlighted in pink are passing through the A-site of the Pm-3m structure.*

References

1. Zhu, Y.; Xu, Y.; Liu, Y.; Luo, C.; Wang, C., Comparison of electrochemical performances of olivine $NaFePO_4$ in sodium-ion batteries and olivine $LiFePO_4$ in lithium-ion batteries. *Nanoscale* **2013,** *5* (2), 780-787.
2. Kim, D.; Kang, S.-H.; Slater, M.; Rood, S.; Vaughey, J. T.; Karan, N.; Balasubramanian, M.; Johnson, C. S., Enabling Sodium Batteries Using Lithium-Substituted Sodium Layered Transition Metal Oxide Cathodes. *Advanced Energy Materials* **2011,** *1* (3), 333-336.
3. Kikkawa, S.; Miyazaki, S.; Koizumi, M., Deintercalated $NaCoO_2$ and $LiCoO_2$. *Journal of Solid State Chemistry* **1986,** *62* (1), 35-39.
4. Song, W.; Ji, X.; Wu, Z.; Zhu, Y.; Yang, Y.; Chen, J.; Jing, M.; Li, F.; Banks, C. E., First exploration of Na-ion migration pathways in the NASICON structure $Na_3V_2(PO_4)_3$. *Journal of Materials Chemistry A* **2014,** *2* (15), 5358-5362.
5. Lu, Y.; Wang, L.; Cheng, J.; Goodenough, J. B., Prussian blue: a new framework of electrode materials for sodium batteries. *Chemical Communications* **2012,** *48* (52), 6544-6546.
6. Kubota, K.; Dahbi, M.; Hosaka, T.; Kumakura, S.; Komaba, S., Towards K-Ion and Na-Ion Batteries as "Beyond Li-Ion". *The Chemical Record* **2018,** *18* (4), 459-479.
7. He, G.; Nazar, L. F., Crystallite Size Control of Prussian White Analogues for Nonaqueous Potassium-Ion Batteries. *ACS Energy Letters* **2017,** *2* (5), 1122-1127.
8. Liu, Y.; Xu, M.; Shen, B.; Xia, Z.; Li, Y.; Wu, Y.; Li, Q., Facile synthesis of mesoporous $NH_4V_4O_{10}$ nanoflowers with high performance as cathode material for lithium battery. *Journal of Materials Science* **2018,** *53* (3), 2045-2053.

9. Yu, S.; Zhang, P.; Wu, S. Q.; Li, A. Y.; Zhu, Z. Z.; Yang, Y., Understanding the structural and electronic properties of the cathode material $NaFeF_3$ in a Na-ion battery. *Journal of Solid State Electrochemistry* **2014,** *18* (8), 2071-2075.
10. Cao, D.; Yin, C.; Shi, D.; Fu, Z.; Zhang, J.; Li, C., Cubic Perovskite Fluoride as Open Framework Cathode for Na-Ion Batteries. *Advanced Functional Materials* **2017,** *27* (28), 1701130.
11. Han, Y.; Hu, J.; Yin, C.; Zhang, Y.; Xie, J.; Yin, D.; Li, C., Iron-based fluorides of tetragonal tungsten bronze structure as potential cathodes for Na-ion batteries. *Journal of Materials Chemistry A* **2016,** *4* (19), 7382-7389.
12. Kong, M.; Liu, K.; Ning, J.; Zhou, J.; Song, H., Perovskite framework NH_4FeF_3/carbon composite nanosheets as a potential anode material for Li and Na ion storage. *Journal of Materials Chemistry A* **2017,** *5* (36), 19280-19288.
13. Wu, X.; Qi, Y.; Hong, J. J.; Li, Z.; Hernandez, A. S.; Ji, X., Rocking-Chair Ammonium-Ion Battery: A Highly Reversible Aqueous Energy Storage System. *Angewandte Chemie International Edition* **2017,** *56* (42), 13026-13.
14. Ali, G.; Lee, J. H.; Chang, W.; Cho, B.-W.; Jung, H.-G.; Nam, K.-W.; Chung, K. Y., Lithium intercalation mechanism into $FeF_3 \cdot 0.5H_2O$ as a highly stable composite cathode material. *Scientific Reports* **2017,** *7* (1), 42237.

Conclusion

Towards our increasing use of portable devices and the replacement of the internal combustion engine by electric motors, the need for high-energy storage technologies is more than ever before present. Alkali-ion systems seem to be the most suitable technologies to power our cars and mobile phones. In order to develop the next generation of these storage devices, active materials presenting higher energy densities have to be found. Transition metal fluorides are very appealing candidates as positive electrodes for the next generation of alkali-ion batteries owing to their high energy densities due to their ability to store more than one lithium ion per transition metal atom, as well as their high electrochemical theoretical potential coming from the high ionic character of the metal-fluorine bond. However, metal fluorides present three major drawbacks. (1) Their performances are hindered by a low capacity retention caused by the conversion reaction involved in their discharge/charge processes. (2) Their low conductivity caused by the high polarization of the metal-fluorine bond is mainly responsible for the low kinetics of reaction that they present. (3) Most of the transition metal fluorides studied as cathodes for alkali-ion batteries do not present alkaline ions, thus lacking an alkali reservoir. In the literature, the synthesis methods for the production of alkaline containing compounds have been barely explored, limiting the performances of such compounds.

The present work addressed this problematic by introducing several original synthesis routes to obtain nano-sized composite materials with a superior electrochemical properties. In this thesis, the syntheses of metal difluorides and different transition metal perovskite structures were conducted through fluorolytic sol-gel reactions, involving the fluorination of dissolved species or solid nano-sized particles. By tuning the reaction conditions, the size and morphology of the synthesized compounds could be controlled. Syntheses based on the fluorination of nanoscale solid oxides with HF have also been developed for the production of anhydrous iron(III) fluoride, allowing the generation of highly crystalline material. The materials introduced in this work were systematically studied by XRD and TEM, as well as other techniques (FTIR, EDX, elemental analysis). The resulting electrochemical properties of these active materials were studied through voltammetric and galvanostatic methods, and this allowed to study in detail the mechanisms involved during their reaction with alkaline species. The mechanisms taking place during the charge/discharge processes were investigated by *ex situ*, but also *operando* methods, involving XRD and TEM, together with electronic structure calculations.

Conclusion

The first part of this work was focused on transition metal fluorides without alkali ion species, specifically cobalt(II) fluoride and anhydrous iron(III) fluoride. The fluorolytic sol-gel reaction of $Co(NO_3)_{2-x}(OH)_x{\cdot}yH_2O$ (with $0 \leq x \leq 1$ and $0 < y \leq 6$) in BnOH led to the generation of particles with different sizes and morphologies depending on the composition of the cobalt precursor. Precursors with a higher content of nitrate functional groups gave larger particles, whereas a higher concentration of hydroxyl functional groups formed nanoparticles. Therefore, by modifying the precursor composition of the fluorolytic sol-gel reaction, the size and morphology of the obtained rutile compound could be tuned. The synthesized materials could be successfully grafted on graphene oxide, and on carbon nanotubes as well. It was found that the different electrochemical properties of the cobalt fluoride materials is related to the size of the particles, with increased capacity for smaller particles. It was confirmed by *ex situ* XRD that large CoF_2 particles (> 50 nm) did not allow the full conversion of the material, while smaller particles (< 30 nm) undergo full conversion. *Ex situ* TEM showed that a large amount of SEI was formed during the first cycle, responsible for the observed extra capacity. It also showed that the integrity of the composite material was lost along the cycles, leading to the decrease of the capacity. The second part of chapter 4 was focused on the synthesis of anhydrous iron(III) fluoride. This synthesis was carried out by the fluorination of iron oxide precursors. This method is the first reported synthetic route under such mild conditions (at 100 °C, 1 hour reaction) allowed the formation of cubic nanoparticles presenting high crystallinity and no impurities. Composite materials made with graphene oxide or carbon black could be produced by the fluorination of a Fe_2O_3/GO composite or by ball-milling of the active material with carbon black. Depending on the fluorination time of the Fe_2O_3/GO precursor, different composite morphologies were obtained. Those materials were cycled above 2.0 V vs. Li/Li^+ in order to study the reaction of only one alkali atom per formula unit. While towards lithium the performance of ball-milled materials was low due to the deterioration of the crystal structure during the process, FeF_3/GO presented excellent performance with full discharge capacity at C/10 and relatively good rate-capability with half of the capacity obtained at 2C. Nonetheless, a severe drop of the delivered capacity could be observed after the first cycle. Towards sodium and potassium, the composite material showed low discharged capacities. *Ex situ* XRD revealed that the crystal structure would not react with lithium only through an insertion reaction, but undergoes drastic reorganization, after the reaction of 0.25 lithium ions, associated to the conversion of the framework to an amorphous material. Such initial collapse of the crystal structure was responsible for the drop of capacity at the first cycle, while the constant capacity decrease could be ascribed to the repeated conversion reaction along the cycles. In the case of

the cycling towards larger ions, it was demonstrated that the crystal structure is too tight to host sodium and potassium, implying low capacities.

The subsequent chapters focused on the synthesis of alkali-containing transition metal fluoride perovskite structures, and the study of their electrochemical properties. $NaFeF_3$ was firstly described in chapter 5. This perovskite structure is made of (FeF_6) corner-shared octahedrons forming a Fe-F-Fe angle equal to ~ 150 °, and sodium atoms 12-fold coordinated by fluorine atoms. Herein, two different synthesis routes were developed. One involved the fluorolytic sol-gel reaction of the nano-scaled rutile metal difluorides synthesized in the previous chapter. It was shown that the conversion of the rutile material, where the (FeF_6) octahedrons are in this structure edge- and corner-shared, to a perovskite structure was possible in the liquid phase in the presence of sodium ethoxide and ammonium fluoride under MW irradiations. This technique allowed the formation of nanoparticles exhibiting high crystallinity and purity. A second technique consisted of directly starting from transition metal(II) acetate using three equivalents of ammonium fluoride with one equivalent of sodium ethoxide to carry out the fluorination in one step. This method granted good control of the synthesis parameters and the resulting morphology of the obtained compounds. However, impurities corresponding to the NH_4MF_3 phase were also. This presence was caused by the high concentration of ammonium ions in the reaction media. Due to these impurities, the materials synthesized from acetate precursors were not used for electrochemical tests, and the active materials obtained from metal difluoride precursors were then preferred. $NaMnF_3$ and $NaCoF_3$ demonstrated poor electrochemical performances due to their not optimal redox potential. On the other hand, the high crystallinity, suitable morphology and alkali dis/insertion mechanisms of $NaFeF_3$ enabled the compound to achieve excellent performances towards sodium, but also towards lithium, where this compound showed outstanding rate-capability. Electrochemical and XRD characterization techniques showed that the sodium ions could be totally disinserted from the perovskite structure, which was resulting in the cubic conformation of the alkali-free framework. It was proven that this atypical conformation was allowing the insertion of the sodium atoms back upon discharge without inducing a conversion reaction, restoring the starting structure. More surprisingly, upon lithium insertion, the cubic conformation enabled the lithium insertion within the crystalline framework without the formation of trirutile species or any conversion reaction, in contrast to the reaction of lithium with hexagonal iron fluoride structure (c.f. chapter 3 section 3.3). The good capacity retention observed for $NaFeF_3$ could be ascribed to the very reversible alkali insertion in this structure, whereas its outstanding rate-capability could be attributed to the low volume change and the large channels of diffusion for

lithium atoms of the cubic fluoride framework. Electronic structure calculations pointed out that the pathway of the reaction was following a kinetically favored mechanism, rather than a thermodynamical one, where the conversion of the crystalline structure could be involved, involving a high-energy activation.

The incorporation of larger ions than sodium in the A-site of the perovskite structure allowed the crystalline framework to adopt a cubic structure. In the last chapter of this thesis, fluoride perovskite structures containing potassium and ammonium cations were studied in detail. The synthesis techniques used in the previous chapter were likewise used for these compounds. It was shown that an excess of potassium precursor led to the formation of pure $KFeF_3$, while the absence of the potassium precursor created NH_4FeF_3. The use of an excess of the alkali precursor was here possible due to the non-formation of potassium fluoride. The cubic shaped nanoparticles obtained from this method are very crystalline and have a mono-dispersed size distribution around 50 nm, for both potassium and ammonium phases. The stabilized cubic perovskite frameworks present large channels, which are suitable for the fast diffusion of ions. As in the previous chapter, during the first charge process of the half-cell, the disinsertion of the cation located in the A-site of the perovskite structure takes place. Interestingly, the framework keeps its cubic conformation after the total extraction of the cation, similar to $NaFeF_3$, but adopting a larger unit cell. This extraction occurs at a higher potential than it was the case for sodium, inducing the need to use a higher cutoff potential for the charge process. This large unit cell enables the extremely fast diffusion of sodium and lithium, with 35 % of the capacity delivered at 40 C for $KFeF_3$ towards lithium, but also permits the cycling towards larger alkali-ions, such as potassium. Upon the insertion of alkali ions, the crystal structure of $KFeF_3$ behaves in a similar way than $NaFeF_3$; a structure relative to the P*nma* space group was obtained after sodium insertion and towards lithium, the cubic conformation is preserved with slight changes of the unit cell during the charge/discharge processes. The large unit cells that present the alkali-free structure were responsible for the superior performance of this material. Towards potassium, it is interesting to note that the structure keeps its cubic conformation too along with the cycles, but with a formula unit having larger cell parameters after the insertion back of the potassium ions. This chapter also described for the first time the use of NH_4FeF_3 as an active material for alkali-ion batteries and the possibility of the NH_4^+ ions to act as a charge carrier in alkali-ions, analogically to the NH_4-ion rocking chair systems. This material demonstrated good rate-capability, but not as high as observed for $KFeF_3$. This behavior could be explained by the drastic decrease of the crystallinity upon the first charge process, which nevertheless, does not present any conversion of the crystalline structure. However, good

capacity retention was reported, due to the maintaining of the structure upon further cycling. In contrast, $KFeF_3$ presented poor cyclability compared to NH_4FeF_3, but also $NaFeF_3$, mainly caused by the gradual loss of the crystallinity, which could be coming from the high cutoff potential used.

Together with their low conductivity, one of the major drawbacks of using transition metal fluoride perovskites is their high instability when they are in contact with oxidant species. To overcome this problem, new strategies of synthesis should be designed in order to embed the active material in a protective matrix presenting electric conductivity with the aim of overcoming the insulating character of such active material. This would not only improve the handling of transition metal fluoride perovskites outside inert atmospheres, but also stabilize the electrolyte/material interface in electrochemical cells during charging processes, and therefore, enhance their cycling stability. Even though this work enlightens the mechanisms involved in $NaFeF_3$ during its charge/discharge processes, some aspects remain unclear, such as the environment of the lithium atoms within the FeF_3 framework. In order to study more into detail the phenomenon, more powerful characterization techniques should be employed to fully understand those mechanisms, for instance pair distribution function or X-ray absorption near edge structure.

To conclude, the present study does not only report the implementation of new techniques of synthesis for the production of nano-scaled metal fluoride materials but also highlights the possibility to stabilize crystalline structures in conformations highly beneficial for their performance. This particular behavior could be endorsed by other material than $NaFeF_3$, which would have electrochemical properties in disadvantage from a thermodynamical point of view, but favored by kinetics. These findings, which represent a breakthrough in the field, could help the design of new active materials for battery application, and furthermore, be useful to the scientific community for a better understanding of the chemistry of such kind of compounds. In addition, this work discussed for the first time the practicability to use cations other than alkali ions, such as NH_4^+, as charge carriers in alkali-ion systems. This cation could be effective in other families of compounds to enlarge their crystalline framework and make their channels of diffusion more suitable for large alkali ions, such as sodium or potassium. All in all, this thesis contributed to enlarge the understanding of the community on active materials for alkali-ion applications.

List of abbreviations

CB	Carbon black
CNRS	Centre national de recherche scientifique
CNTs	Carbon nanotubes
C_{th}	Specific theoretical capacity
CV	Cyclic voltammetry
EDX	Energy dispersive X-ray spectroscopy
FTIR	Fourier transform infrared spectroscopy
GO	Graphene oxide
HTB	Hexagonal Tungsten Bronze
ICE	Intern combustible engine
IPCC	Intergovernmental panel on climate change
LFP	$LiFePO_4$
LIBs	Lithium-ion batteries
LMO	$LiMn_2O_4$
MW	Microwave
M_w	Molar mass
NCA	$LiNi_xCo_{1-x-y}Al_y$
NIBs	Sodium-ion batteries
NMC	$LiNi_xMn_yCo_{1-x-y}$
OCP	Open circuit potential
PBAs	Prussian Blue analogues
PVdF	Polyvinylidene fluoride
rGO	Reduced graphene oxide
STEM	Selected area electron diffraction
SEI	Solid electrolyte interphase
SHE	Standard hydrogen electrode
TEM	Transmission electron microscopy
TMOs	Transition metal oxides
WP	Working potential
XRD	X-ray powder diffraction
Ɵ	Scattering angle

List of figures

Figure 1.1. *Global energy mix (a) in 2011 and (b) previsions in 2035 according to the baseline new policies scenario [19].* 9
Figure 1.2. (a) *Scheme of the distribution and storage within the electrical grid and* **(b)** *comparison of the electrical grid with and without energy storage [25].* 10
Figure 1.3. *Optimistic prevision on the emergence of the electrical vehicles along the years with a British touch of humor [28].* 11
Figure 2.1. *Ragone plot: specific energy versus specific power of various storing and intern-combustion-engine devices. Adapted from Thomas Christen and Martin W. Carlen [8].* 18
Figure 2.2. *Schematic representation of a lithium-ion full-cell during the charge/discharge process (sizes and charges of the atoms are not respected). Adapted from Reddy et al [12].* 22
Figure 2.3. (a) *Influence of the different polarization phenomena on the discharge curve of a lithium-ion cell and* **(b)** *influence of the current density on the polarization. Adapted from Bhaskar Saha and Kai Goebel [22].* 23
Figure 2.4. *Panel of different active materials used as anodes for LIBs.* 25
Figure 2.5. *Illustration of* **(a)** *soft carbon,* **(b)** *hard carbon and* **(c)** *graphite structures. Adapted from N. Loeffler et al [31].* 26
Figure 2.6. *Illustration of* **(a)** *the pulverization of a Si-electrode upon lithium insertion/extraction and* **(b)** *the resulting excessive SEI formation along with cycling.* 27
Figure 2.7. (a) *Principal insertion reacting materials used as positive electrode for LIBs displayed in function of the specific capacities and redox potentials, and crystal structures:* **(b)** *layered structure, spinel structure and (d) olivine structure.* 31
Figure 2.8. *Fraction of the different active materials used as cathodes for NIBs in function of their working potential against their specific capacity.* 35
Figure 2.9. *Working voltage vs. Li/Li$^+$ of the different metal fluorides used as positive electrodes against their theoretical capacities.* 37
Figure 2.10. *Illustrations of the* **(a)** *tetragonal rutile crystal structure of FeF_2, CoF_2, NiF_2, and* **(b)** *monoclinic rutile crystal structure typical for CuF_2.* 39
Figure 2.11. *Illustrations of the different phases that adopt iron(III) fluoride compound depending on their water content, namely* **(a)** *R3-c FeF_3 anhydrous,* **(b)** *$FeF_3{\cdot}0.33H_2O$ Hexagonal Tungsten Bronze and* **(c)** *$FeF_3{\cdot}0.5H_2O$ Pyrochlore phases and* **(d)**, **(e)**, **(f)** *focus on their cell parameters, respectively.* 40
Figure 2.12. *Illustrations of the different perovskite structures:* **(a, b)** *orthorhombic Pnma and* **(c, d)** *cubic Pm-3m perovskites.* 43
Figure 4.1. (a) *Diffraction patterns of the different CoF_2 materials and reference pattern of the rutile structure, and* **(b)**, **(c)**, **(d)**, **(e)**, **(f)** *and* **(h)** *respective TEM images.* 61
Figure 4.2. *TEM images of the* **(a)** *CoF_2-6+rGO,* **(b)** *CoF_2-5+rGO,* **(c)** *CoF_2-2+rGO samples and* **(d)**, **(e)**, **(f)** *their SAED measurement, respectively.* **(h)** *Comparison of the XRD patterns of the CoF_2-2 sample, before and after graphene oxide grafting.* 63
Figure 4.3. *TEM images of* **(a)-(b)** *the $Co(OH)_2$ precursor synthesized in presence of carbon nanotubes and* **(c)-(d)** *of the resulting CoF_2 composite compound (CoF_2-7+fCNTs).* 64
Figure 4.4. (a)-(c) *Galvanostatic profiles of the CoF_2-5+rGO and CoF_2-2+rGO cycled at C/10 towards lithium, and* **(b)-(d)** *corresponding capacity retention plots, respectively.* 65
Figure 4.5. *Cyclic voltammetry experiment of the CoF_2-5+rGO sample carried out at 0.1 mV.s^{-1} in the 2-4.4 V window potential vs. Li/Li$^+$.* 66
Figure 4.6. *Ex-situ XRD patterns of the electrodes materials after discharge and charge for the* **(a)** *CoF_2-5+rGO and* **(b)** *CoF_2-2+rGO.* 67

List of figures

Figure 4.7. *Ex-situ TEM images of the CoF_2-5+rGO electrode material* **(a)-(b)** *after the 1st discharge and* **(c)** *after the 10th cycle,* **(d)** *corresponding SAED measurement.*.....68
Figure 4.8. (a) *XRD patterns of the iron(II) fluoride compounds synthesized from $Fe(Cl)_2$ varying the synthesis parameters and* **(b)**, **(c)**, **(d)**, **(e)**, **(f)** *and* **(g)** *relative TEM images.* 69
Figure 4.9. (a) *XRD patterns of the iron(II) fluoride compounds synthesized from $Fe(ac)_2$ varying the synthesis parameters and* **(b)**, **(c)**, **(d)** *and* **(e)** *relative TEM images.*.....72
Figure 4.10. (a), **(b)**, **(c)** *TEM images of the iron oxide precursors, namely commercial hematite and nanosized hematite and magnetite, and* **(d)** *scheme of the anhydrous FeF_3 synthesis design.* 73
Figure 4.11. (a), **(c)**, **(e)** *XRD patterns of the different iron oxide precursor (black) and their fluorinated products (red) and* **(b)**, **(d)**, **(f)** *the TEM images related to the fluorinated products, respectively.* 75
Figure.4.12. (a) *XRD pattern of the bare iron(III) fluoride nanoparticles ball-milled with carbon black for 1, 4, 8, 16 hours and the pristine sample.* **(b)**, **(c)**, **(d)** *TEM images of the ball-milled samples for 1, 4 and 16 hours, respectively.*.....76
Figure 4.13. (a) *Scheme of the synthesis process of the FeF_3+GO composite. TEM images of* **(b)** *the GO,* **(c)** *Fe_2O_3 nanoparticles grafted onto GO and (d) product of the fluorination.* **(e)** *and* **(f)** *pictures of before and after addition of the Fe_2O_3 solution in the GO dispersion.*.....79
Figure 4.14. (a) *XRD pattern of the synthesized FeF_3+GO composite and* **(b)** *FT-IR spectra of the different intermediate of the composite synthesis process.* 80
Figure 4.15. *TEM images of the fluorinated products* **(a)** *and* **(d)** *after 1 hour,* **(b)** *and* **(e)** *after 4 hours and* **(c)** *and* **(f)** *after 16 hours. (g) FT-IR measurements of the product of fluorination after 1 hour and 16 hours.*.....81
Figure 4.16. (a) *Galvanostatic curves of the FeF_3+GO-1h cycled towards Li at C/10 and* **(b)** *related capacity retention.* **(c)** *Cyclic voltammetry experiment of the FeF_3+GO-1h at the scan rate of 0.1 $mV.s^{-1}$ towards Li.* **(d)** *Capacity retention of the FeF_3+GO-1h at different current densities*.....82
Figure 4.17. (a) *Capacity retention of FeF_3+GO-1h and FeF_3+GO-16h at C/5 towards Li in the 1-4.5 V window potential and* **(b)** *related galvanostatic profile of FeF_3+GO-16h.* 83
Figure 4.18. (a) *Galvanostatic curves of FeF_3+CB-8h cycled towards Li at C/10 and* **(b)** *capacity retention of the different FeF_3+CB materials.* 84
Figure 4.19. (a) *Ex-situ XRD pattern of FeF_3+GO-1h at different state of charge and* **(b)** *dQ/dV profile of the galvanostatic plot cycled at C/10 towards Li.* 85
Figure 4.20. (a) *Galvanostatic curves of FeF_3+GO-1h cycled towards Na at C/10 and* **(b)** *related capacity retention.* **(c)** *Ex-situ XRD pattern of FeF_3+GO-1h after the first discharged at C/50 towards Na and* **(d)** *related galvanostatic.*.....88
Figure A4.1. *The linear relation between the temperature used for the decomposition of the precursor and the remaining content of -NO_3 in the decomposed precursor.* 93
Figure A4.2. *XRD patterns of CoF_2-2 after synthesis and after 1 month of storage in ambient atmosphere.*.....94
Figure A4.3. *Capacity retention of the different cobalt(III) fluoride composites materials cycled at C/10 towards Li in the window potential 1-4.4 V (vs. Li/Li^+).*.....94
Figure A4.4. *XRD patterns of product of synthesis when the Fe_2O_3 precursor is in direct contact with the aqueous HF solution.* 95
Figure A4.5. (a) *Capacity retention of the different iron(III) fluoride composites materials with GO at C/10 towards Li and* **(b)** *related galvanostatic profile of FeF_3+GO-16h* 95
Figure A4.6. (a) *Capacity retention of FeF_3+GO-16h at C/10 towards potassium and* **(b)** *its related galvanostatic profile.* 96
Figure 5.1. (a) *Schematic reaction pathway of the two-step synthesis of $NaFeF_3$.* **(b)** *XRD patterns of $NaCoF_3$ and $NaFeF_3$, and* **(c)** *&* **(d)** *relative TEM images of the products, respectively.* 100

List of figures

Figure 5.2. (a) XRD patterns of $NaCoF_3$, $NaFeF_3$, $NaMnF_3$, and $NaCo_{1/3}Mn_{1/3}Fe_{1/3}F_3$ and **(b)**, **(c)**, **(d)** *&* **(e)** *relative TEM images of the compounds, respectively.* *101*
Figure 5.3. (a) *XRD patterns of $NaFeF_3$ ball-milled with CB for 1 h, 2 h, 4 h & 8 h and* **(b)**, **(c)**, **(d)** *&* **(e)** *relative TEM images of the compounds, respectively.* *103*
Figure 5.4. (a) *Galvanostatic profile of $NaFeF_3$+CB4h compound cycled at C/10 towards sodium and* **(b)** *cyclic voltammetry experiment towards sodium at a scan rate of 0.1 $mV.s^{-1}$.* **(c)** *Capacity retentions of the compound cycled at different current densities and* **(d)** *within different potential windows.* *105*
Figure 5.5. (a) *and* **(b)** *Galvanostatic profiles of $NaCoF_3$ and $NaMnF_3$ ball-milled with CB cycled at C/10 towards sodium, respectively.* **(c)** *Capacity retentions of the compound cycled at different C/10.* **(d)** *Cyclic voltammetry experiments of $NaCoF_3$ and $NaMnF_3$ ball-milled with CB at a scan rate of 0.1 $mV.s^{-1}$.* *106*
Figure 5.6. (a) *Galvanostatic profile of $NaFeF_3$+cb4h compound cycled at C/3 towards lithium and* **(b)** *cyclic voltammetry experiment towards lithium at a scan rate of 0.1 $mV.s^{-1}$.* **(c)** *Capacity retentions of the compound cycled at different high current densities and* **(d)** *relative galvanostatic profiles of the second cycles.* *107*
Figure 5.7. (a) *Galvanostatic profile of the half-cells, $NaFeF_3$//Na and HC//Na cycled at C/10.* **(b)** *Galvanostatic profile of the $NaFeF_3$//HC full cell cycled at C/5 ($NaFeF_3$) and* **(c)** *the relative capacity retention.* *109*
Figure 5.8. (a) *Ex-situ XRD experiment of $NaFeF_3$ at different states of charge, cycled at C/20 towards sodium and (b) relative galvanostatic plot.* *110*
Figure 5.9. *Operando XRD experiment of $NaFeF_3$ conducted at C/20 towards sodium and corresponding galvanostatic plot.* *111*
Figure 5.10. (a) *Ex-situ XRD experiment of $NaFeF_3$ at different states of charge, cycled at C/10 towards lithium (* : PVdF ; + : carbon black) and* **(b)** *relative galvanostatic plot.* *112*
Figure 5.11. *Polymorphism theoretical analysis. (a) Phase stability diagram of Li_xNaFe_3 (empty circles) and Na_xFeF_3 (filled circles) as computed with spin-polarized DFT+U calculations (U_Fe = 5.3 eV). The formation energies $\Delta_f H$ (meV) = $E(A_xFeF_3) - xE(AFeF_3) + (1-x)E(FeF_3)$ are computed with respect to the proportional mixture of the most stable FeF_3 (Pm-3m) and $AFeF_3$ (Pnma) set as the reference energy (horizontal magenta line at zero energy). The initial structures considered in the calculations are $NaFeF_3$ (Pnma), $Li_{0.5}FeF_3$ ($P4_2/mnm$), and FeF_3 (R-3cH, R-3cR, and Pm-3m) from which Li and Na have been removed/added. Only the stable ($\Delta_f H < 0$) and metastable ($0 < \Delta_f H < 160$ meV FU^{-1}) A_xFeF_3 have been reported. (b) Schematic representation of the kinetic barriers associated with the thermodynamically (dotted lines) and kinetically (full line) controlled electrochemical transformations, together with the local structures of the polymorph stabilized during the reaction (Li and Na are not represented for a sake of clarity) showing that the kinetic path involves "easy" tilt and twist of corner-shared FeF_6 octahedrons all along the reaction, whereas the thermodynamic path involves bond breaking/formation and changes in FeF_6 connectivities.* *114*
Figure A5.1. (a) *XRD pattern of the compound after fluorination/sodiation of the FeF_2-1 precursor and (b) respective TEM image.* *117*
Figure A5.2 (a) *Rietveld refinement of the $NaFeF_3$ compound with refinement parameters and* **(b)** *crystal model with refinement parameters.* *117*
Figure A5.3. *XRD pattern of the compound after fluorination/lithiation of the FeF_2-5 precursor.* *118*
Figure A5.4. *XRD patterns of oxidized compounds of $NaFeF_3$.* *118*
Figure A5.5. *Capacity retentions of $NaFeF_3$ ball-milled with CB for different milling times.* ... *118*
Figure A5.6. *Lebail refinement of the resulting phase of $NaFeF_3$ charged state.* *119*
Figure A5.7. *Picture of* **(a)** *the operando half-cell and* **(b)** *the operando set up involving the X-ray diffractometer.* *119*

List of figures

Figure A5.8. (a) *Full range patterns operando measurement.* **(b)** *Initial and final XRD patterns of $NaFeF_3$ after two cycles in operando cell towards sodium and* **(c)** *relative galvanostatic plot.* 120
Figure 6.1. (a) *XRD patterns of the $K_x(NH_4)_yFeF_3$ compounds and* **(b)** *relative atomic ratios obtained by EDX.* 125
Figure 6.2. (a) *XRD patterns of the $KMnF_3$, $KFeF_3$, $KCoF_3$ cubic perovskite fluoride compounds, and* **(b)-(g)** *respective TEM images.* 126
Figure 6.3. (a) *XRD patterns of the $(NH_4)FeF_3$ cubic perovskite fluoride compounds synthesized from FeF_2 nanoparticles and $Fe(ac)_2$, and* **(b)-(e)** *respective TEM images.* 127
Figure 6.4. (a) *Galvanostatic plot of $KFeF_3$ cycled at C/10 towards sodium.* **(b)** *Cyclic voltammetry experiment of $KFeF_3$ at a scan rate of 0.1 $mV.s^{-1}$ towards sodium.* **(c)** *&* **(d)** *Capacity retentions of $KFeF_3$ at different current densities and using different electrolyte systems.* 129
Figure 6.5. (a) *Galvanostatic plot of $KFeF_3$ cycled at C/10 towards lithium.* **(b)** *Cyclic voltammetry experiment of $KFeF_3$ at a scan rate of 0.1 $mV.s^{-1}$ towards lithium.* **(c)** *&* **(d)** *Capacity retention of $KFeF_3$ at different current densities.* 131
Figure 6.6. (a) *Galvanostatic plot of NH_4FeF_3 cycled at C/10 and* **(b)** *at 5C towards sodium.* **(c)** *Capacity retentions of NH_4FeF_3 at different current densities.* **(d)** *Cyclic voltammetry experiment of NH_4FeF_3 at a scan rate of 0.1 $mV.s^{-1}$ towards sodium.* 132
Figure 6.7. (a) *Galvanostatic plot of NH_4FeF_3 cycled at C/10 towards lithium.* **(b)** *Cyclic voltammetry experiment of NH_4FeF_3 at a scan rate of 0.1 $mV.s^{-1}$ towards lithium.* **(c)** *Capacity retentions of NH_4FeF_3 at different current densities and* **(d)** *at 5C during extended cycling.....133*
Figure 6.8. (a) *and* **(c)** *Galvanostatic profiles of $KFeF_3$ and NH_4FeF_3 cycled at C/10 towards potassium,* **(b)** *and* **(d)** *relative capacity retentions, respectively.* 135
Figure 6.9. *Ex situ XRD patterns of $KFeF_3$ cycled at C/20* **(a)** *towards sodium and* **(b) t***owards lithium.* 137
Figure 6.10. (a) *Ex situ XRD patterns of $KFeF_3$ cycled at C/20 towards potassium and* **(b)** *relative galvanostatic profile.* 138
Figure 6.11. (a) *Ex situ XRD patterns of NH_4FeF_3 cycled at C/20 towards lithium and* **(b)** *comparison between the NH_4FeF_3 and $KFeF_3$ at the 1^{st} and 50^{th} cycles towards lithium.* 139
Figure A6.1. *Examples of crystalline plans passing through the middle of the A-site of the cubic perovskite structure, namely here the plan (110) and (111).* 142
Figure A6.2. (a) *EDX measurement,* **(b)** *XRD pattern and* **(c)** *TEM images of $KFeF_3$ synthesized from FeF_2.* 142
Figure A6.3. (a) *XRD patterns of $KFeF_3$ synthesized from $Fe(ac)_2$ before and after ball-milling with CB, and* **(b)** *&* **(c)** *TEM images of $KFeF_3$ after ball-milling with CB.* 143
Figure A6.4. (a) *Capacity retentions of $KFeF_3$ cycled at C/10 with different cutoff potentials and* **(b)** *respective first galvanostatic discharge profiles.* 143
Figure A6.5. (a) *Ex situ XRD patterns of $KFeF_3$ cycled at C/20 towards sodium and* **(b)** *respective galvanostatic profile.* 144

List of tables

Table 2.1. *Main characteristics of the principal secondary cell technologies.* *20*
Table 2.2. *General characteristics of sodium and lithium elements* [62]. *21*
Table 4.1. *Summary of the synthesis parameter of the CoF_2 materials and nitrate remaining content of the precursor calculated from elemental analysis results (***Table A4.1***).* *60*
Table 4.2. (a) *Composition of the different CoF_2 synthesized compounds determined by EDX and* **(b)** *typical profile of an EDX graphic measurement (here, measurement of the CoF_2-6 sample)* *62*
Table 4.3. *Different atomic ratio measured by EDX experiment, as well as crystallite sizes of the FeF_2 synthesized from the chloride precursor calculated by the Scherrer equation.* *71*
Table.4.4. *2Θ position of the reflection (012) and size of the crystallites of the crystallite belonging to the R-3c phase of the materials milled during different times.*..... *78*
Table A4.1. *Atomic percentage composition obtained by Elemental Analysis and calculated nitrogen contents for the different decomposed precursors.* *93*
Table A4.2. *Crystallite sizes of the different CoF_2 synthesized compounds calculated by the Scherrer equation (as the particles are spherical, the shape factor has been taken as K = 0.87) and particle sizes observed by TEM.*..... *93*
Table A5.1. *Relative energies ($E - E_{ref}$ in meV/FU) and volumes ($Å^3$) of the A_xFeF_3 phase (A = Li, Na; x = 0, 0.5, 1) as obtained from full structural relaxation in spin-polarized DFT+U calculations. For each composition, the phase associated with the lowest energy is indicated in bold and the phase having converged towards another crystal-type are noted unstable. All structures were found more stable in the antiferromagnetic (AFM) state.* *121*
Table A6.1. *Relative intensities of the ex situ XRD patterns of* **(a)** *$KFeF_3$ towards sodium and the $NaFeF_3$ reference and* **(b)** *towards lithium and* **(c)** *towards potassium.* **(d)** *Relative intensities of the ex situ XRD patterns of NH_4FeF_3 cycles towards lithium. Plan highlighted in pink are passing through the A-site of the Pm-3m structure.* *144*

I declare that I have completed the thesis independently using only the aids and tools specified. I have not applied for a doctor's degree in the doctoral subject elsewhere and do not hold a corresponding doctor's degree. I have taken due note of the Faculty of Mathematics and Natural Sciences PhD Regulations, published in the Official Gazette of Humboldt-Universität zu Berlin no. 42/2018 on 11/07/2018.

I declare that the written and electronic version of the dissertation written by me in the University Library agrees with the accepted dissertation.